

# Applied Research Laboratory

AD-A207 008

## Technical Report

HIGH RESOLUTION ACOUSTICAL IMAGING

by

Kent Edward Eschenberg

DTIC  
SELECTED  
APR 13 1989  
H

PENNSTATE



DISTRIBUTION STATEMENT A

Approved for public release;  
Distribution Unlimited

89 4 73 062

4

The Pennsylvania State University  
**APPLIED RESEARCH LABORATORY**  
P.O. Box 30  
State College, PA 16804

**HIGH RESOLUTION ACOUSTICAL IMAGING**

by

Kent Edward Eschenberg

Technical Report No. TR 89-001

May 1989

Supported by:  
Naval Sea Systems Command

L.R. Hettche, Director  
Applied Research Laboratory

Approved for public release; distribution unlimited

DTIC  
ELECTE  
APR 13 1989  
S H D

Unclassified

SECURITY CLASSIFICATION OF THIS PAGE

## REPORT DOCUMENTATION PAGE

1a. REPORT SECURITY CLASSIFICATION Unclassified			1b. RESTRICTIVE MARKINGS		
2a. SECURITY CLASSIFICATION AUTHORITY			3. DISTRIBUTION / AVAILABILITY OF REPORT Approved for public release; distribution unlimited.		
2b. DECLASSIFICATION / DOWNGRADING SCHEDULE					
4. PERFORMING ORGANIZATION REPORT NUMBER(S) TR 89-001			5. MONITORING ORGANIZATION REPORT NUMBER(S)		
6a. NAME OF PERFORMING ORGANIZATION Applied Research Laboratory The Pennsylvania State University		6b. OFFICE SYMBOL (If applicable) ARL		7a. NAME OF MONITORING ORGANIZATION Naval Sea Systems Command Department of the Navy	
6c. ADDRESS (City, State, and ZIP Code) P. O. Box 30 State College, PA 16804			7b. ADDRESS (City, State, and ZIP Code) Washington, DC 20362		
8a. NAME OF FUNDING / SPONSORING ORGANIZATION Naval Sea Systems Command		8b. OFFICE SYMBOL (If applicable) NAVSEA		9. PROCUREMENT INSTRUMENT IDENTIFICATION NUMBER	
8c. ADDRESS (City, State, and ZIP Code) Department of the Navy Washington, DC 20362			10. SOURCE OF FUNDING NUMBERS		
			PROGRAM ELEMENT NO.	PROJECT NO.	TASK NO.
			WORK UNIT ACCESSION NO.		
11. TITLE (Include Security Classification) High Resolution Acoustical Imaging					
12. PERSONAL AUTHOR(S) K. E. Eschenberg					
13a. TYPE OF REPORT Ph.D. Thesis		13b. TIME COVERED FROM TO		14. DATE OF REPORT (Year, Month, Day) May 1989	
15. PAGE COUNT 260					
16. SUPPLEMENTARY NOTATION					
17. COSATI CODES			18. SUBJECT TERMS (Continue on reverse if necessary and identify by block number)		
FIELD	GROUP	SUB-GROUP			
			Acoustics, Acoustical imaging, Acoustical holography acoustic waves		
19. ABSTRACT (Continue on reverse if necessary and identify by block number)					
<p>Pressure waves, detected by an array of receivers, can be analyzed to determine the location of the acoustic source, or the location of objects which the waves encountered along their path. This thesis examines high resolution methods which use a linear array to locate stationary objects which have scattered the pressure waves. Several new methods are explored through simulations in air.</p> <p>A theoretical examination of all of the basic and high resolution acoustical imaging methods is first conducted. These methods include holographic reconstruction, beam-forming, a correlation method, autoregressive-moving average (ARMA) spectral estimators and minimum energy methods. This examination summarizes the well-known ability of these methods to locate sound sources while making some new observations on the ability of these methods to located sound scatterers.</p>					
20. DISTRIBUTION / AVAILABILITY OF ABSTRACT <input checked="" type="checkbox"/> UNCLASSIFIED/UNLIMITED <input type="checkbox"/> SAME AS RPT. <input type="checkbox"/> DTIC USERS			21. ABSTRACT SECURITY CLASSIFICATION Unclassified		
22a. NAME OF RESPONSIBLE INDIVIDUAL			22b. TELEPHONE (Include Area Code) (814) 865-6344		22c. OFFICE SYMBOL

DD FORM 1473, 84 MAR

83 APR edition may be used until exhausted.  
All other editions are obsolete.

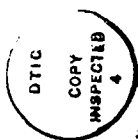
SECURITY CLASSIFICATION OF THIS PAGE

Unclassified

## 19 ABSTRACT - Continued

One of the methods which was examined used the concept of a fictitious source. This concept is developed to yield a new imaging approach called the pattern-match method which is similar to the temporal signal processing technique called the matched filter. In addition, a new technique for comparing signals is used to develop a variation of the pattern-match method called the mismatch method. A series of simulations is used to examine the ability of both methods to locate either one or two acoustic sources. Each simulation is also conducted using the well-known holographic method which thus serves as a point of reference. One new feature of some of these simulations is the introduction of a barrier which diffracts and reflects the pressure wave. It is shown that for many cases pattern matching can offer a superior image while the mismatch method offers a mixture of advantages and disadvantages.

While some imaging methods have used multiple frequencies, it was found that none exploited the fact that an object's scattering pattern can have a characteristic frequency dependence. This characteristic is used for the first time in a new method called swept-frequency imaging. A series of simulations is used to examine the ability of this method to locate a pair of point reflectors and a flat plate. A comparison to the well-known beamforming method indicates that the swept-frequency method is superior at moderate distances, and can be useful at all distances when combined with a range estimator.



Accession For	
NTIS GRA&I	<input checked="checked" type="checkbox"/>
DTIC TAB	<input type="checkbox"/>
Unannounced	<input type="checkbox"/>
Justification	
By	
Distribution/	
Availability Codes	
Avail and/or	
Dist	Special
A-1	



## Abstract

Pressure waves, detected by an array of receivers, can be analyzed to determine the location of the acoustic source, or the location of objects which the waves encountered along their path. This thesis examines high resolution methods which use a linear array to locate stationary objects which have scattered the pressure waves. Several new methods are explored through simulations in air.

A theoretical examination of all of the basic and high resolution acoustical imaging methods is first conducted. These methods include holographic reconstruction, beamforming, a correlation method, autoregressive-moving average (ARMA) spectral estimators and minimum energy methods. This examination summarizes the well-known ability of these methods to locate sound *sources* while making some new observations on the ability of these methods to located sound *scatterers*.

One of the methods which was examined used the concept of a fictitious source. This concept is developed to yield a new imaging approach called the pattern-match method which is similar to the temporal signal processing technique called the matched filter. In addition, a new technique for comparing signals is used to develop a variation of the pattern-match method called the mismatch method. A series of simulations is used to examine the ability of both methods to locate either one or two acoustic sources. Each simulation is also conducted using the well-known holographic method which thus serves as a point of reference. One new feature of some of these simulations is the introduction of a barrier which diffracts and reflects the pressure wave. It is shown that for many cases pattern matching can offer a superior image while the mismatch method

offers a mixture of advantages and disadvantages.

While some imaging methods have used multiple frequencies, it was found that none exploited the fact that an object's scattering pattern can have a characteristic frequency dependence. This characteristic is used for the first time in a new method called swept-frequency imaging. A series of simulations is used to examine the ability of this method to locate a pair of point reflectors and a flat plate. A comparison to the well-known beamforming method indicates that the swept-frequency method is superior at moderate distances, and can be useful at all distances when combined with a range estimator.

## Table of Contents

List of Figures .....	ix
List of Tables .....	xix
Acknowledgments .....	xxi
 Chapter 1. Introduction .....	 1
1.1. Motivation for the Study .....	1
1.2. Assumptions About the Energy Path .....	3
1.3. Scope of the Thesis .....	4
1.4. Definition of the Major Terms .....	4
 Chapter 2. Basic Issues in Array Processing .....	 9
2.1. Holographic Reconstruction .....	9
2.1.1. Holographic Assumptions .....	10
2.1.2. The Holographic Equation .....	11
2.1.3. Discrete Holography .....	13
2.1.4. Definition of Phase .....	15
2.1.5. Evanescent Waves .....	17
2.1.6. Some Limitations to the Holographic Approach .....	19
2.2. Beamforming .....	21
2.2.1. Bartlett Beamformer .....	21
2.2.2. Limitations of the Bartlett Acoustical Model .....	23
2.3. Receiver Correlations .....	25
2.3.1. Basic Correlation Method .....	26
2.3.2. Optimum Correlation Method .....	28
2.3.3. Comments on the Correlation Method .....	28
2.4. Pattern Matching .....	29
2.4.1. Fictitious Scatterers .....	30
2.4.2. Reconstruction as Pattern Matching .....	32
2.4.3. Beamforming as Pattern Matching .....	34
2.4.4. Correlation Method as Pattern Matching .....	34
2.5. Array Geometry .....	37
2.6. Time-of-Flight Information .....	39

## Table of Contents (continued)

Chapter 3. High Resolution Methods .....	43
3.1. Spectral Estimators .....	43
3.1.1. ARMA Methods .....	44
3.1.2. Options for the Subject of Estimation .....	45
3.1.3. Choosing the Estimator Parameters .....	47
3.1.4. The Maximum Entropy Method .....	48
3.1.5. Using the ARMA Methods to Locate Scatterers .....	49
3.2. Minimum Energy Methods .....	51
3.2.1. Discussion of the ME Method .....	51
3.2.2. Eigenvector Analysis .....	53
3.2.3. Linear Predictors .....	54
3.2.4. Using the ME Method in the Absence of Noise .....	55
3.2.5. Using the ME Method to Locate Scatterers .....	55
3.2.5.1. The ME Wave Model .....	56
3.2.5.2. Number of Sources .....	57
3.2.5.3. Coherent Sources .....	58
Chapter 4. Pattern-Match Imaging .....	61
4.1. Simulation of Edge Diffraction .....	61
4.1.1. Defining the Wave Disturbance .....	62
4.1.2. Angle Definitions .....	64
4.1.3. The Total Field .....	67
4.1.4. Shadow Boundary Approximation .....	68
4.1.5. Testing the Barrier Simulation .....	69
4.2. Mismatch Imaging .....	73
4.3. Normalization .....	75
4.4. Locating a Source in Free Space .....	77
4.5. Locating a Source Near a Reflector .....	89
4.6. Locating a Source Behind a Barrier .....	97
4.7. Environmental Errors .....	107
4.8. Locating Two Sources .....	114
4.9. Execution Times .....	119

## Table of Contents (continued)

Chapter 5. Swept-Frequency Imaging .....	121
5.1. Motivation for Sweeping the Frequency .....	121
5.2. Scattering Models .....	125
5.2.1. Specular Scatterers .....	125
5.2.2. Extended Scatterers .....	126
5.2.2.1. Scattering from a Rigid Plate .....	129
5.2.2.2. Plate Scattering Results .....	131
5.2.2.3. Comparison to Closed-Form Expressions .....	131
5.2.2.4. Numerical Suitability of the Summation .....	135
5.2.2.5. Number of Terms .....	139
5.2.2.6. Results Using Higher Precision .....	140
5.2.2.7. Scattering at Large Width-Wavelength Ratios .....	141
5.3. Interpolation .....	147
5.4. Development of the Analysis Method .....	148
5.4.1. Frequency Dependence .....	150
5.4.2. Forming a Swept-Frequency Image .....	158
5.4.3. Choosing the Frequencies .....	161
5.5. Locating Specular Scatterers .....	169
5.5.1. Specular Results at Different Ranges .....	172
5.5.2. Specular Results at Different Bearings .....	176
5.5.3. Specular Results with No Offsets .....	182
5.5.4. Results Using Two Sets of Specular Scatterers .....	182
5.6. Locating Extended Scatterers .....	188
5.6.1. Plate Results at Different Ranges .....	188
5.6.2. Plate Results at Different Bearings .....	192
5.6.3. Plate Results with No Offsets .....	199
5.6.4. Results Using Two Plate Scatterers .....	206
5.7. Comparison to Beam Forming .....	206
5.8. Results With Range Resolution .....	210
5.9. Swept-Frequency Execution Times .....	212

## Table of Contents (continued)

Chapter 6. Summary and Conclusions .....	215
6.1. Basic Issues .....	215
6.2. High Resolution Methods .....	216
6.2.1. ARMA Methods .....	216
6.2.2. ME Methods .....	217
6.3. Pattern-Match and Mismatch Imaging .....	218
6.3.1. Review of the Simulations .....	218
6.3.2. Future Work: Composite Sources .....	220
6.3.3. Future Work: Noise and Interference .....	220
6.3.4. Future Work: Mismatch Variations .....	221
6.3.5. Future Work: Time-of-Flight .....	222
6.4. Swept-Frequency Imaging .....	223
6.4.1. Review of Swept-Frequency Imaging .....	223
6.4.2. Future Work: Amplitude Dependence .....	224
6.4.3. Future Work: Phase Dependence .....	225
6.4.4. Future Work: Noise and Interference .....	226
6.4.5. Future Work: Use of Frequencies .....	226
6.4.6. Future Work: Scatterer Locations .....	227
References .....	229
Appendix. Fourier Derivation of the Holography Equation .....	237

## List of Figures

1.1	Path of pressure wave showing transmitter, scattering object, and receiver array. ....	5
2.1	Beam for source at 1 (solid line), 10 (large dashes), and 10,000 (small dashes) wavelengths. ....	24
4.1	Regions of the field scattered by a barrier, numbered according to the number of components used. The location of the region will change if the location of the source changes. ....	65
4.2	Magnitude of the pressure from a source $100\lambda$ away from the edge of a barrier. The field was evaluated at a radius of $10\lambda$ from the edge. ....	70
4.3	Phase of the pressure from a source $100\lambda$ away from the edge of a barrier. The field was evaluated at a radius of $10\lambda$ from the edge. ..	71
4.4	Magnitude, using the shadow-boundary approximation, of the pressure from a source $100\lambda$ away from the edge of a barrier. The field was evaluated at a radius of $10\lambda$ from the edge. ....	72
4.5	Signal at the receiving array due to the true source (solid line) at $(-5.25\lambda, 15\lambda)$ and the fictitious source (dashed line) at $(-4.75\lambda, 15\lambda)$ , after diffraction around a barrier and no normalization. ....	76
4.6	Signal at the receiving array due to the true source (solid line) at $(-5.25\lambda, 15\lambda)$ and the fictitious source (dashed line) at $(-4.75\lambda, 15\lambda)$ , after diffraction around a barrier and normalization. ....	78
4.7	Reconstruction using the pattern-match method, without normalization, of a point source at $(-5.25\lambda, 15\lambda)$ with diffraction by a barrier extending from $(0, 10\lambda)$ to $(-\infty, 10\lambda)$ . ....	79
4.8	Reconstruction using the mismatch method, without normalization, of a point source at $(-5.25\lambda, 15\lambda)$ with diffraction by a barrier extending from $(0, 10\lambda)$ to $(-\infty, 10\lambda)$ . ....	80
4.9	Holographic reconstruction at $Z = 15\lambda$ of a point source at $(0.25\lambda, 15\lambda)$ . ....	83
4.10	Holographic reconstruction of a point source at $(0.25\lambda, 15\lambda)$ ; contour lines are at 10%, 20%, ..., 90% of the maximum. ....	84

## List of Figures (continued)

4.11	Holographic reconstruction of a point source at $(0.25\lambda, 15\lambda)$ . . . . .	85
4.12	Pattern-match reconstruction of a point source at $(0.25\lambda, 15\lambda)$ . . . . .	86
4.13	Mismatch reconstruction of a point source at $(0.25\lambda, 15\lambda)$ with values below 15% of the maximum amplitude removed for clarity. . .	87
4.14	Mismatch reconstruction of a point source at $(0.25\lambda, 15\lambda)$ ; contour lines are at 10%, 20%, . . . , 90% of the maximum. . . . .	88
4.15	Magnitude of the pressure from a source at $(-5.25\lambda, 7.5\lambda)$ with a barrier extending from $(0, 10\lambda)$ to $(-\infty, 10\lambda)$ . The field was evaluated at a radius of $10\lambda$ from the edge. . . . .	90
4.16	Holographic reconstruction of a point source at $(-5.25\lambda, 7.5\lambda)$ with a barrier extending from $(0, 10\lambda)$ to $(-\infty, 10\lambda)$ . . . . .	91
4.17	Pattern-match reconstruction of a point source at $(-5.25\lambda, 7.5\lambda)$ with a barrier extending from $(0, 10\lambda)$ to $(-\infty, 10\lambda)$ ; contour lines are at 10%, 20%, . . . , 90% of the maximum. . . . .	92
4.18	Pattern-match reconstruction of a point source at $(-5.25\lambda, 7.5\lambda)$ with a barrier extending from $(0, 10\lambda)$ to $(-\infty, 10\lambda)$ . . . . .	94
4.19	Mismatch reconstruction of a point source at $(-5.25\lambda, 7.5\lambda)$ with a barrier extending from $(0, 10\lambda)$ to $(-\infty, 10\lambda)$ . Values below 10% of the maximum have been removed for clarity. . . . .	95
4.20	Mismatch reconstruction of a point source at $(-5.25\lambda, 7.5\lambda)$ with a barrier extending from $(0, 10\lambda)$ to $(-\infty, 10\lambda)$ ; contour lines are at 10%, 20%, . . . , 90% of the maximum. . . . .	96
4.21	Magnitude of the pressure from a source at $(0.25\lambda, 15\lambda)$ with a barrier extending from $(0, 10\lambda)$ to $(-\infty, 10\lambda)$ . The field was evaluated at a radius of $10\lambda$ from the edge. . . . .	98
4.22	Magnitude of the pressure from a source at $(-5.25\lambda, 15.0\lambda)$ with a barrier extending from $(0, 10\lambda)$ to $(-\infty, 10\lambda)$ . The field was evaluated at a radius of $10\lambda$ from the edge. . . . .	99
4.23	Holographic reconstruction of a point source at $(0.25\lambda, 15\lambda)$ with a barrier extending from $(0, 10\lambda)$ to $(-\infty, 10\lambda)$ ; contour lines are at 10%, 20%, . . . , 90% of the maximum. . . . .	100



## List of Figures (continued)

4.24	Holographic reconstruction of a point source at $(-2.25\lambda, 15\lambda)$ with a barrier extending from $(0, 10\lambda)$ to $(-\infty, 10\lambda)$ ; contour lines are at 10%, 20%, ..., 90% of the maximum. ....	101
4.25	Holographic reconstruction of a point source at $(-5.25\lambda, 15\lambda)$ with a barrier extending from $(0, 10\lambda)$ to $(-\infty, 10\lambda)$ ; contour lines are at 10%, 20%, ..., 90% of the maximum. ....	102
4.26	Pattern-match reconstruction of a point source at $(0.25\lambda, 15\lambda)$ with a barrier extending from $(0, 10\lambda)$ to $(-\infty, 10\lambda)$ ; contour lines are at 10%, 20%, ..., 90% of the maximum. ....	103
4.27	Pattern-match reconstruction of a point source at $(0.25\lambda, 15\lambda)$ with a barrier extending from $(0, 10\lambda)$ to $(-\infty, 10\lambda)$ . ....	104
4.28	Pattern-match reconstruction of a point source at $(-2.25\lambda, 15\lambda)$ with a barrier extending from $(0, 10\lambda)$ to $(-\infty, 10\lambda)$ . ....	105
4.29	Pattern-match reconstruction of a point source at $(-5.25\lambda, 15\lambda)$ with a barrier extending from $(0, 10\lambda)$ to $(-\infty, 10\lambda)$ . ....	106
4.30	Mismatch reconstruction of a point source at $(0.25\lambda, 15\lambda)$ with a barrier extending from $(0, 10\lambda)$ to $(-\infty, 10\lambda)$ ; contour lines are at 25%, 50%, and 75% of the maximum. ....	108
4.31	Mismatch reconstruction of a point source at $(0.25\lambda, 15\lambda)$ with a barrier extending from $(0, 10\lambda)$ to $(-\infty, 10\lambda)$ . Values below 50% of the maximum have been removed for clarity. ....	109
4.32	Mismatch reconstruction of a point source at $(-2.25\lambda, 15\lambda)$ with a barrier extending from $(0, 10\lambda)$ to $(-\infty, 10\lambda)$ ; contour lines are at 25%, 50%, and 75% of the maximum. ....	110
4.33	Mismatch reconstruction of a point source at $(-5.25\lambda, 15\lambda)$ with a barrier extending from $(0, 10\lambda)$ to $(-\infty, 10\lambda)$ ; contour lines are at 25%, 50%, and 75% of the maximum. ....	111
4.34	Pattern-match reconstruction, using a false barrier at $Z = 11\lambda$ , of a point source at $(0.25\lambda, 15\lambda)$ with a true barrier at $Z = 10\lambda$ ; contour lines are at 10%, 20%, ..., 90% of the maximum. ....	112
4.35	Mismatch reconstruction, using a false barrier at $Z = 11\lambda$ , of a point source at $(0.25\lambda, 15\lambda)$ with a true barrier at $Z = 10\lambda$ ; contour lines are at 10%, 20%, ..., 90% of the maximum. ....	113

## List of Figures (continued)

4.36	Pattern-match reconstruction of 2 sources, at $(0.25\lambda, 15\lambda)$ and $(10.25\lambda, 15\lambda)$ , with a barrier extending from $(0, 10\lambda)$ to $(-\infty, 10\lambda)$ ; contour lines are at 10%, 20%, ..., 90% of the maximum. ....	115
4.37	Pattern-match reconstruction of 2 sources, at $(0.25\lambda, 15\lambda)$ and $(10.25\lambda, 15\lambda)$ , with a barrier extending from $(0, 10\lambda)$ to $(-\infty, 10\lambda)$ . ....	116
4.38	Mismatch reconstruction of 2 sources, at $(0.25\lambda, 15\lambda)$ and $(10.25\lambda, 15\lambda)$ , with a barrier extending from $(0, 10\lambda)$ to $(-\infty, 10\lambda)$ ; contour lines are at 10%, 20%, ..., 90% of the maximum. ....	117
4.39	Mismatch reconstruction of 2 sources, at $(0.25\lambda, 15\lambda)$ and $(10.25\lambda, 15\lambda)$ , with a barrier extending from $(0, 10\lambda)$ to $(-\infty, 10\lambda)$ . Values below 50% of the maximum have been removed for clarity. ....	118
5.1	Arrangement of components of a proposed imaging system where the transmitter produces a sweep of frequencies. ....	123
5.2	Definition of the equivalent scan vectors in a proposed swept-frequency imaging system. ....	124
5.3	Magnitude of the pressure from a 13,045.2 Hz source at $0^\circ$ , scattered by two point reflectors at the origin and separated by 12". The wavelength is 1". ....	127
5.4	Phase of the pressure from a 13,045.2 Hz source at $0^\circ$ , scattered by two point reflectors at the origin and separated by 12". The wavelength is 1". ....	128
5.5	Magnitude of the pressure from a 13,045.2 Hz source at $0^\circ$ , scattered by a 12" plate. The summation used 200 terms of width 0.06" ( $0.06\lambda$ ). ....	132
5.6	Phase of the pressure from a 13,045.2 Hz source at $0^\circ$ , scattered by a 12" plate. The summation used 200 terms of width 0.06" ( $0.06\lambda$ ). ....	133
5.7	Magnitude of the pressure from a 13,045.2 Hz source at $-45^\circ$ , scattered by a 12" plate at the origin. The summation used 200 terms of width 0.06" ( $0.06\lambda$ ). ....	134

## List of Figures (continued)

- 5.8 Accumulated Huygens-Rayleigh sum as we move across the plate from  $X = -12''$  (the end of the curve with the heavy line) to  $X = +12''$ . The receiver and 13,045.2 Hz source were 100" away at  $0^\circ$ . ..... 137
- 5.9 Individual Huygens-Rayleigh terms as we move across the plate from  $X = -12''$  (the end of the curve with the heavy line) to  $X = +12''$ . The receiver and 13,045.2 Hz source were 100" away at  $0^\circ$ . ..... 138
- 5.10 Magnitude of the pressure from a 30,500 Hz source at  $0^\circ$ , scattered by a 12" plate. The summation used 200 terms of width 0.06" ( $0.140\lambda$ ). ..... 142
- 5.11 Magnitude of the pressure from a source at the origin, scattered by a 12" plate 100" away. The summation used 200 terms of width 0.06". The wavelength varies from 1.305" to 0.177". ..... 143
- 5.12 Magnitude of the pressure from a 13,045.2 Hz source at  $0^\circ$ , scattered by a 48" plate. The summation used 200 terms of width 0.24" ( $0.24\lambda$ ). ..... 144
- 5.13 Magnitude of the pressure from a 13,045.2 Hz source at the origin, scattered by a plate 100" away. The summation used 200 terms of width 0.06" ( $0.06\lambda$ ). ..... 145
- 5.14 Values interpolated using a piecewise cubic polynomial (line) and the control points (large circles) used in the interpolation. Additional values (small circles) are shown for comparison. ..... 149
- 5.15 Patterns at an array on the X-axis (64 receivers) versus frequency (50 frequencies, 250 Hz apart), due to 2 point reflectors centered at  $(-20'', 100'')$  and a source at  $(20'', 0)$ . ..... 153
- 5.16 Patterns, due to 2 point reflectors, at an array, versus frequency. The pattern at each frequency, except 30,000 Hz, has been shifting so as to approximate a pattern at 30,000 Hz. ..... 155
- 5.17 Superimposed shifted patterns, due to 2 point reflectors, at an array, versus frequency. As the frequency decreases, the pattern goes to 0 at a decreasing location in the receiver array. ..... 156
- 5.18 Superimposed shifted patterns, due to plate, at an array, versus frequency. As the frequency decreases, the pattern goes to 0 at a decreasing location in the receiver array. ..... 157

### List of Figures (continued)

5.19	Swept-frequency reconstruction of 2 point reflectors at $Z = 100''$ using $\Delta f = 2.5$ kHz (27.5 and 30 kHz). . . . .	163
5.20	Swept-frequency reconstruction of 2 point reflectors at $Z = 100''$ using $\Delta f = 5$ kHz (25 and 30 kHz). . . . .	164
5.21	Swept-frequency reconstruction of 2 point reflectors at $Z = 100''$ using $\Delta f = 10$ kHz (20 and 30 kHz). . . . .	165
5.22	Swept-frequency reconstruction of 2 point reflectors at $Z = 100''$ using 3 pairs of frequencies having $\Delta f = 5$ kHz (15 and 20 kHz, 20 and 25 kHz, and 25 and 30 kHz). . . . .	167
5.23	Swept-frequency reconstruction of 2 point reflectors at $Z = 100''$ using $\Delta f = 5$ kHz at relatively low frequencies (10 and 15 kHz). . . .	168
5.24	Swept-frequency reconstruction of 2 point reflectors at $Z = 100''$ using a logarithmic distribution of 20 frequencies (10 to 30 kHz) where the value of $\Delta f$ is from 421.5 to 20,000 Hz. . . . .	171
5.25	Swept-frequency reconstruction of 2 point reflectors centered at $(-20'', 25'')$ with a source at $(20'', 0)$ . . . . .	173
5.26	Swept-frequency reconstruction of 2 point reflectors centered at $(-20'', 25'')$ with a source at $(20'', 0)$ , showing a small amount of error in the location of the maximum. . . . .	174
5.27	Swept-frequency reconstruction of 2 point reflectors centered at $(-20'', 25'')$ with a source at $(20'', 0)$ , showing sparse comparisons (spikes) and missed comparisons (plateaus). . . . .	175
5.28	Swept-frequency reconstruction of 2 point reflectors centered at $(-20'', 50'')$ with a source at $(20'', 0)$ . . . . .	177
5.29	Swept-frequency reconstruction of 2 point reflectors centered at $(-20'', 50'')$ with a source at $(20'', 0)$ , showing sparse comparisons (spikes) and missed comparisons (plateaus). . . . .	178
5.30	Swept-frequency reconstruction of 2 point reflectors centered at $(-20'', 100'')$ with a source at $(20'', 0)$ . . . . .	179
5.31	Swept-frequency reconstruction at $Z=400''$ of 2 point reflectors centered at $(-20'', 400'')$ with a source at $(20'', 0)$ . . . . .	180

## List of Figures (continued)

5.32	Swept-frequency reconstruction of 2 point reflectors centered at (0, 50") with a source at (20", 0). . . . .	181
5.33	Swept-frequency reconstruction of 2 point reflectors centered at (0, 50") with a source at (20", 0), showing sparse comparisons (spikes) and missed comparisons (plateaus). . . . .	183
5.34	Swept-frequency reconstruction of 2 point reflectors centered at (20", 50") with a source at (20", 0). . . . .	184
5.35	Swept-frequency reconstruction of 2 point reflectors centered at (20", 50") with a source at (20", 0), showing sparse comparisons (spikes) and missed comparisons (plateaus). . . . .	185
5.36	Swept-frequency reconstruction of 2 point reflectors centered at (0, 50") with a source at (0, 0). . . . .	186
5.37	Swept-frequency reconstruction of 2 point reflectors centered at (0, 50") with a source at (0, 0), showing sparse comparisons (spikes) and missed comparisons (plateaus). . . . .	187
5.38	Swept-frequency reconstruction of 4 point reflectors at $Z = 50''$ and $X = -26''$ , $X = -14''$ , $X = -6''$ and $X = 6''$ with a source at (20", 0). . . . .	189
5.39	Swept-frequency reconstruction of 4 point reflectors at $Z = 50''$ and $X = -26''$ , $X = -14''$ , $X = -6''$ and $X = 6''$ with a source at (20", 0); also showing sparse and missed comparisons. . . . .	190
5.40	Swept-frequency reconstruction of 4 point reflectors at $Z = 50''$ and $X = -26''$ , $X = -14''$ , $X = -6''$ and $X = 6''$ with a source at (20", 0). Match has been renormalized to maximum value in plot. . . . .	191
5.41	Swept-frequency reconstruction of a 12" plate centered at (-20", 25") with a source at (20", 0). . . . .	193
5.42	Swept-frequency reconstruction of a 12" plate centered at (-20", 25") with a source at (20", 0), showing sparse comparisons (spikes) and missed comparisons (plateaus). . . . .	194
5.43	Swept-frequency reconstruction of a 12" plate centered at (-20", 50") with a source at (20", 0). . . . .	195

### List of Figures (continued)

5.44	Swept-frequency reconstruction of a 12" plate centered at $(-20", 50")$ with a source at $(20", 0)$ , showing sparse comparisons (spikes) and missed comparisons (plateaus). . . . .	196
5.45	Swept-frequency reconstruction of a 12" plate centered at $(-20", 100")$ with a source at $(20", 0)$ . . . . .	197
5.46	Swept-frequency reconstruction of a 12" plate centered at $(0, 50")$ with a source at $(20", 0)$ . . . . .	198
5.47	Swept-frequency reconstruction of a 12" plate centered at $(0, 50")$ with a source at $(20", 0)$ , showing sparse comparisons (spikes) and missed comparisons (plateaus). . . . .	200
5.48	Swept-frequency reconstruction of a 12" plate centered at $(20", 50")$ with a source at $(20", 0)$ . . . . .	201
5.49	Swept-frequency reconstruction of a 12" plate centered at $(20", 50")$ with a source at $(20", 0)$ , showing missed comparisons (plateaus). . . . .	202
5.50	Patterns at an array on the X-axis (64 receivers) for 30 kHz (solid line) and 20 kHz (dashed line), due to a 12" plate centered at $(20", 50")$ and a source at $(20", 0)$ . . . . .	203
5.51	Swept-frequency reconstruction of a 12" plate centered at $(0, 50")$ with a source at $(0, 0)$ . . . . .	204
5.52	Swept-frequency reconstruction of a 12" plate centered at $(0, 50")$ with a source at $(0, 0)$ , showing sparse comparisons (spikes) and missed comparisons (plateaus). . . . .	205
5.53	Swept-frequency reconstruction of two 12" plates centered at $(-20", 50")$ and $(0, 50")$ with a source at $(0, 0)$ . . . . .	207
5.54	Swept-frequency reconstruction of two 12" plates centered at $(-20", 50")$ and $(0, 50")$ with a source at $(20", 0)$ , showing missed comparisons (plateaus). . . . .	208
5.55	Reconstruction using swept-frequencies and 2 reflectors (solid line); beam forming and 1 reflector (long dashes); and beam forming and 2 reflectors (short dashes). All reflectors at $Z = 1000"$ . . . . .	209

**List of Figures (continued)**

- 5.56 Reconstruction using swept-frequencies and 2 reflectors (solid line); beam forming and 1 reflector (long dashes); and beam forming and 2 reflectors (short dashes). All reflectors at  $Z = 100''$ . . . . . 211
- 5.57 Swept-frequency reconstruction of 2 point reflectors centered at  $(-20'', 100'')$ , for a source at  $(20'', 0)$ , with simulated range resolution for a bandwidth of 421.5 Hz. . . . . 213
- 5.58 Swept-frequency reconstruction of 2 point reflectors centered at  $(-20'', 100'')$ , for a source at  $(20'', 0)$ , with simulated range resolution for a bandwidth of 20,000 Hz. . . . . 214





## List of Tables

4.1	Rules for determining the region number. ....	67
4.2	Time to reconstruct the images. ....	120
5.1	Maximum angle at which the Fraunhofer approximation is valid. ...	136
5.2	Normalized complex signal at 13,045.2 Hz and 45°. ....	139
5.3	Normalized complex signal at 30,000 Hz and 0°. ....	140
5.4	Logarithmic set of frequency comparisons. ....	170

## Acknowledgments

The author wishes to express his deep appreciation of the encouragement and patience extended to him by his thesis committee and, in particular, by his thesis advisor, Dr. S. I. Hayek, without whom this study could not have been completed. Support for this research was provided through the Applied Research Laboratory's Exploratory and Foundational Research Program. A large debt of gratitude is also owed to my parents for their unfailing financial and moral support.

## Chapter 1

### Introduction

Pressure waves, detected by an array of receivers, can be analyzed to determine the location of the acoustic source, or the location of objects which the waves encountered along their path. This thesis studies those methods of analysis which can provide particularly precise estimates of the locations. Such methods are typically referred to as "super-directivity," "super-resolution," or "optimum" processors.

Subsequent sections of this introduction will describe the questions which motivated the study, list the assumptions which will be used in the analysis of the pressure waves, state the scope of the study, and then conclude with a specification of some of the symbols and relationships used in subsequent chapters.

#### 1.1 Motivation for the Study

Theory and experience in the processing of the signals obtained from an array of receivers has accumulated steadily, with one of the earliest investigations being reported by Oseen<sup>1</sup> in 1922. Because arrays and pressure waves constitute a very general phenomenon, related discoveries have been made in many different disciplines. This has resulted, as pointed out by Miller,<sup>2</sup> in the same fundamental principle sometimes being discovered more than once.

As the basic concepts of existing methods were studied, it became clear that, because of the inter-disciplinary nature of the problem, it was possible that discoveries in one field might have been overlooked by workers in another. Thus,

one motivation for this study was to consider combinations of methods, from perhaps different disciplines, which could be combined in new and productive ways. In particular, the approach of using a "fictitious source," discussed in Chapter 2, is combined with the concept of a matched filter in Chapter 4 to develop two new imaging algorithms called the pattern-match and mismatch methods.

Most previous work has concentrated quite naturally on the pragmatic cases where one wishes to locate a sound source in noise. Some of the more imaginative methods are non-linear or iterative and so defy both traditional closed-form analysis and a straightforward conceptual understanding. The author's interest was thus piqued by the following question: which methods are primarily for noise suppression, and which are utilizing some new insight into the underlying wave phenomena? In addition, we wished to know if these methods, which were developed for waves from sound *sources*, could also be applied to waves from sound *scatterers*. The answer to these questions could be useful in matching the various methods to a given problem.

Finally, several methods touched upon the idea of using a swept-frequency transmitted signal. Indeed, linear FM sweeps have long been used. However, many methods were built upon the assumption that the object which was encountered by the pressure wave was a point-reflector; such an assumption, it seemed, may cause potentially useful information to be lost. A final motivation, then, was to explore a new frequency-swept method which was built upon the assumption of frequency-dependent scattering from these objects.

## 1.2 Assumptions About the Propagation Path

The modeling of the complex phenomenon of a realistic environment is certainly a worthy and demanding pursuit; however, in this study, a far simpler situation will be modeled in order that the fundamental principles can be better understood and simulated.

This study will generally assume that the wave phenomenon occurs in an isotropic, unbounded medium wherein the speed of sound is known and damping is negligible. Wave propagation will be modeled as spherical or planar compressional waves obeying the linear wave equation.

In most cases, the source of the pressure waves will be an omni-directional transmitter whose location is known and which can broadcast acoustic energy of any desired temporal pattern. This pattern will typically be a windowed sine wave at a given frequency, or a series of such sine waves which step through a set of frequencies. Amplitudes will be arbitrary but shall be low enough that the assumption of linear propagation is valid. These assumptions effectively eliminate any question about the location of the source of the pressure waves; thus, this study will focus on discovering the precise location of objects which the waves encountered along their path. However, many methods, which were originally developed to find the source of acoustic energy, can be recast to find these objects.

The detection of the pressure waves will be simulated as an equidistant line array of omni-directional, linear receivers. Except for certain non-linear spectral estimators, the relationship between a one- and two-dimensional array is straightforward and so this study will be limited to the one-dimensional array.

It will be assumed that the objects which are encountered by the waves have a velocity of zero. When more than one object is encountered, it will be assumed that the Born approximation for weak scattering can be applied. Most objects will be modeled as point scatterers, spheres, or disks.

### 1.3 Scope of the Thesis

We wish to find methods, given the assumptions described in Section 1.2, for analyzing samples  $R_i$  of the amplitude of an pressure wave which yield, with the highest possible precision, the location of the object or objects encountered by the pressure wave. The samples will be obtained at locations  $X_i$  which are equally spaced along a line. In the pursuit of these methods, all the existing basic and high resolution methods will be considered; the most promising concepts, along with some new approaches, will be combined to form several new acoustic imaging methods which will then be explored through simulations.

### 1.4 Definition of the Major Terms

The path of the pressure wave begins at the transmitter which is located at position  $(X^E, Z^E)$  as shown in Figure 1.1. The pattern for a windowed sine wave of angular frequency  $\omega (= 2\pi f)$  is given by

$$E(t) = \begin{cases} \sin(\omega t), & \text{if } 0 \leq t \leq T; \\ 0, & \text{otherwise} \end{cases} \quad (1.1)$$

where the period or duration of the signal is  $T$  and the time  $t$  is continuous.

The wave next encounters an object at some unknown position  $(X^S, Z^S)$  with a scattering function  $S(\phi^R | \phi^E)$ . For a point scatterer,  $S$  is a constant (usually 1). Otherwise, it is a function of two angles which are defined relative to

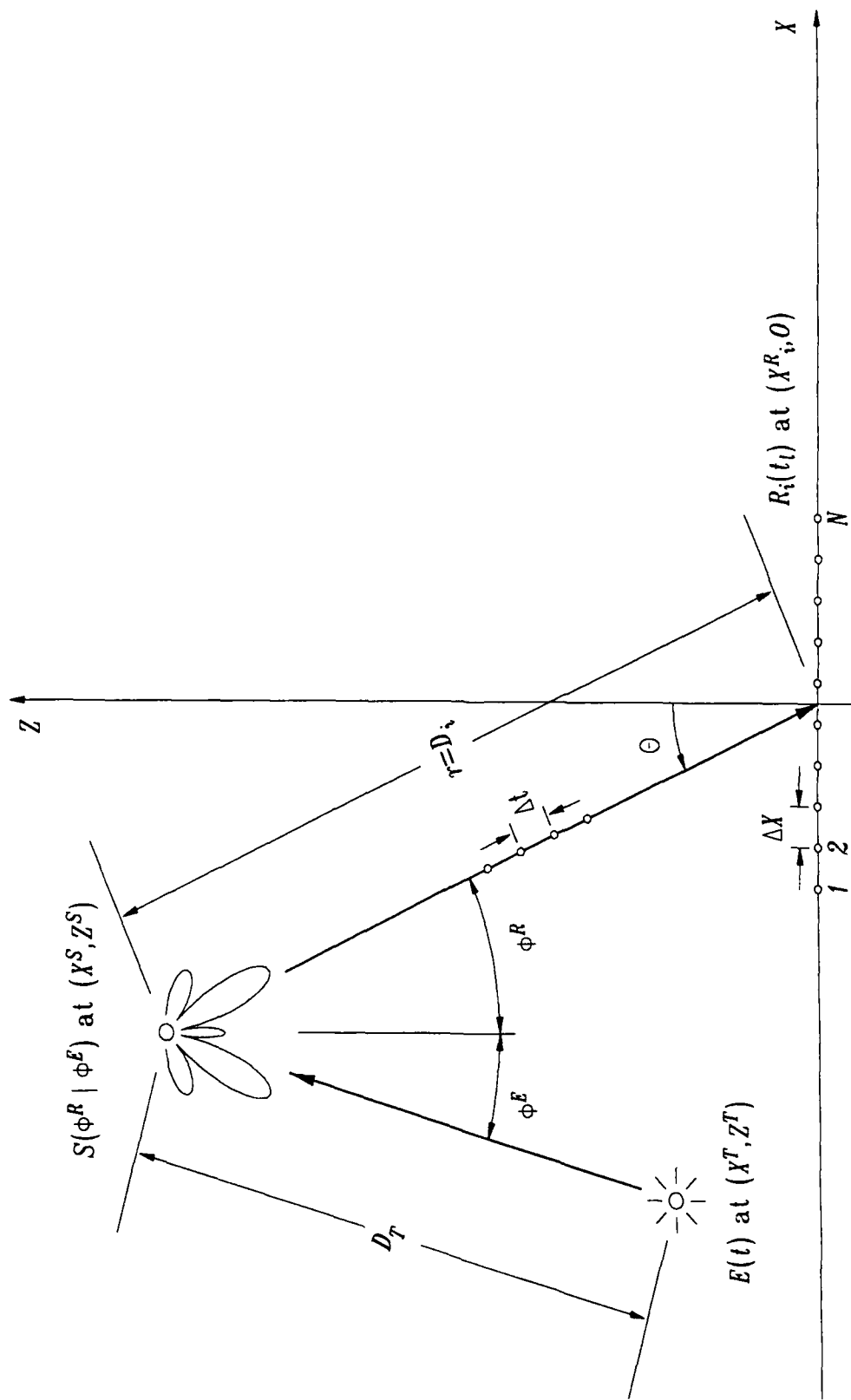


Figure 1.1. Path of pressure wave showing transmitter, scattering object, and receiver array. 57

the scatterer. Given that the pressure wave is arriving at angle  $\phi^E$ , the scattering function then gives the amplitude of the wave which is reflected into the angle  $\phi^R$ . The scattering function will be simulated in most cases as causing no phase shift, i.e., it is a real rather than complex function. When we need to consider more than one scattering object, each object will be at position  $(X_m^S, Z_m^S)$  with scattering function  $S_m(\phi_m^R | \phi_m^E)$  for  $1 \leq m \leq N^S$  where there are  $N^S$  objects.

The pressure wave is sampled at the receivers located at positions  $(X_i^R, 0)$  for  $1 \leq i \leq N^R$  where there are  $N^R$  receivers. The difference between any two receiver positions (the spatial sampling interval) is  $\Delta X$ . The  $Z$  coordinate is always zero since we have chosen to place the line array along the  $X$ -axis. The amplitude of the pressure wave  $R_i(t_l)$  are sampled at times  $t_l$  for  $1 \leq l \leq N^T$  where there are  $N^T$  time samples. The difference between any two time samples (the temporal sampling interval) is  $\Delta t$ .

The signal detected at each receiver can be represented as the linear sum of the pressure reflected from the one or more objects:

$$R_i(t_l) = \sum_{m=1}^{N^S} \frac{1}{D_{im} \cdot D_{Tm}} S_m(\phi_m^E, \phi_m^R) \cdot E(t_l - T_{im}^F); \quad (1.2)$$

$$r = D_{im} = \sqrt{(X_i^R - X_m^S)^2 + (Z_m^S)^2}; \quad (1.3)$$

$$D_{Tm} = \sqrt{(X^T - X_m^S)^2 + (Z^T - Z_m^S)^2}; \quad \text{and} \quad (1.4)$$

$$T_{im}^F = \frac{D_{im} + D_{Tm}}{c}. \quad (1.5)$$

The time of flight  $T_{im}^F$  from the transmitter to the  $i^{th}$  receiver via a reflection from the  $m^{th}$  object is calculated using the length of the flight path, composed of the path from the transmitter to an object (distance  $D_{Tm}$ ) plus the path from



the object to a receiver (distance  $D_{im}$ ), for waves traveling at the speed of sound  $c$  where  $c = \lambda f$ .

When the locations of the objects are known, they can be combined with the location of the transmitter and receivers to compute the scattering angles as

$$\phi_m^E = \arctan \left( \frac{X_m^T - X_m^S}{Z_m^S - Z^T} \right), \quad \text{and} \quad (1.6)$$

$$\phi_m^R = \arctan \left( \frac{X_m^S - X_i^R}{Z_m^S} \right). \quad (1.7)$$

A matrix notation will be used in some cases so that some of the above quantities can be expressed more compactly as

$$\mathbf{R}(t_l) = [R_1(t_l) \ R_2(t_l) \ \dots \ R_N(t_l)]^T \quad \text{and} \quad (1.8)$$

$$\mathbf{X}^R = [X_1^R \ X_2^R \ \dots \ X_N^R]^T \quad (1.9)$$

where  $T$  denotes the transpose operation which make these representations column vectors. When there is only one object, Eq. (1.8) becomes

$$\begin{aligned} \mathbf{R}(t_l) = & \left[ \frac{1}{D_1 \cdot D_T} S(\phi^R | \phi^E) \cdot E(t_l - T_1^F) \right. \\ & \dots \frac{1}{D_i \cdot D_T} S(\phi^R | \phi^E) \cdot E(t_l - T_i^F) \\ & \left. \dots \frac{1}{D_N \cdot D_T} S(\phi^R | \phi^E) \cdot E(t_l - T_N^F) \right]^T \end{aligned} \quad (1.10)$$

where the implicit subscript on  $S$  and the implicit second subscript on  $T^F$  is 1 since there is only one object.



## Chapter 2

### Basic Issues in Array Processing

Subsequent chapters will investigate how various processing methods can increase a receiver array's resolution. This chapter will lay the groundwork for those investigations by examining the basic approaches and issues.

The problem being addressed by this study has been approached from several points of view in various fields which seem, at first glance, to be only vaguely related. This does not seem reasonable, however, since the underlying physics is the same in each case. Therefore, we wish to roughly categorize these approaches, and then seek a unified approach to which all the others are special cases. We expect the various cases to differ only in the nature of their assumptions or their requirement of *a priori* information.

#### 2.1 Holographic Reconstruction

In the traditional study of the propagation of pressure waves, the interaction of the waves with an object is categorized as diffraction. The problem we are addressing in this study is then categorized as *inverse* diffraction. In particular, the holographic reconstruction methods use inverse diffraction to recreate or reconstruct the pressure field in the vicinity of objects which are either scatterers or are themselves acoustic sources.

### 2.1.1 Holographic Assumptions

In the typical three-dimensional case, the receivers are equally spaced across a planar grid, and the objects are assumed to be located on a plane which is parallel to the receiver plane. For this reason, most holographic studies have concentrated on reconstructing this object plane which is then interpreted as an "image" of the objects. The image can be formed to represent the amplitude or phase of the pressure, the vector velocity, the vector intensity, or other quantities.

The interpretation of the image is by no means deterministic - it depends upon the expected nature of the objects. If point objects are expected, each point of the image could be interpreted as the amplitude of the object located at that point where amplitudes which fall below some threshold would indicate that no object is present. On the other hand, if extended objects are expected, each point of the image could be interpreted as the amplitude of the pressure scattered or generated at that location on the object.

The earliest holographic work, such as that by Graham<sup>3</sup> and Watson,<sup>4,5</sup> used optical methods to process the information. This background, and the limited speed of the computers of the time, seems to have motivated the early users of digital processing to make the Fraunhofer or Fresnel approximation as it eliminated the evaluation of a square root in the algorithm. With the work of IBM's VanRooy,<sup>6,7</sup> digital processing eliminated this approximation and the approach became, therefore, valid for both the near and far fields. VanRooy was also one of the first to apply the Fast Fourier Transform (FFT) which significantly reduced the computer time needed; his basic algorithm continues to be used over a decade later for holographic reconstructions in studies such as those by

Stepanishen and Benjamin,<sup>8</sup> Eschenberg and Hayek,<sup>9,10,11</sup> and Williams *et al.*<sup>12</sup>

### 2.1.2 The Holographic Equation

A variety of methods can be used to develop the holographic equation which expresses the pressure field in the object plane as a function of the measured field in the receiver or hologram plane. Cohen<sup>13</sup> used the Rayleigh integral, expressed as a convolution in the space domain and as a multiplication in the spatial frequency domain, to develop his method of processing. Another approach based upon a Fourier transform of the wave equation is shown in Appendix A.

One of the earliest, and still most elegant, developments was provided by Goodman.<sup>14</sup> In the two-dimensional system of this study, the Helmholtz wave equation for harmonic time dependence becomes

$$\nabla^2 R(x, z) + k^2 R(x, z) = \frac{\partial^2 R(x, z)}{\partial x^2} + \frac{\partial^2 R(x, z)}{\partial z^2} + k^2 R(x, z) = 0. \quad (2.1)$$

The signal  $R(x, z)$  can be written in terms of an inverse Fourier transform as

$$\begin{aligned} R(x, z) &= \mathcal{F}^{-1}(\tilde{R}(k_x, z)) \\ &= \frac{1}{\sqrt{2\pi}} \int_{-\infty}^{+\infty} \tilde{R}(k_x, z) \cdot \exp(-j k_x x) dk_x \end{aligned} \quad (2.2)$$

where  $\mathcal{F}^{-1}$  represents the inverse Fourier transform while  $\mathcal{F}$  and  $\tilde{R}$  represents the forward Fourier transform as given by

$$\mathcal{F}(R(x, z)) = \tilde{R}(k_x, z) = \frac{1}{\sqrt{2\pi}} \int_{-\infty}^{+\infty} R(x, z) \cdot \exp(j k_x x) dx. \quad (2.3)$$

The letter  $j$  denotes the square root of minus one. These definitions of the forward and inverse seem to agree with the majority of scientific users of the Fourier

transform<sup>13</sup> but are reversed from some, including the ones used in some previous work by the author.<sup>11</sup> However, simulations have proven that these definitions can be reversed with no effect on, at least, the reconstructed pressure amplitude. Upon substitution of Eq. (2.2) into Eq. (2.1), we note that the integrand of the first term becomes  $-k_x^2 \tilde{R}(k_x, z)$ . Using the relationship between the components of the wavenumber,

$$k^2 = k_x^2 + k_z^2, \quad (2.4)$$

we can combine the integrands to yield

$$\frac{1}{\sqrt{2\pi}} \int_{-\infty}^{+\infty} \left[ \frac{\partial^2 \tilde{R}(k_x, z)}{\partial z^2} + k_z^2 \tilde{R}(k_x, z) \right] \exp(-j k_x x) dk_x = 0. \quad (2.5)$$

The integral can only be zero for all values of the independent variable  $x$  if its integrand is zero; thus, we can write

$$\frac{\partial^2 \tilde{R}(k_x, z)}{\partial z^2} + k_z^2 \tilde{R}(k_x, z) = 0 \quad (2.6)$$

which is the transformed version of the wave equation. One solution to this differential equation is

$$\tilde{R}(k_x, z) = \tilde{R}(k_x, 0) \cdot \exp(j k_z z) \quad (2.7)$$

where  $\tilde{R}(k_x, 0)$  is often written as  $\tilde{R}^H(k_x)$  to emphasize that it is measured in the receiver or hologram plane. Finally, we can substitute Eq. (2.7) into Eq. (2.2) so that the field for a plane at any location  $z$  can be written as

$$R(x, z) = \frac{1}{\sqrt{2\pi}} \int_{-\infty}^{+\infty} \tilde{R}^H(k_x) \cdot \exp(j k_z z - j k_x x) dk_x. \quad (2.8)$$

It is sometimes useful to refer to that part of this equation which represents

the effects of propagation through space as the Green's function in the spatial frequency domain:

$$\tilde{G}(k_z) = \exp(j k_z z). \quad (2.9)$$

### 2.1.3 Discrete Holography

The conversion of the continuous version of the holography equation, Eq. (2.8), to its discrete, sampled form has been described previously<sup>11,13</sup> but is repeated here for completeness, using the terminology of this study. Beginning with the forward Fourier transform of the hologram, Eq. (2.3), we replace the continuous variables with the discrete variables:

$$\begin{aligned} dx &\rightarrow \Delta X, \\ x &\rightarrow i \Delta X, \\ dk_x &\rightarrow \Delta K_x = \frac{2\pi}{L}, \\ L &= N^R \Delta X, \\ k_x &\rightarrow q \Delta K_x \end{aligned} \quad (2.10)$$

It is important to note that the receiver aperture size  $L$  is *not* merely the distance between the receivers at the ends of the array but is  $\Delta X$  larger than that distance. The signal in the receiver aperture,  $R^H(x)$ , is now sampled at the discrete receiver locations  $X_i^R = i \Delta X$  and so could be written  $R^H(i \Delta X)$  or just  $R_i^H$ . Likewise, the signal in the spatial frequency domain is sampled and so  $\tilde{R}^H(k_x)$  becomes  $\tilde{R}^H(q \Delta K_x)$  or just  $\tilde{R}_q^H$ . Substituting into Eq. (2.3), the forward transform becomes

$$\tilde{R}_q^H = \frac{\Delta X}{\sqrt{2\pi}} \sum_{i=1}^{N^R} R_i^H \cdot \exp(j q \Delta K_x i \Delta X). \quad (2.11)$$

With similar substitutions, the holographic reconstruction, Eq. (2.8), becomes

$$R(x, z) = \frac{\Delta K_x}{\sqrt{2\pi}} \sum_{q=1}^{N^R} \tilde{R}_q^H \cdot \exp(j k_z z - j x q \Delta K_x) \quad (2.12)$$

with

$$\begin{aligned} k_z &= \sqrt{k^2 - (q \Delta K_x)^2} \\ &= \sqrt{\left(\frac{2\pi f}{c}\right)^2 - (q \Delta K_x)^2}. \end{aligned} \quad (2.13)$$

Eq. (2.12) is valid for any value of  $R$ 's argument, the continuous variables  $x$  and  $z$ . However, if this is to be implemented as an FFT, we must also convert  $x$  to its discrete form so that we have

$$R(i \Delta X, z) = R_i(z) = \frac{\Delta K_x}{\sqrt{2\pi}} \sum_{q=1}^{N^R} \tilde{R}_q^H \cdot \exp(j k_z z - j q \Delta K_x i \Delta X). \quad (2.14)$$

In many studies, the indices used in discrete equations are arranged so that they, as well as the discrete values of  $x$  and  $k_x$ , are more or less symmetrical about zero. That is, the indices are transformed so that

$$\begin{aligned} 1 \leq i \leq N^R &\rightarrow -\frac{1}{2}N^R \leq i \leq \frac{1}{2}N^R - 1, \\ 1 \leq q \leq N^R &\rightarrow -\frac{1}{2}N^R \leq q \leq \frac{1}{2}N^R - 1. \end{aligned} \quad (2.15)$$

Note that since 0 is included in the shifted domain, we must subtract 1 from one of the limits so that the total number of points continues to be  $N^R$ . As is obvious from Eq. (2.11), these shifts are equivalent to adding a constant value to the phase of the results; therefore, we can choose whichever domain we prefer as long as we are consistent.

There are two reasons for shifting the domain of  $q$ . First, a symmetrical



domain reflects the fact that both positive and negative spatial frequencies are involved. That is, index  $q$  refers to positive and negative spatial frequencies as follows:

$$\text{unshifted: } \begin{cases} 1 \leq q \leq \frac{1}{2}N^R + 1, & \text{positive spatial frequencies;} \\ \frac{1}{2}N^R + 2 \leq q \leq N^R, & \text{negative spatial frequencies;} \end{cases} \quad (2.16)$$

and

$$\text{shifted: } \begin{cases} 0 \leq q \leq \frac{1}{2}N^R, & \text{positive spatial frequencies;} \\ -\frac{1}{2}N^R + 1 \leq q \leq -1, & \text{negative spatial frequencies.} \end{cases} \quad (2.17)$$

Second, most computer implementations of the FFT are arranged so that the spatial frequencies are returned in the order of the shifted domain. That is, the first element of the returned data array corresponds to  $q = -\frac{1}{2}N^R$ . This, however, requires only that we be careful when combining analytically computed terms with those computed by an FFT.

There does not seem to be any particular reason for shifting the domain of  $x$  except for perhaps tradition and to mimic the shifting applied to  $q$ .

#### 2.1.4 Definition of Phase

The sign of the exponent in Eq.(2.7) implies a choice which should be noted and maintained, for consistency, in other equations in this study. The general solution to the wave equation for plane waves is of the form

$$\Phi = A e^{j\omega t - jkr} + B e^{j\omega t + jkr} \quad (2.18)$$

where  $A$  and  $B$  are complex numbers and  $r$  is in the direction of propagation. As noted by Skudrzyk,<sup>15</sup> the choice of sign for  $j\omega t$  is arbitrary; however, by using  $j\omega t$

instead of  $-j\omega t$ , a similarity with electrical equations is maintained. Though this representation is for plane waves, the following discussion of phase and direction will apply to spherical, cylindrical, or any other representation.

Both terms will be needed to express steady-state conditions or situations involving reflections. However, simple propagation can be simplified by using only one of the terms. The choice of term can be made by observing that the first corresponds to wavefronts moving so that  $r$  is increasing while the second corresponds to wavefronts where  $r$  is decreasing. In most cases we are interested in waves which are traveling away from their source, where  $r$  is increasing, and so quite naturally choose to use only the first term. However, where we are interested in waves traveling *back* towards a source (such as Eq. (2.7)), we will need to use the second term.

It is important to note that, because we have chosen the first term of Eq. (2.18), the phase is given by  $-kr$  instead of  $kr$ . Pressure waves arriving at a linear array will take longer to arrive at the distant elements than to arrive at the near elements. While the absolute value of the phase will be greater at the distant elements (because of the  $r$ ), the actual numerical value will be smaller (because of the minus sign). Thus, the simulations will model the phase received at the distant elements as being *less* than the phase received at the near elements. Although this definition of phase is common among theoretical studies, it is the *opposite* from that derived from a simple experimental system where the greater time delay experienced by the distant elements of the array would have been recorded as a greater phase delay.

### 2.1.5 Evanescent Waves

As pointed out by Goodman,<sup>14</sup> each Fourier component of the image can be viewed as a plane wave propagating with a direction cosine given by

$$\alpha = \lambda k_x. \quad (2.19)$$

The  $z$  component of the wavenumber is expressed as

$$k_z = \begin{cases} \sqrt{k^2 - k_x^2}, & k_x \leq k; \\ -j\sqrt{k_x^2 - k^2}, & k_x > k. \end{cases} \quad (2.20)$$

When  $k_x > k$ , the disturbance is propagating as *evanescent waves* and Eq. (2.8) becomes

$$R(x, z) = \frac{1}{\sqrt{2\pi}} \int_{-\infty}^{+\infty} \tilde{R}_H(k_x) \cdot \exp\left(-j k_x x + z\sqrt{k_x^2 - k^2}\right) dk_x. \quad (2.21)$$

These waves have an imaginary direction cosine and are exponentially attenuated as they leave their source. As a result, when they are reconstructed by Eq. (2.21), they should be exponentially amplified. The square roots in Eq. (2.20) each have a positive and a negative solution; we have chosen the negative root for the evanescent waves so that the mathematics properly produce this exponential amplification.

Cohen<sup>13</sup> calls the above algorithm the *backward tracer* since it traces all plane waves back to the source. In most experimental systems where the hologram is recorded several wavelengths or more from the objects, the value of  $\tilde{R}_H(k_x)$  for evanescent waves will represent only noise, numerical roundoff, and aperture effects since these waves will have decayed to almost nothing after several wave-

lengths. The backward tracer will therefore exponentially amplify only noise, producing either poor or utterly useless images. As an alternative, Cohen used what he called the *backward propagator* formed by defining

$$k_z = \begin{cases} \sqrt{k^2 - k_x^2}, & k_x \leq k; \\ j\sqrt{k_x^2 - k^2}, & k_x > k. \end{cases} \quad (2.22)$$

By choosing the positive square root for the  $k_x > k$  case, the evanescent waves are reconstructed using an exponential with a negative, rather than positive, real power; that is, the evanescent waves are filtered out. This approach corresponds to treating each point on the hologram as being itself a source with an amplitude and phase given by  $R_H(x)$ ; thus, the reconstructed image is due to the propagation of these artificial sources back to the plane of the actual sources. Since the propagation is viewed as being *away* from the artificial sources, the evanescent waves are exponentially attenuated.

When working in the extreme nearfield, evanescent waves can be recorded and may be necessary in the reconstruction of the details of the scattering surface or the source of acoustic energy. Even so, the signal-to-noise ratio for these components may be quite low and thus some sort of filtering is appropriate. For a particular experimental holographic system,<sup>11</sup> it was noted that evanescent waves which had decayed by 12dB or more could not be reliably recorded and so should not be reconstructed. This approach was then used to construct a filtered version of the Green's function:

$$\frac{G_F(z)}{\exp(j k_z z)} = \begin{cases} \left(1 - \frac{1}{2} \exp(-6.666(1 - k_x/k_c))\right), & k_x < k_c, \\ \frac{1}{2}, & k_x = k_c, \\ \frac{1}{2} \exp(-6.666(k_x/k_c - 1)), & k_x > k_c, \end{cases} \quad (2.23)$$

where the factor of  $-6.666$  was chosen to yield a relatively sharp slope, and the term  $k_c$  is chosen so that  $G_F$  yields at most a 12db amplification.

### 2.1.6 Some Limitations to the Holographic Approach

The Helmholtz wave equation, upon which the holographic equation is built, is valid only for isotropic media without obstructions or sources. If there were, say, an infinite, perfectly reflecting plane surface in the vicinity of the receiver, the Green's function, Eq. (2.9), would need an additional term to represent this reflection. More complicated situations with multiple reflectors would lead to extremely awkward and complicated Green's functions. It may become impossible to write the Green's function in the spatial frequency domain as is required by Eq. (2.8). As we shall see later, other approaches can provide a much more straightforward method of handling these situations.

In some cases, one may have *a priori* knowledge of the objects reflecting or generating the pressure waves. As a general principle, such knowledge should be used if at all possible to enhance the imaging process. However, there is no direct way to do this using the holographic approach since it describes only pressure waves in free space rather than sources. Technically speaking, the holographic reconstruction can only generate valid images up to, but not including, the plane of the objects.

One of the great advantages of the holographic approach, as formulated in Eq. (2.8), is that it consists mostly of Fourier transforms which can be implemented efficiently on a computer using the FFT algorithm. However, this efficiency is lost and the equations can become awkward when the line (or plane)

of the receivers and the line (or plane) of the objects are not parallel. Approximations to non-planar objects can be made by reconstructing a series of closely spaced lines (or planes) though this still increases the amount of computations. In some cases, a space-domain convolution, as investigated by Cohen,<sup>16</sup> may be more efficient even though it does not use the FFT at all.

The image also becomes ambiguous when there are several discrete objects which do not lie in a plane but are instead spread out over two (or three) dimensions. There is no closed-form method known to detect or reliably analyze this situation although Lang<sup>17</sup> had some success by using pulses and a window in time that accepted only signals from a given distance. Narasimhan *et al.*<sup>18</sup> proposed two methods for determining the range for the special case of a plane reflector illuminated by plane waves. Powers and Mueller<sup>19</sup> developed an algorithm that searched for planes exhibiting peaks in the reconstructed pressure field; planes with the highest peaks were then considered to contain the "true" objects while the other planes were considered to be merely out-of-focus versions of the true objects.

A similar ambiguity occurs even when there is only one object if that object itself extends through several planes. For example, Lang<sup>20</sup> showed the reconstruction of two planes of a cone whose tip is pointed towards the receiver array: one plane at the tip, and one plane at the back face of the cone. In general, it was difficult to distinguish between the phenomena from these two planes — for example, the circle in the plane of the back face could have either been the effects of the backface itself, or an out-of-focus image of the tip.

One way to summarize these last few limitations is to note that, since it

is basically a single-frequency algorithm, the holographic approach has no range information and is therefore ill-suited to any situation where range information is important. Some studies<sup>21,22,23,24</sup> have formed images by combining the images made at different frequencies; none, however, seem to have really overcome the range-focusing problem within the realm of holography. It seems that other approaches, such as will be discussed later in this chapter, are needed.

## 2.2 Beamforming

Perhaps the most traditional method of processing the output of an array is beamforming. It differs from holography in that only the direction (and perhaps the range) of the objects are of interest — it is not used to form an image. The central concept is to choose weights  $A_i$  and time delays  $\tau_i$  to reinforce pressure waves arriving from a given direction  $\theta$ :

$$B(\theta, t_l) = \sum_{i=1}^{N^R} A_i \cdot R_i(t_l - \tau_i). \quad (2.24)$$

A great many variations can be built upon this basic formula.

### 2.2.1 Bartlett Beamformer

One of the most widely used variations is the so-called Bartlett beamformer.<sup>25</sup> It assumes that the signals consists solely of plane waves of a given frequency  $f$ , and that differences in time can be adequately represented by phase. Since differences in time which are greater than one period ( $1/f$  seconds) cannot be unambiguously represented as a phase, this assumes that either the time differences are sufficiently small, or that the ambiguity is insignificant. The received signal  $R_i$  can then be expressed as a complex number which is often calculated

by taking the Fourier transform of the received signal's time history. The time dependence  $t_l$  in the beam output is also replaced with a phase representation, i.e.,  $B$  becomes complex. Finally, we can express the time delay  $\tau_i$  as the phase of the now complex weights to write

$$B(\theta) = \sum_{i=1}^{N^R} A_i^* \cdot R_i = A^\dagger R \quad (2.25)$$

where

$$\begin{aligned} A &= [A_1 \ A_2 \ \dots \ A_N]^T, \\ A_i &= \exp(-j k X_i^R \sin(\theta)), \end{aligned} \quad (2.26)$$

the asterisk (\*) denotes the complex conjugate operation, the  $T$  denotes the transpose operation, and the dagger ( $\dagger$ ) denotes both. This formulation sets the point of zero phase, which is arbitrary, to be at the origin of the coordinate system. Often the power in the beam is of interest and is computed from Eq. (2.24) as

$$\begin{aligned} B^2(\theta, t_l) &= B B^* \\ &= (A^\dagger R) \cdot (A^\dagger R)^* \\ &= A^\dagger R R^\dagger A \\ &= A^\dagger \mathfrak{R} A \end{aligned} \quad (2.27)$$

where  $\mathfrak{R}$  is the spatial cross-correlation matrix. This is a zero time-delay correlation since no delays, beyond the ones naturally occurring due to the time of flight, are introduced. For example, in its simplest form,  $\mathfrak{R}_{ih} = R_i(t_l) \cdot R_h^*(t_l)$  for any two receivers  $i$  and  $h$  including  $i = h$ .



### 2.2.2 Limitations of the Bartlett Acoustical Model

To review, the temporal spectrum can be thought of as an attempt to replace the original time series with a sum of sine waves. Thus, this spectrum has difficulty with time series that are inherently not sine waves. For example, a step function cannot be represented; even if the spectrum extends to infinity, a small overshoot, called Gibb's phenomenon,<sup>26</sup> will remain.

In an analogous manner, the Bartlett beamformer attempts to find sine waves across an equally spaced linear array where each sine corresponds to a plane wave arriving from a specific direction. Because this beamformer is modeling the received field as plane waves, it will have difficulty with pressure waves which are inherently not plane waves, such as spherical waves. This problem is often referred to as "model mismatch."

For example, Figure 2.1 shows the  $B^2$  beam pattern from an array of 10 receivers spaced 0.5 wavelengths apart. These beams were formed using Eq. (2.25) with the received pressure waves simulated by

$$R_i = \frac{1}{r} e^{-jkr},$$

$$r = \sqrt{(X_i^R)^2 + (Z^S)^2} \quad (2.28)$$

with the broadside point source located at  $(0, Z^S)$  for  $Z^S$  equal to 1, 10, or 10,000 wavelengths. As the source moves closer to the receiving array, the assumption that the pressure waves are planar becomes less valid and eventually the beamformer output becomes meaningless.

Actually, there is nothing wrong with the beamformer — we merely need to modify the weights of Eq. (2.26) to correspond to the shape of the pressure

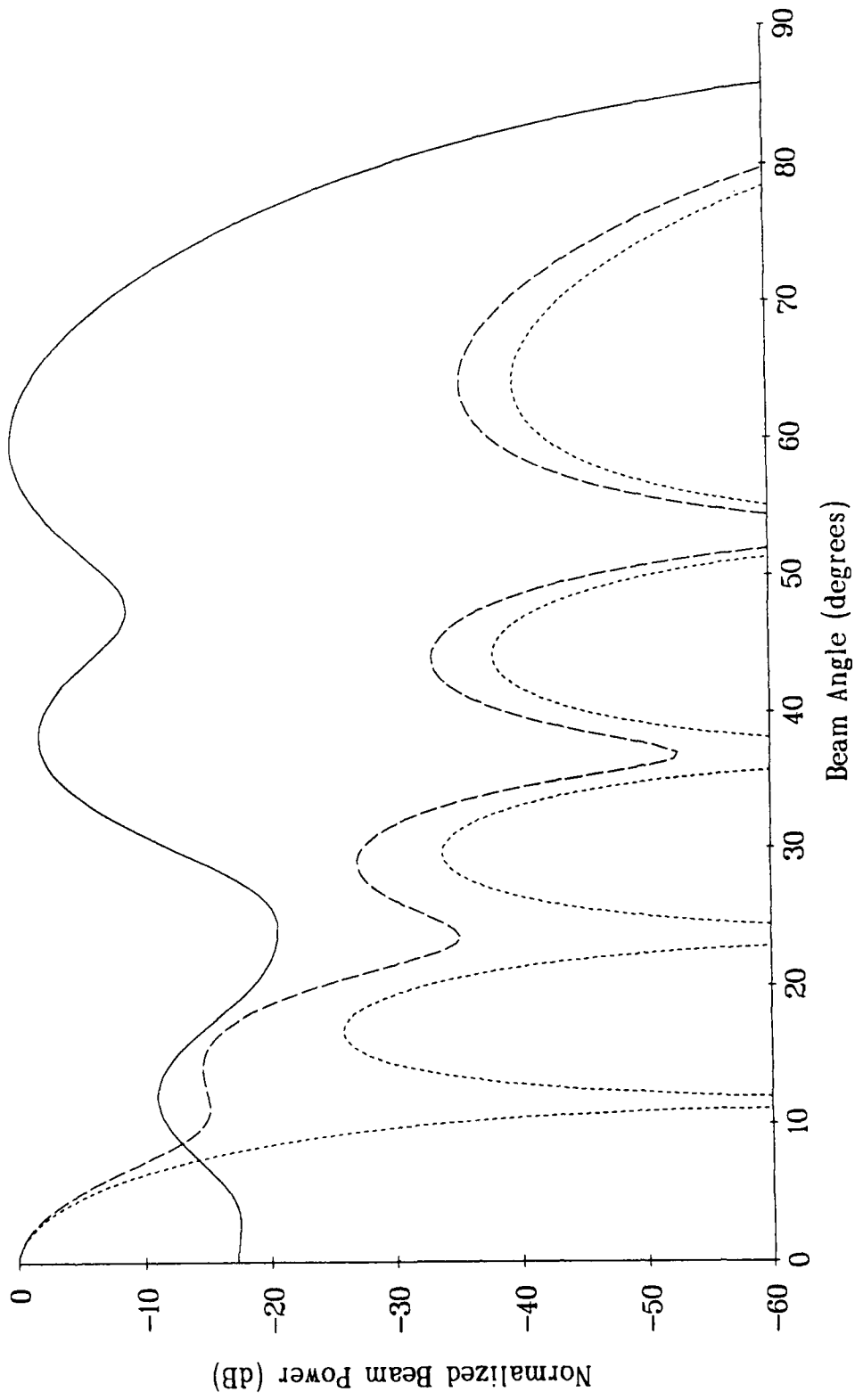


Figure 2.1. Beam for source at 1 (solid line), 10 (large dashes), and 10,000 (small dashes) wavelengths.

wave which is arriving from direction  $\theta$ . Furthermore, in some cases (such as the maximum likelihood processor), it would be desirable to have the beam respond to all pressure waves arriving from direction  $\theta$ , regardless of their shape.

An adaptive beamformer could be constructed, for example, which responds to a spherically spreading pressure wave originating in the direction given by  $\theta$  at some distance  $r$ . The key component of such a processor then becomes the method used to estimate the range  $r$ ; this will be discussed later in this chapter. In Chapter 4, the model mismatch problem is again discussed in relation to the maximum likelihood processor.

It is interesting to note why an analogous problem does not arise with the holographic approach. As with a beamformer, Eq. (2.8) attempts to find sine waves across an equally spaced linear array (via the Fourier transform.) Any mismatch, however, is perfectly "undone" by the inverse Fourier transform which is performed after the propagation effects have been implemented by the Green's function.

### 2.3 Receiver Correlations

Cross-correlations between the signals recorded at the receivers of an array can be used to locate objects. The angle at which the object lies, relative to the array, is estimated using the same plane-wave assumption as a beamformer; the angle is likewise called bearing. However, the cross-correlation method can in addition estimate range by using the curvature of the wavefront. Thus, the range should be great enough that the plane-wave assumption is somewhat correct but not so great that there is no detectable wavefront curvature.

Typically, this method is used to determine the location of objects which are the source of the pressure wave; however, the concept can be adapted to find objects which only scatter the wave and so is relevant to this study.

### 2.3.1 Basic Correlation Method

This derivation will use the geometry shown in Figure 1.1 except that there shall be no transmitter, i.e., the object at  $(X^S, Z^S)$  is itself the source of the pressure wave. To simplify the equations, we shift the linear array so that the first receiver is at the origin, i.e.,  $X_1^R = 0$ . Cross correlations between all possible pairs of receivers are formed, and the time delay  $d_{iq}$  corresponding to the highest peak is chosen from each correlation. The subscripts  $i$  and  $q$  represent any two receivers. This relative time delay can be written in terms of the time delay at each receiver as  $d_{iq} = d_i - d_q$ . The resulting linear system of equations is then solved for the time delays  $d_i$  under the constraint that  $d_1 = 0$ . Thus, we can write the distance  $r$  between the first receiver and the object, and the distance  $r_i$  between the  $i^{th}$  receiver and the object, as

$$r^2 = (X^S)^2 + (Z^S)^2, \quad (2.29)$$

$$r_i^2 = (r + c d_i)^2 = (X_i^R - X^S)^2 + (Z^S)^2, \quad (2.30)$$

respectively. We next subtract two instances of the latter equation, for receivers  $i$  and  $q$ , after first multiplying each by the receiver coordinate of the other. This produces

$$X_q^R r_i^2 - X_i^R r_q^2 \quad (2.31)$$

$$= X_q^R r^2 + 2r X_q^R c d_i + X_q^R c^2 d_i^2 - X_i^R r^2 - 2r X_i^R c d_q - X_i^R c^2 d_q^2$$

$$\begin{aligned}
&= X_q^R (X_i^R)^2 - 2X^S X_i^R X_q^R + X_q^R (X^S)^2 \\
&\quad - X_i^R (X_q^R)^2 + 2X^S X_i^R X_q^R - X_i^R (X^S)^2 \\
&\quad + (X_q^R - X_i^R) (Z^S)^2
\end{aligned}$$

or

$$\begin{aligned}
&2r (X_q^R c d_i - X_i^R c d_q) + (X_q^R c^2 d_i^2 - X_i^R c^2 d_q^2) \\
&= X_i^R X_q^R (X_i^R - X_q^R) + (X_i^R - X_q^R) (r^2 - (X^S)^2 - (Z^S)^2).
\end{aligned} \tag{2.32}$$

Eq. (2.29) can be used to eliminate the last term in Eq. (2.32) so that we can solve for  $r$ :

$$r = \frac{X_i^R X_q^R (X_i^R - X_q^R) - c^2 (X_q^R d_i^2 - X_i^R d_q^2)}{2c (X_q^R d_i - X_i^R d_q)}. \tag{2.33}$$

When there are only three equally spaced receivers with spacing  $L$ , we can let  $X_i^R = L$  and  $X_q^R = -L$  to yield

$$r = \frac{L^2 - \frac{1}{2}c^2 (d_i^2 + d_q^2)}{c(d_i + d_q)}. \tag{2.34}$$

In order to use all available information, we average the estimate of  $r$  from Eq. (2.33) over all possible pairs to obtain

$$r = \sum_{i=1}^{N^R} \sum_{\substack{q=1 \\ q \neq i}}^{N^R} w_{iq} \frac{X_i^R X_q^R (X_i^R - X_q^R) - c^2 (X_q^R d_i^2 - X_i^R d_q^2)}{2c (X_q^R d_i - X_i^R d_q)} \tag{2.35}$$

where normalization is accomplished by letting  $w_{iq} = 1 / (N^R (N^R - 1))$ .

If we can assume that the received waves are planar, the bearing angle  $\theta$  as shown in Figure 1.1 can be computed from each time delay and the results

averaged to yield

$$\theta = \arcsin \left( \sum_{i=1}^{N^R} v_i \frac{c d_i}{X_i^R} \right) \quad (2.36)$$

where normalization is accomplished by letting  $v_i = 1/N^R$ .

### 2.3.2 Optimum Correlation Method

The optimum estimation of range and bearing using correlations was addressed by Hahn<sup>27</sup> for linear arrays of receivers. The object producing the pressure wave was assumed to emit wide-band, zero-mean Gaussian noise, while additional, independent noise was introduced at each receiver.

In Hahn's results, the weights are chosen to not only provide normalization but to also minimize the error covariance matrix and thus approach the "optimum" Cramér-Rao bound, the theoretically optimum performance of an array. Hahn states that the calculation of the weights is trivial in the numerical case but complicated for most theoretical cases. He provides a formula for the weights only for the case of arrays arranged symmetrically around the origin where the noise level is the same at each receiver.

### 2.3.3 Comments on the Correlation Method

The ambiguity function corresponding to each time delay  $d_i$  used in the correlation method is a straight line given by one term of Eq. (2.36). The range estimate of Eq. (2.35) can therefore be viewed as a calculation of where two of these lines, as defined by  $d_i$  and  $d_q$ , intersect.

From this viewpoint it is easy to see where failure can occur: if the two time delays used in each term of Eq. (2.35) are incompatible, the resulting two lines

may cross at a location far removed from the actual object. The incompatibility can occur because the delays  $d_{iq}$  are calculated by picking the highest peak in the correlation; this picking process may not be robust when there are several nearly equal peaks such as would occur when there are several objects or an extended object emitting pressure waves. That is, even if  $d_i$  is due to one object while  $d_q$  is due to another, the algorithm will continue attempt to determine a single range and a single bearing in each term of Eq. (2.35).

Hahn notes that, if more than one source exists, the signals must be preprocessed so as to introduce nulls in the direction of the additional sources. This is perhaps the greatest weakness of this approach and is a strong motivation for seeking other methods which use similar correlation techniques but which can better accommodate multiple or extended objects.

## 2.4 Pattern Matching

Even before one begins to consider the concepts of super resolution, it becomes apparent that the traditional methods of the previous sections have difficulty accommodating additional features such as *a priori* information about the objects, multiple frequencies, or more complex propagation models. It may be that these added features could not have been seriously considered before the arrival of the modern digital computer, since they would have been difficult or impossible to implement with simple sum-and-delay beamformers, or with the optical reconstruction methods used in the early days of holographic imaging.

One has the sense that the added features, as well as the traditional methods, should all fit into some general model since they are all based upon the wave

equation's ability to describe the propagation of pressure waves through a homogeneous acoustic medium. In the following sections, such a general model is constructed around the concept of a fictitious scatterer; then, several special cases of the general model are considered, two of which correspond to the traditional holographic and beamforming methods.

#### 2.4.1 Fictitious Scatterers

It is possible that several workers have proposed the approach discussed in this section; however, the author's introduction to this approach came from a particularly clear paper published by Ermert and Karg<sup>28</sup> which described their theoretical and experimental development of what they called multifrequency acoustical holography.

They begin by noting that the theory for a matched filter is the basis for their approach. First, they assume that only a single scatterer at some specific location is present and then calculate what this fictitious scatterer would have yielded at their receivers. Second, they correlate the complex conjugate of the signal from this fictitious scatterer with the signals actually received. And third, the fictitious scatterer is moved through all locations in object space, i.e., all locations which could possibly contain an actual scatterer. The locations at which we find peaks in the output of the correlation, then, are interpreted as the locations of the true object or objects. The correlation  $\Psi$ , from their Eq. (8), would be expressed in the notation of this study for continuous time and a continuous receiving aperture as

$$\Psi(X^S, Z^S) = \left| \int_{-\infty}^{+\infty} \int_{-\infty}^{+\infty} R^H(x, t) \cdot (R^F(x, t))^* dx dt \right| \quad (2.37)$$



where  $R^H$  and  $R^F$  are the actual and fictitious signals, respectively, at receiver aperture locations  $X^R$ . The vertical bars ( $|\dots|$ ) denote the absolute value operation. The fictitious scattering object is at  $(X^S, Z^S)$ . When the aperture and time are sampled, the infinite integrals are replaced by finite sums to yield

$$\Psi(X^S, Z^S) = \left| \Delta X \Delta t \sum_{i=1}^{N^R} \sum_{l=1}^{N^T} R_{il}^H \cdot (R_{il}^F)^* \right|. \quad (2.38)$$

Through the concept of a fictitious scatterer, the power and generality of matched filter theory, originally developed for analyzing time histories, has been extended to analyze the space-time patterns received at the array. Virtually any type of transmitted signal can be accommodated (Ermer and Karg used a linear frequency sweep) as well as any spatial arrangement of receivers.

Furthermore, any sequence of events that affect the propagation of the pressure wave can be incorporated. The sequence of events can include closed-form formulas; for example,  $R^F$  could be calculated for simple free-space propagation using Eq. (1.2). But, more importantly, sequences of events which can, say, be described only numerically can also be incorporated. Even propagation effects known only empirically due to, say, preliminary system tests<sup>29,30</sup> could be used to generate the fictitious receiver signals for the desired locations of the fictitious scatterers.

Some of these variations will be examined in subsequent sections of this chapter and in Chapter 5.

### 2.4.2 Reconstruction as Pattern Matching

When a single frequency sine wave is used, the integral over time in Eq. (2.37) merely multiplies the result by a constant that can be dropped. The pattern-matching formula thus becomes

$$\Psi(X^S, Z^S) = \left| \int_{-\infty}^{+\infty} R^H(x) \cdot (R^F(x))^* dx \right| \quad (2.39)$$

The reconstruction represented by Eq. (2.8) can be rewritten as an inverse Fourier transform or a convolution:

$$R(X^S, Z^S) = \frac{1}{\sqrt{2\pi}} \int_{-\infty}^{+\infty} \tilde{R}^H(k_x) \cdot \exp(j k_z Z^S - j k_x x) dk_x, \quad (2.40)$$

$$= \mathcal{F}^{-1} \left( \tilde{R}^H(k_x) \cdot \exp(j k_z Z^S) \right), \quad (2.41)$$

$$= \int_{-\infty}^{+\infty} R^H(x) \cdot G(X^S - x, Z^S) dx \quad (2.42)$$

where  $\mathcal{F}(G(x, Z^S)) = \exp(j k_z Z^S)$ . In this comparison between holography and pattern matching, it is sufficient to consider only the non-evanescent waves; for this case, Cohen<sup>31</sup> has shown that  $G$  for a given  $Z^S$  (or, in his notation,  $G_n^*$  for a given  $D$ ), is equal to

$$G(x, Z^S) = -\frac{1}{2\pi} \left( \frac{Z^S}{r} \right) \left( \frac{1}{r} - jk \right) \frac{\exp(j k r)}{r} \quad (2.43)$$

where  $r^2 = x^2 + (Z^S)^2$ . When  $r \gg \lambda$ , terms on the order of  $\frac{1}{r}$  are negligible compared to terms on the order of  $\frac{1}{\lambda}$ . Thus,

$$G(x, Z^S) \approx \frac{jk}{2\pi} \left( \frac{Z^S}{r} \right) \frac{\exp(j k r)}{r}. \quad (2.44)$$

Upon examining Eq. (2.39) and Eq. (2.42) we see that

$$G(X^S - x, Z^S) = (R^F(x))^* \quad (2.45)$$

or

$$R^F(x) = -\frac{jk}{2\pi} \left( \frac{Z^S}{r} \right) \frac{\exp(-jk r)}{r} \quad (2.46)$$

where  $x \rightarrow X^S - x$  so that we now have  $r^2 = (X^S - x)^2 + (Z^S)^2$ . A comparison of Eq. (2.39) and Eq. (2.42) indicates that the two formula are identical when the fictitious source is given by Eq. (2.46). Although not explicitly used in Eq. (2.8), an absolute value operation is typically added when the image is plotted.

The source radiation expressed by Eq. (2.46) consists of spherically spreading waves with a radiation pattern given by

$$\cos(\phi) = \frac{Z^S}{r} \quad (2.47)$$

where  $\phi = 0$  points towards the negative  $Z$  axis. As explained by Skudrzyk,<sup>32</sup> this pattern is due to the fact that for the development of the Helmholtz-Huygens integral, the equivalent sources at the hologram needed to have zero radiation in the backwards direction. This was accomplished by equating each of these sources to the sum of a point source and a dipole, with the consequence that a cardioid radiation pattern was generated.

In some applications of holography, such as nearfield studies, the angle  $\phi$  between a source of acoustic energy and a point in the hologram may become quite large, or even approach 90 degrees. In these cases, the fictitious source used by the holographic equation, with its cardioid radiation pattern, may do a poor job of modeling the more omnidirectional radiation from, say, a point on a

vibrating surface. Thus, the pattern-matching approach could provide a distinct advantage by allowing us to use an omnidirectional source in the analysis.

The two methods share the ambiguities in the interpretation of their image. Either can be used to estimate the object field at arbitrary points  $(X^S, Z^S)$ , although holography can product a more efficient calculation when the object field is evaluated at the same locations along the  $X$  axis as the receivers, i.e., at  $X_m^S = X_i^R$ .

As shown by Ermert and Karg, their integral over time, combined with a sufficiently large bandwidth, can reduce the range ambiguity inherent in holography. This capability will be examined again in Chapter 5.

#### 2.4.3 Beamforming as Pattern Matching

A comparison of the Bartlett beamformer, as given by Eq. (2.25), and the pattern matching, as given by Eq. (2.39), shows that the fictitious source used in beamforming is given by

$$R_i^F = \exp(-j k X_i^R \sin(\theta)) \quad (2.48)$$

which is of course just the pressure which would have been received from a source radiating plane waves.

#### 2.4.4 Correlation Method as Pattern Matching

The pattern-matching approach can be categorized as a hypothesis tester: one selects a suitable domain of possible object locations, and then tests each hypothesis with Eq. (2.38). On the other hand, the correlation method provides

an immediate estimate of the object location. The advantage in such a direct estimate is that fewer calculations are needed to reach a conclusion; the disadvantage is that it can fail disastrously when there is more than one object, i.e., there exists no single answer. In these situations, the pattern-matching approach would seem to be more robust as it can handle multiple sources.

Because of the fundamental difference in the approach used by the two methods, as noted in the previous paragraph, forming a direct mathematical comparison may be impossible. An initial comparison of the two methods would suggest that the integral of the received and fictitious patterns over time is the main source of range information, and as such is somewhat analogous to the correlation method's calculation of range, Eq. (2.35). The integral over space is somewhat analogous to the correlation method's calculation of bearing, Eq. (2.36).

A further comparison of how the time-history information is used can be formed by first simplifying the algorithm: assume that the bearing  $\theta = 0$ ; and that changes in the amplitude of the received signals across the array are negligible. This means that we only need to seek the value of the unknown range  $r$ , which is equivalent to seeking the value of the time delays since the speed of sound is a known constant.

When these assumptions are applied to the correlation method, Eq. (2.35), we find that the information obtained through the inter-element time delays  $d_{iq}$  (the location of the peak in the cross-correlation between the signals from receivers  $i$  and  $q$ ) can now be obtained instead through the time delays  $d_{i1}$  (the location of the peak in the cross-correlation between the signals from receivers  $i$  and 1). This also eliminates the need to solve the simultaneous system of

equations since  $d_{i1} = d_i - d_1$  and  $d_1 \equiv 0$ . We can roughly summarize the resulting process as follows where the first two steps constitute the cross correlation:

- (1) For some time delay  $\tau_i$ , evaluate the match  
using  $\sum_{l=1}^{N^T} R_1(t_l) \cdot R_i^*(t_l + \tau_i)$ ;
- (2) Repeat for all time delays where  $\tau_{min} < \tau_i < \tau_{max}$ .
- (3) Let  $d_i = \tau_i - \tau_1$  using the value of  $\tau_i$  that produced the best match;
- (4) Repeat for all receivers  $i$  where  $1 < i < N^R$ ; then
- (5) Calculate the range by inserting the  $d_i$  into Eq. (2.35).

Turning now to the pattern-matching method, we can roughly summarize its algorithm as follows:

- (1) For some range  $r_{test}$ , calculate the corresponding fictitious  $r_i$  at receiver  $i$ ;
- (2) Repeat for all receivers  $i$  where  $1 < i < N^R$ ;
- (3) Evaluate the match using Eq. (2.38);
- (4) Repeat for all ranges where  $r_{min} < r_{test} < r_{max}$ ; then
- (5) Let  $r$  equal the value of  $r_{test}$  that produced the best match.

Both methods use two loops: one over receivers, and one over either time delays (step 2 in the correlation method) or, equivalently, over range (step 4 in pattern matching). The result is then merely the value that produced the best match. The main difference between the two methods, therefore, seems to be that the pattern-matching method has reversed the order of its two loops relative to the correlation method.

## 2.5 Array Geometry

In this study, we have limited our investigations to processing methods which use a linear array. However, it seems prudent to at least review other methods, using two- or three-dimensional arrays, to determine if there might be some techniques or beneficial receiver spacing which could be applied to a one-dimensional array.

An explicit inversion of the Helmholtz equation was used by Ball *et al.*<sup>33</sup> to develop a method for reconstruction using measurements chosen to lie on the surface of a sphere. The resulting expressions were in terms of spherical harmonics and could accommodate both plane wave and spherical wave ultrasonic sources. Norton and Linzer<sup>34</sup> investigated the exact inverse scattering solution for plane, cylindrical, and spherical arrays. However, in order to simplify the mathematics, they only considered backscattering; i.e., each receiver individually operated as first a transmitter and then a receiver so that a given receiver never encountered waves arising from the other receiver-transmitter locations. In both of these studies, the goal was to estimate the velocity and hence the density of the media within the spherical array. In neither case were any particular requirements for the spacing or arrangement of the receivers in the array noted.

The reconstruction of a three-dimensional field from a partial sphere of measurements with a low signal-to-noise ratio was investigated by Bresler and Macovski.<sup>35</sup> Their statistical description of the object of interest and its relationship to the measurement locations has the potential of offering some sound guidelines to array configurations; unfortunately, they did not address that issue. The reconstruction of three-dimensional domains using two-dimensional arrays

was also considered by Koppelman and Keating<sup>36</sup> for a rectangular array and by Norton<sup>37</sup> for a circular array.

A review of two-dimensional arrays by Nigam<sup>38</sup> provides insights which are, after 15 years, still relevant. The number and size of the elements, the overall size of the array, and the electronic challenge of connecting large numbers of transducers were discussed; however, only fully populated arrays with equally spaced elements were considered.

One of the most comprehensive studies of a linear array was presented by Carter.<sup>39</sup> In particular, he examined the case wherein the array was constrained to be of a given length  $L$  with a given number of receivers  $M$ . Ideally,  $M$  is large enough so that there is a receiver every half-wavelength. Carter considered the question of how to optimally distribute the receivers when less than the ideal number were available. When the goal was to minimize the variance of the bearing estimate, the optimum configuration was shown to be one where half the receivers were at each end of the array. If instead the goal is to minimize the variance of the range estimate, the optimum arrangement was shown to be one with half the elements at the center with one-quarter of the elements at each end. To minimize the *area* of uncertainty (roughly, the product of the range and bearing variance), Carter found numerically that the optimum arrangement was one with one-third of the receivers in the center and one-third at each end. However, at very short ranges, the minimum area of uncertainty was shown to result using the arrangement that minimized the bearing variance while for very large ranges the arrangement that minimized the range variance was recommended. In every case, the receivers were spaced a half-wavelength apart in each subarray.



A similar question was addressed by Pillai *et al.*<sup>40</sup> who sought the optimum placement of receivers in a linear array for use in spatial spectrum estimation (i.e., bearing estimation) using one of the methods based upon the eigenstructure of the covariance matrix (discussed further in the next chapter). It was shown that the  $M$  receivers should be placed at locations equal to a half-wavelength multiplied by a set of integers known as a Caratheódory sequence. For example, when  $M = 4$ , the receivers should be located at  $0$ ,  $\frac{2}{3}\lambda$ ,  $\frac{5}{3}\lambda$ , and  $\frac{8}{3}\lambda$ .

Two conclusions seem to be in order. First, the optimum array geometry and receiver spacing is seldom a universal one; it instead depends upon which parameter one wishes to optimize and which processing method is to be used with the resulting array. Second, when using a one-dimensional linear array, there seems to be no method which claims to improve the results beyond what can be obtained when the array is fully populated from end to end with elements spaced every half-wavelength. Since the simulations used in Chapters 4 and 5 always use such an ideal array, the issue of receiver spacing does not arise.

## 2.6 Time-of-Flight Information

One strong motivation for *not* using the full time-history of the signal is that it is difficult to analytically represent processing operations on such a signal. Nevertheless, it is illustrative to consider what is being lost by not using the full time-history.

The simplest system for determining the location of a scattering object is a single transmitter and a single receiver. The general expression for  $R_i$ , given in

Eq. (1.2), becomes

$$R_1(t_l) = S_1 \frac{E(t - T_1^F)}{D_1 \cdot D_T} \quad (2.49)$$

where  $S_1$  is the reflection coefficient. The time-of-flight (TOF)  $T_1^F$  and the distances were defined in Section 1.4. The amplitude of  $R_1$  is relatively insensitive to small changes in the distances, and includes the unknown coefficient  $S_1$ . The TOF is related to the length of the path traveled by the pressure wave through

$$T_1^F = \frac{D_1 + D_T}{c}. \quad (2.50)$$

Unfortunately, this value is identical for all points on an ellipse which has its foci at the transmitter and receiver. That is, in an experiment, we do not know  $D_1$  and  $D_T$  separately — we only know their sum by using the measured TOF and Eq. (2.50). Thus, knowing the TOF is not the same as knowing the range of the scatterer since the range or distance is different to each point on the ellipse.

The next logical step is to add either additional transmitters or additional receivers, where one ellipse of ambiguity is contributed by each transmitter-receiver pair. If additional transmitters are used, we must be able, at each receiver, to determine which transmitter was the source in order to calculate the ellipse of ambiguity from the time delay. This can be done either by encoding the signals, or by activating the transmitters one at a time.

A less complicated system can be formed by instead using only one transmitter and multiple receivers. In general, all ellipses will add coherently only at the one location which corresponds to the scatterer. However, there will in general be many secondary peaks generated where any two ellipses cross. When there are multiple scattering objects, each contributes its own set of ellipses of

ambiguity to the image.

The previous paragraphs have assumed that the TOF has been used. Many imaging methods, however, do not use this time directly; instead, they assume that the pressure waves consist of a single frequency and then represent, in effect, the TOF as the phase of the complex signal

$$R_1 = S_1 \frac{\exp(j k (D_1 + D_T))}{D_1 \cdot D_T}. \quad (2.51)$$

While this is fundamentally the same information, a phase ambiguity of  $2\pi$  has been introduced. This is equivalent to a time ambiguity of one period or a distance ambiguity of one wavelength ( $\lambda$ ). Thus, instead of one ellipse for each transmitter-receiver pair, there are an infinity of concentric ellipses where the TOF for any two adjacent ellipses differ by one period.

Some methods are built upon a correlation between the signal at each receiver and the transmitted signal. A full cross-correlation, using a full set of inner-signal delays, would identify the TOF as the value of the inner-signal delay at which the best correlation was obtained. However, in most cases, the method uses only the zero-delay correlation — that is, they only examine how well the two signals being compared match “as is” by calculating only one correlation with an inner-signal delay of zero. Thus, ambiguities are again introduced. A similar ambiguity also results when the correlations are between receivers. And, as noted in Section 2.3.3, the process of choosing the one peak which yields the TOF may not be robust.

The conclusion, then, is that any processing method that reduces the TOF information from the receivers to a single complex number is discarding

information that could, potentially, be used to improve the resolution. Although the simulations used in Chapters 4 and 5 do not use this TOF information, a brief discussion of how to incorporate the TOF into the matching methods will be given in Chapter 6.

## Chapter 3

### High Resolution Methods

The methods for processing signals from an array which are examined in this chapter will include ones seeking high resolution, or the ability to distinguish two closely space objects, as well as methods which seek high accuracy, or the ability to determine the location of a single object with high precision. This type of accuracy is sometimes also described as the variability of the location or the variance of the range and bearing estimates. Although, technically speaking, these are different goals, the methods for achieving them are similar enough that we can refer to all the methods as high resolution ones.

#### 3.1 Spectral Estimators

In the analysis of the spectrum of a time series — that is, a sequence of samples of some phenomena versus time — the simplest method for obtaining the spectrum is to form its Fourier transform. This results in a spectral resolution of  $1/T$  where  $T$  is the length of the sampling period. A high-resolution spectral estimator attempts to generate a result which has the same effect as an increase in  $T$  with a corresponding increase in the resolution of the spectrum.

This idea can be transferred to line arrays by letting the location along the array take on the role of time and the vector wavenumber take on the role of frequency. Then, the enhancements generate a result which has the same effect as an increase in the array length  $L$  with a corresponding increase in the resolution of the spatial spectrum. Thus, any spectral estimator that can be used to enhance

the temporal spectrum can be applied to the spatial spectrum. Several of the methods discussed later in this chapter can be classified as spectral estimators, and were originally developed for the time domain.

It is important to not confuse this method, which increases the resolution of the spectrum, with those that instead extend the spectrum to higher spatial frequencies. The latter effect is the same as taking the samples closer together in space. Such an effect cannot yield any additional information when the samples are already half a wavelength or closer together except when evanescent waves are involved.

It is also important to note that most spectral estimators, including the FFT, produce estimates which are equally spaced in the wavenumber domain but not in angle. For example, in the two-dimensional space used in this study, we would have estimates at  $k_x = 0, \pm\Delta k_x, \pm2\Delta k_x, \dots$  where  $\Delta k_x = 2\pi/L$  for an array of length  $L$ . Using the angular spectrum interpretation of Goodman,<sup>14</sup> each of these wavenumbers correspond to a plane wave of frequency  $f$  and wavenumber  $k$  arriving at angle  $\theta$  so that  $k_x = k \sin(\theta)$  or  $\theta = \arcsin(k_x/k)$ . Thus, the estimates are relatively far apart around  $\theta = 0$  and most closely spaced around  $\theta = \pm 90^\circ$ . Unfortunately, we often are seeking the highest accuracy in bearing around broadside or  $\theta = 0$ .

### 3.1.1 ARMA Methods

One of the more widely used class of spectral estimators consist of either a polynomial, the inverse of a polynomial, or the ratio of two polynomials. Equivalent names for the polynomial estimator are all-zero, moving average (MA), and

feedforward filter while equivalent names for the inverse-polynomial estimator are all-pole, autoregressive (AR), and feedback filter. An ARMA estimator combines both and is the ratio of two polynomials. The all-zero and all-pole designations refer to the Laplace transform of the filter. The coefficients of these polynomials are first determined using the available data; then, the polynomials can be used to generate additional synthetic data between existing data points (interpolation) or beyond the domain of the existing data points (extrapolation).

In addition to the choice to use an AR, MA, or ARMA model, one must also select the method for determining the order of the polynomial(s), the method for the calculation of the polynomial coefficients (either directly or through iteration), and the subject of estimation.

### 3.1.2 Options for the Subject of Estimation

One of the difficulties in assembling this review of ARMA methods has been the fact that the polynomials can be fitted to, and used to estimate, several different aspects of the signal. The most useful basis on which to categorize these variations seems to be whether the estimator operates on time-domain data (i.e., the time-history of the signal at each receiver) or on space-domain data. In the former case, the improvements are equivalent to sampling the signal either more rapidly or for a longer period of time. Since neither of these directly affect the processing of data from an array, they shall not be considered further.

Estimators which operate on space-domain data require that the information at each receiver first be represented as a complex number — that is, the time-history of the signal cannot be used directly. Thus, the ambiguities dis-

cussed in Section 2.6 are inherent in ARMA methods. These estimators can also operate either directly on the data, or on some function of the data. For example, some fit the polynomial  $\Psi(i)$  to the ratio of the complex signal at adjacent receivers  $R_i$  and  $R_{i+1}$  so that

$$\frac{R_{i+1}}{R_i} = \Psi(k) \quad \text{for } i = 1, 2, \dots, N. \quad (3.1)$$

Other versions may operate on the Fourier transform of the signals, i.e., in the wavenumber domain.

The literature which has been reviewed suggests that there are several goals to be considered when choosing the data or function of the data which is to be the subject of estimation (SE):

- Some technique must exist for the selection of the correct model (MA, AR, or ARMA) for the SE.
- Some technique must exist for the selection of the correct order for the polynomial(s) to be fitted to the SE.
- There must be a closed-form or convergent iterative method for evaluating the coefficients from existing SE data.
- The SE should be resistant to noise and measurement errors.

As an example of this last goal,<sup>41</sup> it has been found that the average of the cross-correlation between receiver pairs is more robust than the cross-correlation of the average receiver signal since, in the former, the cross-correlation helps remove noise before the averaging process is applied. The optimum compromise between



these goals is not always obvious.

### 3.1.3 Choosing the Estimator Parameters

The error in the estimation will be minimized when the model and order match the underlying physical process. A study of 11 categories of methods for the estimation of the power spectral density of discrete time series by Kay and Marple<sup>42</sup> concluded that "if the model is inappropriate ... poor (biased) spectral estimates will result." The question of interest is whether, in the absence of any prior knowledge, the model and order can be derived robustly from the data.

The MA and ARMA methods were used by Abdel-Aal *et al.*<sup>43</sup> to estimate, in the space domain, the ratio of the signal from adjacent receivers. The source of the acoustic waves in their computer simulations was either one or two point sources. They found that the MA model led to errors so large that it was not useful when there was more than one source. While the ARMA model yielded better results, no discussion on the choice of model order is provided. They seemed to have simply tried different model orders until the predictions matched what they knew beforehand.

The MA, AR and ARMA models were used by Gutowski *et al.*<sup>44</sup> to predict the spectrum of three time series which were designed to be purely MA, purely AR, or ARMA. Their simulations revealed that using a model which is incorrect for the data can result in predicted spectra which have the wrong shape or peaks which do not coincide with the true spectral peaks. In conclusion, they state:

One problem which, in our opinion, remains essentially unsolved, is a practical means to determine a priori whether a real life situation

corresponds to an AR, MA, or ARMA process. Another problem is how to effectively determine the order of a given process other than (by) the empirical methods used here. For the AR model, the order of the feedback component can be determined from the behavior of the partial correlation coefficient. This test, however, often breaks down when applied to the ARMA model.

More recently, Wax<sup>45</sup> noted that two of the methods which have been proposed for estimating the order of an AR model (called AIC and MDL) are appropriate only when there are a large number of data samples (because the estimates are asymptotic) and the data can be modeled as Gaussian. He went on to describe a method for choosing the order using lattice filters. Li and Dickinson<sup>46</sup> have also proposed a lattice filter approach for the case where the noise is white.

### 3.1.4 The Maximum Entropy Method

In a foundational paper on information theory, Shannon<sup>47</sup> described the entropy  $H$  of the random variable  $x$  as

$$H = - \sum_{i=1}^I p_i \log p_i \quad (3.2)$$

where there was a probability  $p_i$  that the random variable would take on the value  $x_i$ . In a paper published in 1957, Jaynes<sup>48</sup> proposed that the underlying probability density functions for statistical mechanics should be modeled as having the maximum randomness, or maximum entropy, as this entailed the least number of assumptions. This concept became more widely known in the field of array processing as the maximum entropy method (MEM) due to Burg<sup>49</sup>

in 1967 when he applied the concept to spectral estimation.

A compact derivation has been given by McDonough<sup>50</sup> for the case where the noise is Gaussian. For a uniformly spaced line array the result is

$$B^2(\theta) = \frac{1}{\sum_{i,j=1}^N V_{ij} \exp(j2\pi k(x_i - x_j) \cos \theta)} \quad (3.3)$$

$$= \frac{1}{\mathbf{E}^T \mathbf{V} \mathbf{E}} \quad (3.4)$$

where the variables  $V_{ij}$  are derived using the spatial cross-correlation matrix  $\mathfrak{R}$  and the requirement

$$\mathfrak{R}_{ij} = \int \frac{\exp(j2\pi k(z_i - z_j) \cos \theta)}{\sum_{k,l=1}^N V_{kl} \exp(j2\pi k(x_k - x_l) \cos \theta)} d\theta \quad (3.5)$$

$$= \int \frac{\mathbf{E} \mathbf{E}^T}{\mathbf{E}^T \mathbf{V} \mathbf{E}} d\theta \quad (3.6)$$

with the integral extending over all values of  $\theta$  from which energy is arriving. The symbols  $(^T)$  denote the conjugate transpose operation and  $\mathbf{E}$  denotes a simple plane wave steering vector. As noted by Johnson,<sup>25</sup> Eq. (3.3) corresponds to the linear predictor or autoregressive solution; thus, all results from the previous discussion of the AR model applies here.

### 3.1.5 Using the ARMA Methods to Locate Scatterers

We wish to consider whether these methods could be used to predict the data beyond the ends of a line array. We can think of this situation as being one where there is a well-defined, but unknown, scattering function which describes the strength of the energy reflected from the source or sources as a function of

angle. Our finite-sized line array has recorded a subset of this function, over a subset of angles. The question before us is then whether we can use this recording to predict the scattering function at the other, unmeasured angles.

Such a prediction would seem to be fundamentally unsound in some cases when we have no knowledge of the underlying scattering function. For example, the measured scattering patterns from spheres shown by Pierce<sup>51</sup> for  $ka > 1$  exhibit a complexity near the nulls that would be hard to predict from a recording of only a small subset of angles. In the next chapter, Figure 4.1 shows the diffraction from a barrier; note that, near the shadow boundaries at  $0^\circ$  and  $180^\circ$ , there are fundamental changes in the pattern. Likewise, the reflected pattern from plates above a certain size exhibit discontinuities in the nature of the pattern at certain angles, as is shown in Figure 5.13. No empirical method for determining the correct model and order for an unknown scatterer is known to this author. It would also follow that prediction of some *function* of a scattering pattern may also be difficult.

A fundamental assumption in MEM is that the object of prediction can be modeled as having a Gaussian distribution. MEM, in effect, expects the scattering pattern as a function of angle (or its Fourier transform) to be Gaussian — an unusual if not impossible case.

Of course, if we are sufficiently far from the source, the acoustical wave is merely a plane wave and we can easily extrapolate it to larger apertures by shifting the phase of the plane wave. However, when one processes the data from the new, simulated receivers, the processing function must also be phase shifted by the same amount; thus, the result is essentially the same as multiplying the

original information by some constant and then, upon normalization, dividing by the same constant.

Such considerations seem to lead to the conclusion that perhaps the advantages attributed to ARMA by Abdel-Aal *et al.*<sup>43</sup> are actually due to the fact that their source happened to match the ARMA model.

Another problem which must be addressed when using ARMA (or most other high-resolution methods) is their tendency to produce false peaks whenever they model the source field as an AR or all-pole process. False peaks occurred when Byrne and Fitzgerald<sup>52</sup> used MEM with an array whose receivers were spaced less than a half-wavelength apart although Kaveh and Lippert<sup>53</sup> suggested an energy-taper approach that eliminated much of the problem.

### 3.2 Minimum Energy Methods

In the 1960's a large aperture seismic array (LASA) was built in Montana to measure the vector velocity of propagating seismic waves. The purpose of LASA was to discriminate distant underground nuclear blast tests from natural earth tremors. In a paper published in 1969, Capon<sup>54</sup> developed a high-resolution method for estimating the frequency-wavenumber spectrum received by this array; he called this a maximum likelihood (ML) wavenumber filter.

#### 3.2.1 Discussion of the ME Method

This method is an extension of earlier time domain work by Capon *et al.*<sup>55</sup> which had maximized a likelihood function. Johnson<sup>25</sup> noted that the method should more correctly be called a minimum energy (ME) filter since it minimizes

the energy in a beam pattern subject to a constraint but does not maximize a likelihood function. McDonough<sup>50</sup> provided an elegant method for deriving this filter that is based upon finding a wavenumber filter that has a value of 1 in the direction of interest  $\theta$  but which otherwise yields the minimum energy. His expression for the ME method is

$$B^2(\theta) = \frac{1}{E^T \mathfrak{R}^{-1} E} \quad (3.7)$$

where  $E$  is a simple plane wave steering vector and  $\mathfrak{R}$  is the spatial cross-correlation matrix formed from the zero-delay correlation between all possible receiver pairs.

This beamformer is described by McDonough<sup>50</sup> and others as one which reduces its side lobes the most in those directions from which the greatest amounts of energy is arriving; which allows its side lobes to grow in those directions from which lesser amounts of energy are arriving; and which passes without change *plane* waves from the direction of interest  $\theta$ . These characteristics have led to the ME method being described as a wavenumber filter. Also, because it does not have a fixed response but instead varies with the data, it must also be classified as a non-linear processor.

Note that the filter itself makes no distinction between signal and noise — the filter attempts to suppress energy, regardless of its source, if that energy arrives from angles other than the one of interest. When operated in this manner, the ME filter is said to be based upon the signal-plus-noise cross-correlation matrix. However, when it is desirable and possible to estimate  $\mathfrak{R}$  from signal-free inputs, the ME filter is said to be based upon the noise-only cross-correlation

matrix. There seems to be no other standard nomenclature for describing these two versions of the ME filter.

### 3.2.2 Eigenvector Analysis

A powerful enhancement to the ME method was introduced<sup>56,57</sup> when it was noted that, if the spatial cross-correlation matrix  $\mathfrak{R}$  could be inverted, it could also be decomposed into a set of orthogonal eigenvectors. Furthermore, the magnitude of the eigenvalue associated with each vector corresponds to the energy represented by the vector. When the number of energy sources is limited to, say,  $N^S$ , then the largest  $N^S$  eigenvectors correspond to these sources and can be said to span the signal subspace. When there are  $N^R$  receivers, there will then be  $N^R - N^S$  eigenvectors with relatively small eigenvalues which correspond to noise and can therefore be said to span the noise subspace. Since eigenvectors are mutually orthogonal, an eigenvector from one subspace is orthogonal to the other subspace. In particular, when the steering vector  $\mathbf{E}$  is aimed precisely at the bearing of an actual source, it will reside in the signal subspace and so it too will be orthogonal to the noise subspace.

This characteristic can be exploited by modifying Eq. (3.7) so that  $\mathfrak{R}$  is replaced with  $\mathfrak{R}^n$  which represents the noise subspace and is constructed using only the eigenvectors and eigenvalues which correspond to noise. Then, as  $\mathbf{E}$  approaches a true source, the denominator in the modified Eq. (3.7) will approach zero and the beamformer output will approach infinity.

### 3.2.3 Linear Predictors

The linear predictor method, as discussed by Johnson,<sup>25</sup> is based upon the prediction of a selected, single element of the array by a linear, weighted sum of the other elements of the array:

$$R_q = - \sum_{m \neq q} a_m R_m. \quad (3.8)$$

The true value of  $R_q$  is known, and the coefficients  $a_m$  are found by minimizing the mean-squared error subject to the constraint that  $a_q = 1$ . Johnson notes that this is a constrained optimization problem of the same form as that encountered for the minimum energy method, and also corresponds to an autoregressive model of the signal. The solution to this problem is then

$$LP_q^4(\theta) = \frac{\mathbf{U}_q^{T*} \mathbf{R}^{-1} \mathbf{U}_q}{(\mathbf{U}_q^{T*} \mathbf{R}^{-1} \mathbf{E})^2} \quad (3.9)$$

where  $\mathbf{U}_q$  is a column vector with the  $q$ th element equal to one and the other elements equal to zero. The name of this function includes a power of 4 since it, in this form, is proportional to the square of the power. A modified version is often used so that it is similar to other beamformers and is given by

$$LP_q^2(\theta) = \frac{1}{|\mathbf{U}_q^{T*} \mathbf{R}^{-1} \mathbf{E}|}. \quad (3.10)$$

Typically, the value for the the center receiver or one of the receivers at the ends of a line array are chosen for prediction. In a comprehensive comparison between the LP, ME, and Bartlett beamformers, DeGraff and Johnson<sup>58</sup> found that the LP method generally yielded the highest resolution although it needed large amounts of averaging and could also produce false peaks and exhibit in-



creased bias in some situations. Furthermore, Johnson<sup>25</sup> notes that “a criterion for the ‘proper’ choice of the predictive element ( $q$ ) has not been found to date.”

### 3.2.4 Using the ME Method in the Absence of Noise

Johnson<sup>25</sup> has expressed the inverse of the cross-correlation matrix for the case of white, uncorrelated noise as

$$\mathfrak{R}^{-1} = \frac{1}{\sigma_n^2} \left| I - \frac{\sigma_s^2}{N^R \sigma_s^2 + \sigma_n^2} E E^{T*} \right| \quad (3.11)$$

where  $I$  is the identity matrix,  $E$  is a plane wave steering vector, and the power levels of the signal and noise are given by  $\sigma_s^2$  and  $\sigma_n^2$ , respectively. In this case, it is clear that letting  $\sigma_n^2 \rightarrow 0$  would be unacceptable. The eigenvector analysis suggests why this occurs. As the noise goes to zero, the eigenvectors of  $\mathfrak{R}$  corresponding to noise become identical, their eigenvalues go to zero, and so the inverse of  $\mathfrak{R}$  no longer exists.

Of course, even a simulation will suffer noise, even if only digital noise due to numerical roundoff. However, it is not clear what difficulties may be encountered at extremely low levels of noise; in these cases, some of the techniques discussed later in this chapter, for accommodating coherent sources, could be employed.

### 3.2.5 Using the ME Method to Locate Scatterers

We now wish to explore the strengths and weaknesses of this method from the point of view of one wishing to use a linear array to locate scatterers.

### 3.2.5.1 The ME Wave Model

In Section 2.2.2, it was noted that the Bartlett beamformer could fail when its model of the energy waves (it expects plane waves) does not correspond to the actual energy wave. The ME method could fail for a similar reason: it would interpret a complicated wavefront arriving from a single direction as simple planar wavefronts arriving from many directions. This problem has been addressed by Seligson<sup>59</sup> and further discussed by McDonough.<sup>60</sup> The problem can become so severe in some cases that the ME resolution could be worse than that of the Bartlett beamformer or even degenerate to totally useless information. The general experience has been that the problem is worst when there are a relatively small number of strong sources with relatively weak background noise.

Seligson<sup>59</sup> attempted to construct a variation of the ME method which used a given shape for the wavefront. He found that the processor produced worse resolution than the Bartlett beamformer when the received shape differed from the expected shape, or when the amplitudes of the signals differed more than a certain amount between receivers. McDonough<sup>60</sup> attempted to build a processor that was more tolerant of such problems by extending Seligson's approach to consider a family of wave shapes consisting of limited perturbations of the given shape.

The central ideal of the ME design is to make the filter transparent to *all* waves from the direction of interest  $\theta$ , regardless of the shape of the wavefront. It is theoretically possible to adapt the steering vector  $\mathbf{E}$  to correspond to a wavefront of any desired shape; however, even then, two problems remain: first, some means must be found for knowing what curvature to choose; and second,

the filter will now not necessarily be the minimum energy filter.

### 3.2.5.2 Number of Sources

The eigenvector analysis requires that the number of sources  $N^S$  be estimated using the cross-correlation matrix. Although several methods have been proposed,<sup>61</sup> it remains a difficult decision. Johnson and DeGraaf<sup>62</sup> found that the basic ME method yielded  $N^S$  peaks no matter how many actual sources were really present; an eigenvector analysis, on the other hand, was much more tolerant. They provided one example where three peaks were produced, correctly locating the three actual sources, in spite of having set  $N^S = 6$ . However, they conclude that "reasonably accurate methods of determining (the number of sources) from the eigenvalues of  $\mathfrak{R}$  are not known at this time."

Zou and Liu<sup>63</sup> also reported false peaks using the LP method but found that improvements could be made by using the average of two LP variations.

The eigenvector analysis can accommodate up to  $N^R - 1$  uncorrelated sources when there are  $N^R$  receivers. When the sources are correlated, Bresler and Macovski<sup>64</sup> note that this analysis is then limited to  $\frac{1}{2}N^R$ . However, they go on to establish a theoretical maximum which can be much higher, depending on the signal-to-noise ratio and the angular distribution of sources. Pillai *et al.*<sup>40</sup> showed that  $N^R(N^R - 1)$  sources could be resolved if the receivers were spaced according to a minimum-redundancy pattern called a Caratheódory sequence.

It would seem that an eigenvector analysis would have difficulty with an extended scatterer which acts like an extremely large number of scattering sources. However, the key requirement is that the  $N^S$  eigenvectors with the

largest eigenvalues *span* the source subspace — the number of actual or equivalent sources does not itself have to equal  $N^S$ . Thus, the results depend upon the relative geometry of the array and the scatterer. A simulation by Duckworth<sup>41</sup> was indeed able to provide reasonable results for a particular extended scatterer, with much sharper boundaries than a conventional beamformer. The general conditions, however, under which extended scatterers can be accommodated have yet to be established.

### 3.2.5.3 Coherent Sources

When two or more of the sources are coherent, we can find neither the inverse nor the eigenvectors of the cross-correlation matrix  $\mathfrak{R}$ . This will result in all cases when the sources are simply scattering energy from the same transmitter.

A method called spatial smoothing was proposed by Shan and Kailath<sup>65</sup> wherein the linear array was treated as  $\frac{1}{2}N^R$  subarrays, each of which shared all but one receiver with each neighbor. The cross-correlation matrices from each of these subarrays were then averaged to form a single cross-correlation matrix in which the coherence between sources has been broken. This method assumes, however, that the full array be such that it can be subdivided into *identical* subarrays. It further depends upon uncorrelated noise existing at the receivers for the loss of coherence; if there is little noise, the method may work poorly. Worst of all, the effective size of the array is now half the original size which works against the high resolution we are attempting to achieve. A variation which does not cause as great a reduction in the effective array size and is called the modified spatial smoothing (MSS) method was described by Evans *et al.*<sup>66</sup> although it has been noted that the method may fail in some special cases.<sup>67</sup>

A similar method called frequency smoothing was proposed by Wang and Kaveh<sup>68</sup> which averages the  $\Re$  obtained at each frequency. In particular, they combine the information from each frequency in a manner they describe as "coherent addition" so as to avoid the threshold effect which has kept similar methods using an incoherent addition from succeeding. However, as noted by Williams *et al.*,<sup>67</sup> this approach requires either prior knowledge of the general source locations or a very good estimate.

Duckworth<sup>41</sup> found that sources also became decorrelated when the cross-correlation matrices from several sets of data were averaged if there was a small amount of motion between the transmitter, source, and receiver between sets of data.

Several other methods for breaking the correlation have begun to be investigated<sup>69</sup> including a method by Bresler *et al.*<sup>70</sup> which combines each group of coherent sources into one equivalent source.



## Chapter 4

### Pattern-Match Imaging

It was claimed in Chapter 2 that the pattern-matching approach can accommodate events, such as diffraction and reflection, which can occur during the propagation of the pressure wave. To investigate this claim, two new imaging techniques, called the pattern-match method and the mismatch method, are developed in this chapter using the concept of a fictitious source introduced in Section 2.4. A simulation of the diffraction of waves around a barrier is also implemented and is used to examine the capabilities of the new methods. Each simulation will also be repeated using the well-known holographic reconstruction method so that all 3 techniques can be compared. Additional simulations for a selection of special cases will be included to round out the investigation; these cases include a free-field environment (i.e., the diffracting barrier is eliminated), a case where the location of the barrier, used in the reconstruction, is in error; and a case where there are two sources.

#### 4.1 Simulation of Edge Diffraction

The performance of the pattern-matching method depends upon the degree to which the signals  $R^F$  received from the fictitious source agree with the true physical phenomena. While this is no challenge in a free-space situation, it may become a limiting factor when attempting to apply the method to cases where the pressure wave has undergone diffraction and reflection.

When the received signal is simulated, as it will be in this chapter, there

is no problem: whatever formula we use to simulate the received signals is used to represent the fictitious source. Nevertheless, we should choose a non-trivial case so that artifacts and limitations of the method, if any, might be observed. These artifacts may include bias (the source location is in error), resolution (the precision with which the source has been located), and non-uniqueness (false sources are reported).

#### 4.1.1 Defining the Wave Disturbance

The scattering of pressure waves by a sphere is an attractive physical phenomenon for research since a entire series of scattering patterns can be generated merely by adjusting the term  $ka$  where  $k$  is the wavenumber and  $a$  is the radius of the sphere. Pierce<sup>71</sup> writes the scattered component as

$$p_{sc} = \frac{-k^2 B}{4\pi} \left( \frac{4}{3}\pi a^3 \right) \left[ 1 - \frac{3}{2} \cos \left( \theta \left( 1 + \frac{j}{kr} \right) \right) \right] \frac{\exp(jkr)}{r} \quad (4.1)$$

where  $B$  is the peak amplitude of the incident plane wave,  $r$  is the distance from the sphere to a point in the scattered field, and  $\theta$  is the angle between  $r$  and the direction of the incident wave. Unfortunately, this simple formula holds only for  $ka \ll 1$  which translates to  $a \sim 0.016\lambda$  in this study where the wavelength is one. This radius enters into Eq. (4.1) in the term that calculates the volume of the sphere and results in the scattered component having an amplitude five to six orders of magnitude lower than the non-scattered component. It was estimated that when considering the total field, equal to the sum of these two components, the scattered component amplitude would be too small an effect to demonstrate the abilities of pattern matching over holography.

A more pronounced effect would be generated by the edge of a barrier.



Pierce<sup>72</sup> has expressed the diffracted component of the field when the distance of both the source and field point from the edge is large compared to a wavelength as

$$p_d = S \frac{\exp(jk(r_s + r_f))}{r_s + r_f} \frac{\exp(j\frac{\pi}{4})}{\sqrt{2}} \cdot \sum_{+,-} \frac{\sin(\nu\pi)}{\sqrt{1 - \cos(\nu\pi) \cdot \cos(\nu\phi^\pm)}} A_D(\Gamma \cdot M_\nu(\phi^\pm)) \quad (4.2)$$

where the summation consists of two terms. The angle comparison  $\phi^\pm$ , discussed further in the next section, is given by

$$\phi^\chi = \begin{cases} \phi^R + \phi^S + 3\pi, & \text{if } \chi \text{ is plus;} \\ \phi^R - \phi^S, & \text{if } \chi \text{ is minus.} \end{cases} \quad (4.3)$$

The source is located a distance  $r_s$  from the edge of the barrier at angle  $\phi^S$  and transmits waves of amplitude  $S$ . The field point where we wish to evaluate the diffracted field is a distance  $r_f$  from the edge at angle  $\phi^R$ . The wedge index  $\nu$  is  $\frac{1}{2}$  for a thin barrier. We also have

$$\Gamma = \sqrt{\frac{2r_f r_s}{\lambda(r_f + r_s)}}, \quad (4.4)$$

$$M_\nu(\phi) = \frac{\cos(\nu\pi) - \cos(\nu\phi)}{\nu\sqrt{1 - \cos(\nu\pi) \cdot \cos(\nu\phi)}} \quad (4.5)$$

$$= -2\cos(\tfrac{1}{2}\phi) \quad \text{for } \nu = \tfrac{1}{2}. \quad (4.6)$$

For simplicity, we set  $\lambda = 1$ . The term  $A_D$  is the diffraction integral which can be written in terms of the Fresnel integrals

$$\begin{aligned} C(\mu) &= \int_0^\mu \cos\left(\frac{\pi}{2}t^2\right) dt, \\ S(\mu) &= \int_0^\mu \sin\left(\frac{\pi}{2}t^2\right) dt, \end{aligned} \quad (4.7)$$

as

$$A_D(\mu) = \frac{1-j}{2} \exp\left(-j \frac{\pi}{2} \mu^2\right) \left(\text{SIGN}(\mu) - (1-j)(C(\mu) + jS(\mu))\right) \quad (4.8)$$

where

$$\text{SIGN}(\mu) = \begin{cases} 1, & \mu \geq 0; \\ -1, & \mu < 0. \end{cases} \quad (4.9)$$

Some routines for the evaluation of the Fresnel integrals use the absolute value of their argument, thereby failing to include the odd symmetry. In these cases, we can move the SIGN operation to correct for this so that Eq. (4.8) becomes

$$A_D(\mu) = \frac{1-j}{2} \exp\left(-j \frac{\pi}{2} \mu^2\right) \text{SIGN}(\mu) \left(1 - (1-j)(C(|\mu|) + jS(|\mu|))\right) \quad (4.10)$$

where  $|\dots|$  denotes the absolute value operation.

#### 4.1.2 Angle Definitions

It is convenient to define the angles which describe the location of the source ( $\phi^S$ ) and field point ( $\phi^R$ ) in the manner most useful for the situation. Unfortunately, this has led to three different reference points for these angles and so a note on these definitions is appropriate. In all cases, the angles increase in a counter-clockwise direction — these definitions differ only in the location of the 0° point.

On polar plots, the angular origin will be on the positive Z-axis, as is shown in Figure 4.1, and will be expressed in degrees. In this figure, two angles are shown as examples:  $\phi^S$ , the angle of the source; and  $\phi^R$ , the angle of a receiver or field point. Note that both of these are examples of *negative* angles.

The radial distance of the source on this and subsequent figures is not

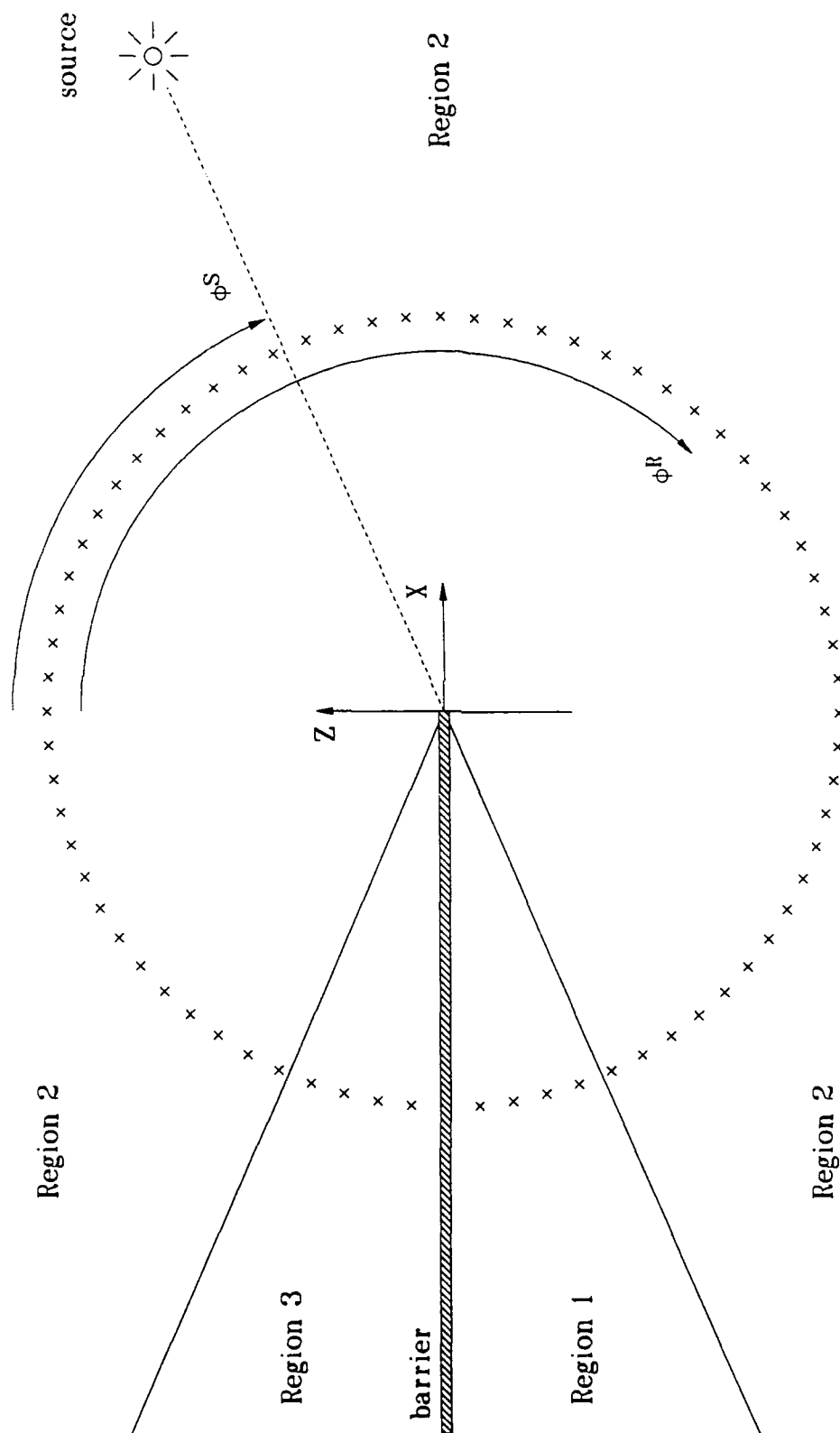


Figure 4.1. Regions of the field scattered by a barrier, numbered according to the number of components used. The location of the regions will change if the location of the source changes.

drawn to scale — in fact, on subsequent plots, radial distances will instead represent the signal level in dB.

The sketch of the barrier is also not drawn to scale; it is included at the  $+90^\circ$  location only as a reminder of the angular location of the barrier.

In Figure 4.1, the edge of the barrier is shown as being located at the origin of the coordinate system. This convention will be used on all subsequent polar plots. However, in the simulations, the edge of the barrier is *never* at the origin but is instead at some other given location. This requires a coordinate transformation, which is made automatically in the subroutine which calculates the diffraction.

The second angular reference point is found in the FORTRAN routines where it was more convenient to put the angular origin on the positive X-axis so that the inverse tangent routine could directly use the X and Z coordinates of a point in the calculation of the angle. The third angular reference point is found in Pierce<sup>71</sup> in his development of the diffraction equations where he sets the angular origin at the shadow side of the barrier, which would be the negative X axis in this study.

The angles used on the plots will agree with those used in equations in this study so that the reader need not consider these other definitions except when examining the computer code or other texts. The necessary conversion is embedded in the offset of  $\frac{3}{2}\pi$  added to *each* angle in Eq. (4.3).

### 4.1.3 The Total Field

The total field consists of the diffracted component ( $p_d$ ), discussed previously, plus, in some regions, a directly incident component ( $p_i$ ) and a reflected component ( $p_r$ ). These regions can be uniquely numbered according to the number of components which are needed since all regions include  $p_d$  while none include  $p_r$  without  $p_i$ .

Figure 4.1 shows the regions which result for a particular source location. The line dividing Region 1 from Region 2 is called the incident shadow boundary, while the line dividing Region 2 from Region 3 is called the reflection shadow boundary.

Table 4.1 shows the logic which is used in the subroutine to determine the region number based upon the definition of  $\phi$  used in the plots and equations.

Table 4.1. Rules for determining the region number.

$\phi^S$	$\phi^R$	Region	Components
$-\frac{1}{2}\pi \leq \leq \frac{1}{2}\pi$	$-\frac{3}{2}\pi \leq \leq \phi^S - \pi$	1	$p_d$
$-\frac{1}{2}\pi \leq \leq \frac{1}{2}\pi$	$\phi^S - \pi < \leq -\phi^S$	2	$p_d + p_i$
$-\frac{1}{2}\pi \leq \leq \frac{1}{2}\pi$	$-\phi^S < < \frac{1}{2}\pi$	3	$p_d + p_i + p_r$
$-\frac{3}{2}\pi < < -\frac{1}{2}\pi$	$-\frac{3}{2}\pi \leq \leq -\phi^S$	3	$p_d + p_i + p_r$
$-\frac{3}{2}\pi < < -\frac{1}{2}\pi$	$-\phi^S < \leq \phi^S + \pi$	2	$p_d + p_i$
$-\frac{3}{2}\pi < < -\frac{1}{2}\pi$	$\phi^S + \pi < < \frac{1}{2}\pi$	1	$p_d$

The incident component, when needed, is given by

$$p_i = S \frac{\exp(j k r)}{r} \quad (4.11)$$

where  $r$  is the direct distance between the source and the field point. The reflected component, when needed, is given by

$$p_r = S \frac{\exp(j k (r_{xs} + r_{xf}))}{r_{xs} \cdot r_{xf}} \quad (4.12)$$

where  $r_{xs}$  and  $r_{xf}$  are the distances between the point of reflection and the source and field point, respectively. Given the source location  $(X^S, Z^S)$ , the field point location  $(X^F, Z^F)$ , and the barrier's coordinate  $Z^B$  (it has no X coordinate as it is parallel to the X-axis), the point of reflection  $(X, Z^B)$  is given by

$$X = \frac{X^F \cdot |Z^B - Z^S| + X^S \cdot |Z^B - Z^F|}{|Z^B - Z^S| \cdot |Z^B - Z^F|}. \quad (4.13)$$

The sign of the complex exponents in Eq. (4.11) and (4.12) are positive in order to agree with Eq. (4.2). However, the complex conjugate, of the sum of all components, must be taken so that the phase agrees with the definition of phase used in this study.

#### 4.1.4 Shadow Boundary Approximation

When the receiver is near the shadow boundary, Pierce<sup>72</sup> has developed an approximate solution which would replace Eq. (4.2) with

$$p_d = S \frac{\exp(j k (r_s + r_f))}{r_s + r_f} \frac{\exp(j \frac{\pi}{4})}{\sqrt{2}} A_D(\Gamma \phi^-). \quad (4.14)$$

This approximation could cut the number of evaluations of the diffraction integral

$A_D$  in half and so will be considered in the next section.

#### 4.1.5 Testing the Barrier Simulation

The absolute value of the Fresnel integrals were calculated in a **FORTRAN** subroutine using a power series. Results for a selection of arguments from 0.0 to 5.0 were compared to the tables in Abramowitz and Stegun.<sup>73</sup> The values differed by at most  $\pm 1$  in the last digit; that is, the computed results seemed to be accurate to  $\pm 10^{-7}$ . Single-precision arithmetic (i.e., 32 bits were used to represent a number) caused 2–5 times as many differences between the subroutine and the tables; therefore, double-precision arithmetic (using 64 bits to represent a number) is used in the subroutine.

Another **FORTRAN** subroutine then makes use of the Fresnel integrals to evaluate the diffraction integral and the pressure at given points. This subroutine was tested by evaluating the diffracted wave for the case of a source at  $(X, Z) = (0, 100\lambda)$  and a barrier beginning at  $(0, 10\lambda)$  and extending towards  $X = -\infty$ . The magnitude and phase of the field, at points located every quarter degree on a circle of radius  $10\lambda$  around the edge of the barrier, is shown in Figures 4.2 and 4.3, respectively. The phase shown has been “linearized” by adding or subtracting integer multiples of  $360^\circ$  to each value so as to minimize the difference between the value and its neighboring values. These results look reasonable and seem compatible with a similar case described by Kendig and Hayek.<sup>74</sup>

The same case using the shadow boundary approximation is shown in Figure 4.4. Given the assumptions which were used, the results are remarkably good. Nevertheless, an increase in the relative size of the ripples at negative angles, and

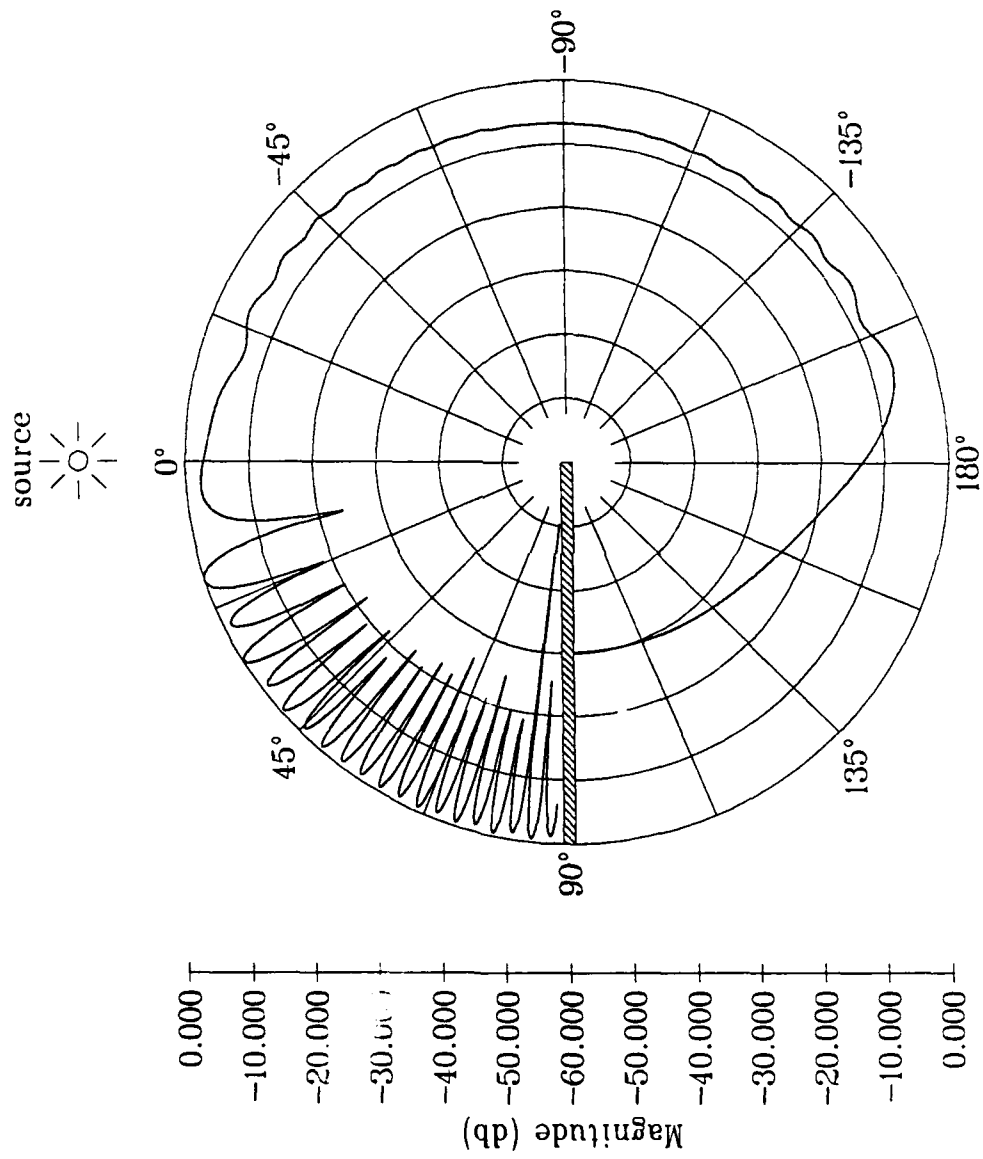


Figure 4.2. Magnitude of the pressure from a source  $100\lambda$  away from the edge of a barrier. The field was evaluated at a radius of  $10\lambda$  from the edge.



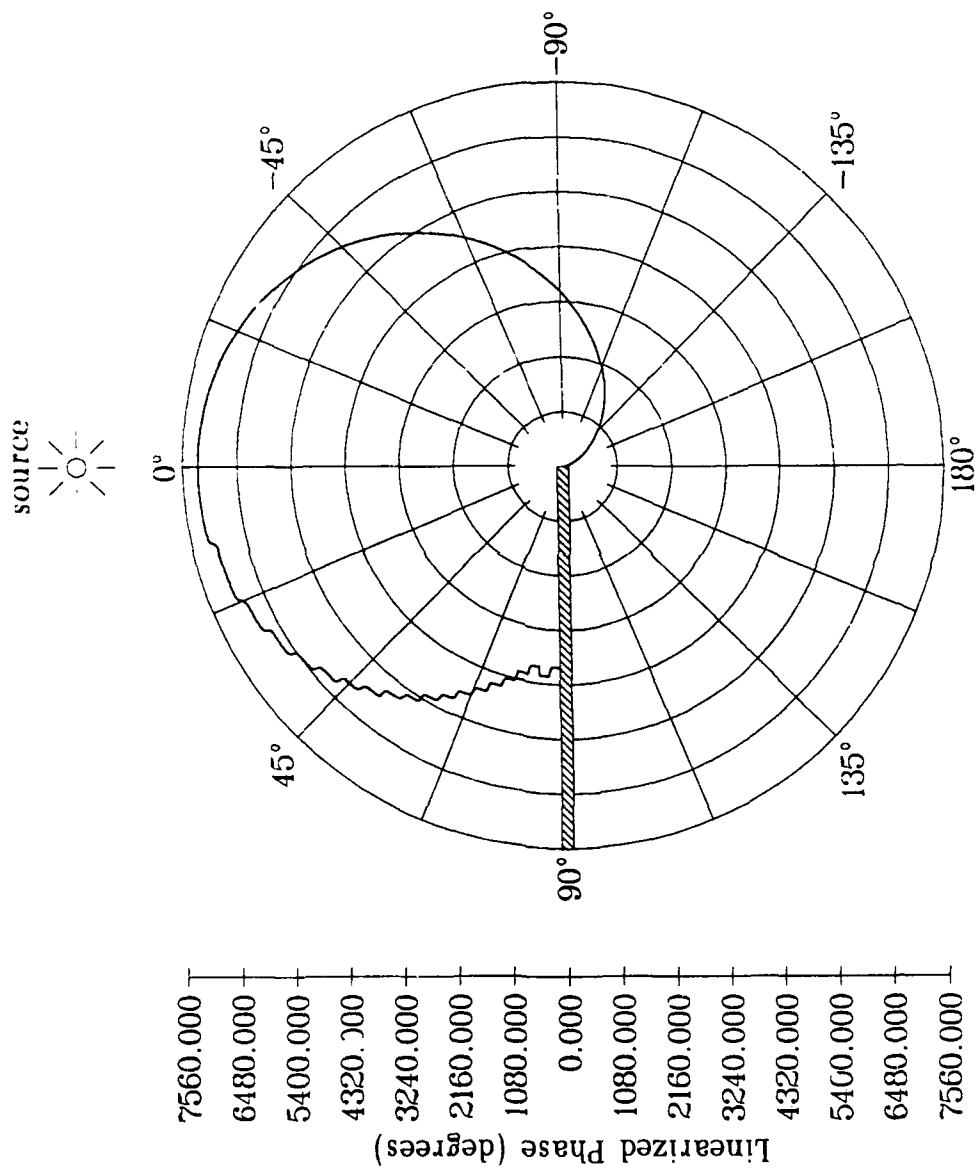


Figure 4.3. Phase of the pressure from a source  $100\lambda$  away from the edge of a barrier. The field was evaluated at a radius of  $10\lambda$  from the edge.

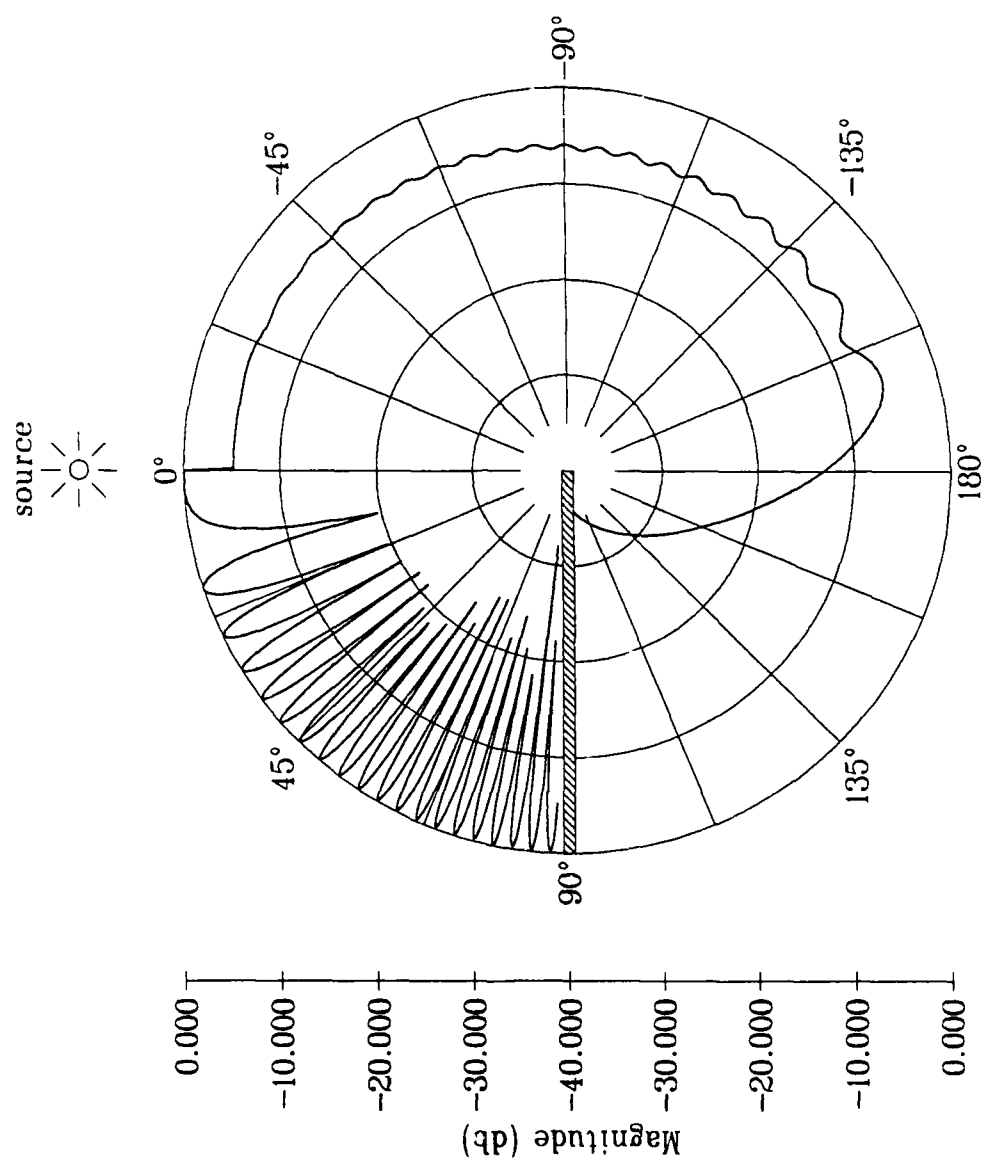


Figure 4.4. Magnitude, using the shadow-boundary approximation, of the pressure from a source  $100\lambda$  away from the edge of a barrier. The field was evaluated at a radius of  $10\lambda$  from the edge.

a discontinuity at  $\theta = 0^\circ$ , would make this approximation unacceptable for some situations. Testing has also indicated that the time saved was not significant for this study, and so this approximation was not used further.

## 4.2 Mismatch Imaging

During the investigations of this chapter, it was noted that the pattern-match method seemed to yield a poorer image in some situations than was expected. That is, the value of  $z_1 \cdot z_2^*$ , where  $*$  denotes the complex conjugate, decreases more slowly than was desired as the complex numbers  $z_1$  and  $z_2$  began to differ.

An approach to improving this situation is suggested by the minimum energy (ME) method discussed in the previous chapter. In that method, the "match" is provided by

$$B^2(\theta) = \frac{1}{\mathbf{E} \mathbf{R}^{-1} \mathbf{E}} \quad (4.15)$$

where  $\mathbf{E}$  is a vector that steers the reception to angle  $\theta$  and as such somewhat plays the role of the fictitious source in the pattern-match method. The basic form of Eq. (4.15) suggests that the denominator is calculating the amount of *mismatch*, rather than match, between the fictitious source of plane waves and the patterns actually received. Thus, when the fictitious source approaches an actual source, the amount of mismatch approaches zero and the sharp peaks typical of the ME method result.

What we desire, therefore, is a comparison of two complex values which yields a result proportional to the degree to which they differ. In the complex plane, every complex value is represented by a point, and so the concept of the

distance between any two points  $z_1$  and  $z_2$  could be defined as

$$z_d = \sqrt{(a_1 - a_2)^2 + (b_1 - b_2)^2} \quad (4.16)$$

where  $z_1 = (a_1 + jb_1)$  and  $z_2 = (a_2 + jb_2)$ . Actually, we desired  $z_d^2$  so that a squared quantity results as with  $z_1 \cdot z_2^*$  or the correlation between two arrays of numbers. This quantity will be used to implement what shall be called the mismatch method. Any comparison method using  $z_1 \cdot z_2^*$  shall continue to be called the pattern-match method. In subsequent tests in this chapter, the results of both match methods will be compared to that of holography.

In plots, it is conventional for higher values to represent stronger peaks. We need, therefore, to either use  $1/z_d^2$  or  $-z_d^2$ . The former would exhibit the non-linear response typical of the ME method and would actually be quite effective for finding point sources. However, we choose to use the latter because it retains its linearity and can therefore be more directly compared to the results from the pattern-match method and holography.

Using the pattern-match method, the lower bound of zero represents the worst possible match while the upper bound, representing the best match, can be easily normalized to a peak value of one. We wish to map the new values from the mismatch method to this same domain. The *upper* bound of  $-z_d^2$  is zero, representing the best possible match (or worst possible mismatch), while the lower bound is some negative number corresponding to the worst match (or greatest mismatch). While it is clear that these values should be adjusted so that the best match is always mapped to one, it is not so clear which (negative) value ought to be mapped to zero. After some experimentation, the most useful results

were obtained by mapping the average (negative) value to zero, and setting values less than the average (representing very poor matches) equal to zero.

This transformation is implemented by first calculating all values of  $z_d^2$ , their average  $\bar{z}_d^2$ , and the minimum value corresponding to the best match  $\bar{z}_d^2$ . Then, the result of the new method  $\Psi$  which will be used for plotting and comparison is given by

$$\Psi(x, z) = \text{MAX} \left( 0, \frac{\bar{z}_d^2 - z_d^2(x, z)}{\bar{z}_d^2 - \bar{z}_d^2} \right) \quad (4.17)$$

where the MAX operation chooses the larger of its two operands.

### 4.3 Normalization

In early tests, the pattern match method failed to produce a maxima in some cases when the fictitious source passed through the location of the true source. To investigate, one particular case was examined in depth. In this case, a barrier beginning at  $(0, 10\lambda)$  and extending towards  $X = -\infty$  diffracts the pressure waves from a point source at  $(-5.25\lambda, 15\lambda)$ . An array of 64 receivers spaced  $0.5\lambda$  apart is centered on the X-axis. The pattern received at this array, and the pattern from a fictitious source at  $(-4.75\lambda, 15\lambda)$ , are shown in Figure 4.5. When the fictitious source was at the exact location of the source, its pattern matched exactly the received pattern (the solid line in Figure 4.5).

When the fictitious source was at the true source, the match value was 0.0162. However, when the fictitious source moved to the location shown in Figure 4.5, the match value *increased* to 0.0183. This was the phenomenon which was causing the pattern-match method to fail to produce the expected maxima.

What has happened is that the pattern from the fictitious source, as it

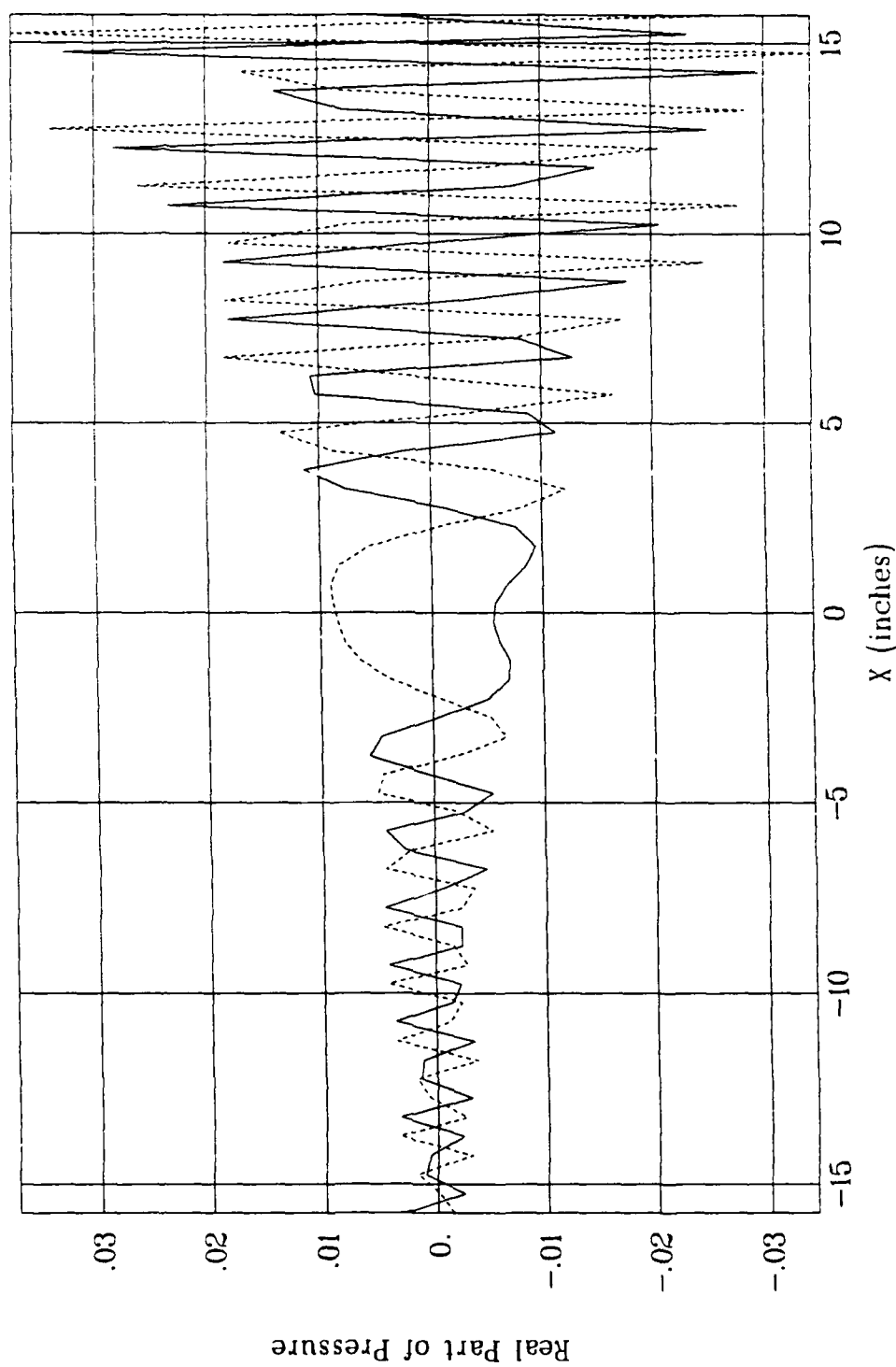


Figure 4.5. Signal at the receiving array due to the true source (solid line) at  $(-5.25\lambda, 15\lambda)$  and the fictitious source (dashed line) at  $(-4.75\lambda, 15\lambda)$ , after diffraction around a barrier and no normalization.

moved towards the edge, increased enough (more energy was getting around the barrier) to more than compensate for the misalignment of the patterns. This phenomenon, it turns out, is often observed in signal processing, and can be elegantly suppressed by normalizing the power of each pattern *before* comparison:

$$R_i \rightarrow \frac{R_i}{\sum R_i^2}. \quad (4.18)$$

Thus, the absolute and relative amplitudes are changed, as shown in Figure 4.6.

The effects of this normalization can be dramatic. The results shown in Figure 4.29 later in this chapter had originally appeared as shown in Figure 4.7 when the pattern-match method was used without normalization (note that these figures differ in their rotation by  $180^\circ$ ). The rapid rise near  $Z = 0$  in Figure 4.7 is due to the  $p_i$  component whose  $\frac{1}{r}$  term grows to infinity as the fictitious source approaches the location of a receiver.

The large positive peaks in Figure 4.7 become large negative peaks when the mismatch method is used. Thus, the results shown in Figure 4.33 later in this chapter had originally appeared as shown in Figure 4.8 without normalization. The elevated area or plateau is due to the large negative peaks causing an inappropriate shift in the value of  $\bar{z}_d^2$  used in Eq. (4.17).

#### 4.4 Locating a Source in Free Space

A simulation was prepared of a single harmonic point source whose signals were recorded at an array of 64 receivers. The point source was located at  $(X, Z) = (0.25\lambda, 15\lambda)$ . This slightly off-center point was chosen so that the source would fall upon one of the reconstruction locations; this prevents some of

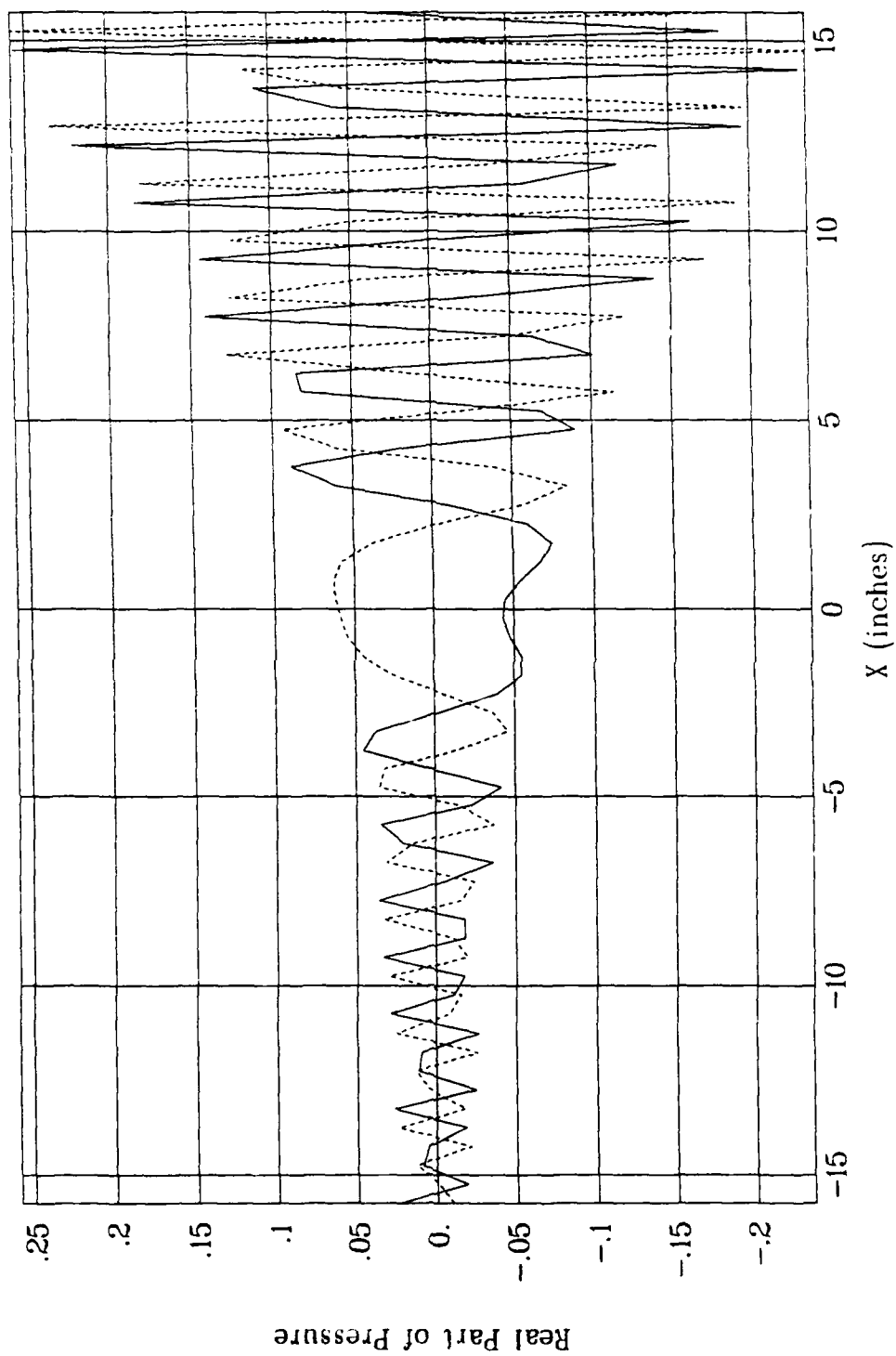


Figure 4.6. Signal at the receiving array due to the true source (solid line) at  $(-5.25\lambda, 15\lambda)$  and the fictitious source (dashed line) at  $(-4.75\lambda, 15\lambda)$ , after diffraction around a barrier and normalization.



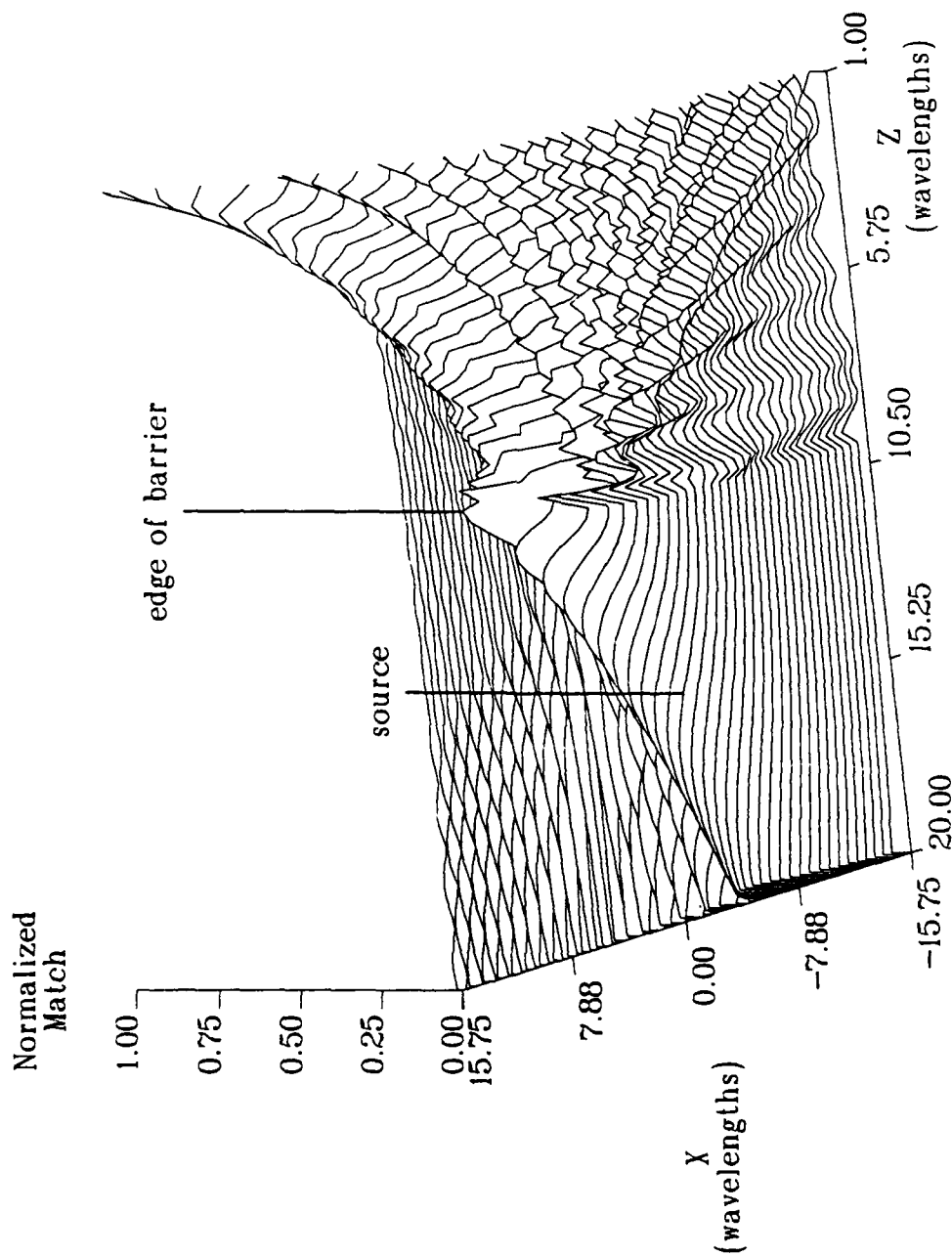


Figure 4.7. Reconstruction using the pattern-match method, without normalization, of a point source at  $(-5.25\lambda, 15\lambda)$  with diffraction by a barrier extending from  $(0, 10\lambda)$  to  $(-\infty, 10\lambda)$ .

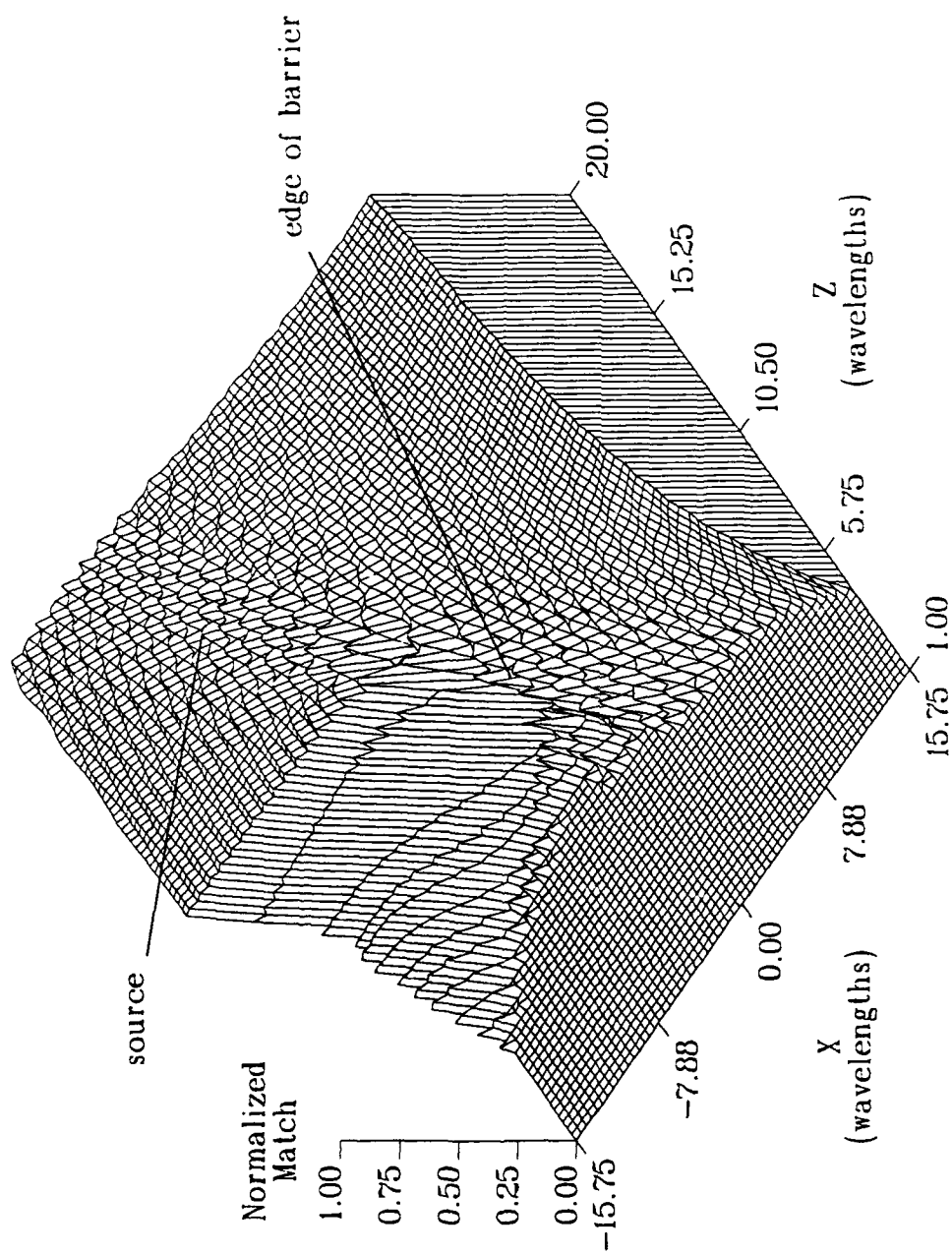


Figure 4.8. Reconstruction using the mismatch method, without normalization, of a point source at  $(-5.25\lambda, 15\lambda)$  with diffraction by a barrier extending from  $(0, 10\lambda)$  to  $(-\infty, 10\lambda)$ .

the minor anomalies which can occur when the source falls between reconstruction locations. The receivers were located on the  $X$  axis at intervals of  $\frac{1}{2}\lambda$  with the array centered so that its ends were at  $\pm 15.75\lambda$ .

In this section, and all subsequent sections in this chapter, the selection of the  $Z$  coordinate of points in the reconstructed field is arbitrary. Thus, we are free to select values which span the region of interest, i.e., from near the receiver array ( $Z = 1\lambda$ ) to beyond the source location (typically,  $Z = 15\lambda$  or  $Z = 20\lambda$ ). The reconstructed field was evaluated at intervals of 1 wavelength (i.e.,  $Z = 1\lambda$ ,  $Z = 2\lambda$ , ...) so that it was unlikely that any feature would be missed.

The choice of the  $X$  coordinate of points in the holographic reconstructions is, unfortunately, not arbitrary — the reconstructed points must lie at the same  $X$  coordinates as the receivers due to the demands of the FFT. Although this restriction does not apply to the pattern-match or mismatch methods, it was adhered to in all of the reconstructions produced in this chapter so that the results could be more easily compared.

In the parlance of holography, the field points are the locations at which the pressure field was “reconstructed.” In the parlance of pattern matching, the fictitious source was placed at these locations. In this study, the word “reconstructed” will henceforth be used to refer to the estimate of the source location(s) regardless of the method by which that estimate is made.

The holography method was implemented in a FORTRAN program, while both pattern-matching methods were implemented in a second FORTRAN program. Input parameters in these programs selects whether or not the fictitious source

is obstructed by a barrier; whether or not the shadow-boundary approximation is used; and which match method is used.

Figure 4.9 exhibits the expected  $\frac{\sin(x)}{x}$  curve when the holography method reconstructed the field at the source (i.e., at  $Z = 15\lambda$ ).

In Figure 4.10, equal-level or contour lines through the field have been generated, while in Figure 4.11, a hidden-line surface plot has been used to present the results. The contour lines use a linear interpolation between adjacent  $X$  values and adjacent  $Z$  values to improve the quality of the plot. While this does not distort the data, it may produce artificially sharp bends in some lines. Also, an occasional spike in the contour lines may result when the algorithm attempts to determine a contour through a group of points which have nearly the same value, such as near  $(-1\lambda, 5\lambda)$  in Figure 4.10.

The reconstruction using the pattern-match method, shown in Figure 4.12, is virtually identical with Figure 4.11 — only a small reduction near  $Z = 0$  can be seen. The reconstruction using the mismatch method was somewhat difficult to display as it consisted of many vertical spikes. Thus, in Figure 4.13, only a portion of the information around the source is shown, and the values which fell below 15% of the maximum have been erased from the plot. In Figure 4.14, this same portion of the information is shown as a contour plot.

One (of many) interpretations of a reconstruction is that it is estimating, at each reconstructed location, the “probability” that there is a source at that location. Ideally, by using better reconstruction methods, we can “push down” the probability at as many reconstruction locations as is possible; this helps

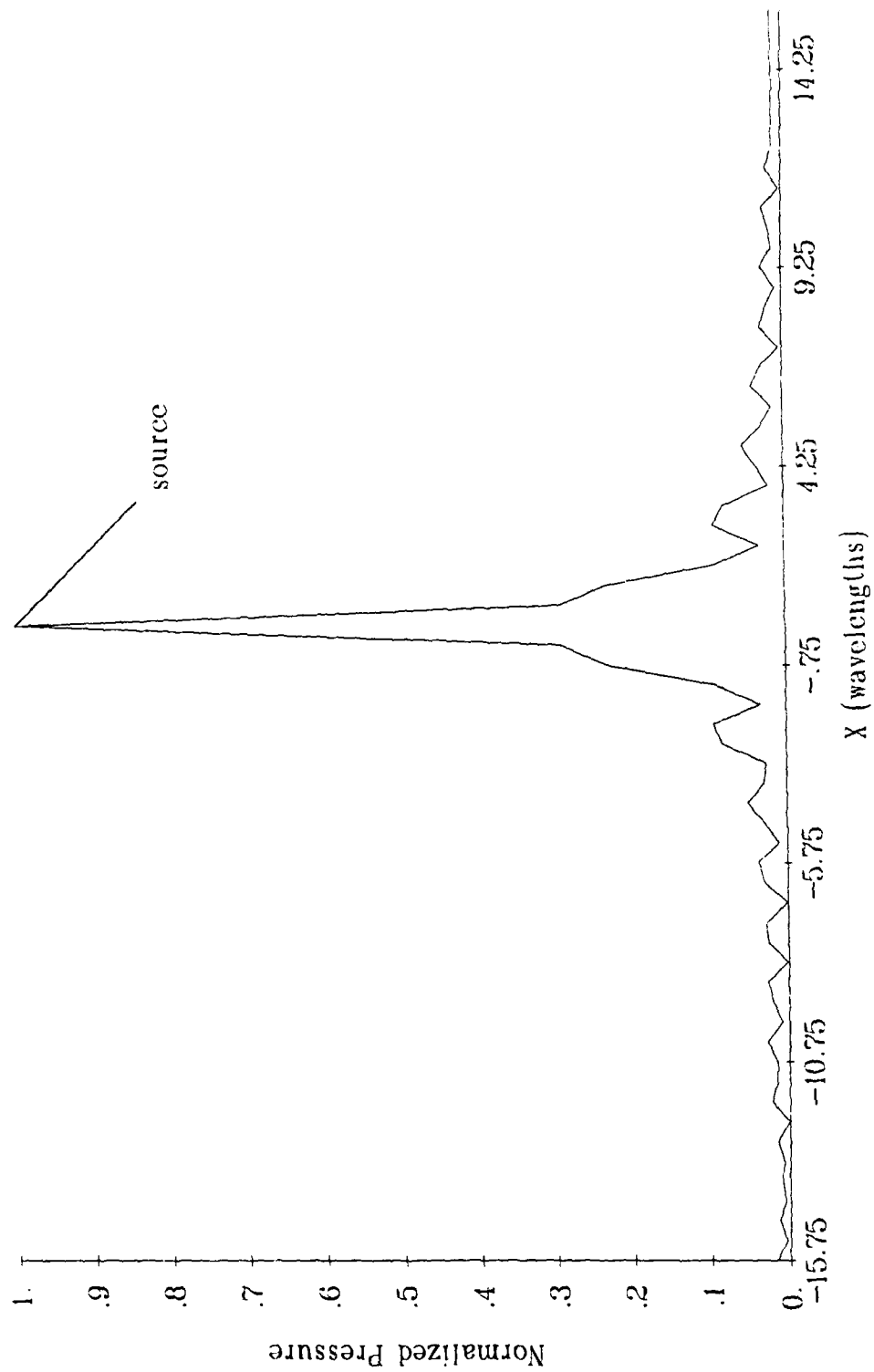


Figure 4.9. Holographic reconstruction at  $Z=15\lambda$  of a point source at  $(0.25\lambda, 15\lambda)$ .

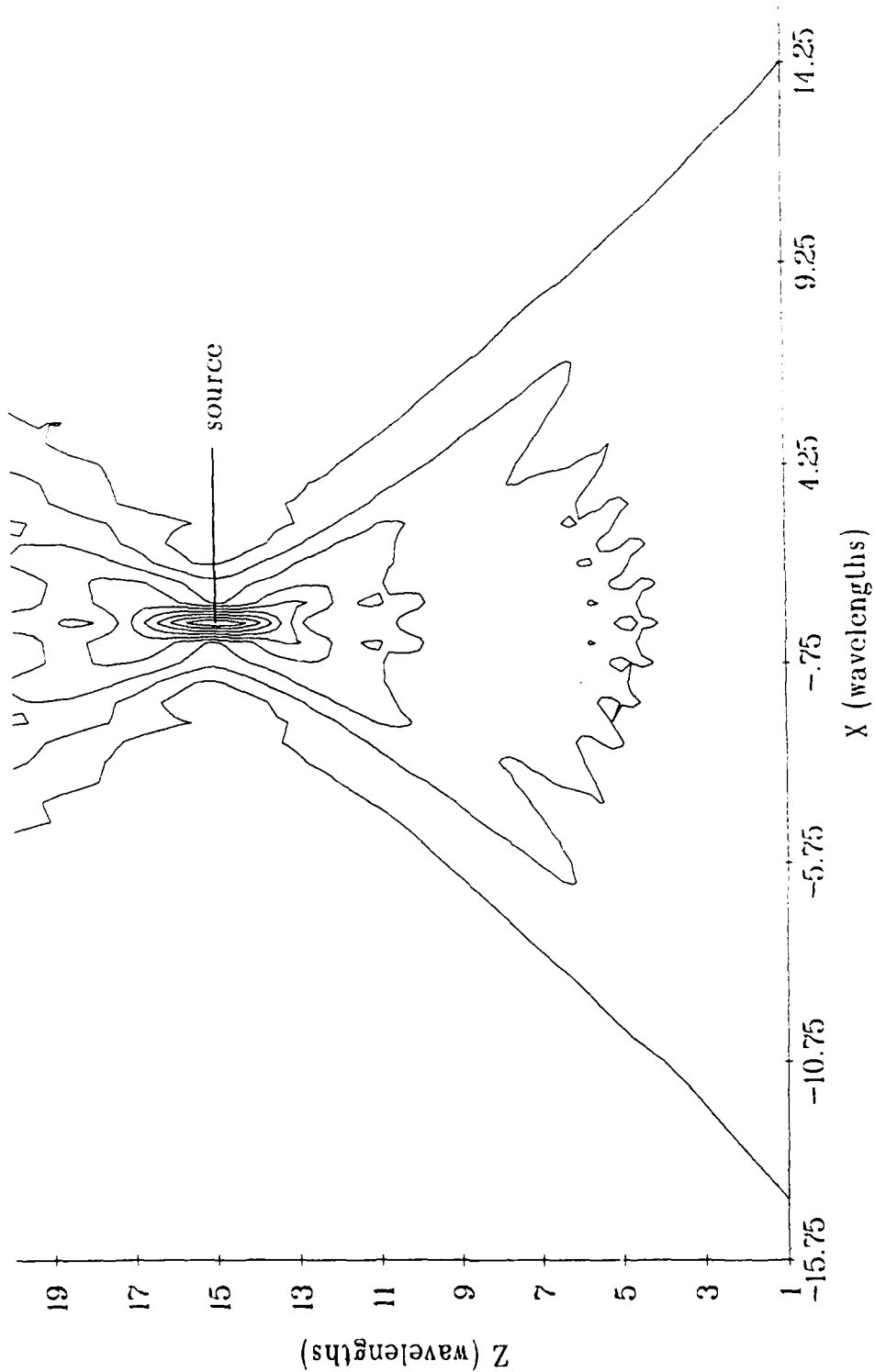


Figure 4.10. Holographic reconstruction of a point source at  $(0.25\lambda, 15\lambda)$ ; contour lines are at 10%, 20%, ..., 90% of the maximum.

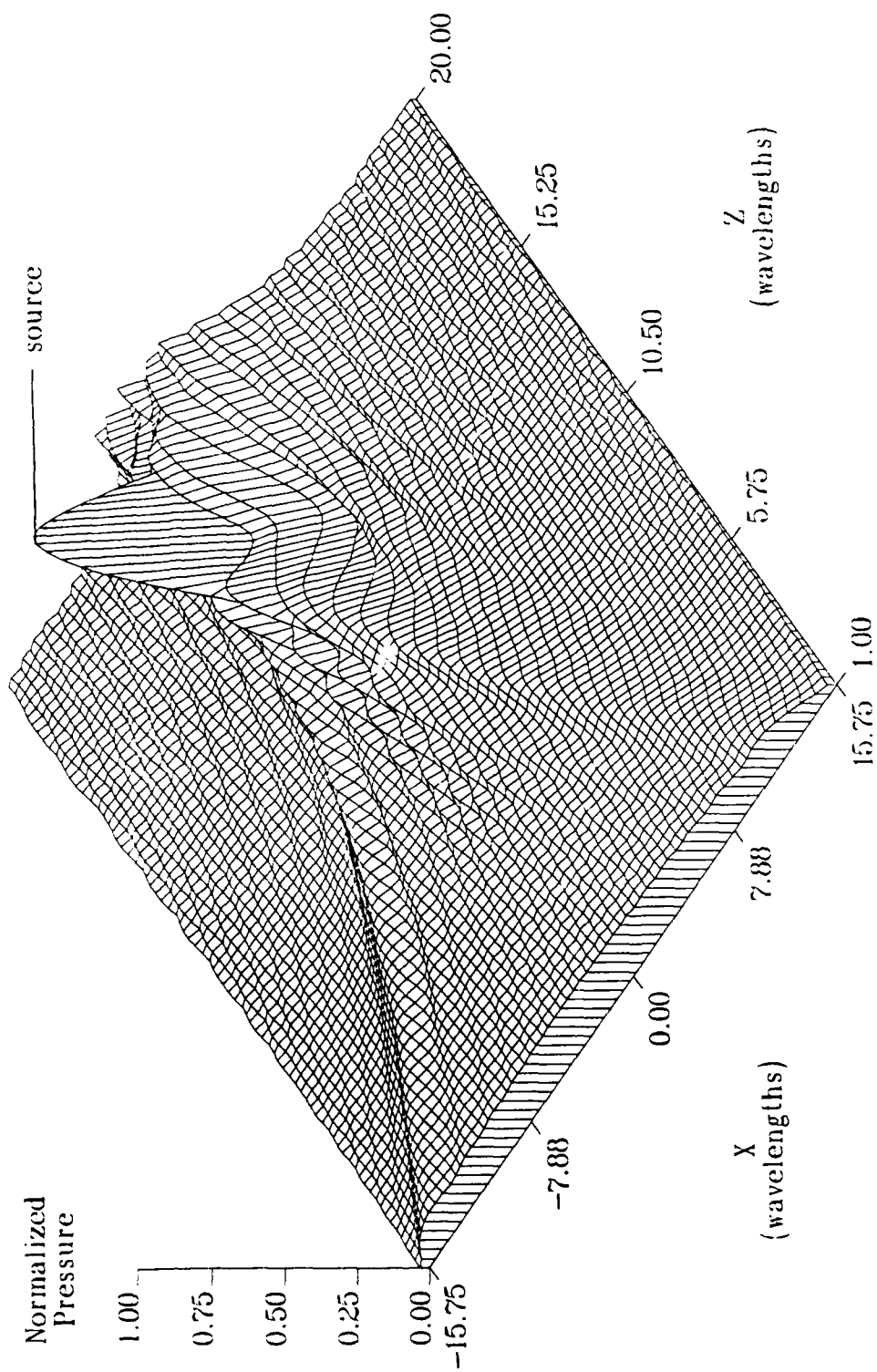


Figure 4.11. Holographic reconstruction of a point source at  $(0.25\lambda, 15\lambda)$ .

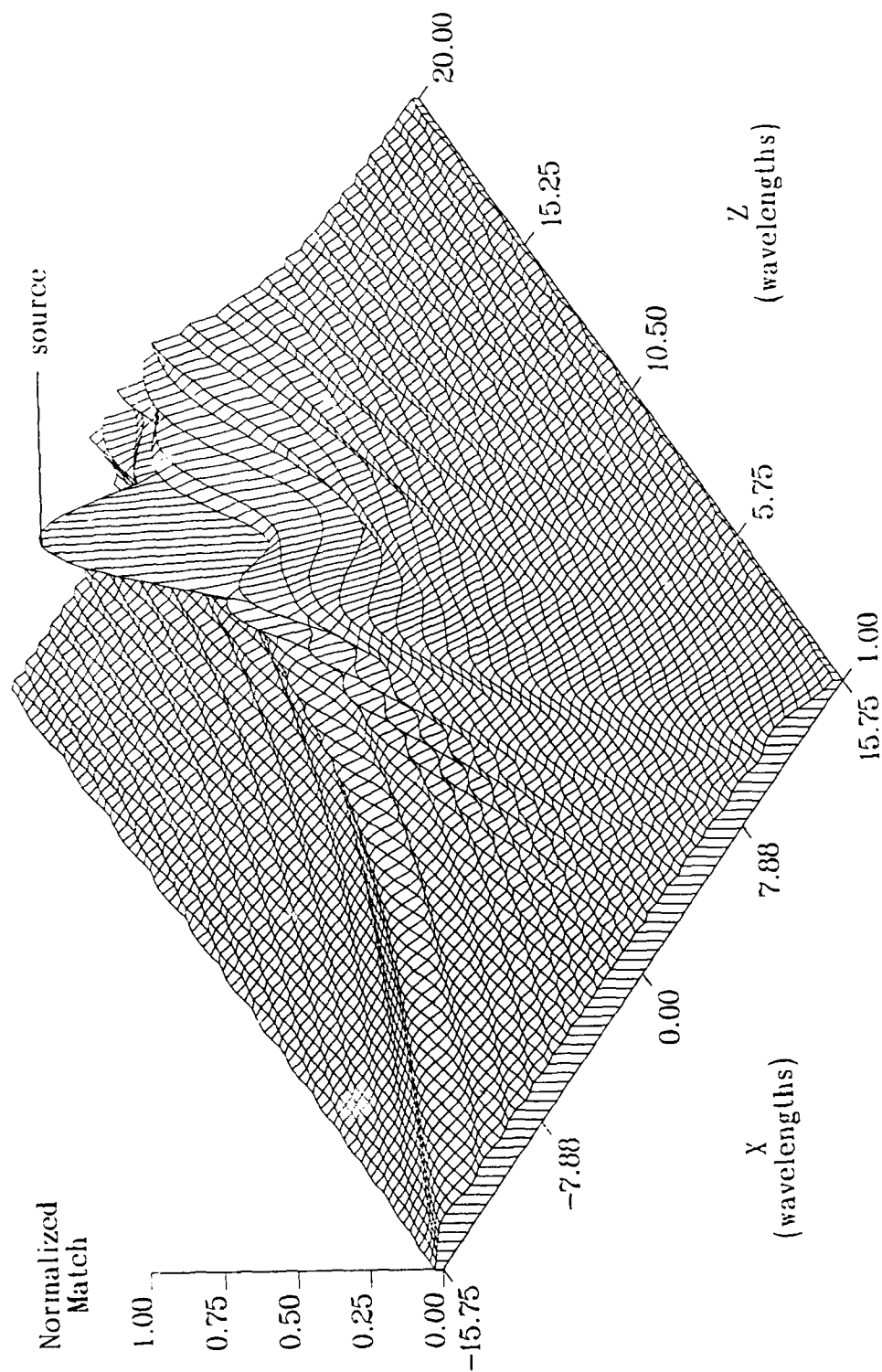


Figure 4.12. Pattern-match reconstruction of a point source at  $(0.25\lambda, 15\lambda)$ .



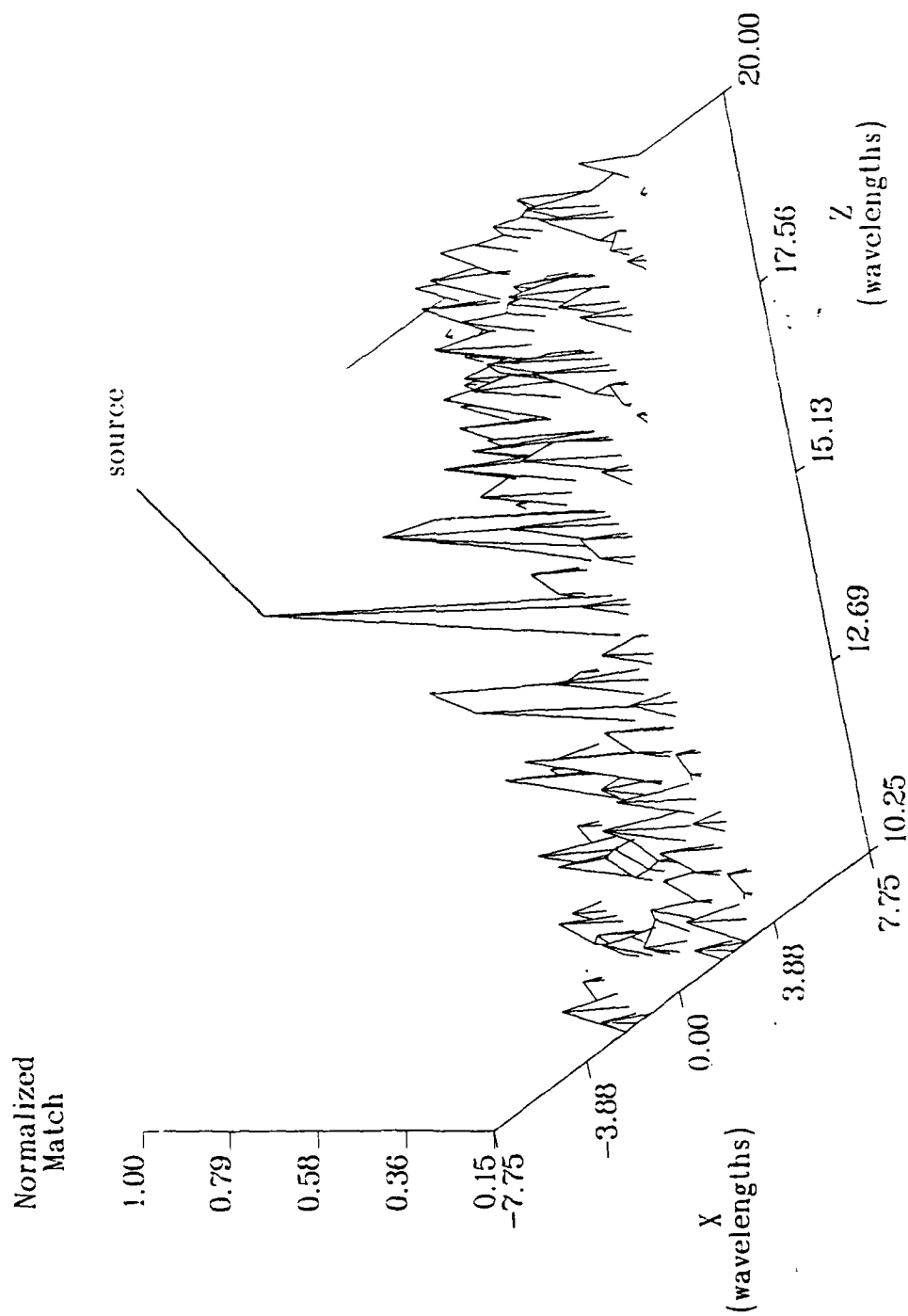


Figure 4.13. Mismatch reconstruction of a point source at  $(0.25\lambda, 15\lambda)$  with values below 15% of the maximum amplitude removed for clarity.

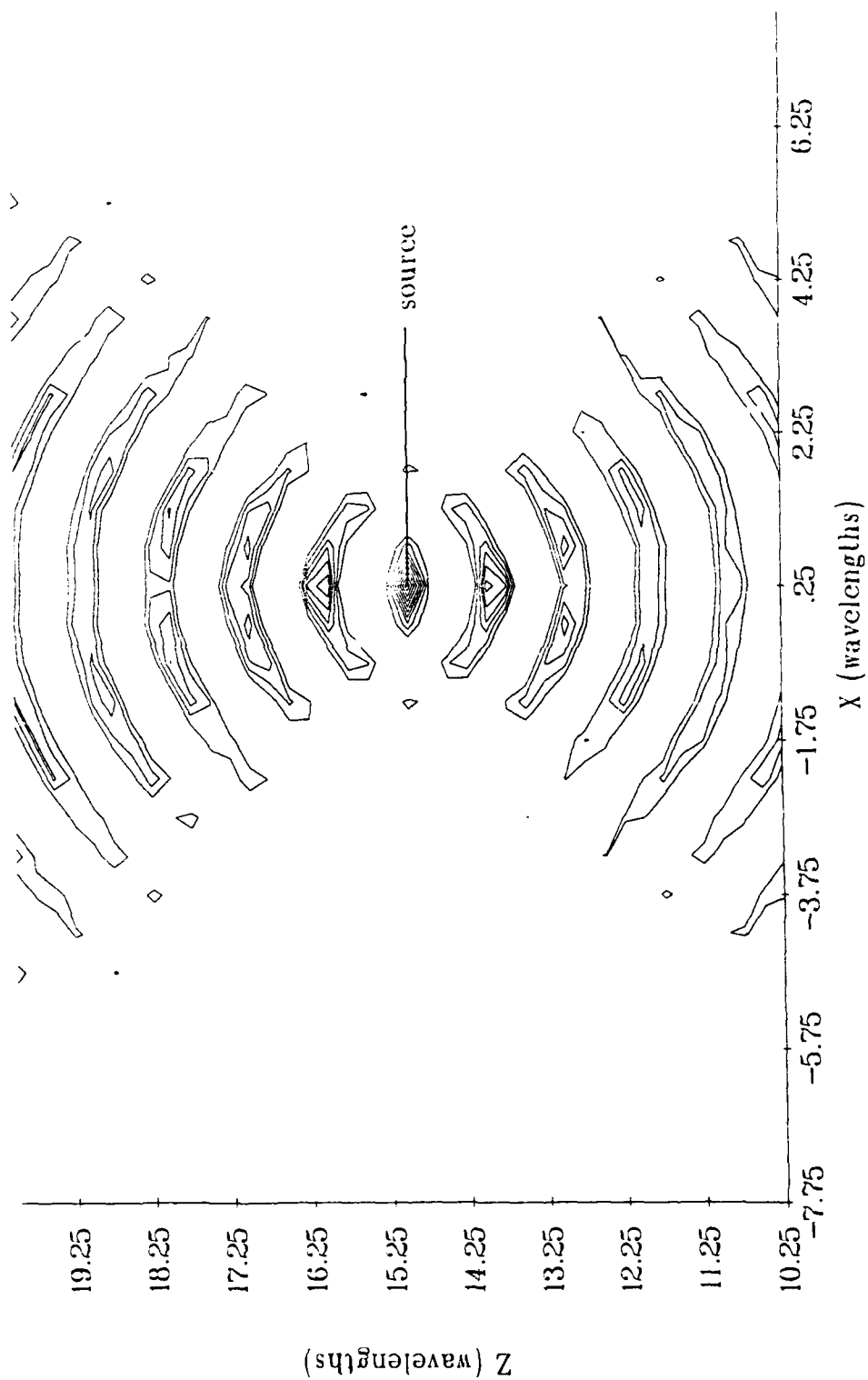


Figure 4.14. Mismatch reconstruction of a point source at  $(0.25\lambda, 15\lambda)$ ; contour lines are at 10%, 20%, ..., 90% of the maximum.

eliminate these locations from consideration, leaving (hopefully) only one location where the source could possibly be located.

These figures, and many others not shown here, lead to the observation that the *envelope* of the mismatch spikes is quite similar to the results provided by the holography and pattern-match methods. Thus, the mismatch method, at the location of its spikes, is making the same estimate as the other methods — no better, no worse. On the other hand, at the nulls between the spikes, the mismatch method has pushed down the probability, thus eliminating these regions from consideration. In particular, measurements of Figure 4.14 indicate that the peaks around the true source location form partial rings separate by about one wavelength. This seems reasonable since the transmitter is producing sinusoids which exactly repeat every wavelength.

#### 4.5 Locating a Source Near a Reflector

A barrier is now introduced which extends from  $(X, Z) = (0, 10\lambda)$  to  $(-\infty, 10\lambda)$ . Otherwise, the simulation is identical with that of the previous section. The barrier's height, in the  $Y$  direction, is irrelevant since the simulation is being conducted in only two dimensions. The field generated by a source in this location is shown in Figure 4.15.

The holographic reconstruction, shown in Figure 4.16, exhibits a false source, as would be expected, due to the reflection of the true source by the barrier.

The pattern-match reconstruction, shown in Figure 4.17, does not exhibit a false source but does show some additional peaks. These additional peaks can

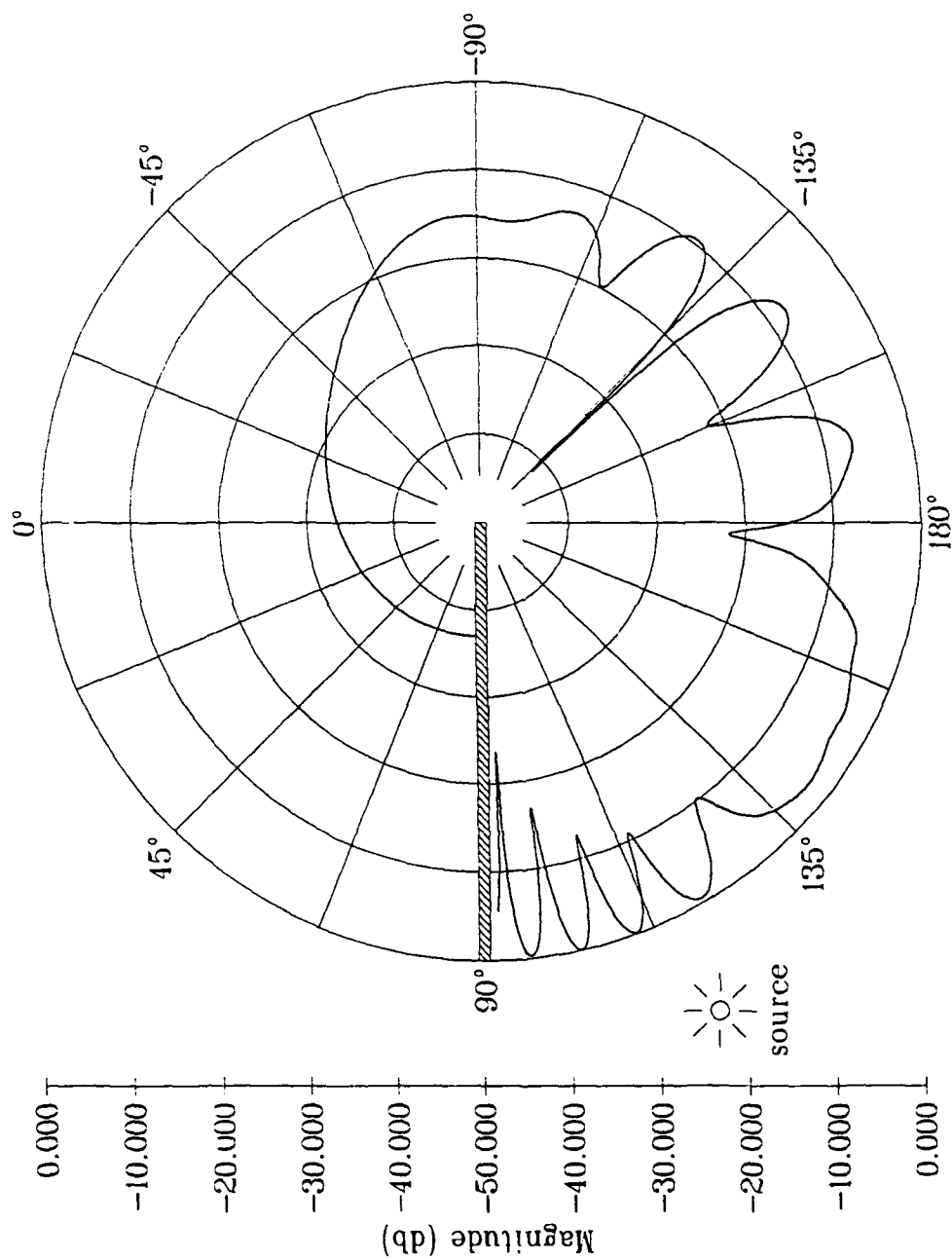


Figure 4.15. Magnitude of the pressure from a source at  $(-5.25\lambda, 7.5\lambda)$  with a barrier extending from  $(0, 10\lambda)$  to  $(-\infty, 10\lambda)$ . The field was evaluated at a radius of  $10\lambda$  from the edge.

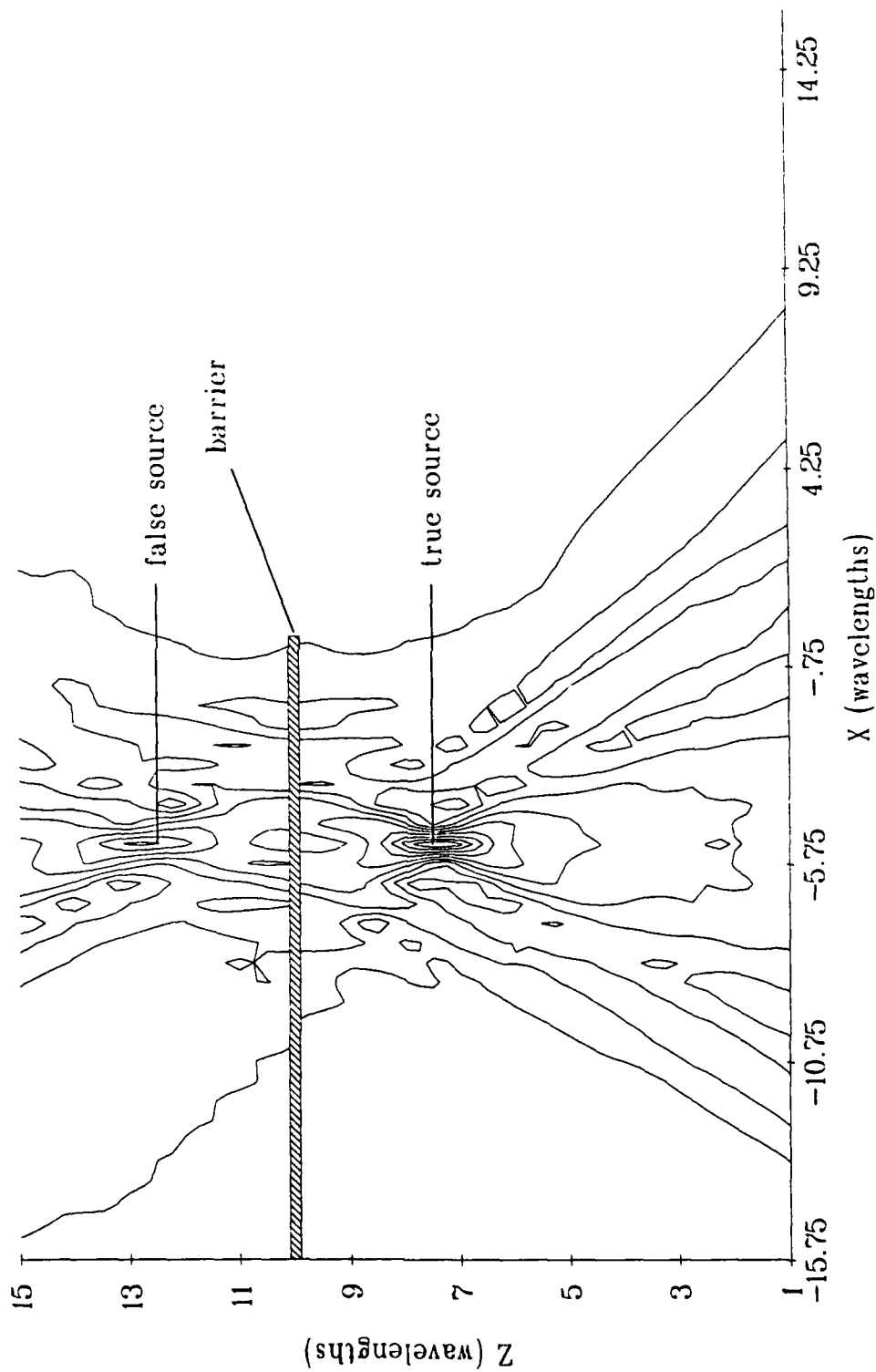


Figure 4.16. Holographic reconstruction of a point source at  $(-5.25\lambda, 7.5\lambda)$  with a barrier extending from  $(0, 10\lambda)$  to  $(-\infty, 10\lambda)$ .

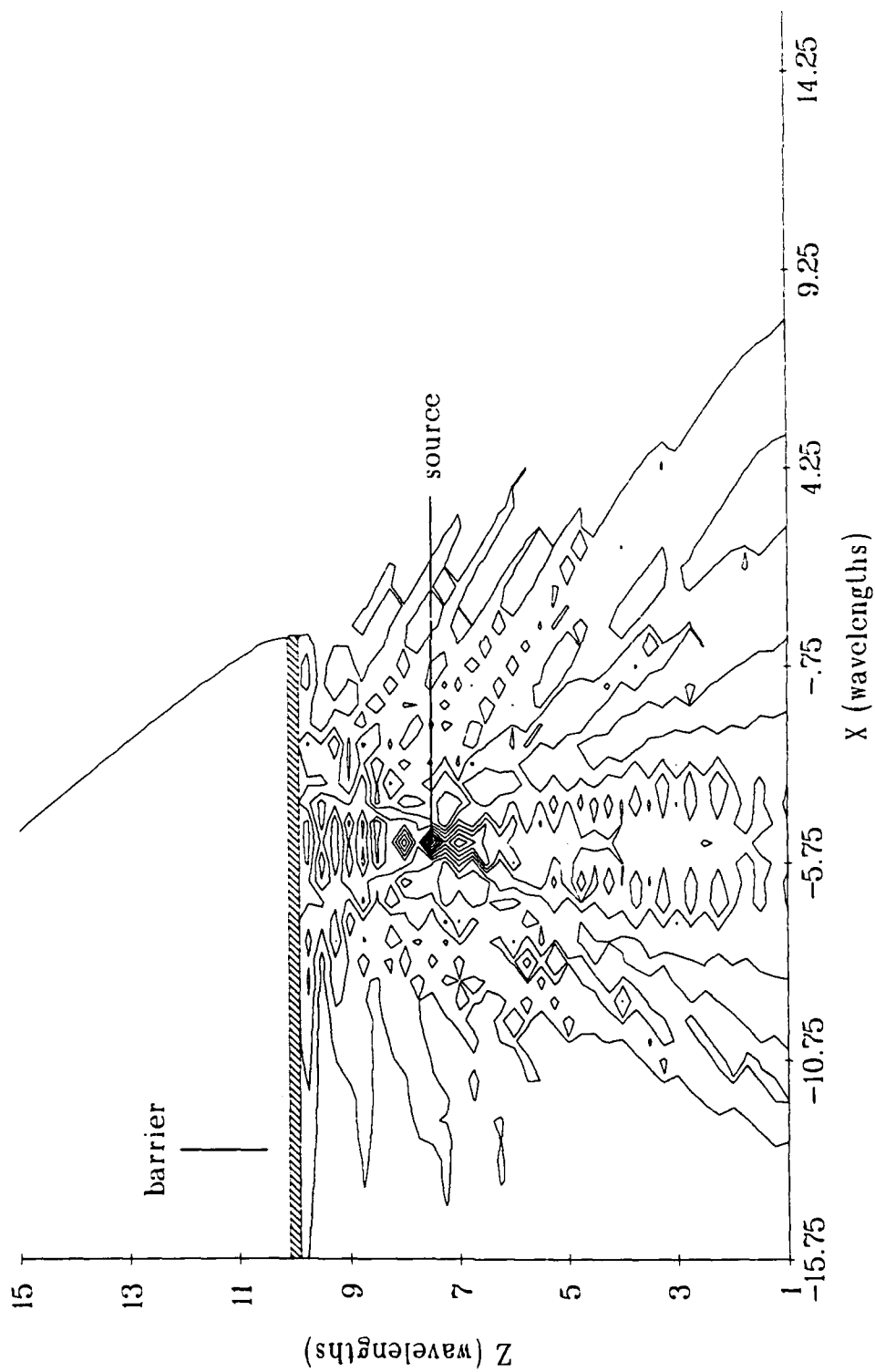


Figure 4.17. Pattern-match reconstruction of a point source at  $(-5.25\lambda, 7.5\lambda)$  with a barrier extending from  $(0, 10\lambda)$  to  $(-\infty, 10\lambda)$ ; contour lines are at 10%, 20%, ..., 90% of the maximum.

be seen more clearly in Figure 4.18 where only the information near the true source has been retained.

The mismatch method reconstruction, shown in Figure 4.19, has had values below 10% of the maximum removed for clarity. A contour plot of this reconstruction, shown in Figure 4.20, exhibits partial rings of peaks around the true source, separated by about one wavelength, similar to that shown in Figure 4.14 for the free-space case.

In addition, the mismatch method exhibits some low-level matches along lines *behind* the barrier with the lines separated by about a wavelength. There may be several reasons for these matches behind the barrier. First, in this region, one of the basic assumptions of the diffraction equation has been partially violated since some of the points are not many wavelengths from the edge. Second, as shown by Figure 4.6, the signal at the receiving array from points behind the barrier look very much like a sine wave and so may produce a low level match with almost anything. Such a phenomenon would somewhat repeat for every additional wavelength that the fictitious source is moved away from the edge of the barrier.

In many imaging situations, the sources are identified as being at those locations where the image level is above some threshold. If a threshold were set at, say, 50% of the maximum, the mismatch method would provide the most precise location of the source. At a lower threshold, all methods exhibit some problems: both matching methods show additional peaks; and the holography method shows a false source due to reflection.

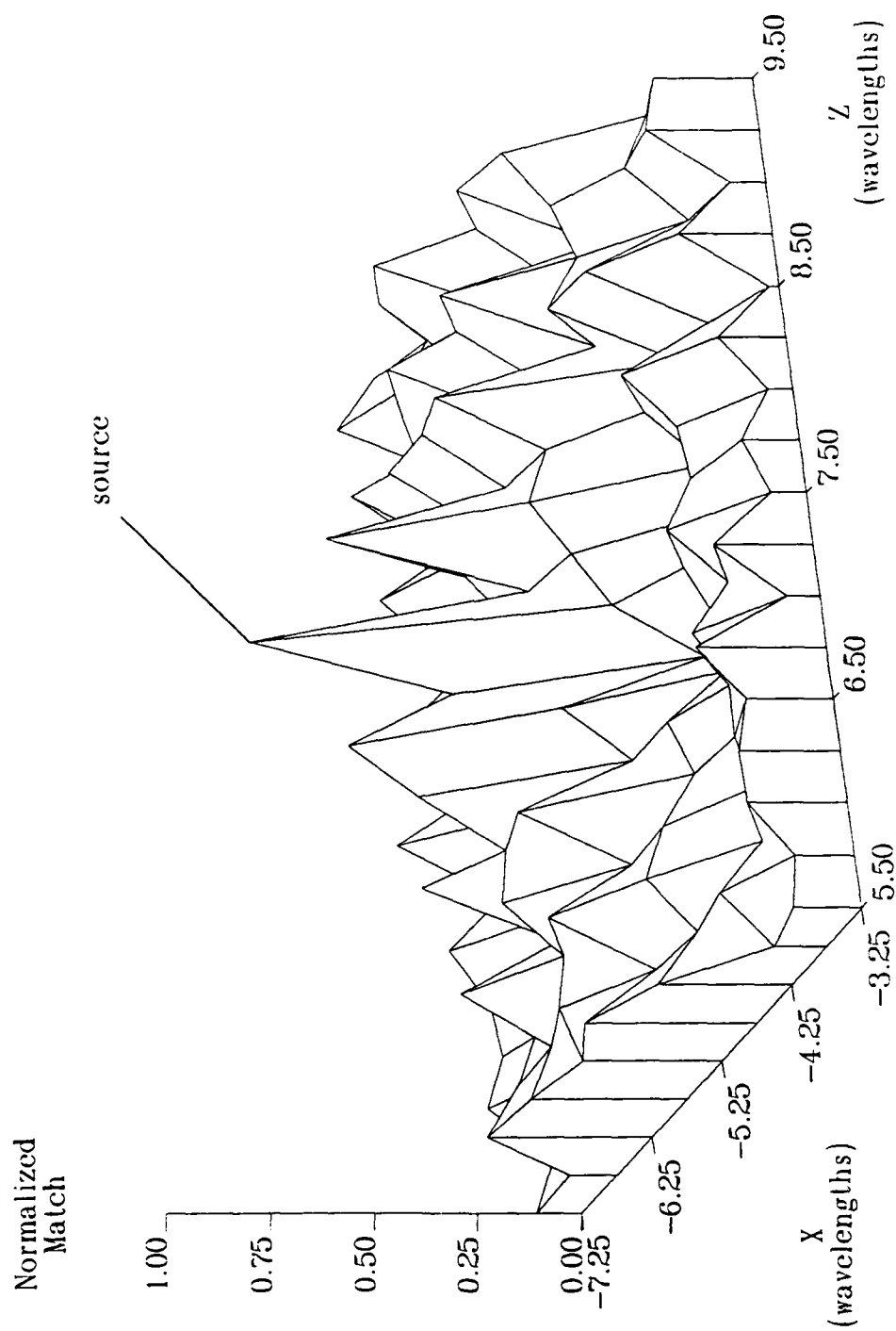


Figure 4.18. Pattern-match reconstruction of a point source at  $(-5.25\lambda, 7.5\lambda)$  with a barrier extending from  $(0, 10\lambda)$  to  $(-\infty, 10\lambda)$ .



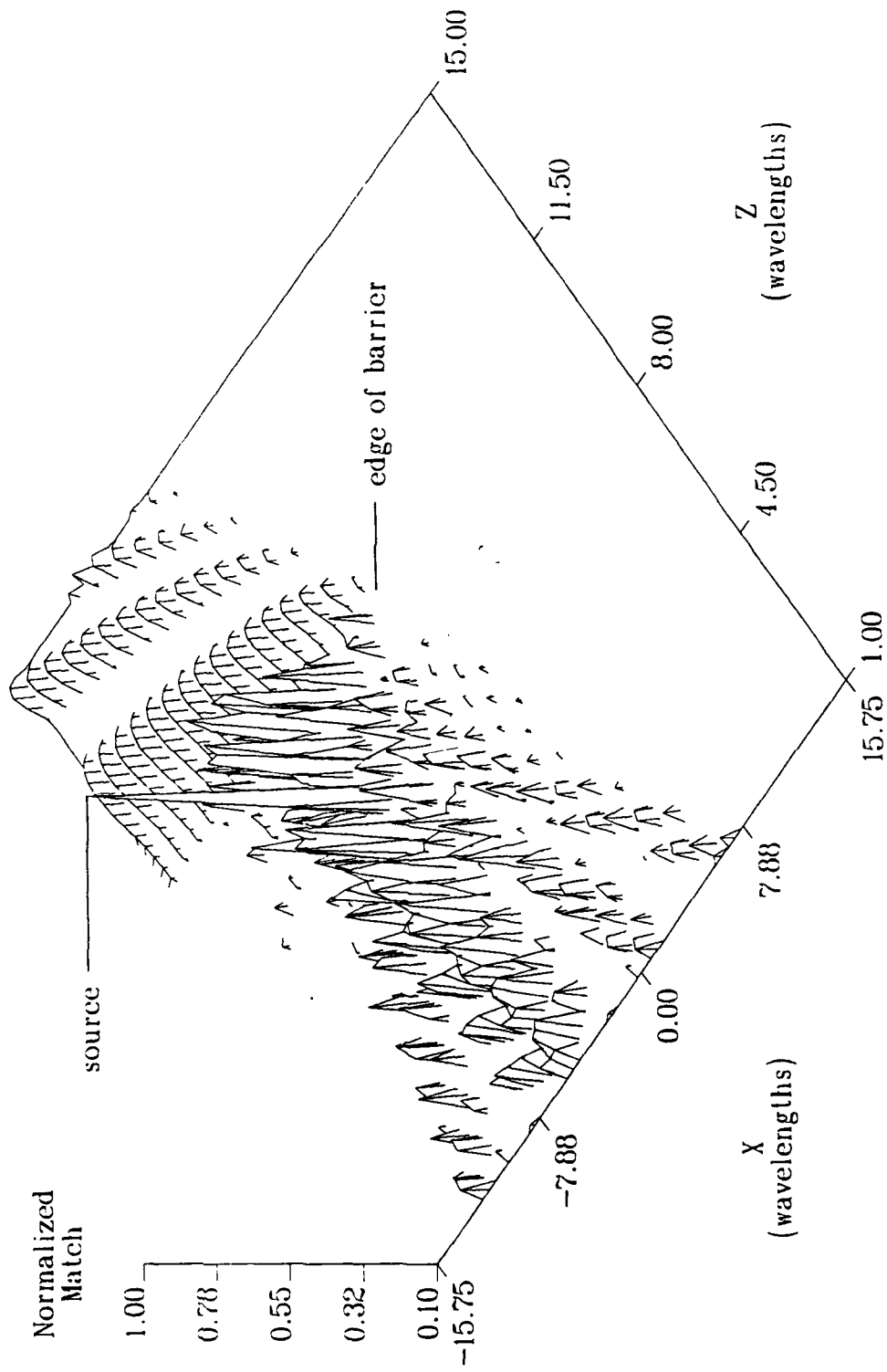


Figure 4.19. Mismatch reconstruction of a point source at  $(-5.25\lambda, 7.5\lambda)$  with a barrier extending from  $(0, 10\lambda)$  to  $(-\infty, 10\lambda)$ . Values below 10% of the maximum have been removed for clarity.

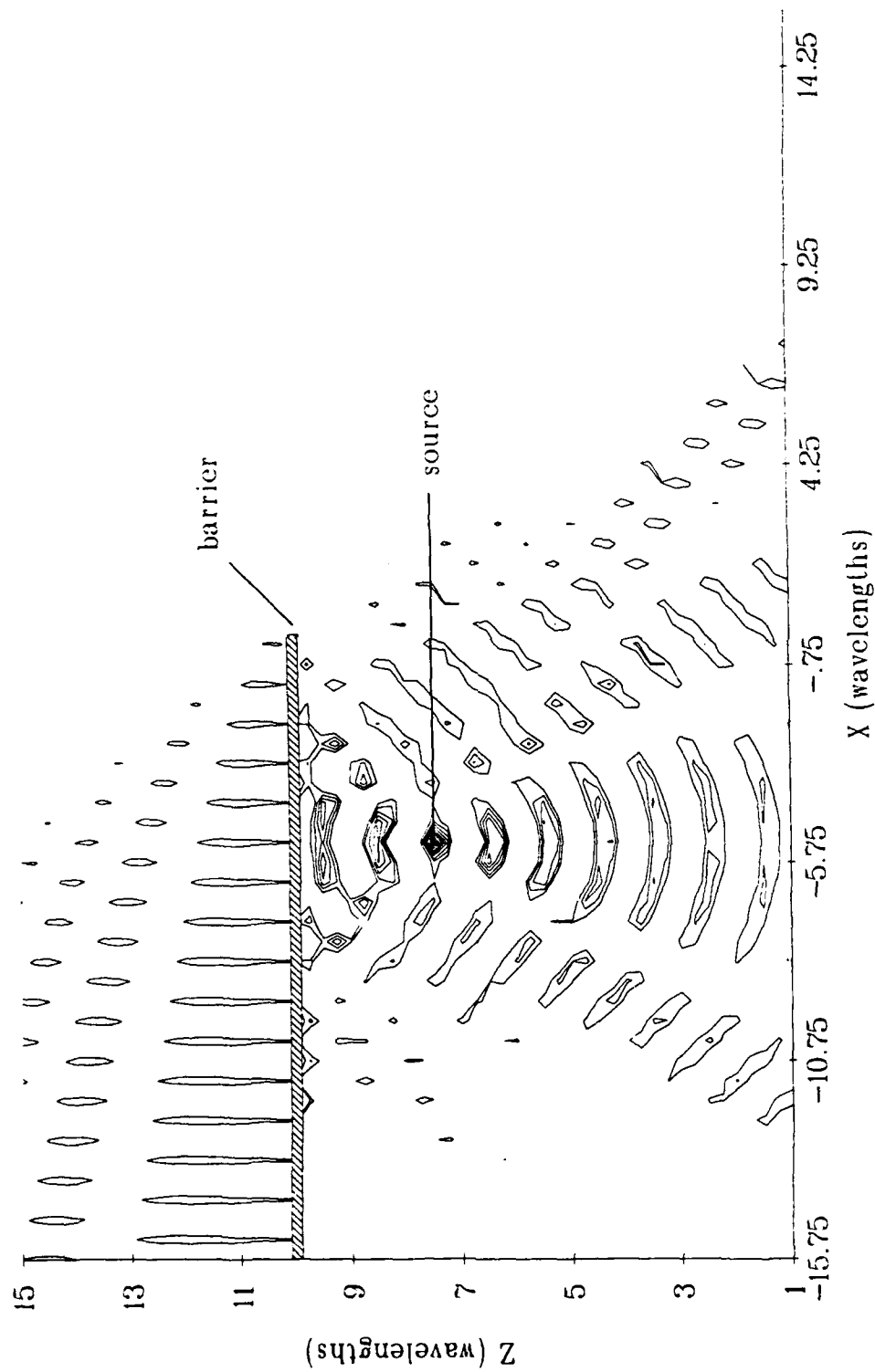


Figure 4.20. Mismatch reconstruction of a point source at  $(-5.25\lambda, 7.5\lambda)$  with a barrier extending from  $(0, 10\lambda)$  to  $(-\infty, 10\lambda)$ ; contour lines are at 10%, 20%, ..., 90% of the maximum.

#### 4.6 Locating a Source Behind a Barrier

The situation investigated in the previous section is now repeated except that the source is moved behind the barrier so that the transmitted energy is, to various degrees, blocked by the barrier. The source will be located at one of three  $X$  locations along the line at  $Z = 15\lambda$ :  $X = 0.25\lambda$ ;  $X = -2.25\lambda$ ; and  $X = -5.25\lambda$ . The field for the first and last of these three locations is shown in Figures 4.21 and 4.22, respectively.

The reconstructions provided by the holography method are shown in Figures 4.23–4.25. A comparison with the free space holographic reconstruction shows that, as the source becomes hidden behind the barrier, the reconstructed peak moves closer to the edge of the barrier. When the source is almost completely hidden (Figure 4.25), the peak at the barrier's edge seems to be the only disturbance — there is little to even suggest that there is a source behind the barrier.

The pattern-match reconstruction for a source at  $(0.25\lambda, 15\lambda)$  is shown in Figure 4.26 and seems to be a little poorer than the corresponding holographic reconstruction (Figure 4.23) because the main peak seems to have become slightly spread. In addition, Figure 4.27 shows that there is a slightly higher match in the “hidden region” which falls between the barrier and what will be called the boundary line. This boundary line begins at the edge of the barrier and runs through the true source location onto infinity. As the source is moved to locations further behind the barrier, the main change in the reconstruction, shown in Figures 4.28 and 4.29, is that the match in the hidden region rises.

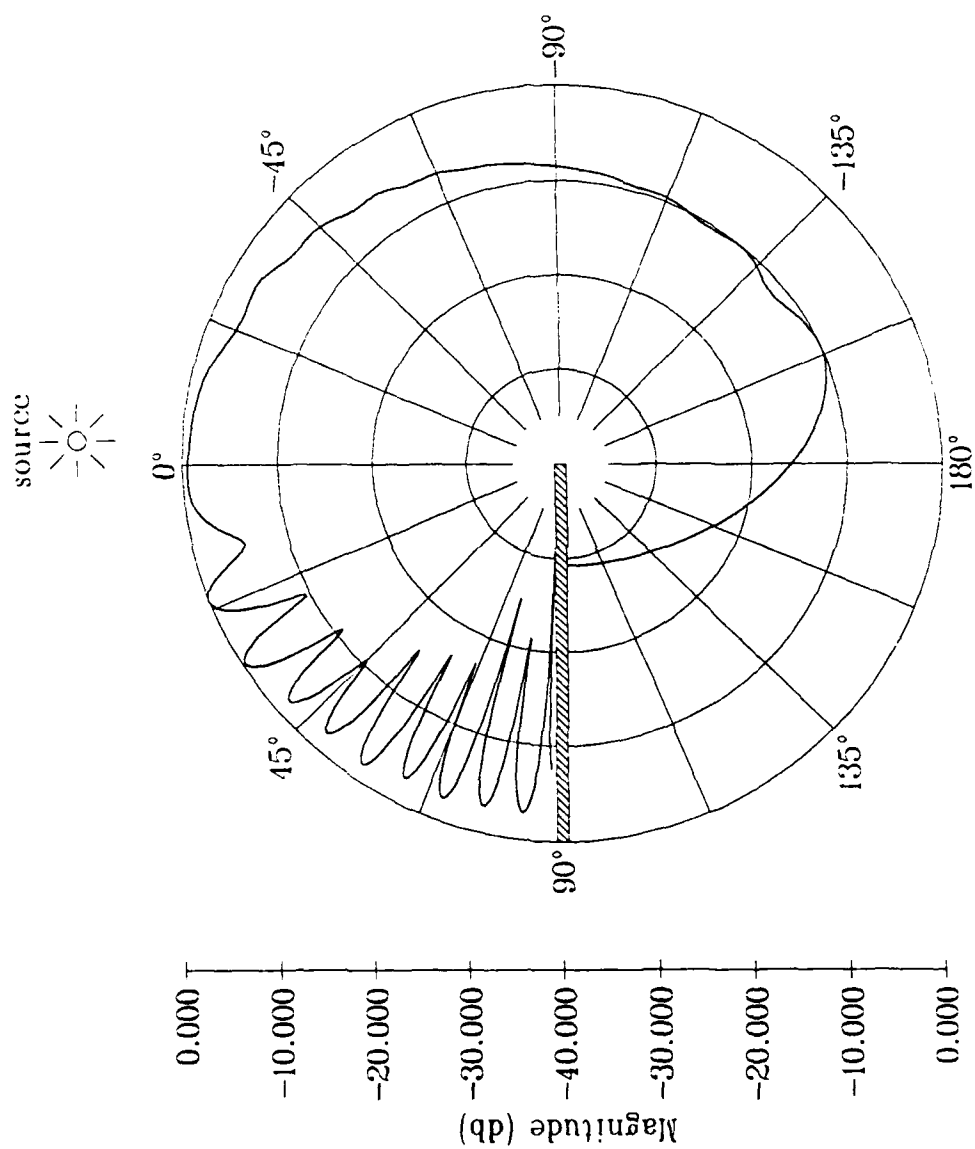


Figure 4.21. Magnitude of the pressure from a source at  $(0.25\lambda, 15\lambda)$  with a barrier extending from  $(0, 10\lambda)$  to  $(-\infty, 10\lambda)$ . The field was evaluated at a radius of  $10\lambda$  from the edge.

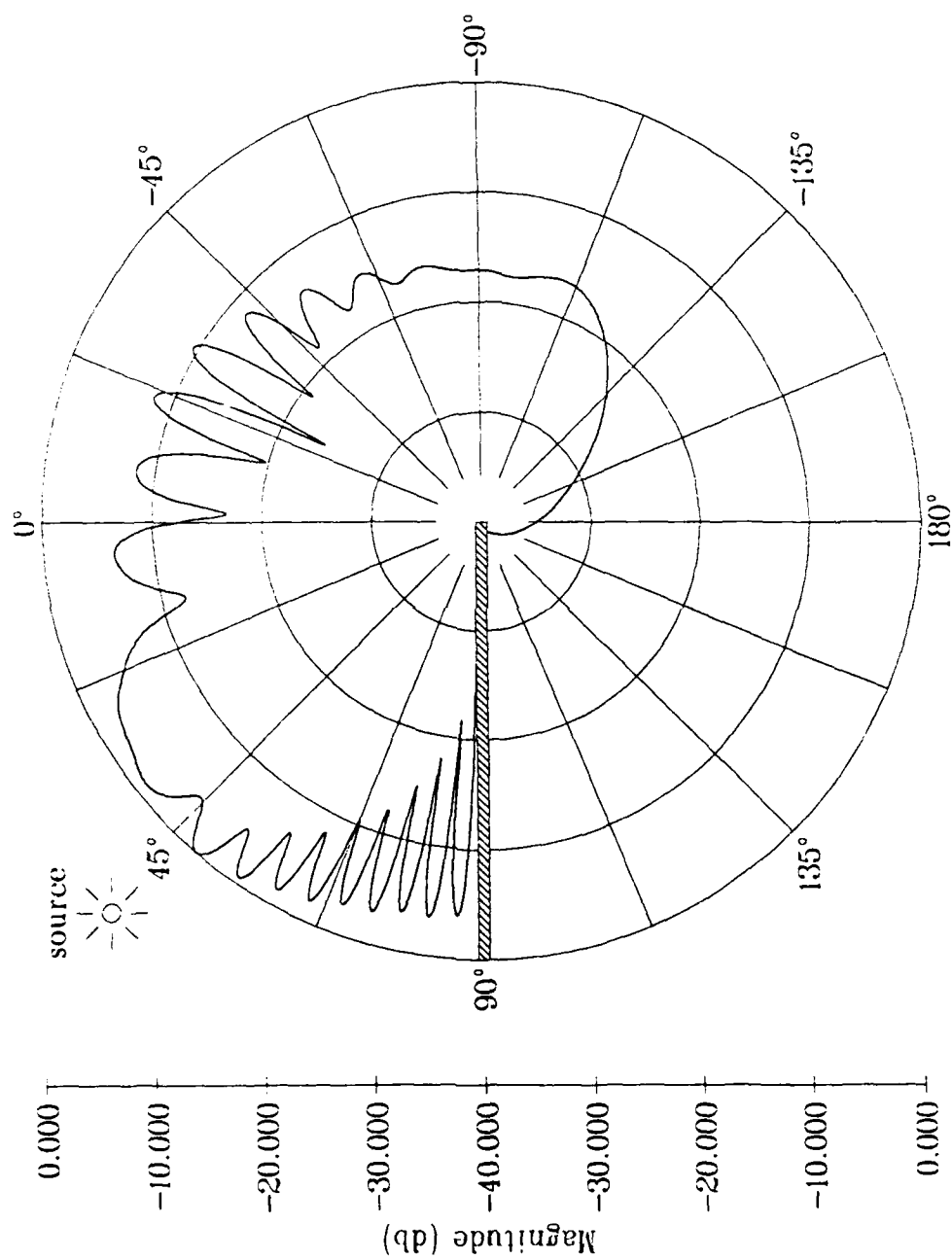


Figure 4.22. Magnitude of the pressure from a source at  $(-5.25\lambda, 15\lambda)$  with a barrier extending from  $(0, 10\lambda)$  to  $(-\infty, 10\lambda)$ . The field was evaluated at a radius of  $10\lambda$  from the edge.

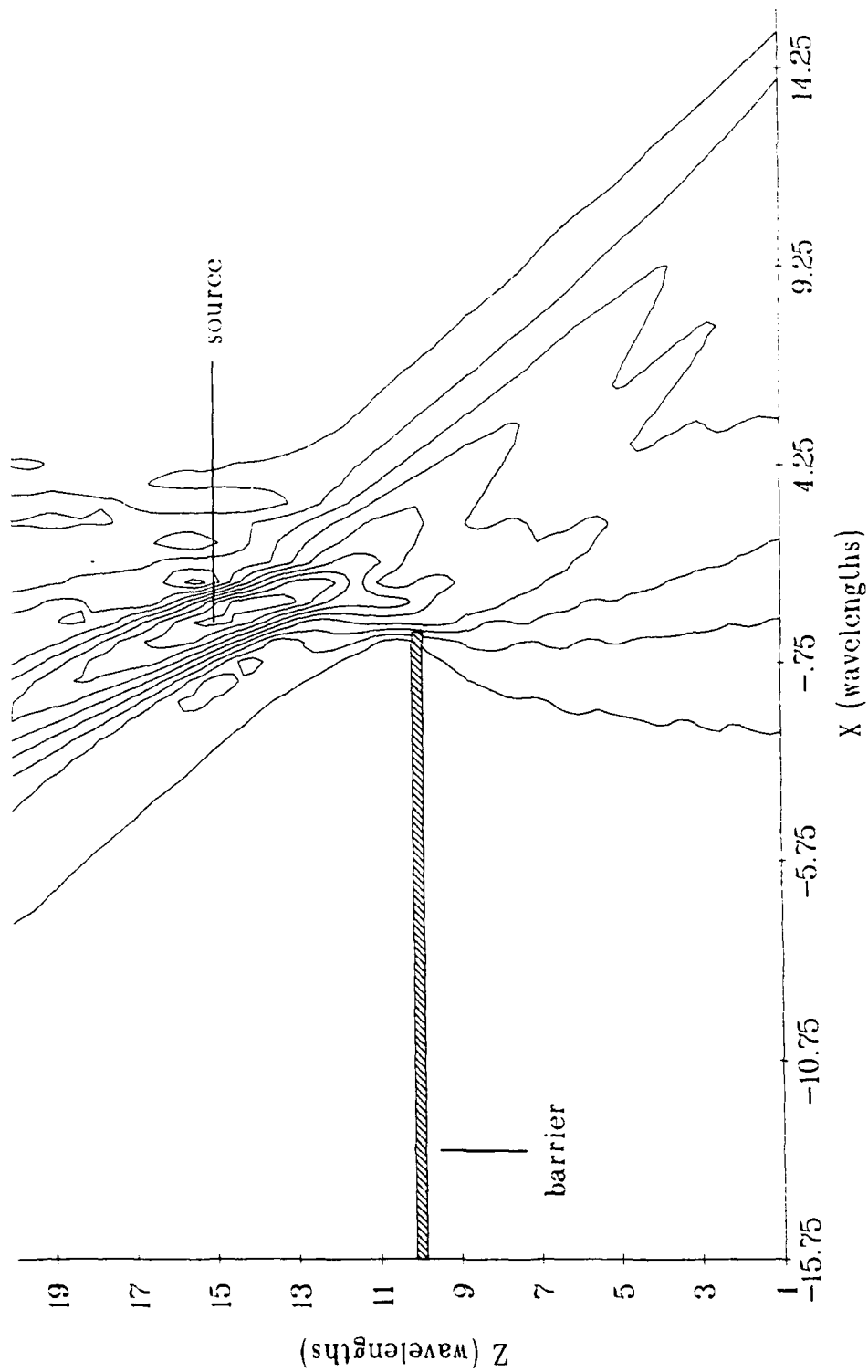


Figure 4.23. Holographic reconstruction of a point source at  $(0.25\lambda, 15\lambda)$  with a barrier extending from  $(0, 10\lambda)$  to  $(-\infty, 10\lambda)$ ; contour lines are at 10%, 20%, ..., 90% of the maximum.

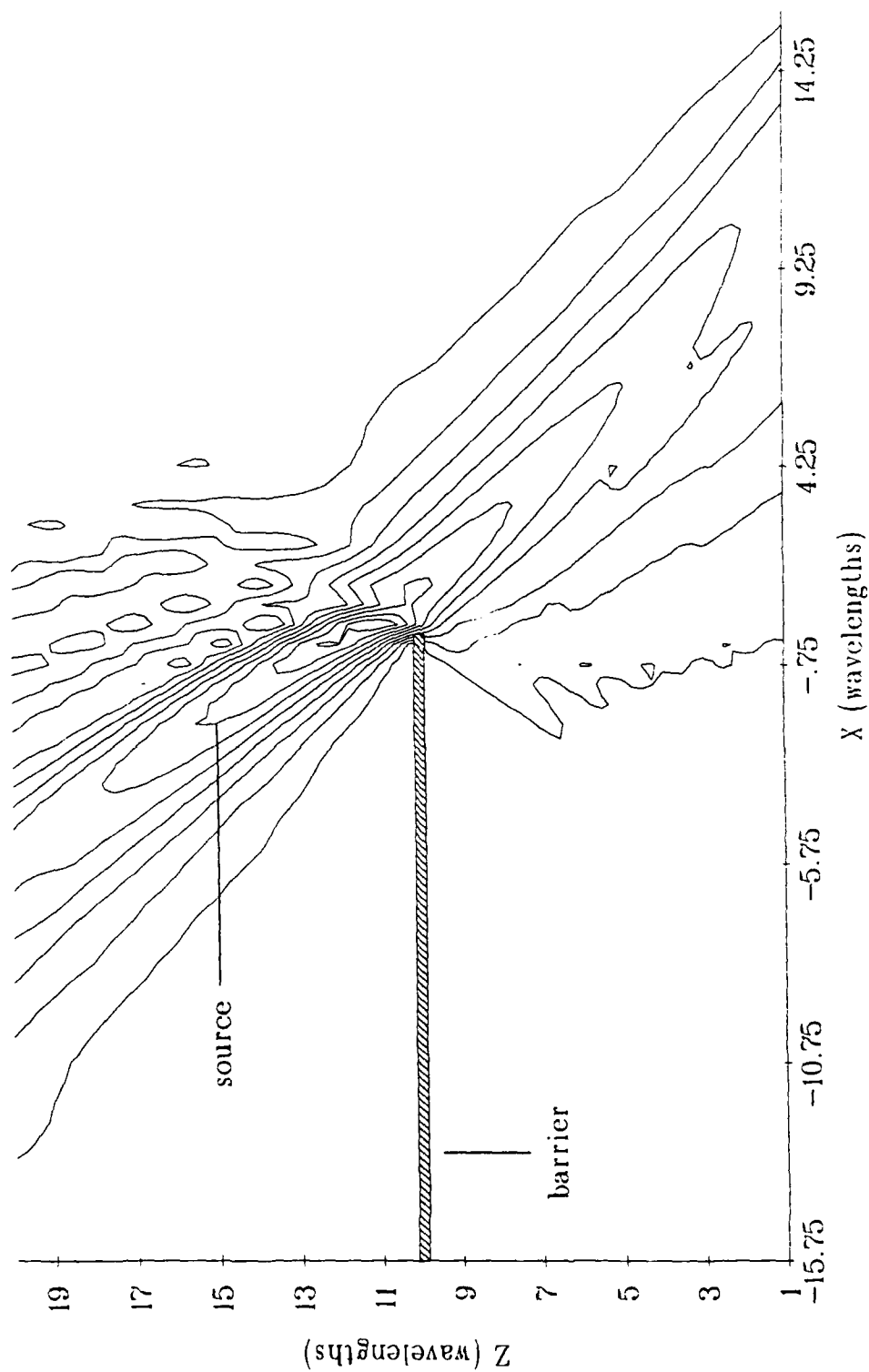


Figure 4.24. Holographic reconstruction of a point source at  $(-2.25\lambda, 15\lambda)$  with a barrier extending from  $(0, 10\lambda)$  to  $(-\infty, 10\lambda)$ ; contour lines are at 10%, 20%, ..., 90% of the maximum.

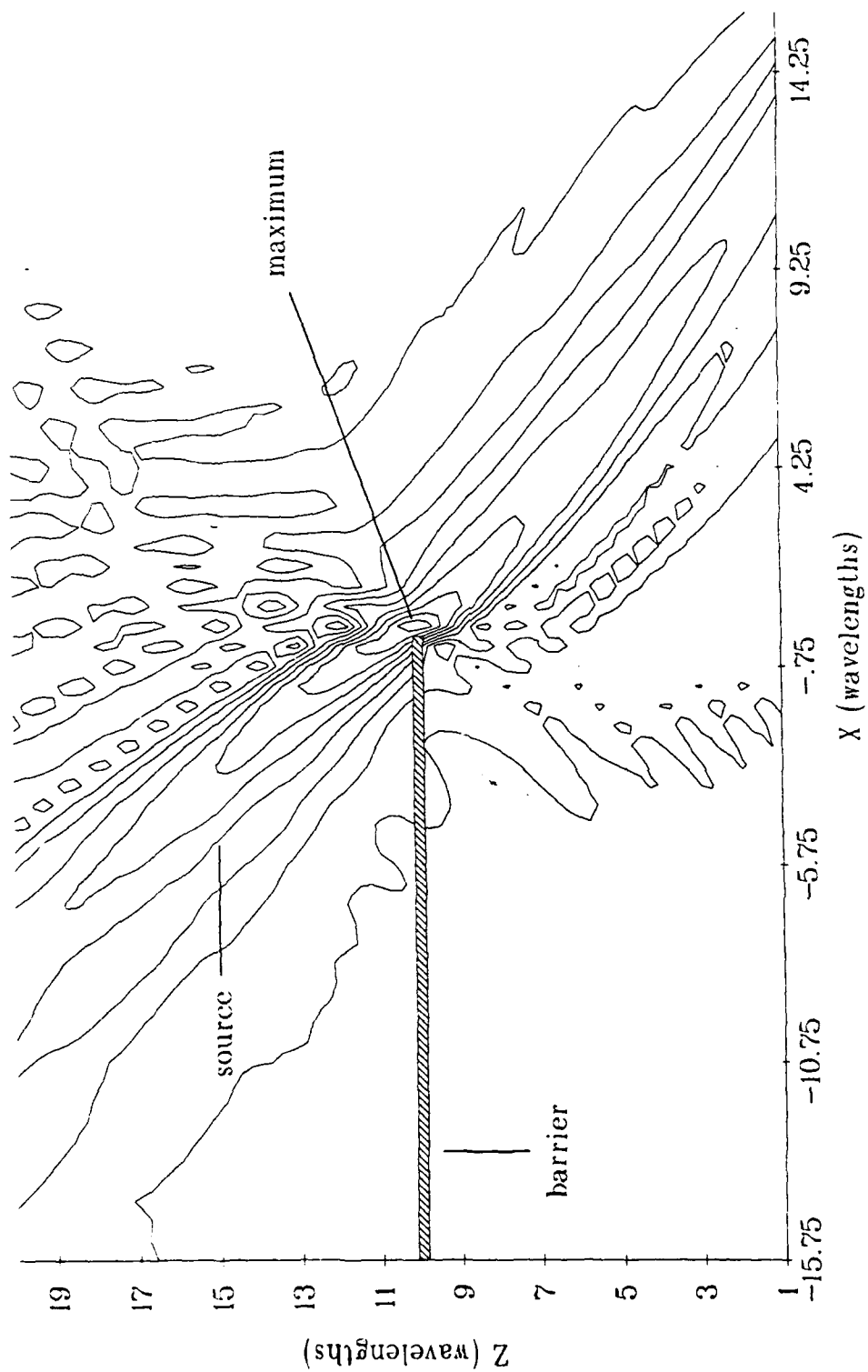


Figure 4.25. Holographic reconstruction of a point source at  $(-5.25\lambda, 15\lambda)$  with a barrier extending from  $(0, 10\lambda)$  to  $(-\infty, 10\lambda)$ ; contour lines are at 10%, 20%, ..., 90% of the maximum.



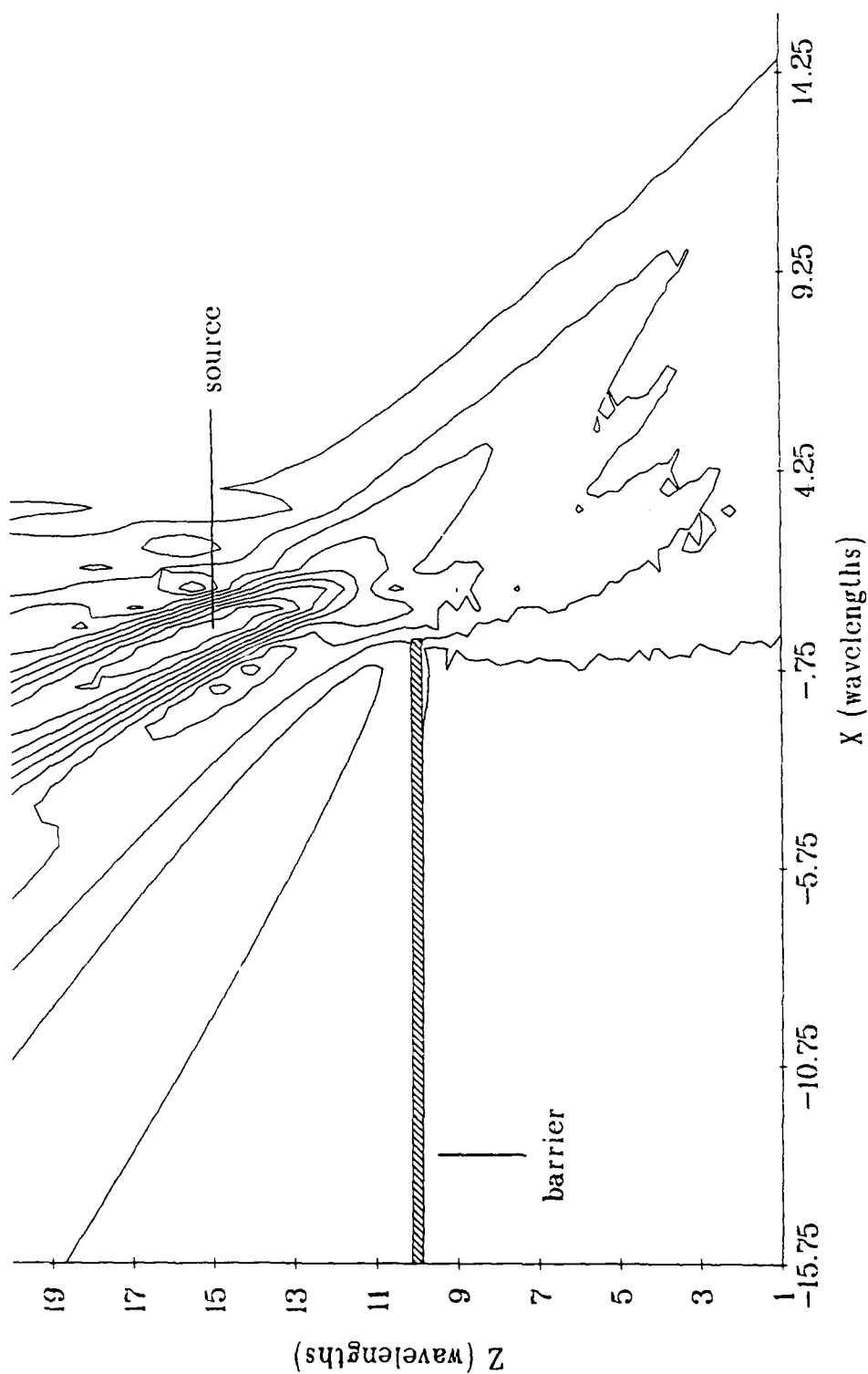


Figure 4.26. Pattern-match reconstruction of a point source at  $(0.25\lambda, 15\lambda)$  with a barrier extending from  $(-\infty, 10\lambda)$  to  $(-\infty, 10\lambda)$ ; contour lines are at 10%, 20%, ..., 90% of the maximum.

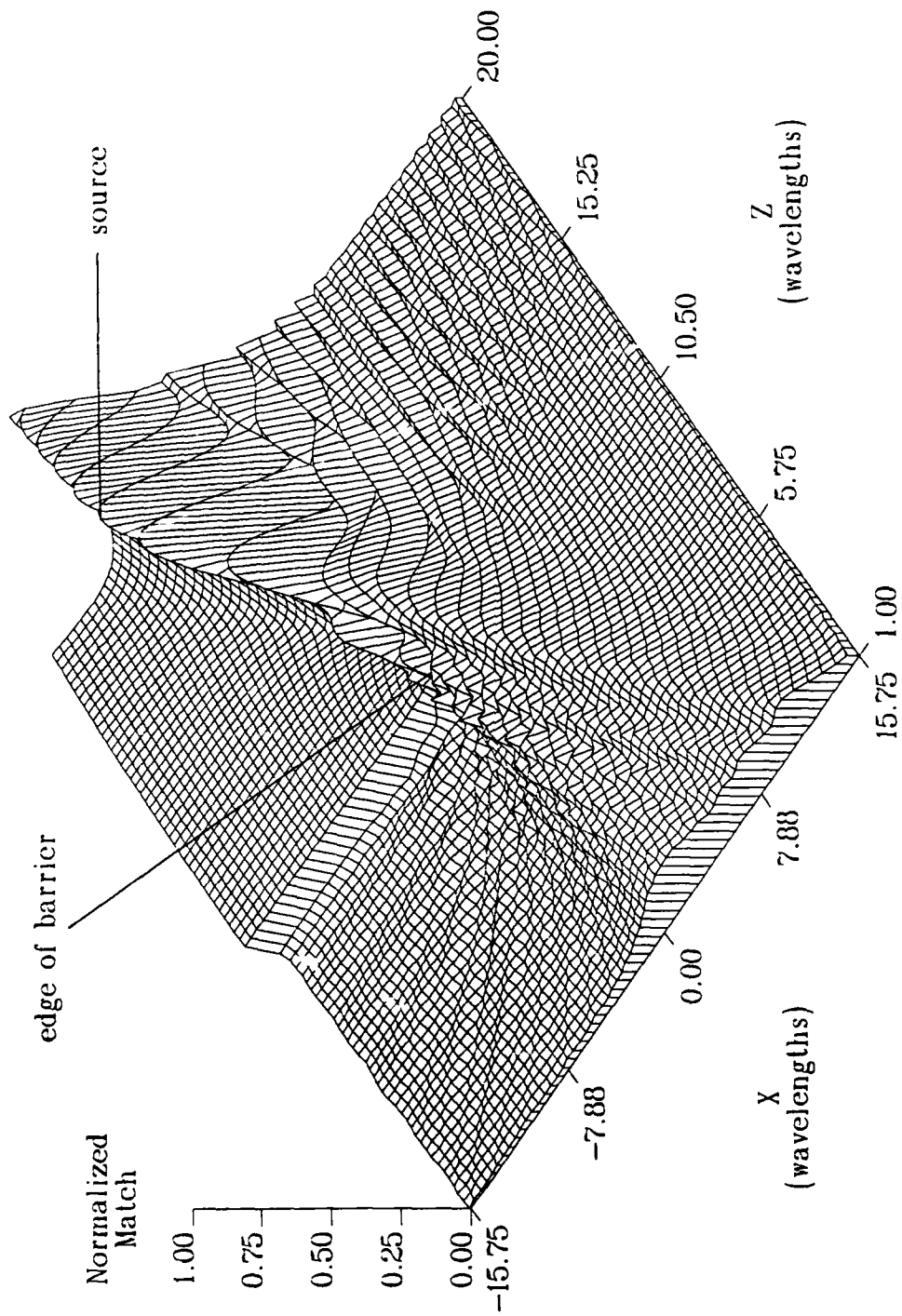


Figure 4.27. Pattern-match reconstruction of a point source at  $(0.25\lambda, 15\lambda)$  with a barrier extending from  $(0, 10\lambda)$  to  $(-\infty, 10\lambda)$ .

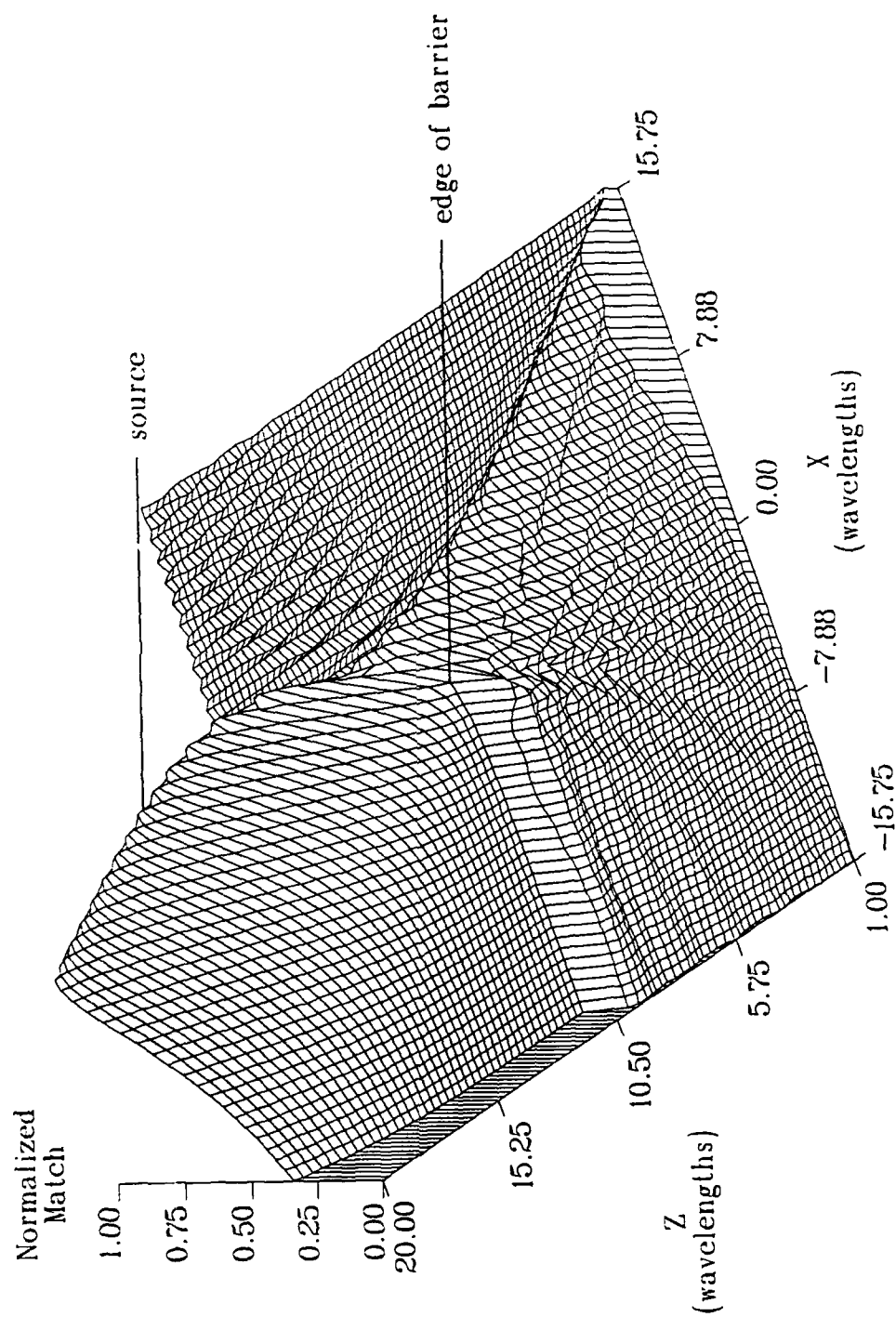


Figure 4.28. Pattern-match reconstruction of a point source at  $(-2.25\lambda, 15\lambda)$  with a barrier extending from  $(0, 10\lambda)$  to  $(-\infty, 10\lambda)$ .

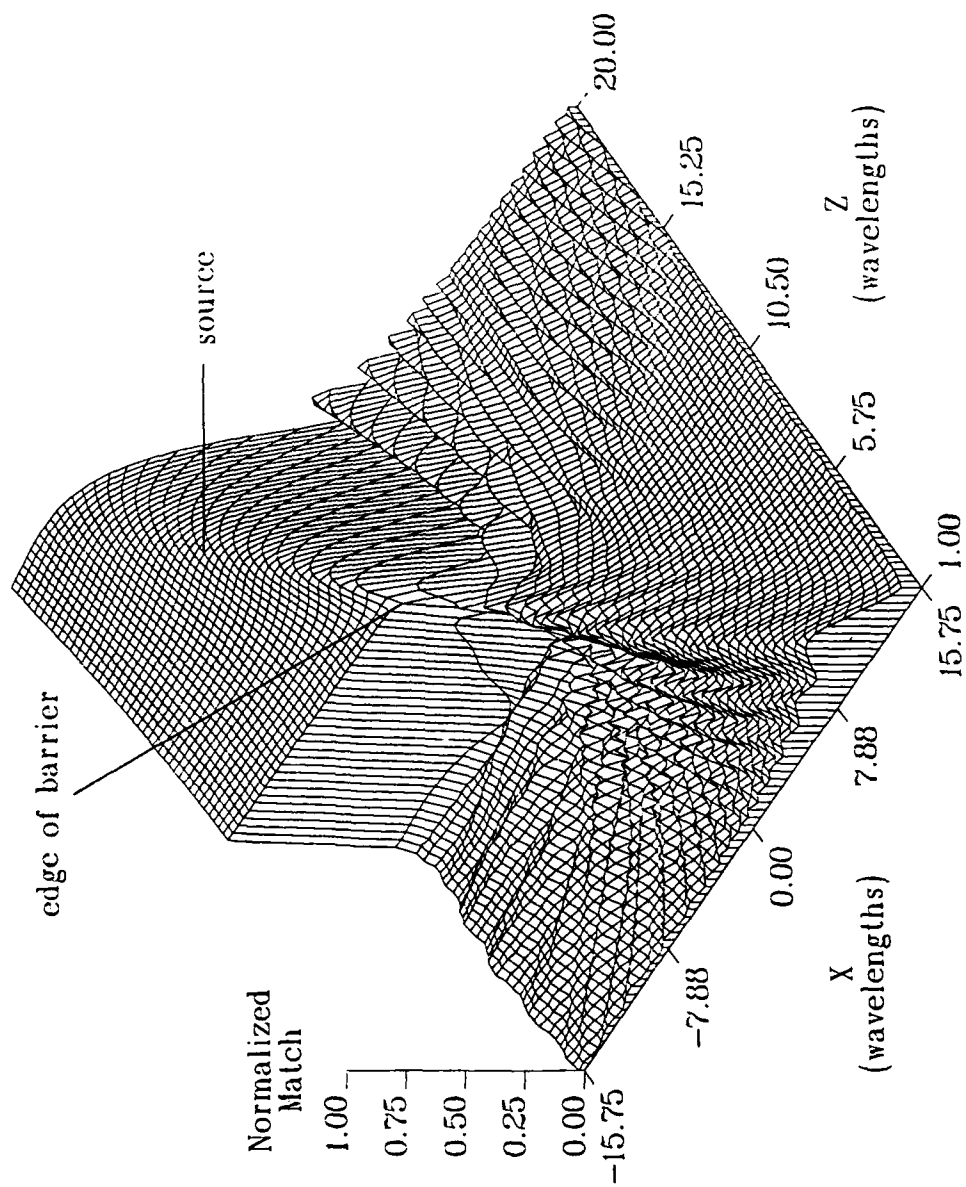


Figure 4.29. Pattern-match reconstruction of a point source at  $(-5.25\lambda, 15\lambda)$  with a barrier extending from  $(0, 10\lambda)$  to  $(-\infty, 10\lambda)$ .

The mismatch reconstruction for a source at  $(0.25\lambda, 15\lambda)$ , shown in Figure 4.30, exhibits peaks which, as in earlier cases, have an envelope similar to the pattern-match reconstruction and a spacing roughly equal to a wavelength. As seen in Figure 4.31, the peak at the location of the true source is the largest, but only by a small amount. Likewise, as the source is moved further behind the barrier, Figures 4.32 and 4.33 exhibit peaks falling within the envelope of the corresponding pattern-match results.

These cases suggest that some general rules might be stated which roughly describe how each imaging method responds as the source becomes hidden further behind the barrier: (1) holographic imaging moves its reconstructed peak towards the edge of the barrier; (2) pattern-match imaging indicates only that the source is somewhere in the hidden region, with a decreasing likelihood that the source is near the boundary line as the true source moves further behind the barrier; and (3) mismatch imaging produces peaks within the envelope of the pattern-match results, arranged in groups which are multiples of a wavelength from the barrier edge.

#### 4.7 Environmental Errors

The two pattern-matching reconstruction methods use knowledge of the barrier in their analysis of the received signals. It would not be unusual for there to be small errors in this knowledge; therefore, the case of a source behind the edge of a barrier was repeated with an error deliberately introduced. The results for the pattern-match and mismatch methods are shown in Figures 4.34 and 4.35, respectively. In these simulations, the received signals were calculated using the true location of the barrier, at  $Z = 10\lambda$ , while the reconstruction used a false

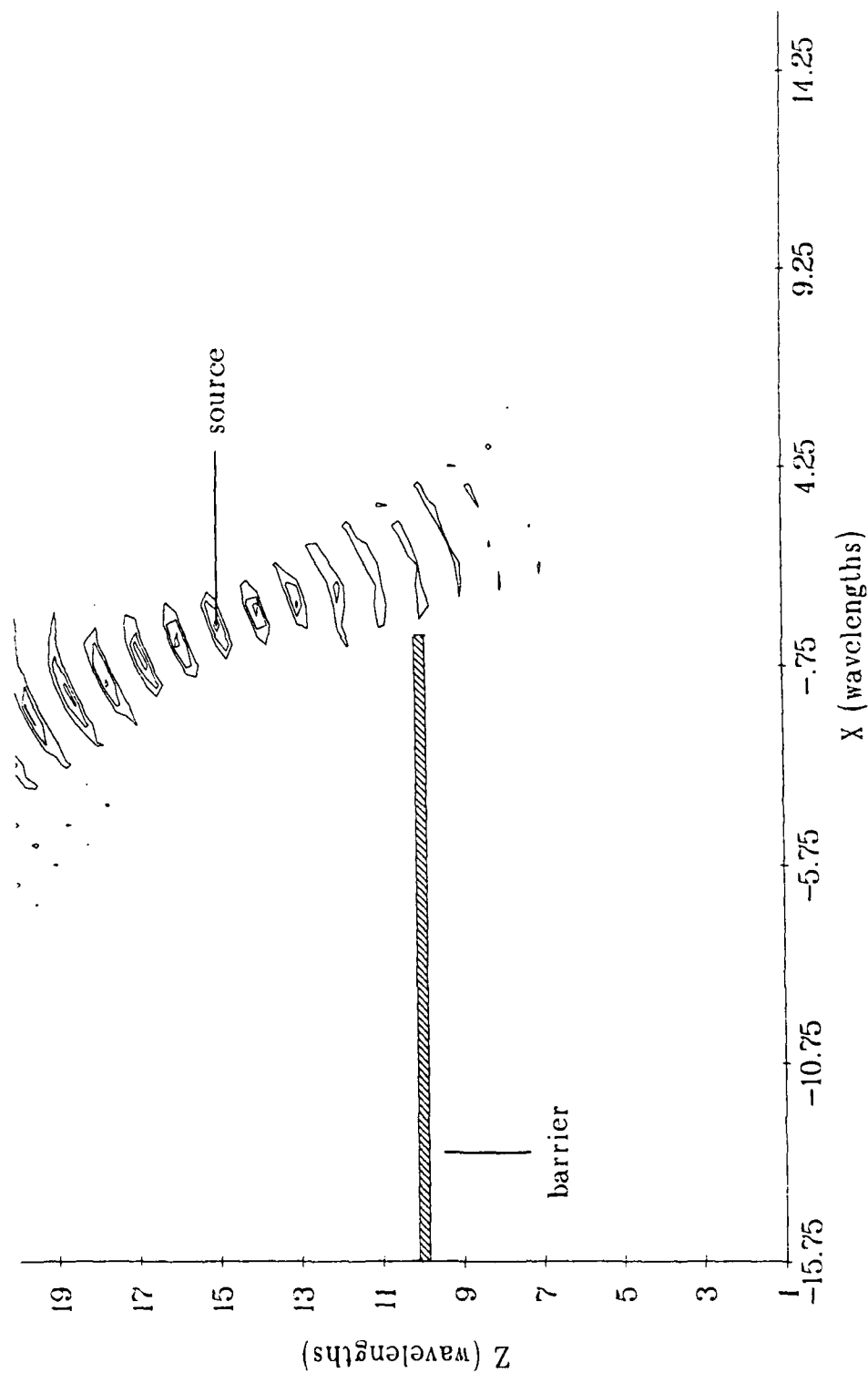


Figure 4.30. Mismatch reconstruction of a point source at  $(0.25\lambda, 15\lambda)$  with a barrier extending from  $(0, 10\lambda)$  to  $(-\infty, 10\lambda)$ ; contour lines are at 25%, 50%, and 75% of the maximum.

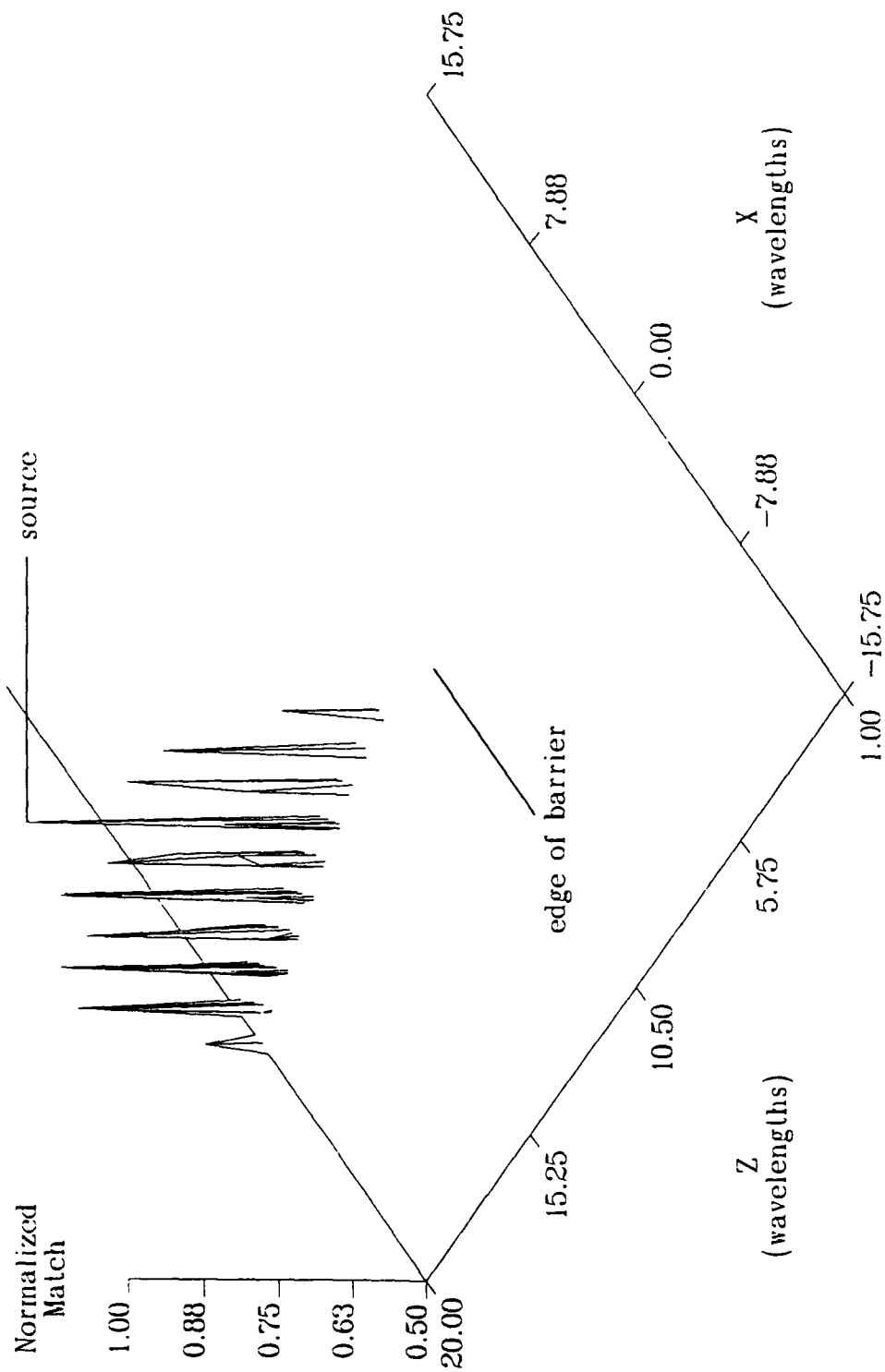


Figure 4.31. Mismatch reconstruction of a point source at  $(0.25\lambda, 15\lambda)$  with a barrier extending from  $(0, 10\lambda)$  to  $(-\infty, 10\lambda)$ . Values below 50% of the maximum have been removed for clarity.

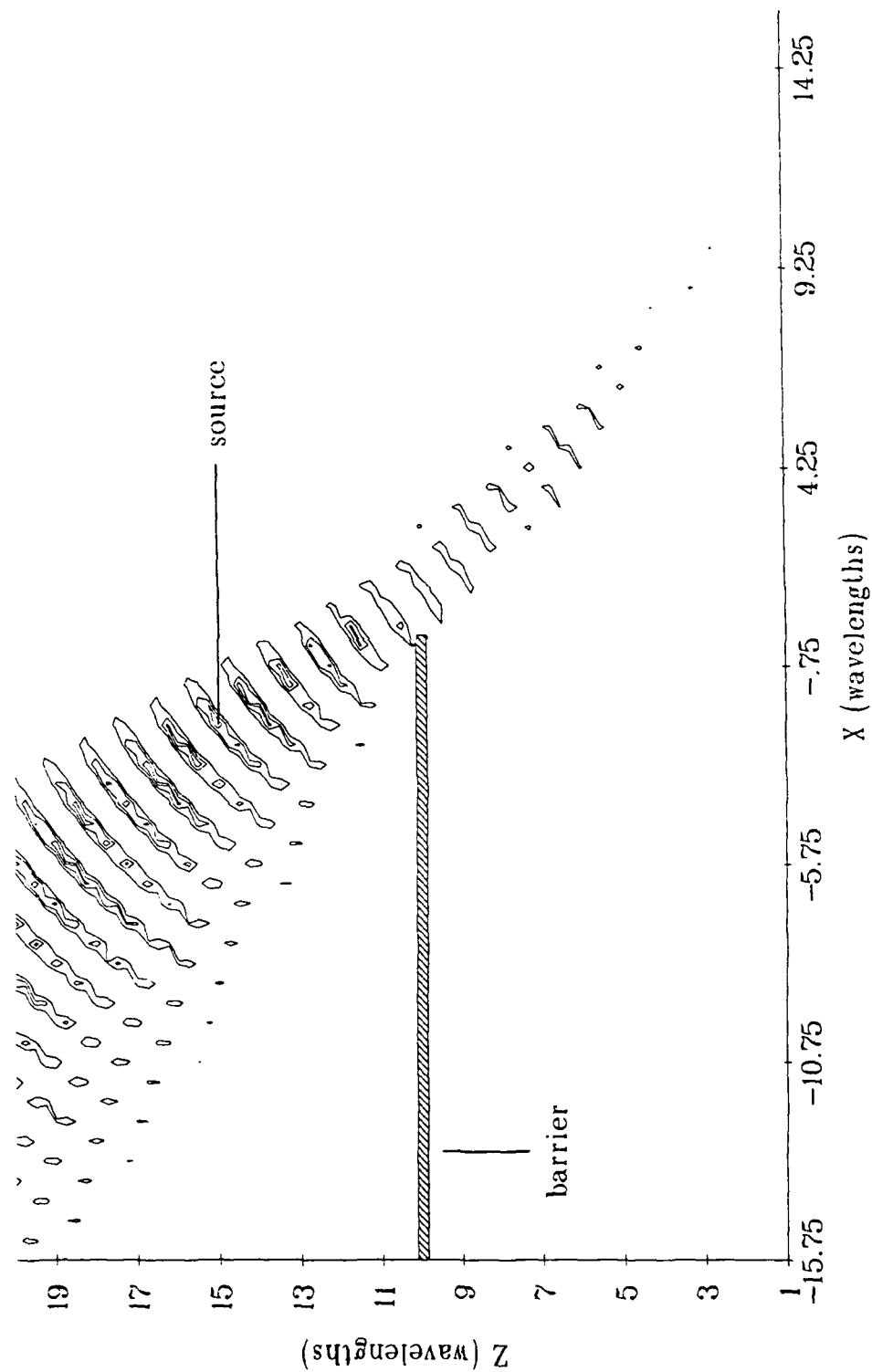


Figure 4.32. Mismatch reconstruction of a point source at  $(-2.25\lambda, 15\lambda)$  with a barrier extending from  $(0, 10\lambda)$  to  $(-\infty, 10\lambda)$ ; contour lines are at 25%, 50%, and 75% of the maximum.



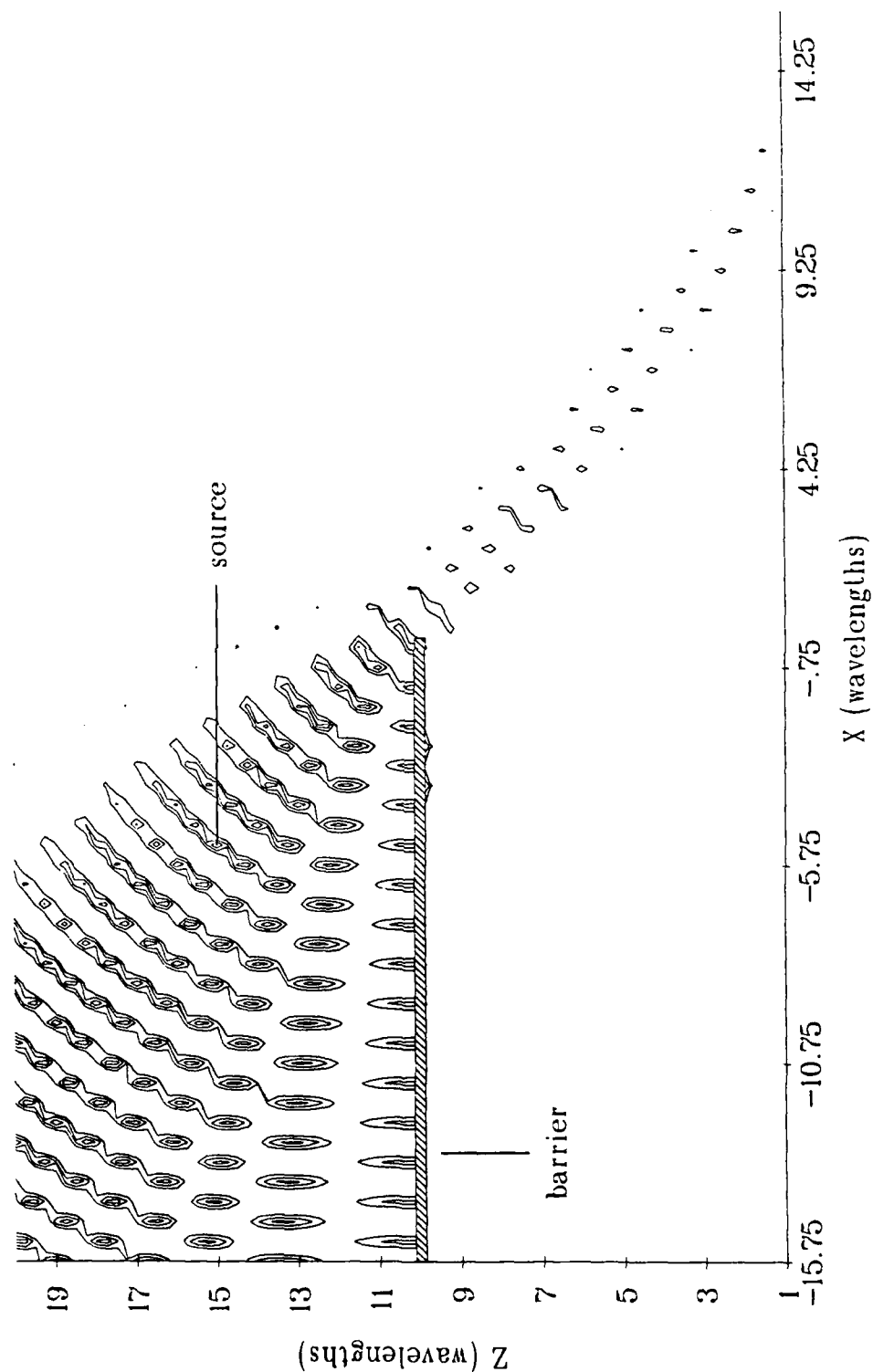


Figure 4.33. Mismatch reconstruction of a point source at  $(-5.25\lambda, 15\lambda)$  with a barrier extending from  $(0, 10\lambda)$  to  $(-\infty, 10\lambda)$ ; contour lines are at 25%, 50%, and 75% of the maximum.

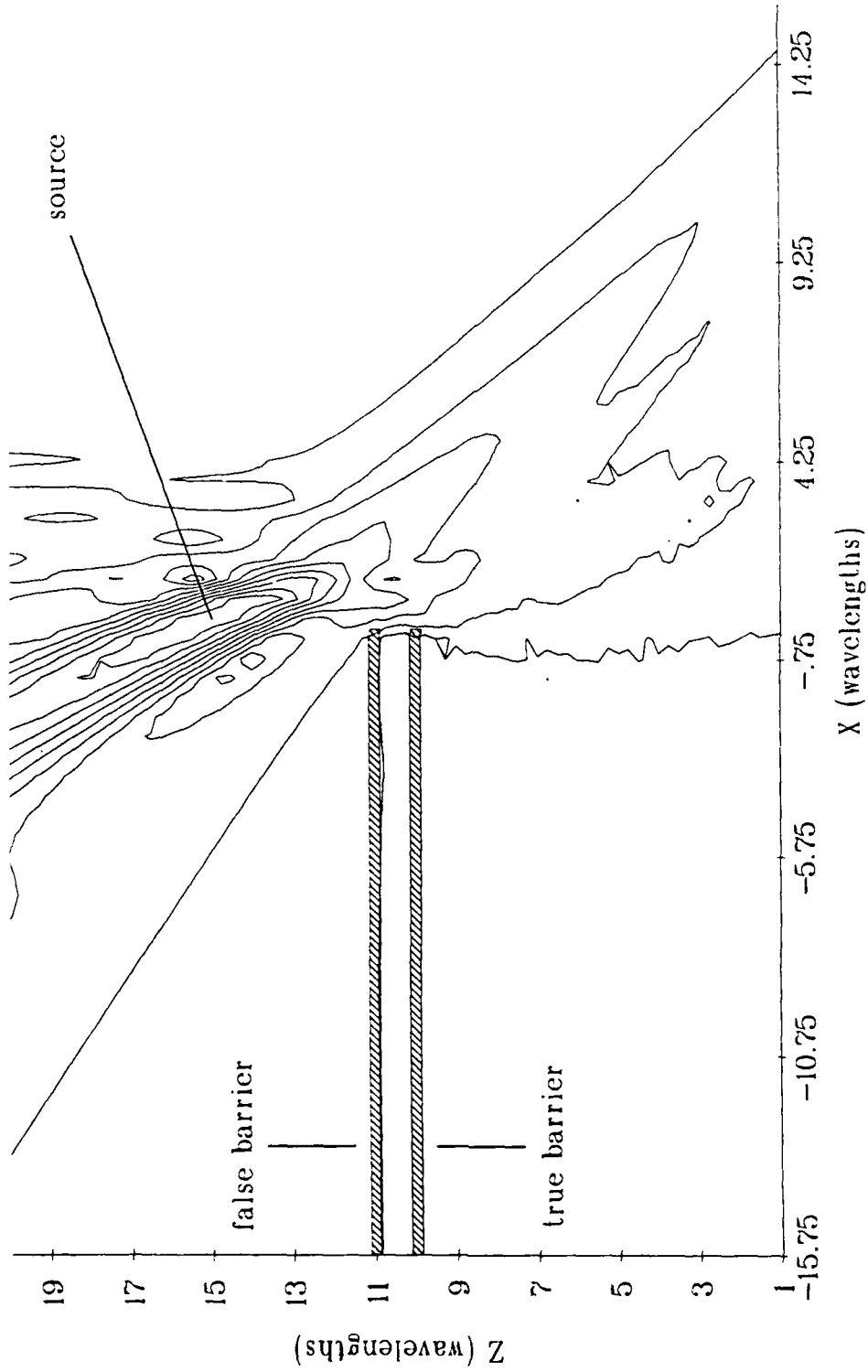


Figure 4.34. Pattern-match reconstruction, using a false barrier at  $Z=11\lambda$ , of a point source at  $(0.25\lambda, 15\lambda)$  with a true barrier at  $Z=10\lambda$ ; contour lines are at 10%, 20%, ..., 90% of the maximum.

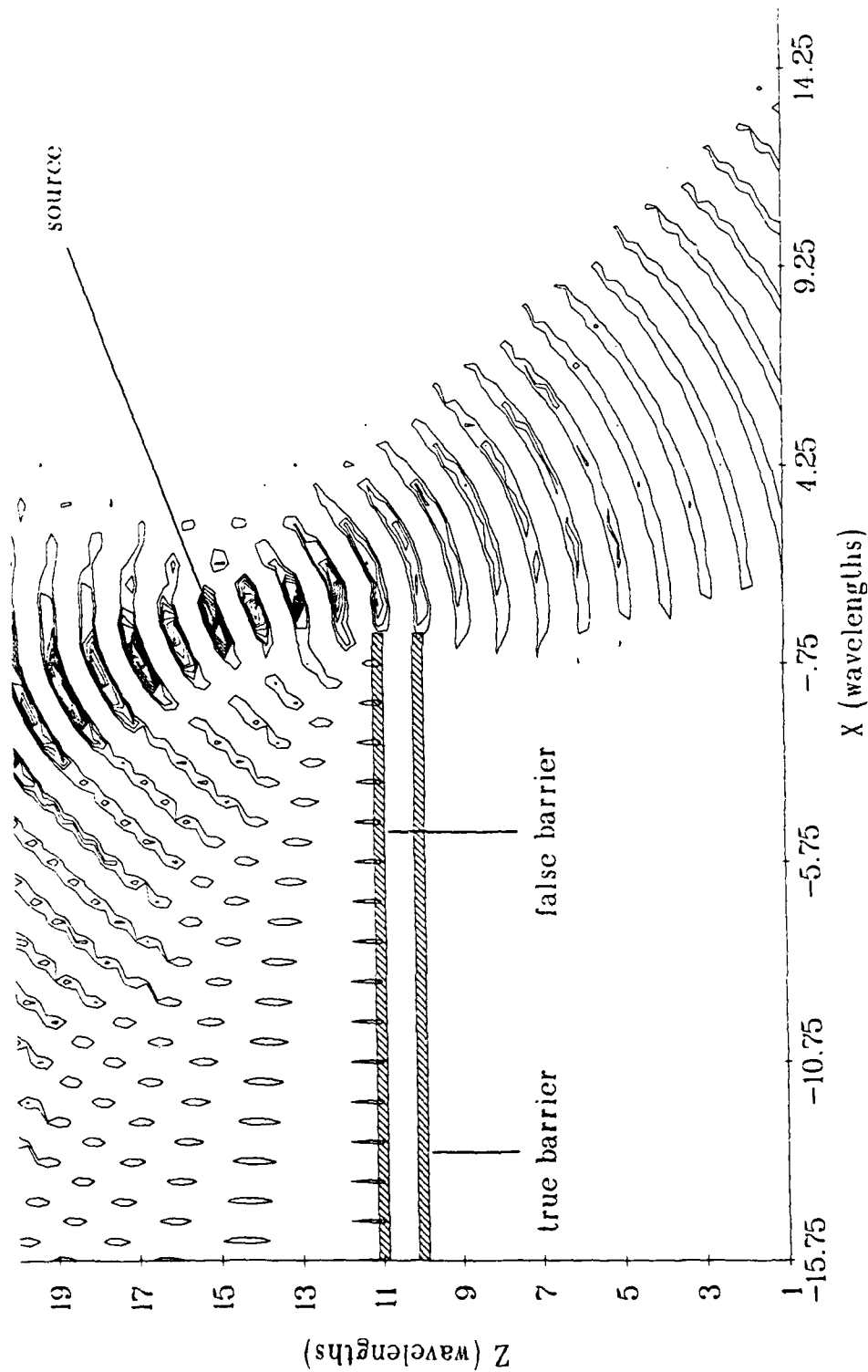


Figure 4.35. Mismatch reconstruction, using a false barrier at  $Z=11\lambda$ , of a point source at  $(0.25\lambda, 15\lambda)$  with a true barrier at  $Z=10\lambda$ ; contour lines are at 10%, 20%, ..., 90% of the maximum.

location, at  $Z = 11\lambda$ . A comparison with the corresponding results with no error. Figures 4.26 and 4.30, indicate that the error did not significantly affect the reconstructions (note that only 3 contour levels were used in Figure 4.30 while 9 levels were used in Figure 4.35).

#### 4.8 Locating Two Sources

When more than one source is present, a linear superposition of the signals from the sources is recorded at each receiver. However, since it is difficult to classify the pattern-match and mismatch methods as either linear or non-linear, it is not clear whether multiple sources could be reconstructed.

To explore this question, a simulation was run with two equal-strength and in-phase sources located at  $(0.25\lambda, 15\lambda)$  and  $(10.25\lambda, 15\lambda)$ . The result using the pattern-match method is shown in Figure 4.36. The field near the left source, at  $(0.25\lambda, 15\lambda)$ , is nearly identical to the corresponding area, in Figure 4.26, when only the left source was used. However, as can be clearly seen in Figure 4.37, the two sources are not located with the same resolution due to the influence of the barrier.

The result using the mismatch method is shown in Figure 4.38. Again, the field near the left source is nearly identical to the corresponding area, in Figure 4.30, when only the left source was used (note that only 3 contour levels were used in Figure 4.30 while 9 levels were used in Figure 4.38). Figure 4.39 shows that while both sources have been located with nearly the same resolution, their apparent strengths are not equal.

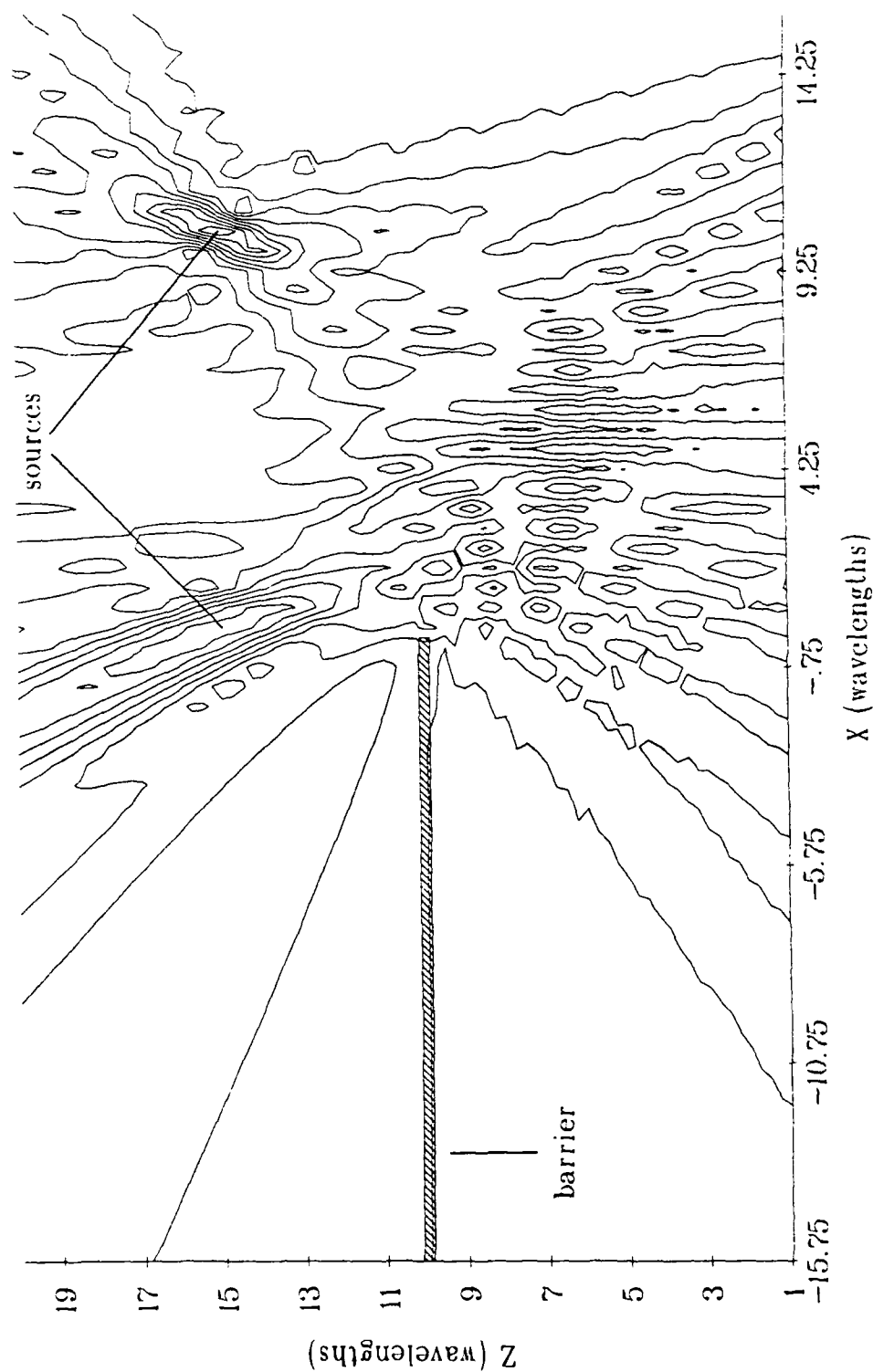


Figure 4.36. Pattern-match reconstruction of 2 sources, at  $(0.25\lambda, 15\lambda)$  and  $(10.25\lambda, 15\lambda)$ , with a barrier extending from  $(0, 10\lambda)$  to  $(-\infty, 10\lambda)$ ; contour lines are at 10%, 20%, ..., 90% of the maximum.

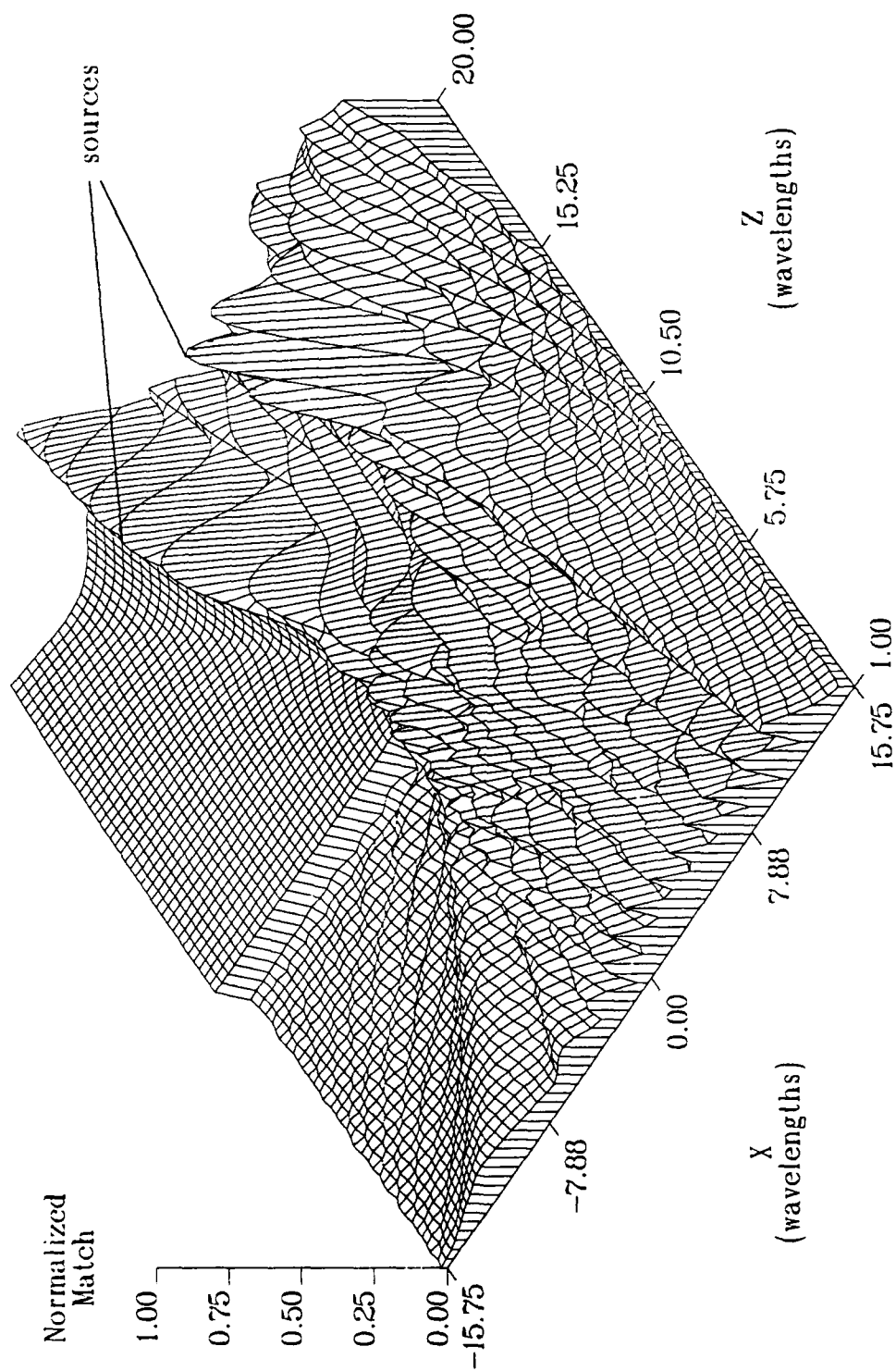


Figure 4.37. Pattern-match reconstruction of 2 sources, at  $(0.25\lambda, 15\lambda)$  and  $(10.25\lambda, 15\lambda)$ , with a barrier extending from  $(0, 10\lambda)$  to  $(-\infty, 10\lambda)$ .

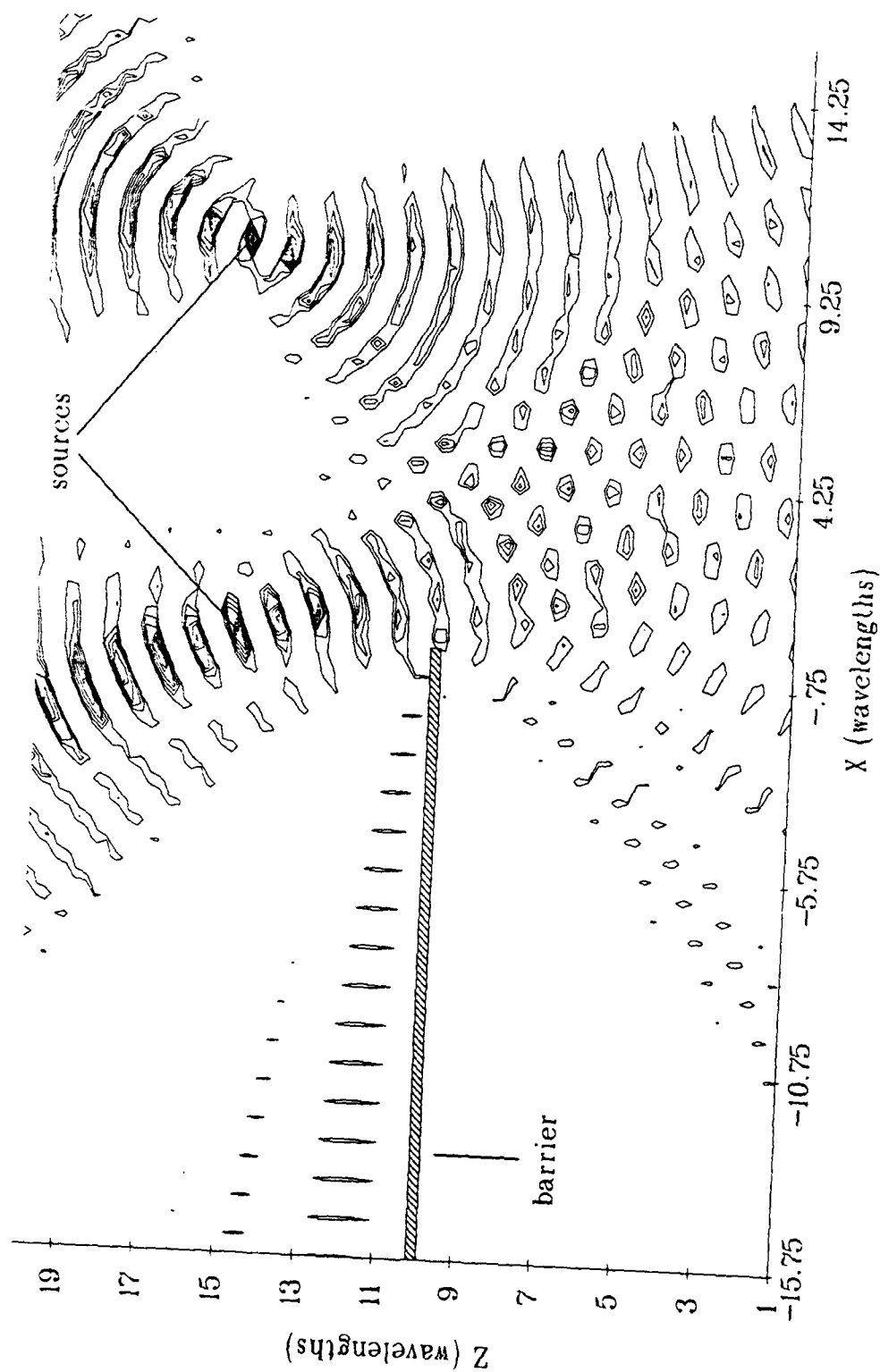


Figure 4.38. Mismatch reconstruction of 2 sources, at  $(0.25\lambda, 15\lambda)$  and  $(10.25\lambda, 15\lambda)$ , with a barrier extending from  $(0, 10\lambda)$  to  $(-\infty, 10\lambda)$ ; contour lines are at 10%, 20%, ..., 90% of the maximum.

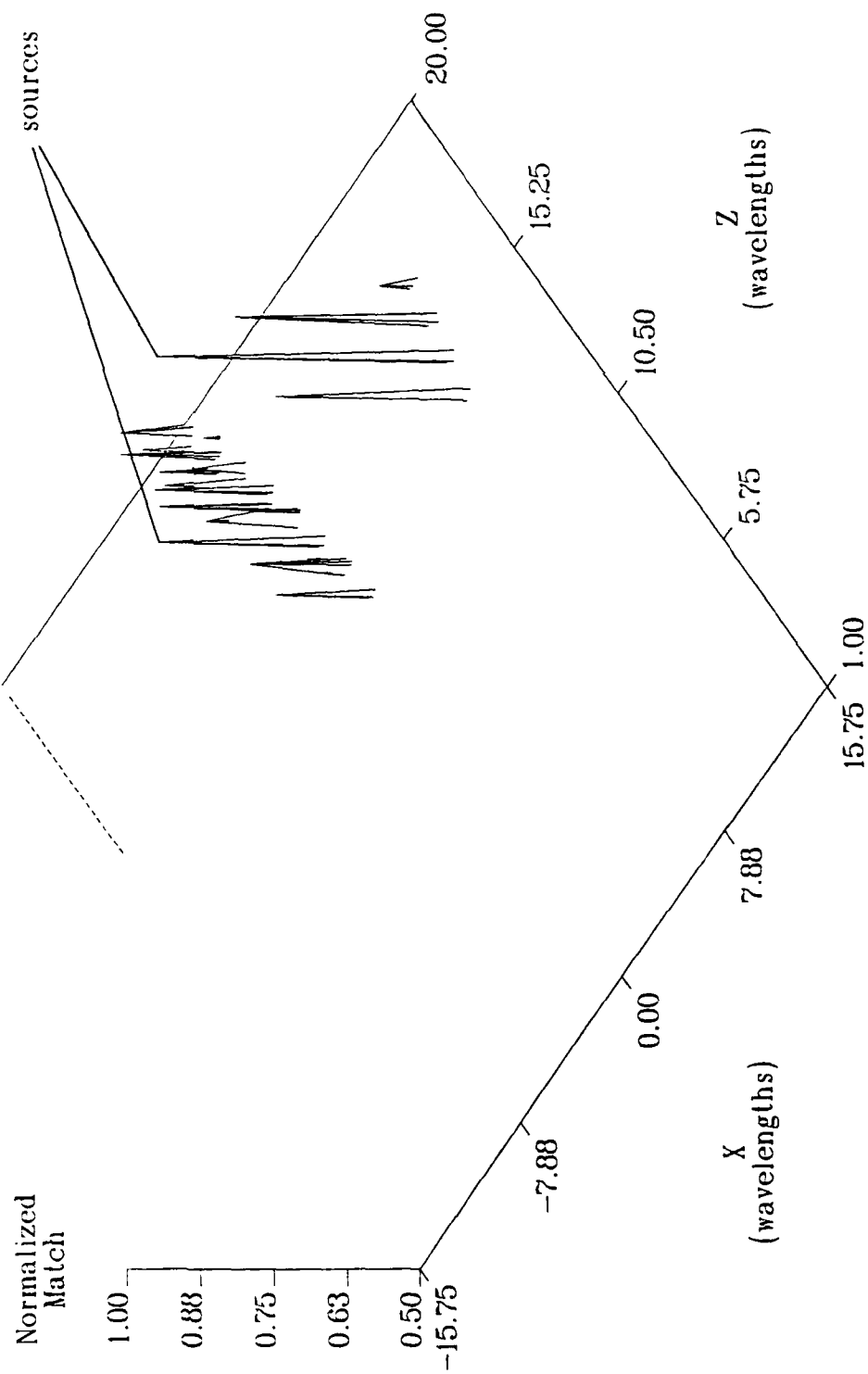


Figure 4.39. Mismatch reconstruction of 2 sources, at  $(0.25\lambda, 15\lambda)$  and  $(10.25\lambda, 15\lambda)$ , with a barrier extending from  $(0, 10\lambda)$  to  $(-\infty, 10\lambda)$ . Values below 50% of the maximum have been removed for clarity.



## 4.9 Execution Times

The time needed to complete the reconstruction was measured using the computer system's internal clock, which is claimed to be accurate to within 0.01 seconds. Note that the measurements are made so that input, output, plotting, and overall normalization operations are excluded. However, the time needed to perform the normalization of the fictitious source signals for the pattern-match method is included. The reconstructions were performed at a varying number of points, depending upon the situation; therefore, the total time for each reconstruction has been divided by the number of points so that the times can be directly compared. The results are shown in Table 4.2 and can be used to evaluate the relative speed of the various methods.

The speed of the holography method is the same when the source is partially or fully hidden, or when it yields a reflection, since it does not vary its calculations as the environment varies. The pattern-matching methods are, as expected, significantly slower than holography since they cannot take advantage of the efficiencies of the FFT. However, there is no obvious reason why the mismatch method was generally faster than the pattern-match method — the mismatch algorithm is slightly more complicated and so it was expected that it would be slightly slower.

These times are for execution on the MicroVAX II processor and floating point accelerator manufactured by the Digital Equipment Corporation (DEC). If a modern super computer or array processor had been used instead, the time to reconstruct an image could probably be reduced by at least two orders of magnitude.

Table 4.2. Time to reconstruct the images.

Environment	Source	Method	Total Time	Time/Point
free	$(0.25\lambda, 15\lambda)$	holography	0.2m	2.5ms
free	$(0.25\lambda, 15\lambda)$	pattern match	3.1m	37.7ms
free	$(0.25\lambda, 15\lambda)$	mismatch	3.1m	37.2ms
reflections	$(-5.25\lambda, 7.5\lambda)$	holography	0.2m	2.5ms
reflections	$(-5.25\lambda, 7.5\lambda)$	pattern match	24.1m	396.8ms
reflections	$(-5.25\lambda, 7.5\lambda)$	mismatch	24.1m	395.9ms
hidden	$(0.25\lambda, 15\lambda)$	holography	0.2m	2.5ms
hidden	$(0.25\lambda, 15\lambda)$	pattern match	32.0m	390.2ms
hidden	$(0.25\lambda, 15\lambda)$	mismatch	31.4m	382.5ms
hidden	$(-2.25\lambda, 15\lambda)$	holography	0.2m	2.5ms
hidden	$(-2.25\lambda, 15\lambda)$	pattern match	31.7m	386.0ms
hidden	$(-2.25\lambda, 15\lambda)$	mismatch	31.4m	382.9ms
hidden	$(-5.25\lambda, 15\lambda)$	holography	0.2m	2.5ms
hidden	$(-5.25\lambda, 15\lambda)$	pattern match	31.4m	382.2ms
hidden	$(-5.25\lambda, 15\lambda)$	mismatch	31.5m	382.9ms

 $\lambda$  - wavelengths

m - minutes

ms - milliseconds

## Chapter 5

### Swept-Frequency Imaging

One of the purposes of this study was the development of a new method of imaging which is based upon a sweep of the transmitted signal through a series of frequencies. This chapter develops the method and conducts a variety of simulations in order to explore its capabilities.

#### 5.1 Motivation for Sweeping the Frequency

A number of the methods examined by this study make use of multiple frequencies. When there are several sources differing in their spectral content, the eigenvector approach uses this fact to help separate the information belonging to the sources and thereby increase its resolving capabilities. The correlation method uses pairs of receivers to estimate the relative time delay and bearing, and so more precisely locates the peak in the correlation as the bandwidth is increased. Other methods, such as beamforming and holography, can process only one frequency at a time, and so can only combine the results for multiple frequencies at the end.<sup>23,24</sup>

One thing which all these approaches have in common is that they concentrate on the signal processing viewpoint, treating the information at each frequency as being unrelated to the information at other frequencies. However, if we look at the underlying physics, it is obvious that such a situation would be unusual, if not impossible, for scatterers of acoustic waves since their scattering must depend upon the frequency in some deterministic if unknown manner.

Such a frequency dependence was exploited by Chan *et al.*<sup>75</sup> to emulate motion by the receivers along "equivalent scan vectors" so that the effective size of the receiving array was increased. A modest body of work was produced by this group,<sup>76,77,78</sup> along with observations by other parties that some of the reported results were unacceptable<sup>79</sup> or exhibited ambiguities.<sup>80</sup> Although a lack of further publications seems to indicate that this work has not been pursued, it seems clear that in some situations the effective size of the array in one of the dimensions can be increased by a factor proportional to the bandwidth of the frequency sweep.

One of the weaknesses of Chan's approach is that the calculation of the equivalent scan vectors requires that the center of the scattering object be known. Figures 5.1 and 5.2 depict the coordinate system and scan vectors for a rectangular scatterer with its center on the Z axis. It is obvious that the scan vectors cannot be calculated if the center of the scatterer is not known.

A solution to this limitation presents itself when we consider the abilities of the pattern-match method discussed in Chapters 2 and 3, in place of the concept of scan vectors.

In the pattern-matching method, rather than assume that we know the center of the scatterer, we move the fictitious scatterer through all locations in object space, i.e., all locations which could possibly contain an actual scatterer. At each of these locations, the received signals are compared to what would have been received from the fictitious scatterer, at the given frequency.

However, to the extent that the frequency-dependence of the scatterer is predictable, another type of match could be performed. Using the received pat-

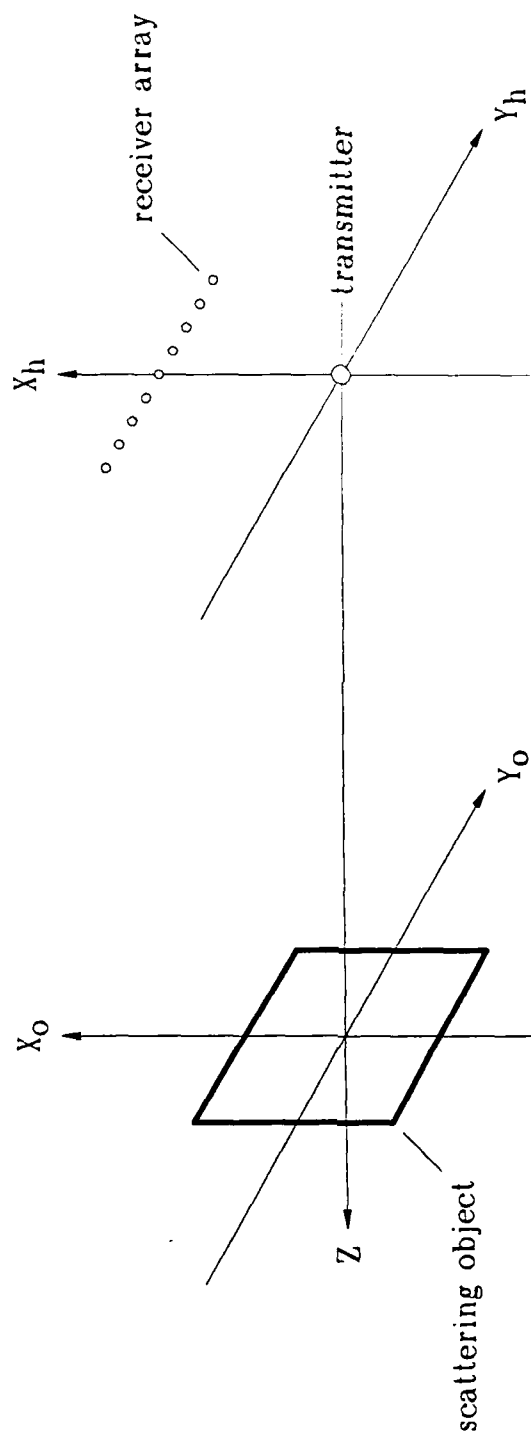


Figure 5.1. Arrangement of components of a proposed imaging system where the transmitter produces a sweep of frequencies.

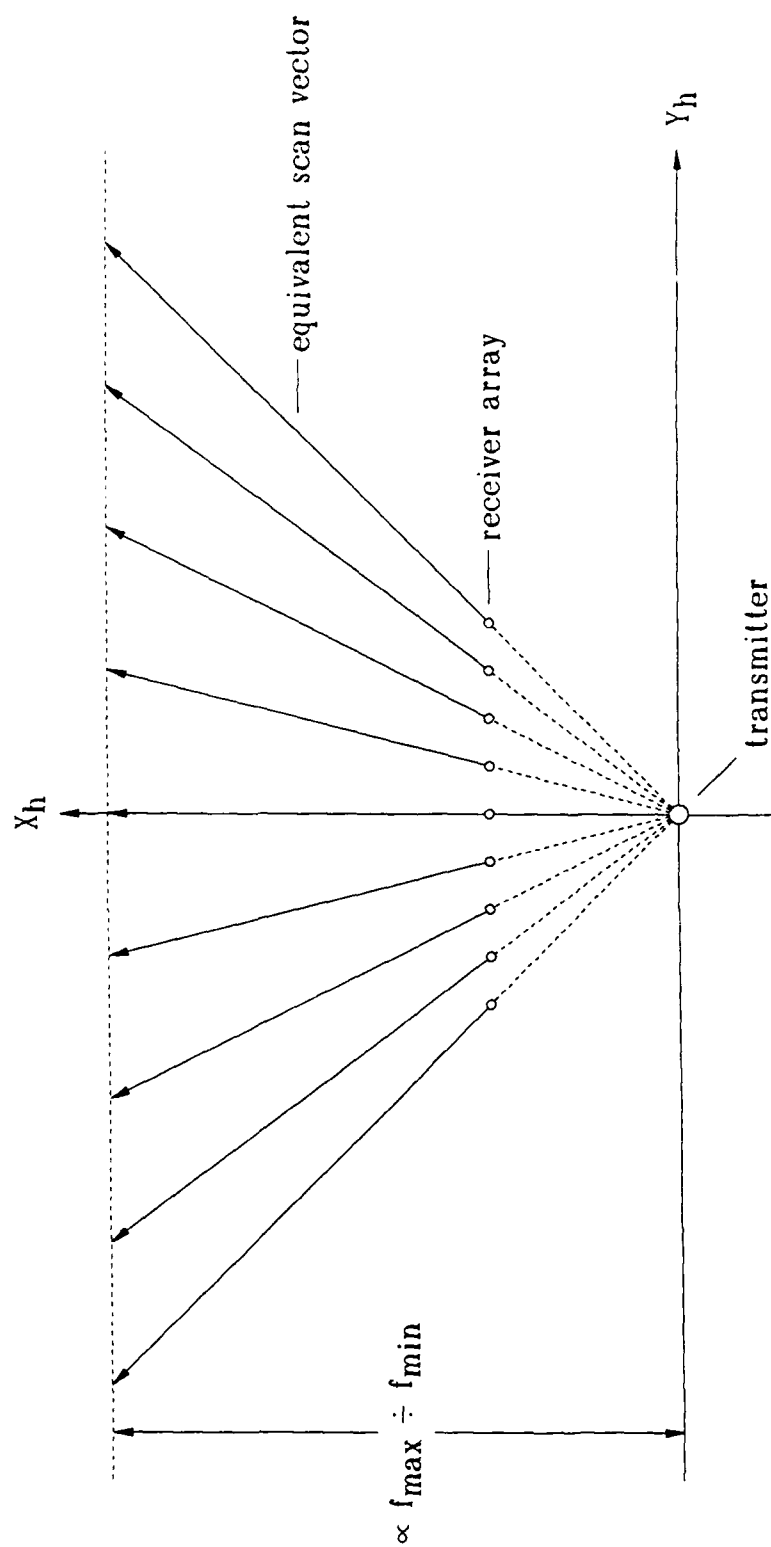


Figure 5.2. Definition of the equivalent scan vectors in a proposed swept-frequency imaging system.

tern across the array at, say, the lowest frequency, we can predict how the pattern will shift and scale as the frequency is swept up to higher frequencies, given the location of the fictitious scatterer and the known location of the transmitter and receivers. The degree to which the actual and predicted signals match, summed over the entire frequency sweep, then constitute the total match at that location in object space. As before, we then interpret the best match or matches in object space as the location of the source or sources.

## 5.2 Scattering Models

The purpose of the scattering model used in this chapter of the study is to provide the frequency-swept imaging simulations with "received" signals which should mimic features of real, physical phenomena with reasonable accuracy when these features may have an effect on the imaging method. Thus, the frequency dependence of the scattering should be faithfully simulated. On the other hand, the absolute levels of the simulated signals is probably irrelevant.

It seems that two categories of frequency-dependent scattering would suffice. First, a pair of closely spaced point scatterers will be used to represent specular reflections. While an individual point scatterer has no frequency dependence, a system of two or more will exhibit frequency-dependent interference patterns. Second, a rigid plate reflector will be used to represent an extended scatterer.

### 5.2.1 Specular Scatterers

The expression for point scatterers is very nearly identical to the general case given as part of the definition of terms in Eq. (1.2). For the following sim-

ulations, we simplify the formula by setting the scattering strength to unity so that  $S_m = 1$ . The transmitted signal is chosen to be a continuous sine wave of unity amplitude so that the time-shifted signal,  $E(t_l - T_{im}^F)$ , can be replaced by a phase-shifted signal,  $\exp(-j 2\pi f (t_l - T_{im}^F))$  with  $T_{im}^F$  given by Eq. (1.5). Finally, since the time at which we sample the complex received signal is irrelevant while using continuous sine waves (as long as all the receivers are sampled at the same time), we can set  $t_l = 0$  so that the expression for the received signal becomes

$$R_i(X_i^R) = \sum_{m=1}^{N^S} \frac{\exp(-j k (D_{im} + D_{Tm}))}{D_{im} \cdot D_{Tm}}. \quad (5.1)$$

The distance  $D_{im}$  is that between the  $m$ th reflector and the  $i$ th receiver located at  $(X_i^R, Z_i^R)$  where we have chosen to locate our linear receiver array along the Z-axis so that  $Z_i^R = 0$ . The distance  $D_{Tm}$  is that between the  $m$ th reflector and the point source at  $(X^T, Z^T)$ . These coordinates and distances are shown in Figure 1.1, and the distances are given by Eq. (1.3) and Eq. (1.4).

Eq. (5.1) was implemented in the **FORTRAN** subroutine and then used to generate Figures 5.3 and 5.4 for the case of two reflectors separated by 12". In these figures, the reflectors were centered around the origin along the X-axis, and the reflected field was evaluated at a radius of 100" from the origin. Several other source locations were also examined but not shown here; in all of these other cases, the magnitude and phase peaks moved as expected from 0° to the negative of the source angle.

### 5.2.2 Extended Scatterers

The classical theories of Huygens shall be used to construct a simulation of the scattering of an acoustic wave by a finite rigid plate. The incident wave is



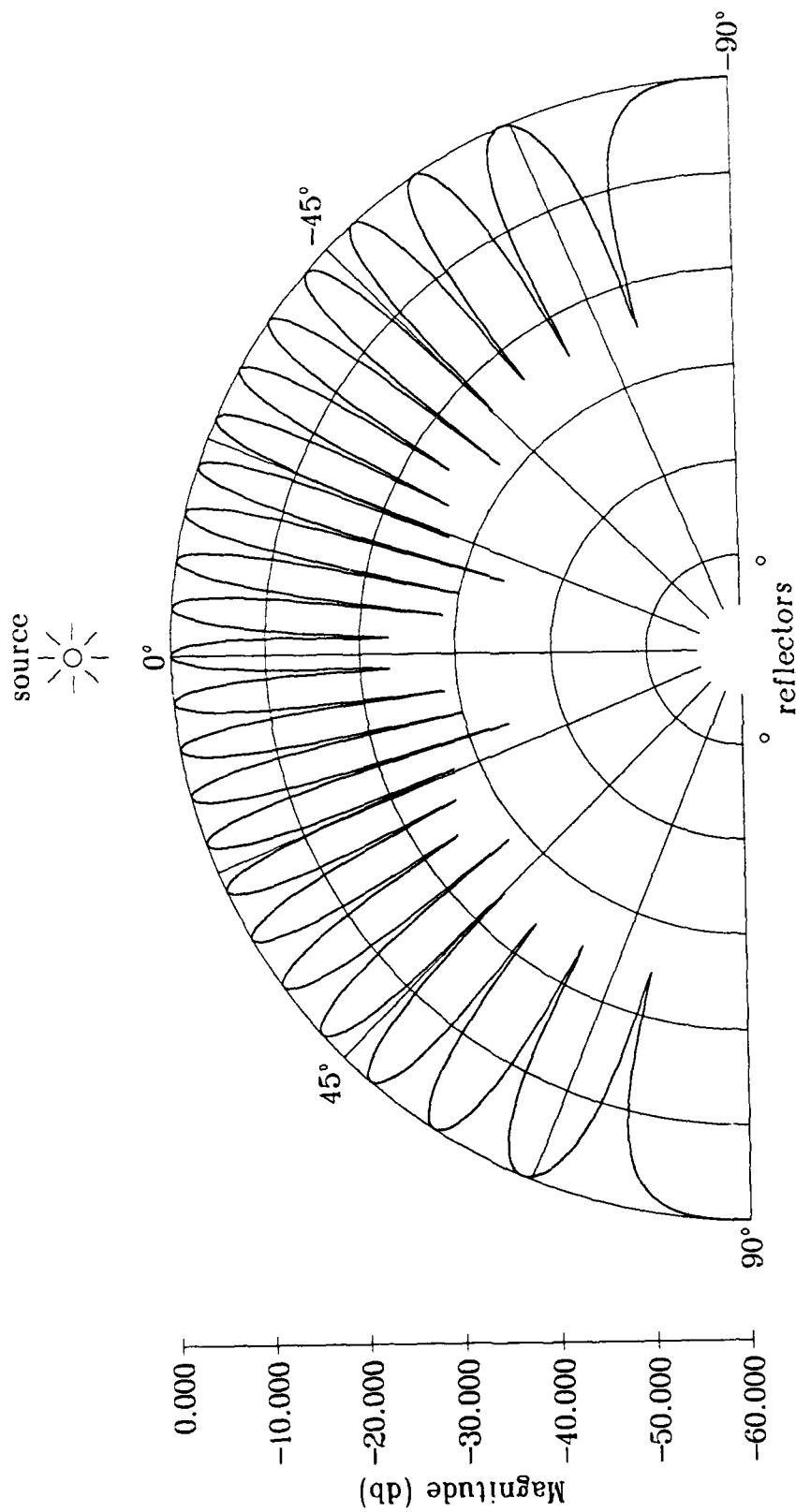


Figure 5.3. Magnitude of the pressure from a 13,045.2 Hz source at 0°, scattered by two point reflectors at the origin and separated by 12". The wavelength is 1".

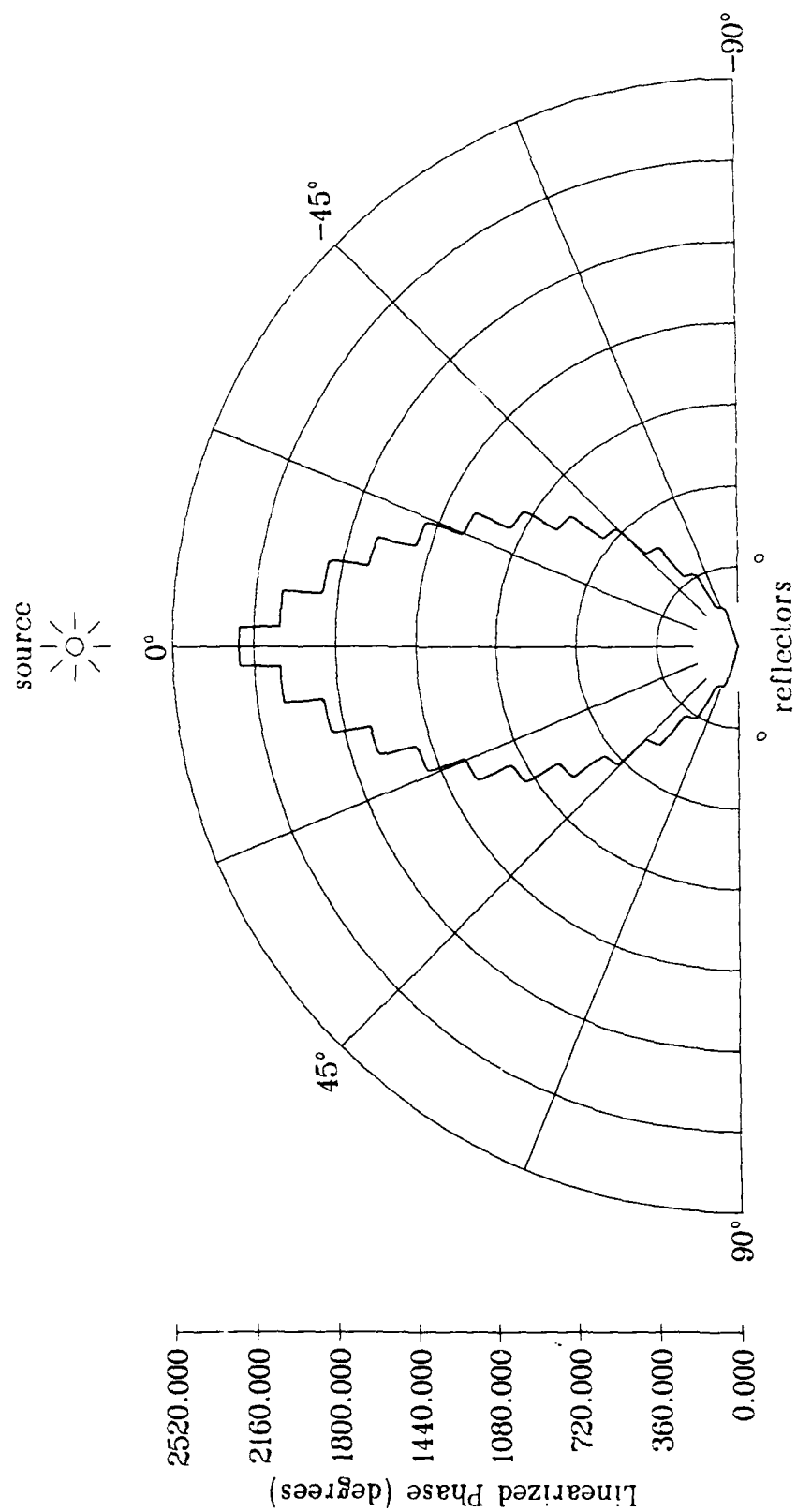


Figure 5.4. Phase of the pressure from a 13,045.2 Hz source at 0°, scattered by two point reflectors at the origin and separated by 12". The wavelength is 1".

modeled as a harmonic, spherically spreading one originating at a point source. We are interested in the field reflected back towards our linear receiver array which is in the general vicinity of the source; that is, the model does not need to consider diffraction around the plate. Thus, we can apply Huygen's principle wherein each point on the plate is considered to be a point-source of radiation with a phase and amplitude equal to that of the incident wave.

To be rigorous, the signal at each receiver should not only include waves reflected from the plate but also waves arriving directly from the transmitter. We shall delete this direct path in this simulation. In an experiment, the signals arriving along the direct path could be subtracted out since the exact location of the transmitter and receivers, and the speed of sound, is known. Or, windowed sine waves could be used instead of a continuous wave so that the two signals can be distinguished by a time window at the receivers.

After a presentation of the integral and discrete expressions for the scattered waves, subsequent sections will exercise the simulation. An extra amount of effort was put into testing the algorithm as part of an attempt to explain an unexpected scattering pattern which occurs when the plate's width becomes large relative to a wavelength.

### 5.2.2.1 Scattering from a Rigid Plate

The Huygens-Rayleigh integral for scattering from a plate can be expressed in terms of the incident pressure<sup>81</sup> as

$$R_i(X_i^R, Y_i^R, Z_i^R) = \frac{j k}{2\pi} \int_{X_{min}}^{X_{max}} \int_{Y_{min}}^{Y_{max}} \frac{P_I(x, y) \exp(-j k D_i)}{D_i} dy dx. \quad (5.2)$$

where the integrals are over the surface of the plate. In this study, we are considering only the two dimensional X-Z plane and so the dependence and integral over Y will be dropped. Also, we have chosen to locate our linear receiver array along the Z-axis and so  $Z_i^R = 0$ . The incident pressure  $P_I$  is given by

$$P_I(x) = P_0 \frac{\exp(-j k D_T)}{D_T}. \quad (5.3)$$

The distances  $D_i$  and  $D_T$  are given by Eq. (1.3) and Eq. (1.4), respectively, except that  $X_m^S$ , the location of the sources, is now  $x$ , the variable of integration — i.e., the location of Huygen's equivalent sources on the plate. With these assumptions and definitions, Eq. (5.2) becomes

$$R_i(X_i^R) = \frac{j k P_0}{2\pi} \int_{X_{min}}^{X_{max}} \frac{\exp(-j k (D_i + D_T))}{D_i \cdot D_T} dx. \quad (5.4)$$

There does not seem to be an exact closed-form solution to this integral. Approximations to the square root in the  $D_i$  and  $D_T$  can allow the integral to be evaluated in the Fraunhofer zone, or when the receiver is near the axis of the plate<sup>82</sup>. Unfortunately, the resulting expressions would be invalid for some of the arrangements we wish to consider for the frequency-swept imaging simulations. Thus, we shall evaluate the integral numerically with a simple but robust summation. If we wish to break the integral into  $N^P$  divisions, we let

$$\begin{aligned} dx &\rightarrow \Delta X, \\ \Delta X &= \frac{X_{max} - X_{min}}{N^P}. \end{aligned} \quad (5.5)$$

Then, Eq. (5.4) becomes

$$R_i(X_i^R) = \frac{j k P_0 \Delta X}{2\pi} \sum_{m=1}^{N^P} \frac{\exp(-j k (D_{im} + D_{Tm}))}{D_{im} \cdot D_{Tm}} \quad (5.6)$$

where

$$X_m^S = X_{min} + \Delta X \cdot (m - 0.5) \quad (5.7)$$

This summation is arranged so the the integral over each division is approximated by the value of the integral at the center of the division.

### 5.2.2.2 Plate Scattering Results

The simulation of plate scattering was first exercised for the case of a 12" plate located at the origin. In Figures 5.5 and 5.6, the magnitude and phase, respectively, of the reflected pressure are shown due to a source 100" from the origin at 0°. Figure 5.7 shows a similar case except that the source is at -45°. In all of these, the field was evaluated at locations which were 100" from the origin, at angular increments of 0.25° — that is, each plot consists of 721 points.

### 5.2.2.3 Comparison to Closed-Form Expressions

It would be encouraging to be able to compare the figures of the previous section to the closed-form expressions obtained by making the Fraunhofer approximation. This approximation is made in the distances  $D_i$  and  $D_T$  in Eq. (5.4). A small error in the distances will cause only a small error where they are used in the denominator of Eq. (5.4). On the other hand, the complex exponential is very sensitive to such errors; and, the problem is made worse by the multiplicative factor  $k$ .

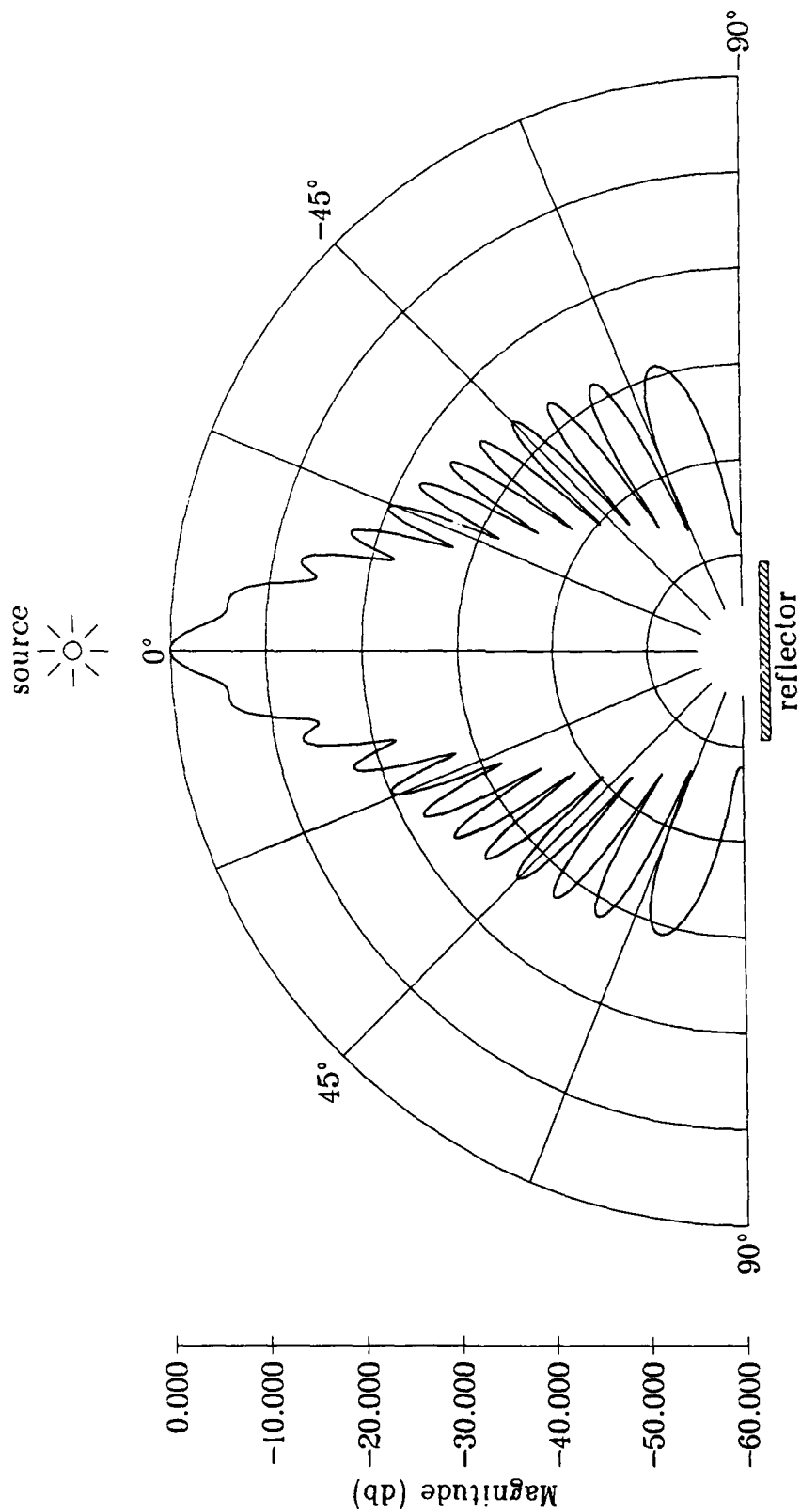


Figure 5.5. Magnitude of the pressure from a 13,045.2 Hz source at 0°, scattered by a 12' plate. The summation used 200 terms of width 0.06'' (0.06 $\lambda$ ).

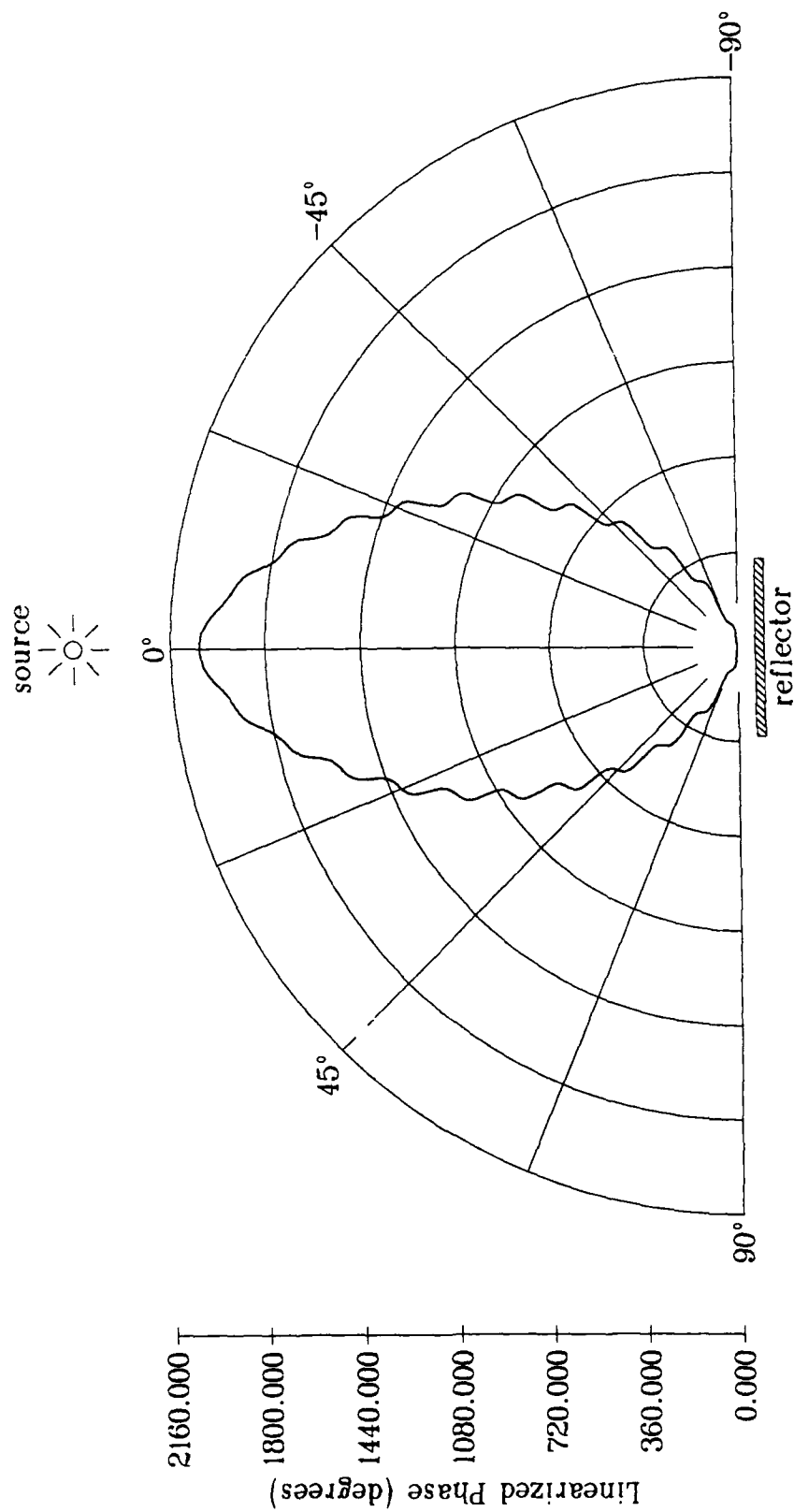


Figure 5.6. Phase of the pressure from a 13,045.2 Hz source at 0°, scattered by a 12'' plate. The summation used 200 terms of width 0.06'' (0.06 $\lambda$ ).

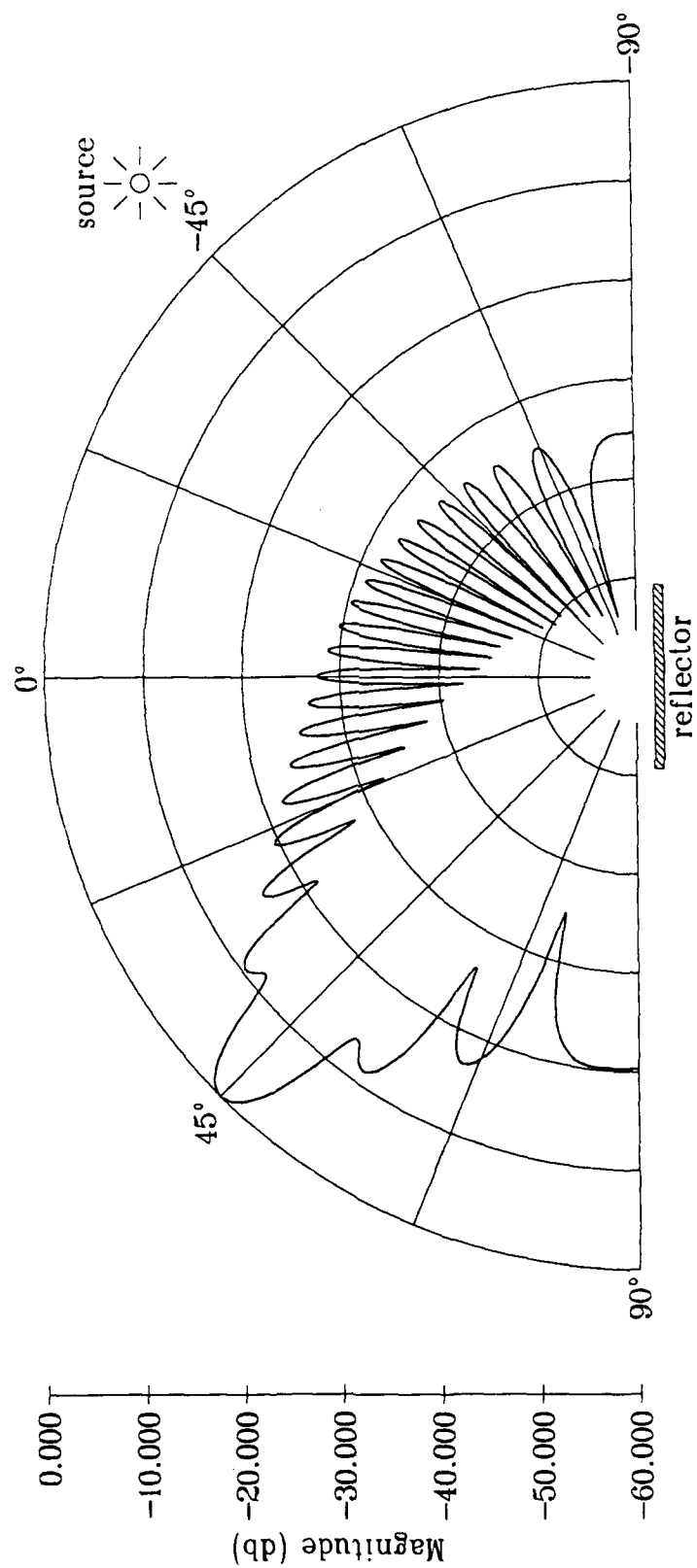


Figure 5.7. Magnitude of the pressure from a 13,045.2 Hz source at  $-45^\circ$ , scattered by a 12" plate. The summation used 200 terms of width  $0.06''$  ( $0.06\lambda$ ).



If we wish to limit the error in the phase of this exponential to, say,  $10^\circ$ , we must limit the error in the distances to

$$10^\circ \cdot \frac{\pi \text{ radians}}{180^\circ} \cdot \frac{1}{k} = 0.028'' \quad (5.8)$$

where we have set  $\lambda = 1''$  so that  $k = 2\pi$ . We are interested in simulations of a  $12''$  plate; thus, the greatest error will occur when computing the distance between the edge of the plate and a field point at some distance  $Z$  at some angle  $\theta$ . This distance can be computed without and with the Fraunhofer approximation as

$$D_{\text{exact}} = \sqrt{(Z \cos(\theta) - 6)^2 + Z^2}, \quad (5.9)$$

$$D_{\text{Fraunhofer}} = Z - 6 \sin(\theta). \quad (5.10)$$

These two distances were compared for various values of  $Z$  as  $\theta$  was increased to discover the maximum angle for which the Fraunhofer approximation met the error limit. The results, shown in Table 5.1, indicate that around and below  $Z = 600''$ , the Fraunhofer approximation fails the criteria at all angles. Since we are interested in using this simulation for distances of around  $Z = 100''$ , comparison to closed-form expressions using the approximation cannot be used.

#### 5.2.2.4 Numerical Suitability of the Summation

One of the common causes of a loss of numerical accuracy is that large and small numbers are added together in an inappropriate order, so that the contributions from the small numbers are lost. In order to explore this possibility, the scattering shown in Figure 5.5 was recalculated with the accumulated complex value of the summation shown in Figure 5.8, and the individual complex terms

Table 5.1. Maximum angle at which the Fraunhofer approximation is valid.

Z	$\theta$
$\leq 600.0$ inches	none
700.0 inches	0.1350 degrees
1,000.0 inches	0.2521 degrees
10,000.0 inches	0.1310 degrees
100,000.0 inches	0.0378 degrees
1,000,000.0 inches	0.0184 degrees

of the summation plotted in Figures 5.9. Note that the width of the plate was increased, from that used in earlier figures to 24", so as to better illustrate the process.

The summation shown in Figure 5.8 begins at zero; therefore, the first point on the curve (at the end with the heavy line) is the same as the first term. The last point on this curve is the final value of the summation. In Figure 5.9, only *half* the terms seem to be present. Actually, they are all present: because of symmetry, the terms for one half of the plate are exactly equal to the terms for the other half, and so pairs of points plot exactly on top of one another.

These figures indicate that the evaluation of Eq. (5.6) should be a numerically accurate process since the summation terms have nearly the same magnitude, and are within approximately one order of magnitude of the final result.

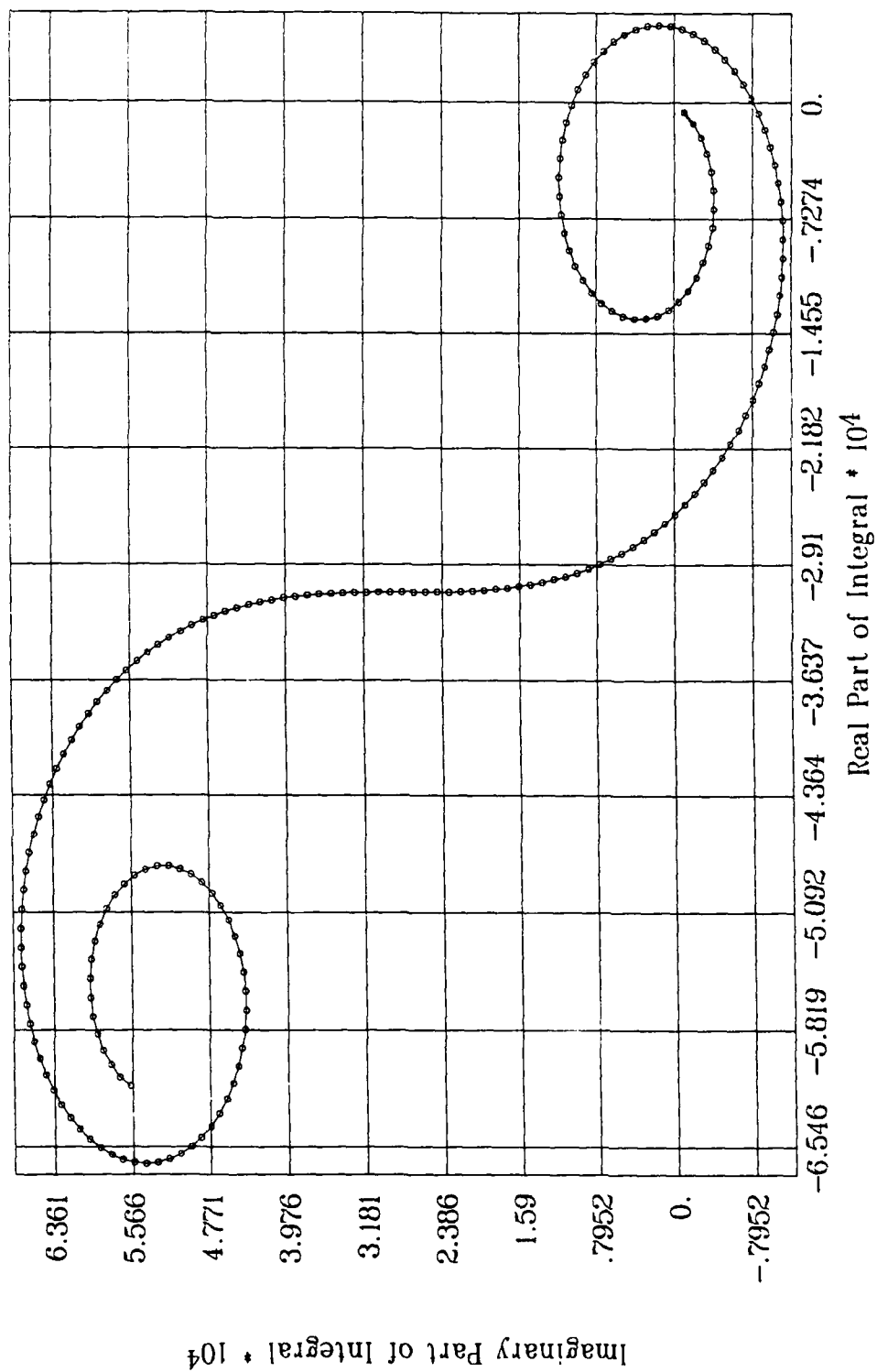


Figure 5.8. Accumulated Huygens-Rayleigh sum as we move across the plate from  $X=-12''$  (the end of the curve with the heavy line) to  $X=+12''$ . The receiver and 13,045.2 Hz source were 100' away at  $0^\circ$ .

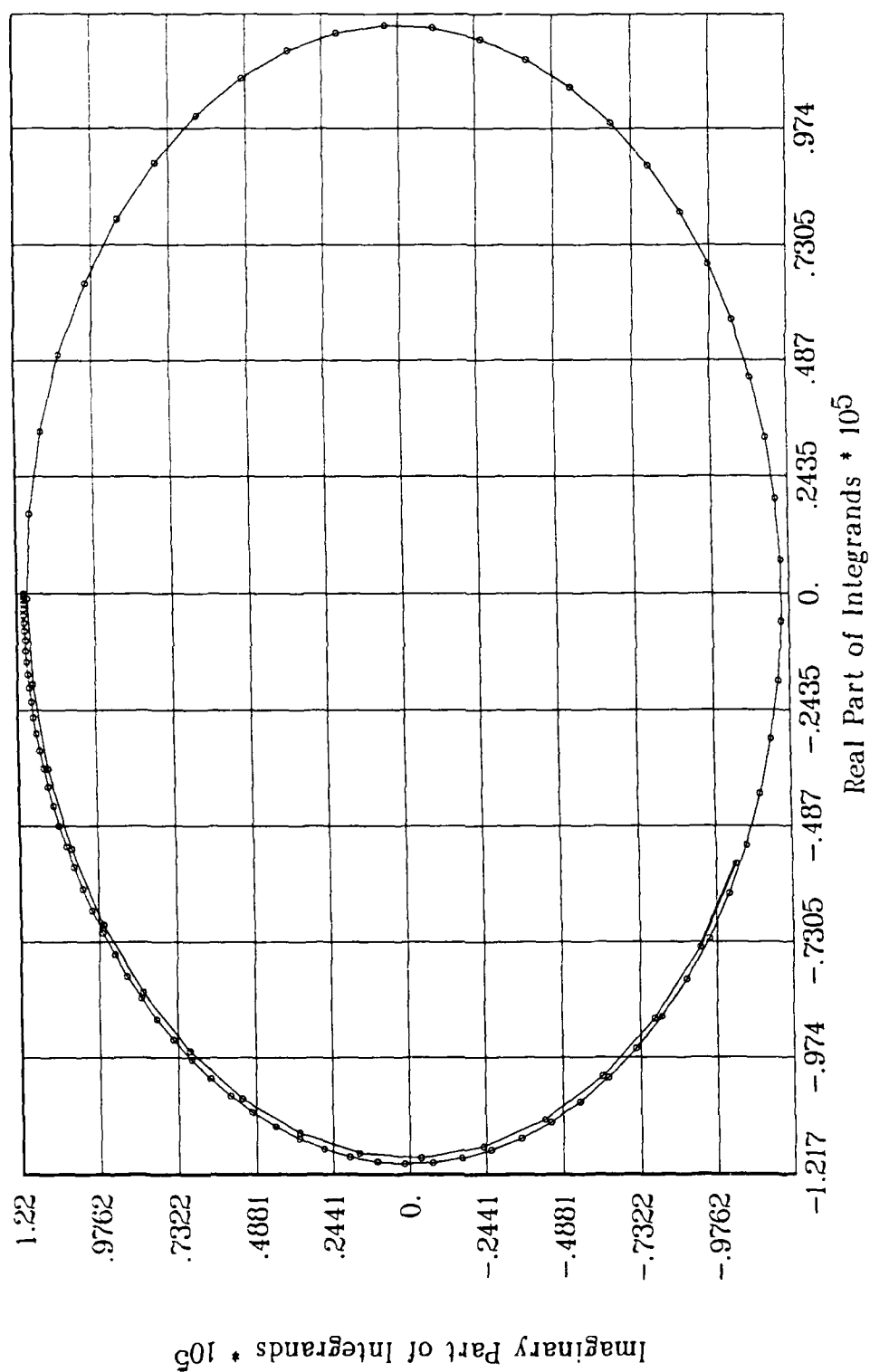


Figure 5.9. Individual Huygens-Rayleigh terms as we move across the plate from  $X=-12''$  (the end of the curve with the heavy line) to  $X=+12''$ . The receiver and 13,045.2 Hz source were 100'' away at  $0^\circ$ .

### 5.2.2.5 Number of Terms

The accuracy by which the summation of Eq. (5.6) approximates the integral of Eq. (5.4) is governed by the number of terms  $N^P$ ; therefore, it seems prudent to examine the convergence of the sum as  $N^P$  is increased. As illustrated in Figures 5.8 and 5.9, the summation is essentially one of vector addition in the complex plane where the length of the vectors are nearly equal. However, the direction of these vectors will vary more rapidly as the frequency or distances are increased.

A series of tests were run where a 12"-wide plate scattered waves from a 13,045.2 Hz source located on the axis of the plate at a distance of 100". The normalized field at a point 100" away at an angle of 45° is reported in Table 5.2. The results obtained using 10,000 terms was used as the reference value for normalization, which was done separately for the real and imaginary parts. Given that the wavelength is 1", the results for using only a small number of divisions are remarkably good.

Table 5.2. Normalized complex signal at 13,045.2 Hz and 45°.

$N^P$	Width of Term	Real Part	Imaginary Part
30 terms	0.4000 inches	1.1410	1.1271
60 terms	0.2000 inches	1.0327	1.0301
100 terms	0.1200 inches	1.0116	1.0100
1,000 terms	0.0120 inches	1.0002	1.0000
10,000 terms	0.0012 inches	1.0000	1.0000

A similar series of test were then run where the field point was moved to  $0^\circ$  and the frequency was increased to 30,000 Hz so that the wavelength is now 0.435". The results, shown in Table 5.3, also show good convergence. Because of these tests, it was decided to set  $N^P = 200$  for the simulation of plate reflection in this study although higher numbers might be used at very high frequencies.

Table 5.3. Normalized complex signal at 30,000 Hz and  $0^\circ$ .

$N^P$	Width of Term	Real Part	Imaginary Part
10 terms	1.2000 inches	0.9926	0.9255
50 terms	0.2400 inches	0.9995	0.9974
100 terms	0.1200 inches	0.9999	0.9993
1,000 terms	0.0120 inches	1.0000	1.0000
10,000 terms	0.0012 inches	1.0000	1.0000

#### 5.2.2.6 Results Using Higher Precision

The simulation of reflections from a plate was implemented in "double-precision" arithmetic which means that the computer's internal memory represents each number, or each part of a complex number, with an accuracy equal to approximately 16 decimal digits. Maintenance of this accuracy, of course, depends upon the numerical methods employed in an algorithm. However, the support routines, such as for the evaluation of the sine and cosine functions, are designed to deliver this accuracy.

The computer being used can also support "quadruple-precision" arith-

metic where each number and the support routines yield approximately 33 decimal digits of accuracy. A special version of the simulation was prepared and the values shown in Table 5.3 were recalculated using this higher precision. A comparison between the normalized quadruple- and double-precision results revealed no differences within the first 5 digits. Because of these tests, it was decided that the faster double-precision arithmetic was adequate.

#### 5.2.2.7 Scattering at Large Width-Wavelength Ratios

In preparation for the imaging simulations, the plate simulation was exercised by varying the plate width, location, and the frequency of the source. At higher frequencies, an anomaly occurred. We expected the scattering pattern shown in Figure 5.5 to be essentially reproduced at higher frequencies except that the pattern would be compressed towards the angle of incidence, which was  $0^\circ$  in these exercises. However, Figure 5.10 shows that we instead obtained a pattern with a dip where we expected the central peak. To explore this further, the pattern across an array of receivers was generated for a sweep of frequencies. The results, shown in Figure 5.11, indicate that while the sidelobes do indeed compress as expected as the frequency is increased, the anomalous region not only continues but increases in size.

Other tests had revealed that the width of the plate was also a factor in these unexpected results. In Figure 5.12, we have reproduced the simulation used in Figure 5.5 except that the width of the plate has been increased from 12" to 48". In order to observe the progressive effect of plate width, the width was swept from 12" to 48", in steps of 0.5", and the normalized results displayed in Figure 5.13. Note that as the width of the plate is varied, the width of the anomalous

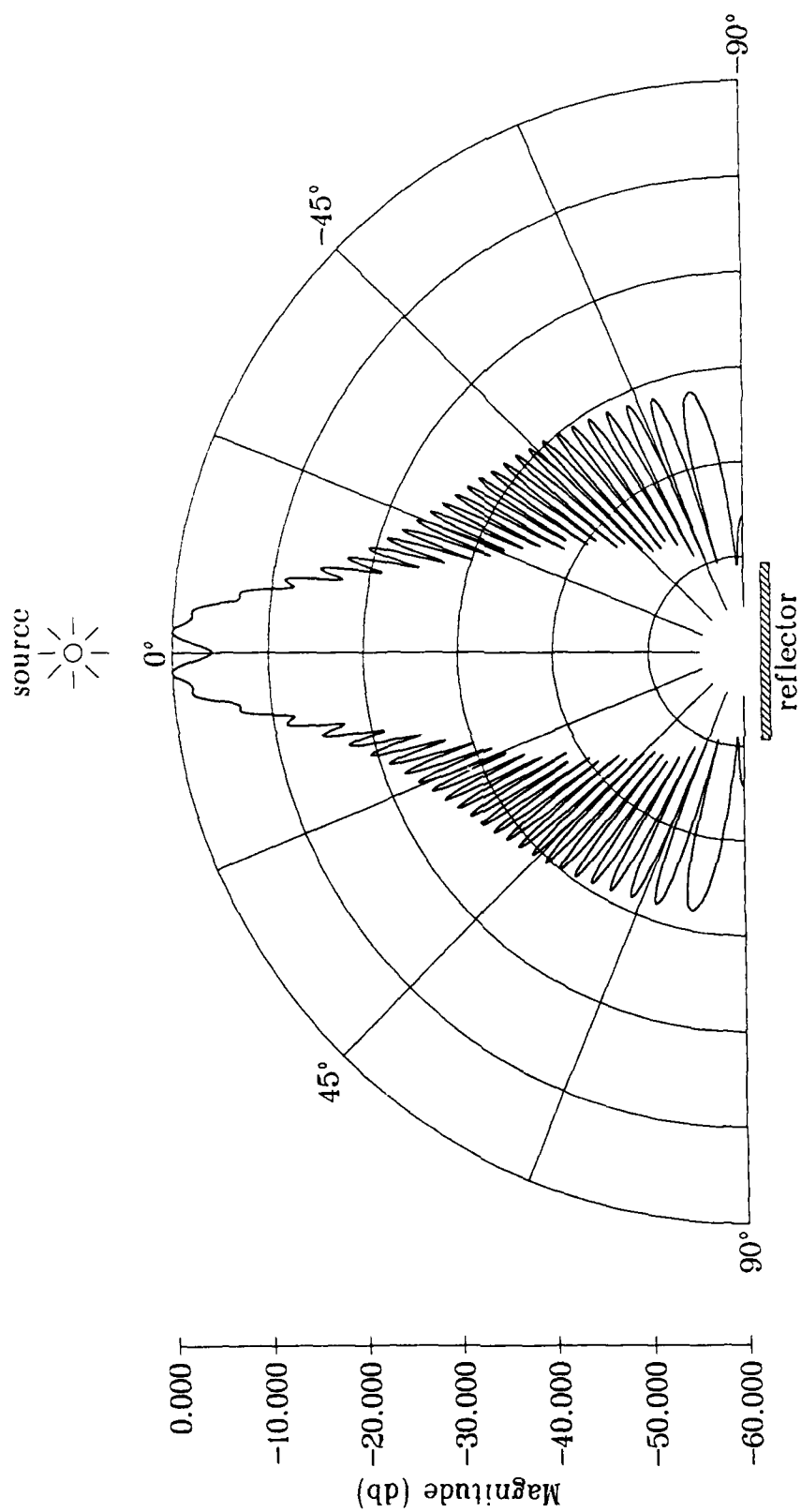


Figure 5.10. Magnitude of the pressure from a 30,500 Hz source at 0°, scattered by a 12" plate. The summation used 200 terms of width 0.06" (0.14 $\lambda$ ).



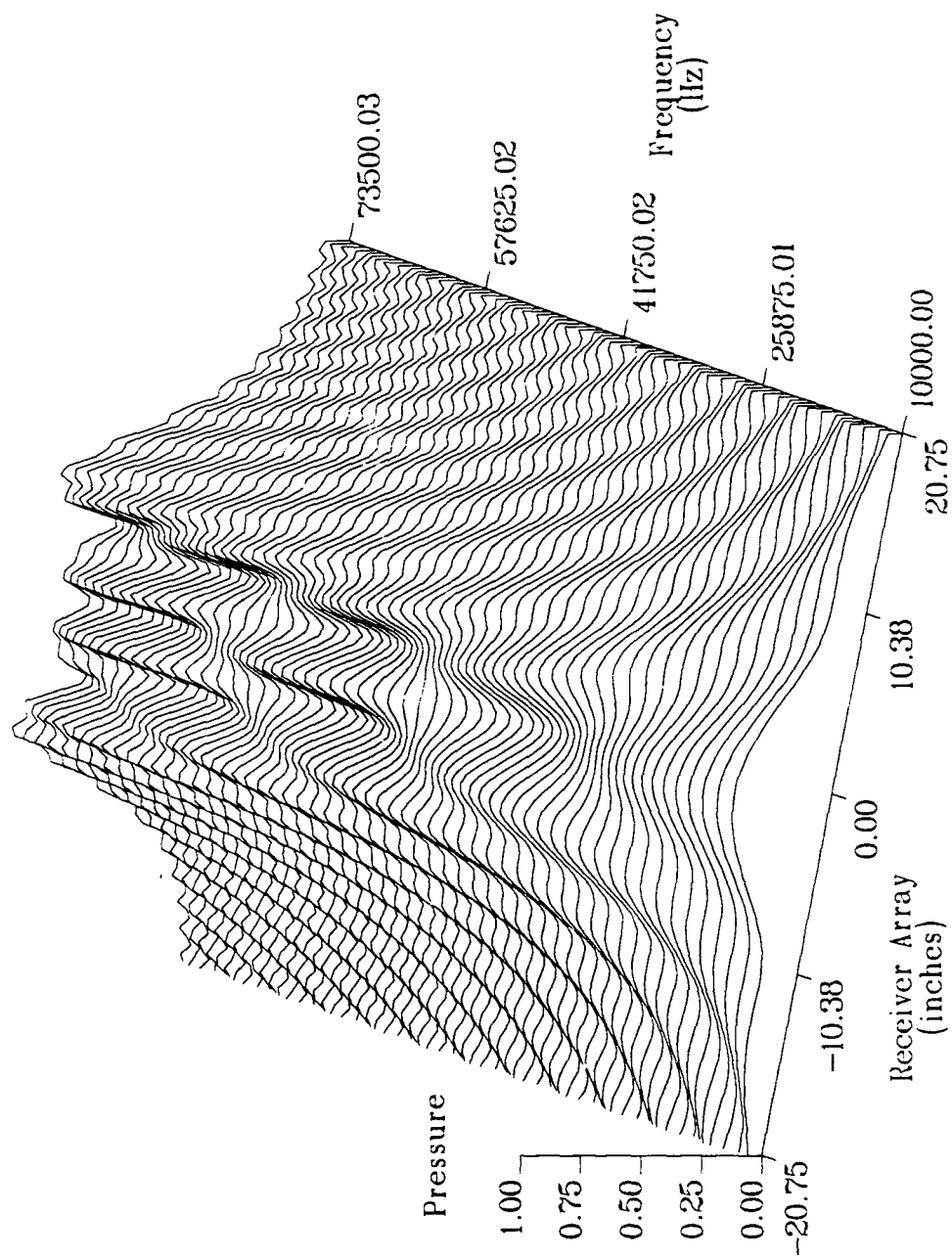


Figure 5.11. Magnitude of the pressure from a source at the origin, scattered by a 12" plate 100" away. The summation used 200 terms of width 0.06". The wavelength varies from 1.305" to 0.177".

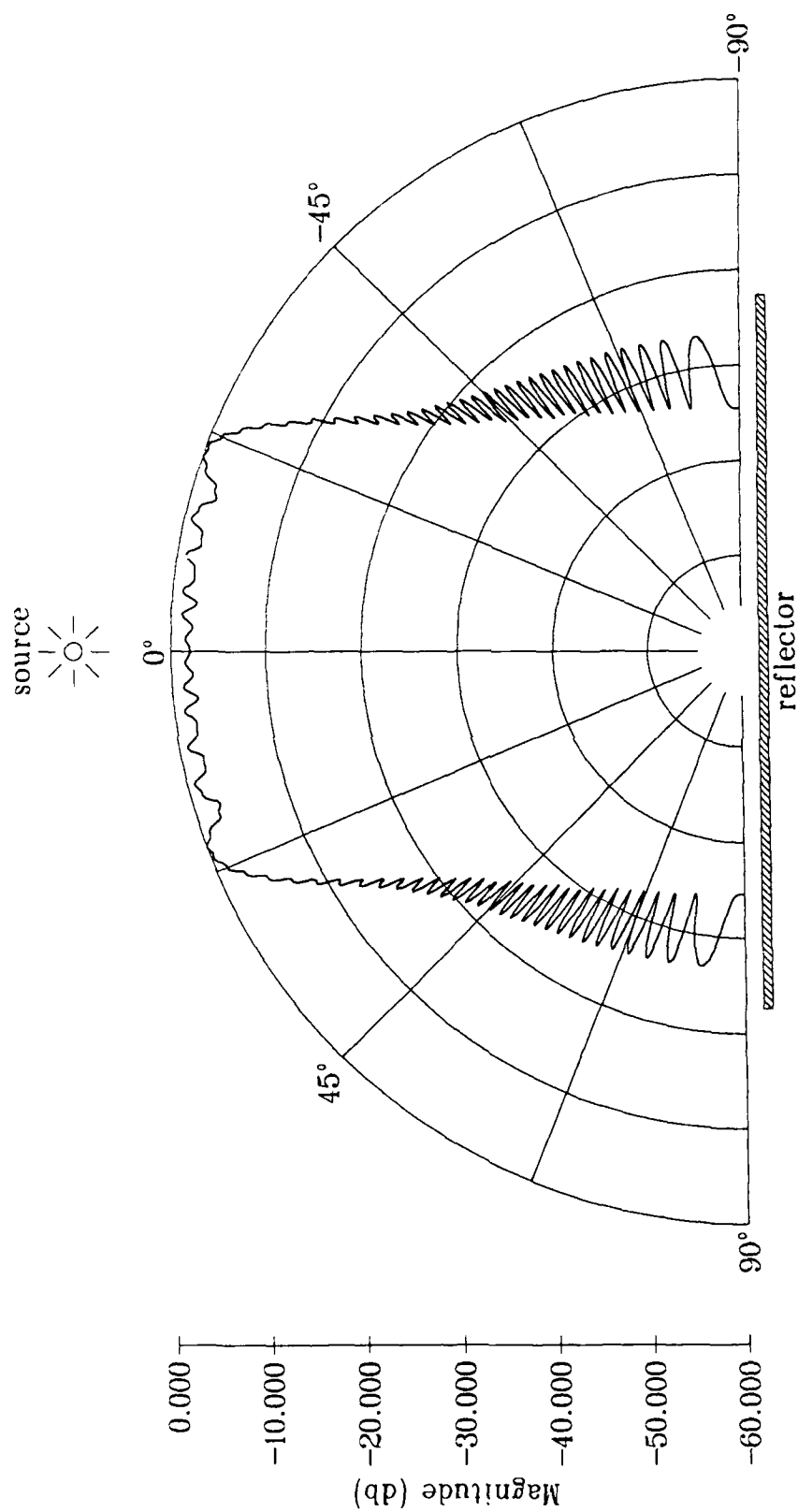


Figure 5.12. Magnitude of the pressure from a 13,045.2 Hz source at 0°, scattered by a 48" plate. The summation used 200 terms of width 0.24" (0.24λ).

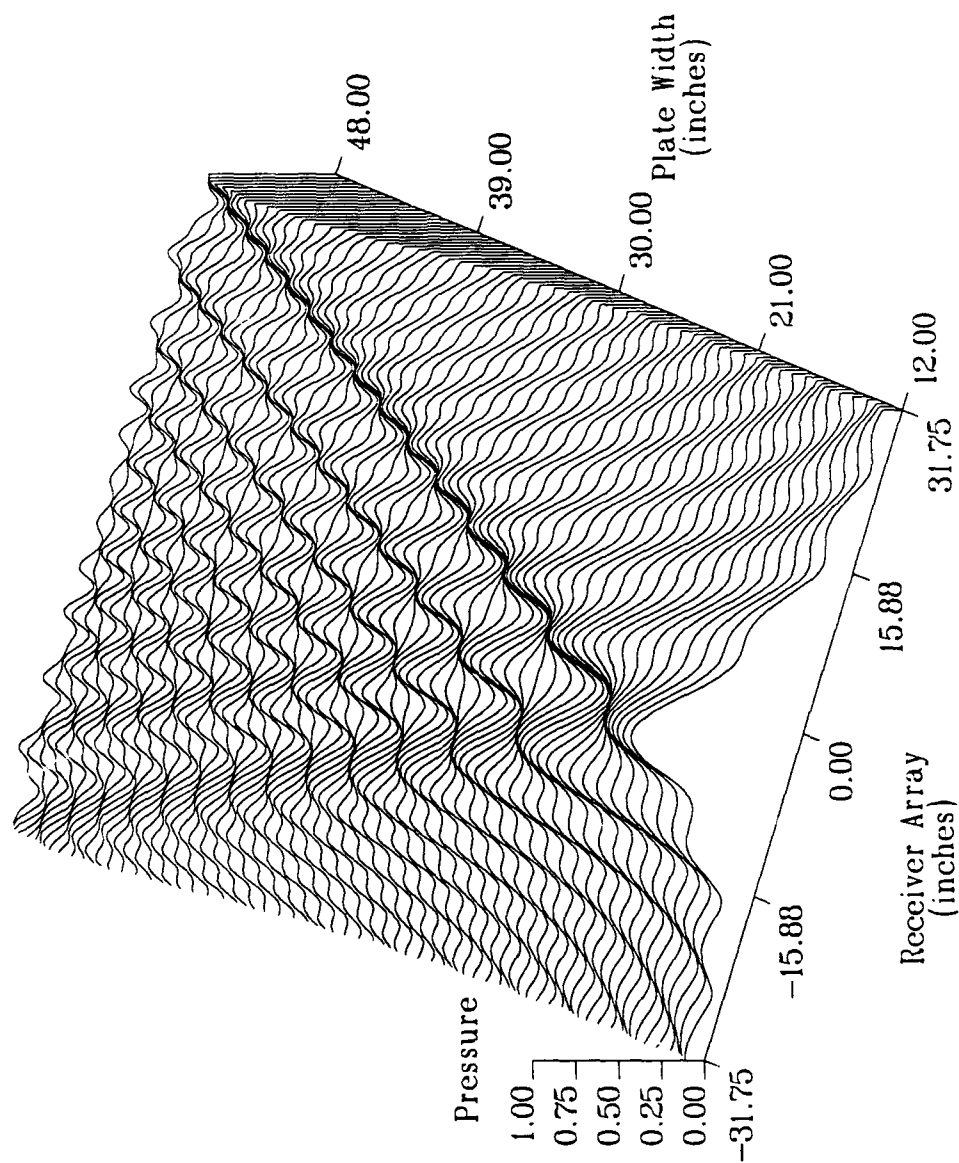


Figure 5.13. Magnitude of the pressure from a 13,045.2 Hz source at the origin, scattered by a plate 100" away. The summation used 200 terms of width 0.06" ( $0.06\lambda$ ).

region varies proportionally.

We can gain a better understanding of these simulations by applying Babinet's principle;<sup>83</sup> that is, we replace the rigid plate in its plane with an infinite baffle in the same plane which contains an aperture where the plate had formerly been located. In addition, we replace the point-source transmitter with its mirror image, located on the opposite side of the plane. In this alternative arrangement, the phase and amplitude at each location in the new aperture is identical with that which had formerly existed at the same locations on the surface of the plate. Thus, Eq. (5.4) continues to describe the signal at the receivers.

The effects seen in Figure 5.13 can now be interpreted as the field of a point source after passing through, and experiencing diffraction at, an aperture. For the special case of the point source location being on the axis of the aperture (i.e., opposite its center), Skudrzyk<sup>84</sup> noted that the field consists of the interference between the incident wave and a contribution that originates at the boundary of the aperture. The special case applies here since the transmitter has been located on the Z-axis about which the plate has also been centered. Given the speed of sound  $c = 13045.2$  inches/second, we find that the edge of the first or central Huygens zone to be 10.01, 6.543, or 4.214 inches from the origin when the frequency is 13045.2, 30,500, or 73,500 cycles/second, in that order. This corresponds to zones with a diameter (or width, in our two-dimensional case) of 20.02, 13.086, or 8.428 inches, in that order.

It therefore seems reasonable that the earlier examples, such as Figure 5.5, did not exhibit the interference between the incident and boundary waves because the plate was not large enough to encompass even the first Huygens zone.

The small dip where the central peak had been expected in Figure 5.10 is not an anomaly but is instead due to the plate between just wide enough, relative to a wavelength, for this interference to be observed.

### 5.3 Interpolation

The central idea in the swept-frequency method developed in the next section is the comparison of the pattern recorded across the receiving array at one frequency to that recorded at another frequency. The approach (discussed later) shall be to use the higher of the two frequencies directly. Thus, we shall need to compress the pattern at the lower frequency to estimate how it would look at the higher frequency. That is, the signal  $R_i$  recorded at the lower frequency at location  $X_i^R$  in the linear array is moved to a new location  $\hat{X}_i^R$  representing the compression caused by the increase in frequency.

In general, the new locations  $\hat{X}_i^R$  will not happen to be equal to the original receiver locations at which the higher frequency is known. We will therefore need to interpolate on the compressed pattern to find its value at the original receiver locations. While this is in some ways a minor point in the development, it is central to the analysis not only in terms of the accuracy of the results but also in terms of the speed of execution.

A piecewise-cubic Hermite interpolation algorithm was adapted from an algorithm given by Conte and de Boor<sup>85</sup> and implemented as a FORTRAN subroutine. This algorithm requires the slope of the function at each point. Since the slope of the scattering pattern across the array cannot be directly measured, the slope

$y'_i$  is estimated as

$$y'_i = \frac{y_{i+1} - y_{i-1}}{x_{i+1} - x_{i-1}} \quad (5.11)$$

where the  $y_i$  are the function's values at locations  $x_i$ .

It was felt that it would be better for this operation to return no value than to blindly estimate answers which were not robustly supported by the given data; therefore, the interpolation subroutine signals that it has set the result to zero if the requested point of interpolation is outside certain limits. The limits have been chosen so that there is always at least two points between the point of interpolation and the beginning or end of the table of given data. These limits were selected because the algorithm needs one point on either side of the point of interpolation for the calculation of slope.

Since the pattern across the array often looks like a sine wave, a test was run using 9 samples of a sine wave every  $45^\circ$ . Interpolated values, shown in Figure 5.14, were requested every  $1^\circ$ . As expected, zeroes were returned beyond the interpolation limits. The maximum error, occurring near the peaks, are acceptable for this study.

#### 5.4 Development of the Analysis Method

In Section 5.2, the scattering patterns from point and extended scatterers were examined for correctness; now, we examine them again to determine their frequency dependence which will then be used to develop the new swept-frequency imaging method.

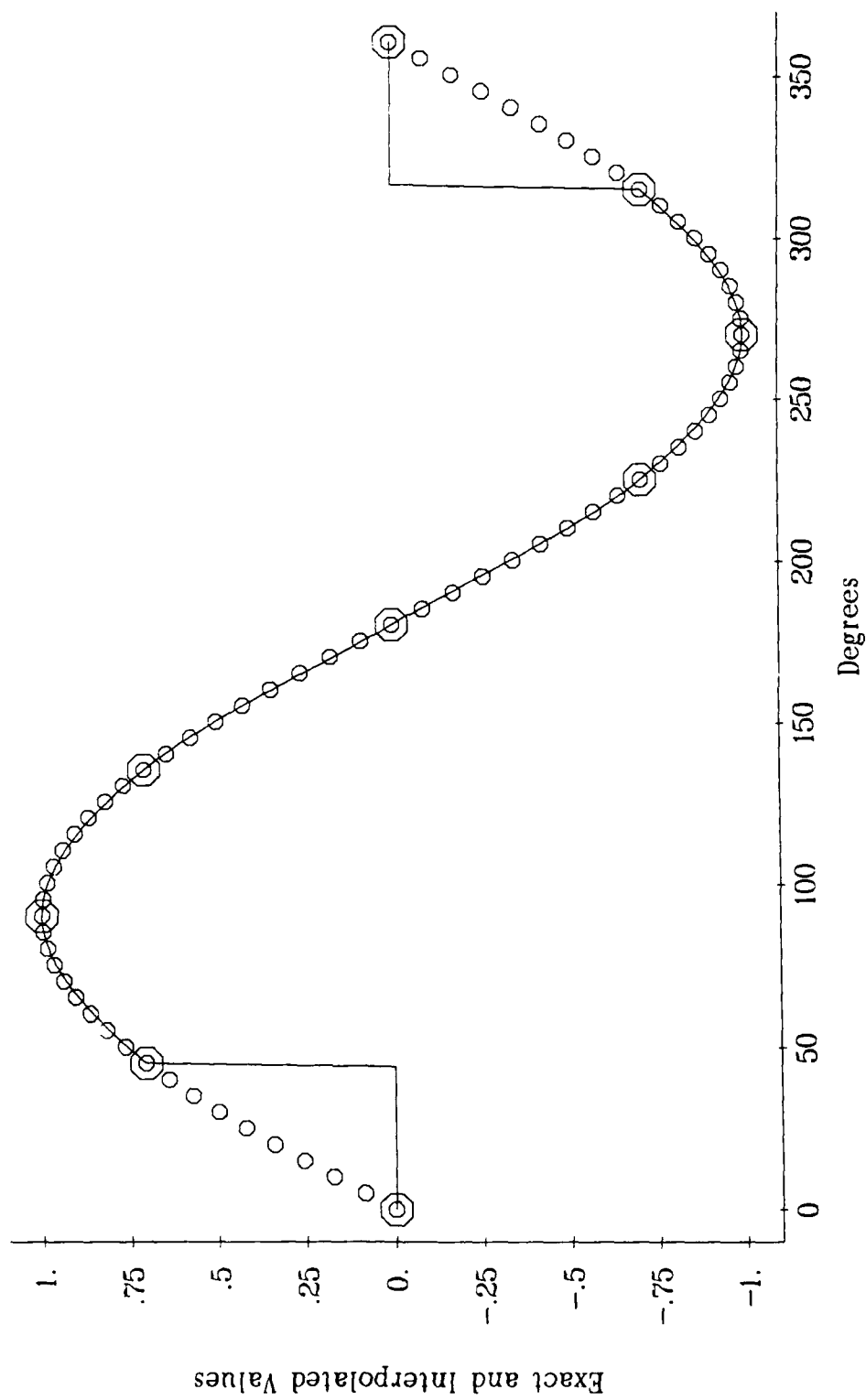


Figure 5.14. Values interpolated using a piecewise cubic polynomial (line) and the control points (large circles) used in the interpolation. Additional values (small circles) are shown for comparison.

### 5.4.1 Frequency Dependence

We wish to develop a model of the frequency dependence of a scattering pattern. The approach shall be to develop the model for the rather simple case of two point reflectors, but then test the model for both pairs of point reflectors as well as plates.

The basic geometry for determining the signal scattered by a point reflector is given in Figure 1.1. The signal at a particular receiver located at  $(X^R, Z^R)$  due to one reflector is given by Eqs.(1.2) to (1.5) with  $N^S = 2$ . For a single-frequency source, the time delays can be written as phase delays. Then, we merely sum the contributions from the two reflectors so that we have

$$R(X^R, Z^R) = \frac{\exp(-j k (D_{T1} + D_{R1}))}{D_{T1} \cdot D_{R1}} + \frac{\exp(-j k (D_{T2} + D_{R2}))}{D_{T2} \cdot D_{R2}} \quad (5.12)$$

where the  $D_{Ts}$  are the distances between the transmitter and scatterer  $s$  and the  $D_{Rs}$  are the distances between scatterer  $s$  and the receiver. When the distance  $d$  between the scatterers is small relative to the distance to the source and to the receiver, we can make an approximation where we treat the pressure waves as being planar instead of spherical. This lets us write the previous distances in terms of the distances to the point midway between the reflectors. If  $D_T$  is the distance to this point from the transmitter, and  $D_R$  is the distance to this point



from the receiver, we can write

$$\begin{aligned}
 D_{T1} &\rightarrow D_T - \frac{1}{2}d \sin(\phi^T), \\
 D_{T2} &\rightarrow D_T + \frac{1}{2}d \sin(\phi^T), \\
 D_{R1} &\rightarrow D_R - \frac{1}{2}d \sin(\phi^R), \\
 D_{R2} &\rightarrow D_R + \frac{1}{2}d \sin(\phi^R)
 \end{aligned}
 \tag{5.13}$$

where  $\phi^T$  and  $\phi^R$  are the angles to the transmitter and receiver, respectively, relative to the normal to the line connecting the reflectors. Implicit in these equations is the fact that the line connecting the point reflectors is parallel to the X-axis, and that reflector 2 lies at an X-coordinate greater than that of reflector 1. We are mainly interested in the scattering pattern's angular rather than amplitude dependence upon frequency; furthermore, the amplitude terms change very slowly with frequency. Therefore, we can drop the amplitude factors, leaving

$$\begin{aligned}
 R(X^R, Z^R) &\approx \exp\left(-j k \left(D_T + D_R - \frac{1}{2}d \left(\sin(\phi^T) + \sin(\phi^R)\right)\right)\right) \\
 &\quad + \exp\left(-j k \left(D_T + D_R + \frac{1}{2}d \left(\sin(\phi^T) + \sin(\phi^R)\right)\right)\right), \\
 &= 2 \exp(-j k (D_T + D_R)) \cdot \cos\left(\frac{1}{2}k d \left(\sin(\phi^T) + \sin(\phi^R)\right)\right).
 \end{aligned}
 \tag{5.14}$$

The term  $\cos(\dots)$  in Eq. (5.14) describes the directivity of the scattering pattern at a given frequency  $f$  where  $k = \frac{2\pi f}{c}$ . We wish to determine how the directivity will change when we shift to a new frequency  $\hat{f}$ . That is, if some particular feature in the pattern (a peak, a null, or any feature inbetween) is at angle  $\phi^R$  at frequency  $f$ , to what new angle  $\hat{\phi}^R$  does the feature move at new frequency

$\hat{f}$ ? It is convenient to answer this question by examining the  $n$ th maximum since the entire pattern must exhibit the same frequency dependence. The maximum points in the pattern will occur at

$$\frac{1}{2} k d \left( \sin(\phi^T) + \sin(\phi^R) \right) = n \pi \quad \text{for } n = 1, 2, 3, \dots, \quad (5.15)$$

where we have excluded the central maximum at  $n = 0$ . The parameters  $n$  and  $d$  do not change with frequency. Therefore, we solve for these parameters for frequencies  $f$  and  $\hat{f}$  and equate the results so that we have

$$\frac{f}{c} \cdot \left( \sin(\phi^T) + \sin(\phi^R) \right) = \frac{\hat{f}}{c} \cdot \left( \sin(\phi^T) + \sin(\hat{\phi}^R) \right) \quad (5.16)$$

or

$$\hat{\phi}^R = \arcsin \left( -\sin(\phi^T) + \frac{f}{\hat{f}} \cdot \left( \sin(\phi^T) + \sin(\phi^R) \right) \right). \quad (5.17)$$

If the scattering center (the point midway between the two reflectors) is, or is assumed to be, located at  $(X^F, Z^F)$ , then we can convert the *angular* frequency dependence, given by Eq. (5.17), into a *linear* frequency dependence, for locations  $(X_i^R, 0)$  in the linear receiver array. This relationship is

$$\hat{X}_i^R = X^F + Z^F \cdot \tan(\hat{\phi}_i^R) \quad (5.18)$$

where  $\phi_i^R$  and  $\hat{\phi}_i^R$  are the angular locations of the  $i$ th receiver relative to the scattering center.

The ability of Eq. (5.18) to represent the frequency dependence of a scattering pattern was explored by first calculating the pattern, due to two point reflectors, at a linear, equally spaced receiver array for a set of frequencies. The results are shown in Figure 5.15 with the lower 90% of the data removed so that

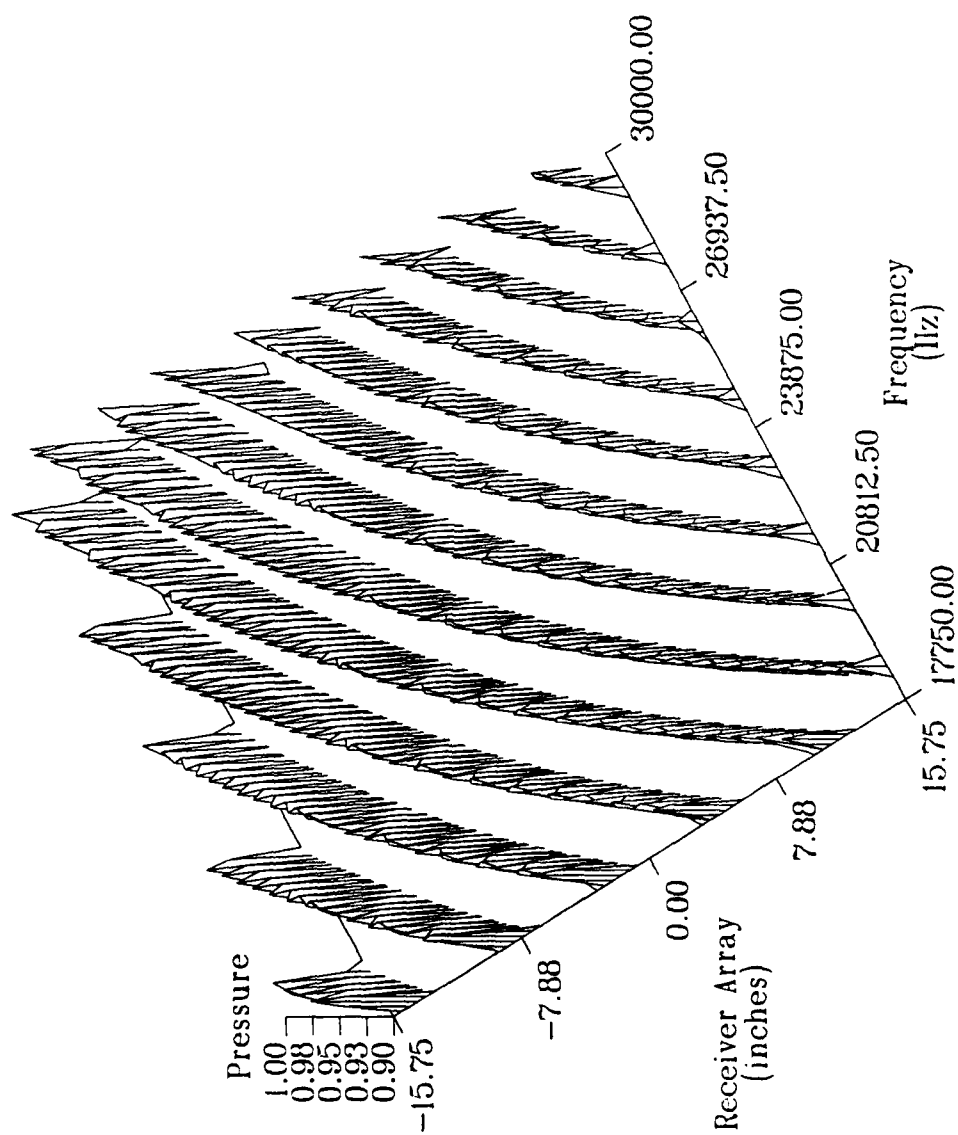


Figure 5.15. Patterns at an array on the X-axis (64 receivers) versus frequency (50 frequencies, 250 Hz apart), due to 2 point reflectors centered at  $(-20', 100')$  and a source at  $(20', 0)$ .

the location of the peaks can be more easily seen. Then, Eq. (5.18) was applied to shift all frequencies, except 30,000 Hz, to  $\hat{f} = 30,000$  Hz. The shifted results in Figure 5.16 exhibit two phenomena. First, the patterns at all frequencies are now aligned, indicating that Eq. (5.18) has done a good job of predicting the frequency dependence. Second, there are regions of the shifted pattern which cannot be determined (i.e., the interpolation returned a zero); these correspond to regions which had been off the end of the array before the shift. The undetermined region is greatest where the shifting is greatest, at the lower frequencies. This phenomenon means that *even if* we can predict the frequency-induced shift of a pattern, the results may be less than useful if the value of  $\Delta f$  (i.e., the difference between  $f$  and  $\hat{f}$ ) is too great.

The same information shown in Figure 5.16 is shown again in Figure 5.17 as a series of superimposed curves. A repeating cycle of solid, long-dash, and short-dash lines were used to plot the curves, beginning at the highest frequency. Note that only the highest frequency, a solid line, extends all the way to the right-hand side of the plot — as the frequency decreases, the undetermined region of the shifted pattern increases and so the curve ends (goes to 0) at some decreasing location in  $X$ . This figure exhibits an excellent frequency compensation for the lateral location of the pattern. Unfortunately, the lack of any frequency compensation for the amplitude of the pattern in Eq. (5.18) can be seen in the different levels at the peaks and nulls.

The information shown in Figure 5.17 has been regenerated for Figure 5.18 except that the pair of point reflectors has now been replaced with a plate 12" wide. The frequency compensation for the lateral location of the pattern

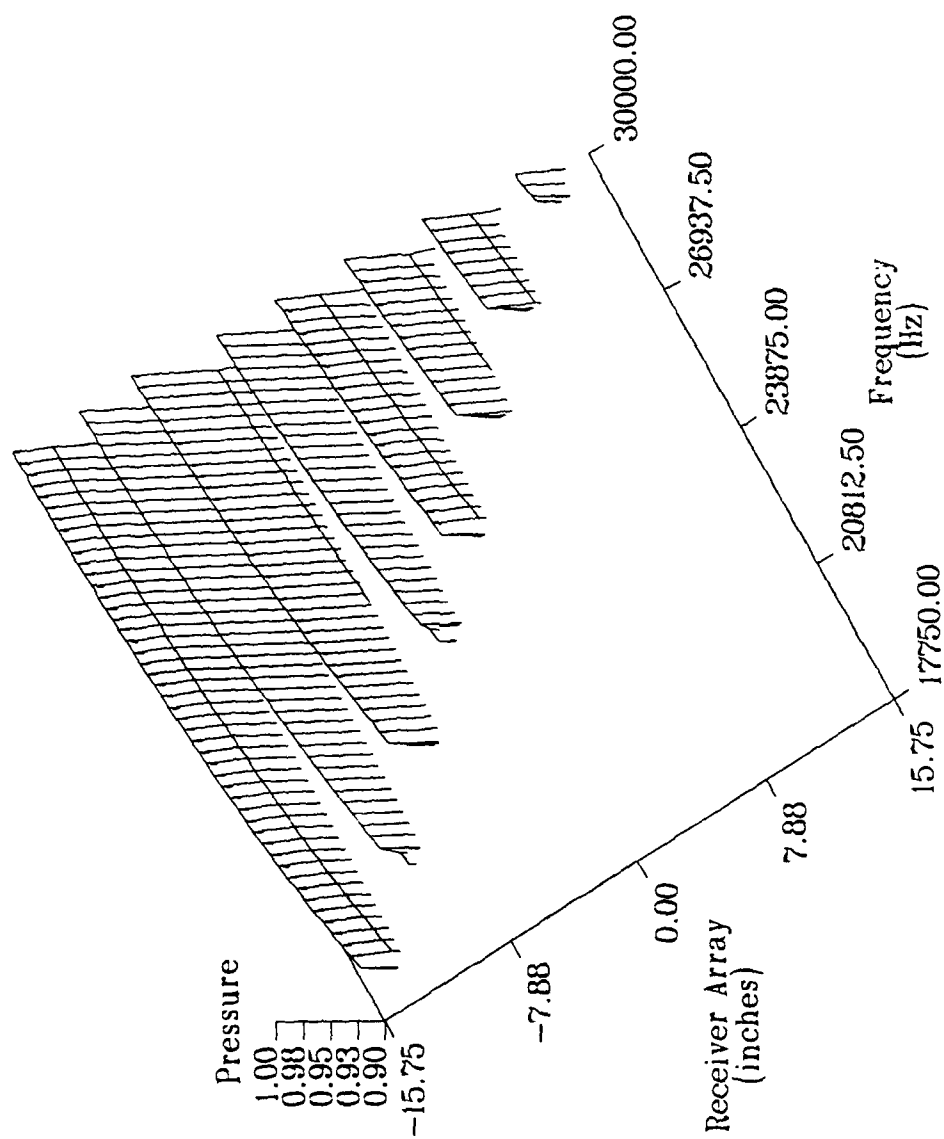


Figure 5.16. Patterns, due to 2 point reflectors, at an array, versus frequency. The pattern at each frequency, except 30,000 Hz, has been shifting so as to approximate a pattern at 30,000 Hz.

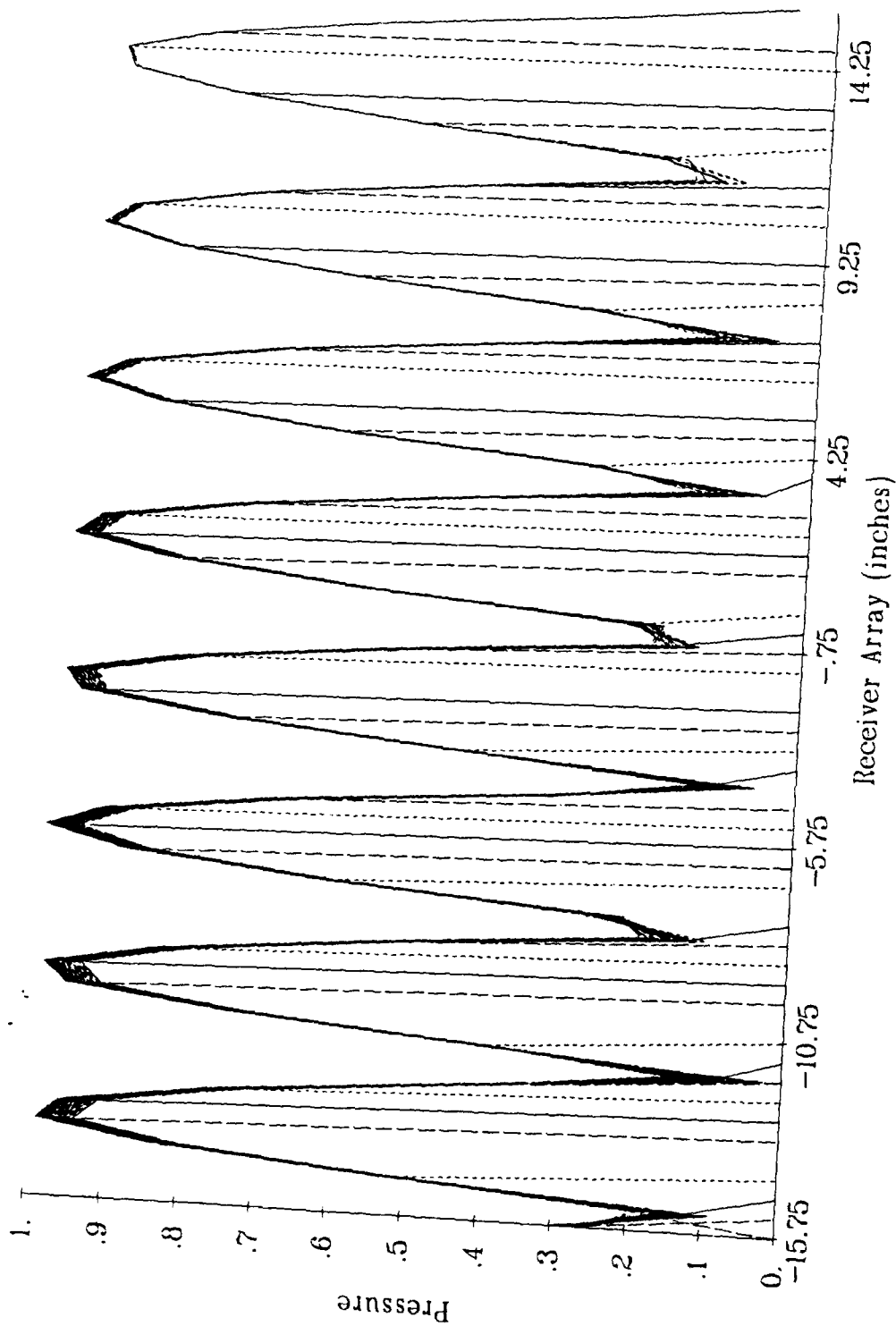


Figure 5.17. Superimposed shifted patterns, due to 2 point reflectors, at an array, versus frequency. As the frequency decreases, the pattern goes to 0 at a decreasing location in the receiver array.

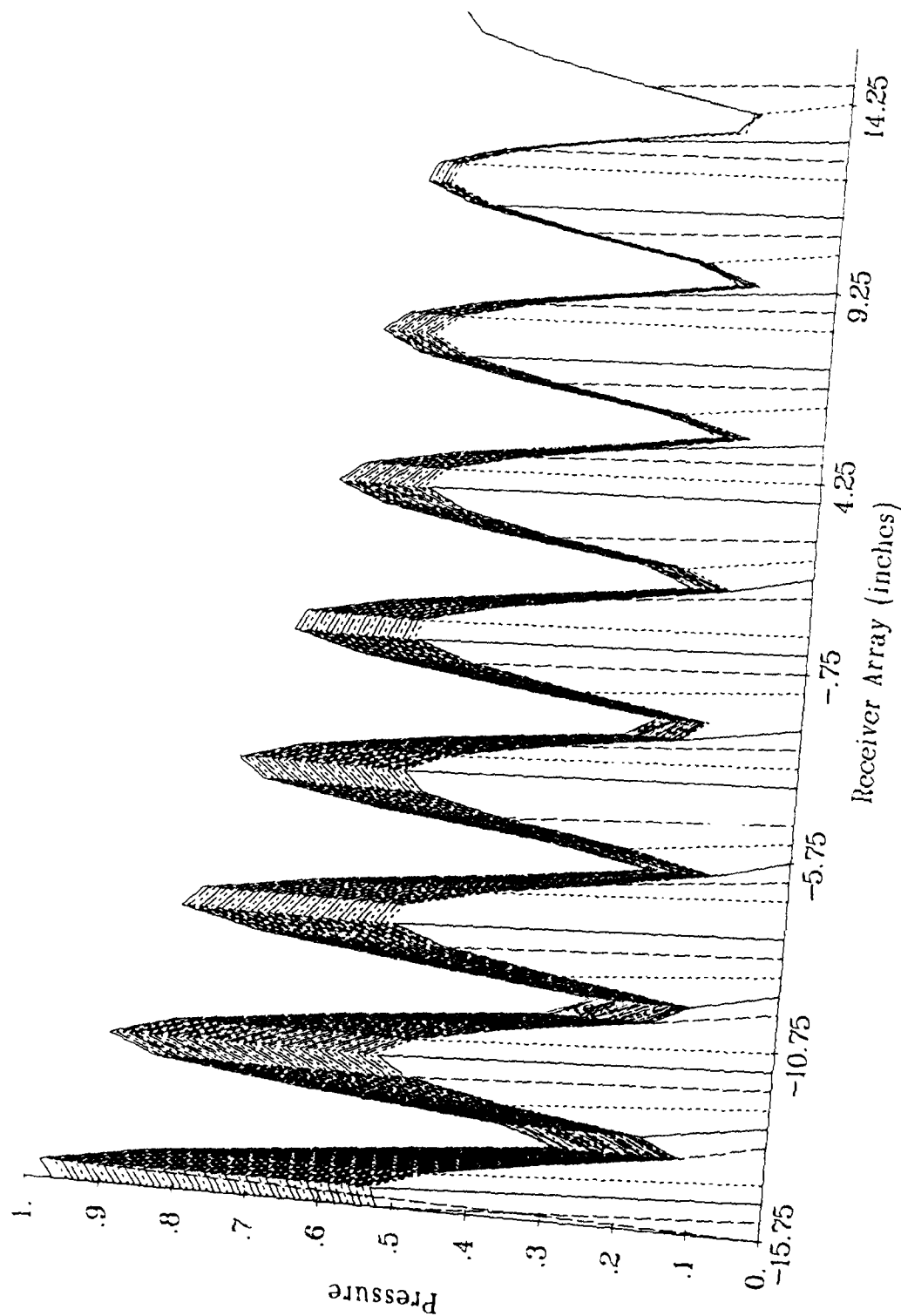


Figure 5.18. Superimposed shifted patterns, due to plate, at an array, versus frequency. As the frequency decreases, the pattern goes to 0 at a decreasing location in the receiver array.

is remarkably good, especially in light of the fact that Eq.(5.18) was derived for two point reflectors. This success is probably due to the fact that the two edges of a reflective plate are the major contributors to its scattering pattern. The frequency dependence of the amplitude of the plate's pattern, however, has resulted in relatively large differences at the peaks in the pattern. The only way in which this difference could be minimized is to minimize  $\Delta f$ .

#### 5.4.2 Forming a Swept-Frequency Image

We wish that the input to this new imaging method be a set of data like that shown in Figure 5.15: a received signal, versus receiver location, versus frequency. We also wish that this new imaging method produce an output as in, say, Figure 4.11, where the numerical value at each point in the reconstructed field represents the degree to which there seems to be a scatterer at that point.

The obvious approach seems to be to somewhat repeat the concept of the pattern-match method. That is, we first assume that there is a single fictitious scatterer (actually, a scattering center) at some specific location whose scattering pattern exhibits the frequency dependence given by Eq.(5.18). Second, we test this hypothesis by using Eq.(5.18) to shift the information actually received, from one frequency to another. If the hypothesis is correct, the shifted patterns should line up as seen in Figure 5.17; if not, they should not line up. And third, the fictitious scatterer is moved through all locations in object space, i.e., all locations which could possibly contain an actual scatterer. The location at which the shifted patterns became aligned the best are then interpreted as the location of the true scatterer.



The most important issue which remains can be expressed as a question: what metric should be used to quantify how well the shifted patterns “line up?” Before this question can be answered, we must first answer a related one: do we use the complex received signal, or its magnitude (as was used in Figures 5.15 to 5.18)?

There are at least two arguments in favor of avoiding the complex signal. First, for non-reverberant scatterers, the phase of the received signals is determined by the wavelength and the path length. That is, though the phase varies with the angle  $\phi^R$  to a receiver, the variation is due only to the change in the path length to the receiver — there is no additional variation due to some scattering phenomenon. Second, after the received pattern at one frequency has been shifted to another frequency, we would need to add some additional compensation to the phase since each point in the shifted pattern is now at a new location in the receiver array and therefore at a new distance from the scatterer. It is not clear at this time if such an additional compensation could be determined. For these reasons, only the magnitude of the received pattern shall be used.

We now return to the original question on determining how well the shifted patterns line up. This question is quite similar to the one addressed by the mismatch method developed in Section 4.2 if we instead ask the question: how well do the shifted patterns *not* line up? To measure this, we redefine the metric  $z_d^2$ , originally developed for comparing complex numbers, to be

$$z_d^2 = \frac{1}{NM} \sum_{q=1}^{N^C} \sum_{i=1}^{N^R} \left( \hat{R}_i(f(q)) - R_i(\hat{f}(q)) \right)^2 \quad (5.19)$$

where  $N^C$  is the number of frequency pairs which are being compared. The

two frequencies  $f(q)$  and  $\hat{f}(q)$  are any two frequencies at which data has been recorded (the appropriate selection of these frequencies will be investigated in the next section). The values  $\hat{R}_i(f(q))$  represent the pattern at array locations  $X_i^R$  which have been shifted from frequency  $f(q)$  to frequency  $\hat{f}(q)$ . The values  $R_i(\hat{f}(q))$  also represent the pattern at array locations  $X_i^R$ ; however, these are values which have *not* been shifted in frequency but which have instead remained at their original frequency  $\hat{f}(q)$ . Thus, if the patterns at each pair of frequencies line up, we have  $z_d^2 = 0$ ; otherwise,  $z_d^2$  can grow to be a very large number.

The normalization factor  $\frac{1}{NM}$  in Eq. (5.19) is equal to the number of terms compared and is ideally given by  $N^M = N^C \cdot N^R$  where  $N^R$  is the number of receivers. However, as was seen in Figure 5.16, the number of terms compared will be decreased when there are one or more undetermined points after a frequency shift.

Each term of Eq. (5.19) compares two values:  $R_i(\hat{f}(q))$  and  $\hat{R}_i(f(q))$ . The former requires no calculation as it is one of the values directly measured at the  $i$ th receiver. The latter, however, must be estimated as follows. First, we calculate the shifted pattern locations using Eq. (5.18) with  $f \rightarrow f(q)$  and  $\hat{f} \rightarrow \hat{f}(q)$ . That is, the data values  $R_i$  which were originally recorded at receiver locations  $X_i^R$  are now considered to be data values at the shifted receiver locations  $\hat{X}_i^R$ . Second, we must use interpolation to evaluate the shifted pattern at the original receiver locations since we only know the values  $R_i(\hat{f}(q))$  at those locations. We can write this as

$$\hat{R}_i(f(q)) = \text{INTERPOLATE} \left( X_i^R, R(\hat{X}_m^R, f(q)) \text{ for } m = 1, 2, \dots, N^R \right) \quad (5.20)$$

where the INTERPOLATE operation uses the set of values in its second operand to estimate the function at its first operand.

Once all values of  $z_q^2$  have been computed, a final transformation is performed as given in Eq. (4.17). That is, the cases where the frequency-shifted patterns line up the best (i.e., there is a minimum of mismatch) are mapped to 1 while the average case is mapped to 0.

### 5.4.3 Choosing the Frequencies

One of the input parameters to the program which generates the swept-frequency image is a table describing the pairs of frequencies which are to be compared:

$$f(q) \text{ and } \hat{f}(q) \text{ for } q = 1, 2, \dots, N^C. \quad (5.21)$$

Although such a table can accommodate any possible combination of frequencies, several pragmatic considerations limit the combinations. First, in order to help simplify the specification of the table, we always assign the higher frequency to the second member of the pair so that  $\hat{f}(q) > f(q)$ . Second, we always shift the lower frequency to the higher frequency since there will be more sinusoid-like cycles across the array at the higher frequencies and thus a greater sensitivity to mismatch.

To better understand how the choice of frequencies affected the new imaging method, a simulation was prepared and run for a variety of frequencies. All of the results reported in the remainder of this section use this same simulation.

The simulation consists of a source at  $(20'', 0)$  with a pair of point reflectors centered at  $(-20'', 100'')$  and separated by  $12''$  so that the line connecting the

reflectors is parallel to the X-axis. An array of 64 receivers, spaced 0.5" apart, is centered on the X-axis. Only a one-dimensional reconstruction along a line at  $Z = 100$ " was generated in these tests since we were mainly interested in lateral resolution.

The first three tests, shown in Figures 5.19, 5.20, and 5.21, use a single pair of frequencies arranged so that  $\Delta f = 2.5$  kHz,  $\Delta f = 5$  kHz, and  $\Delta f = 10$  kHz, in that order. These figures reveal several phenomena. First, a rough measurement of the distance between the peaks reveal that they are separated by a distance proportional to the wavelength of the *difference* in frequencies,  $c/\Delta f$ , rather than the wavelength of either of the two frequencies actually used. Second, as the separation of the peaks becomes less, there are more false peaks. Third, the peaks become more narrow as the difference in frequencies  $\Delta f$  increases, even though the higher frequency (30 kHz) was the same in all cases.

A fourth phenomenon, which we shall call a "missed comparison," arises at either end of the curve for the largest  $\Delta f$ , in Figure 5.21. This phenomenon was first noted in Section 5.4.1 and is due to the fact that the frequency-shifted pattern has moved completely off the array, making it impossible to compare it to the unshifted pattern. So that we can distinguish this phenomenon from that of zero mismatch, the imaging program assigns a value of 0.01 or 1% of the maximum to the image when this problem occurs. These values thus appear as low-level plateaus. These missed comparisons are more likely to occur whenever (1) the value of  $\Delta f$  is large, and (2) the fictitious scatter is at a large angle relative to the Z-axis.

What we would like is to have the high precision which occurs when  $\Delta f$  is

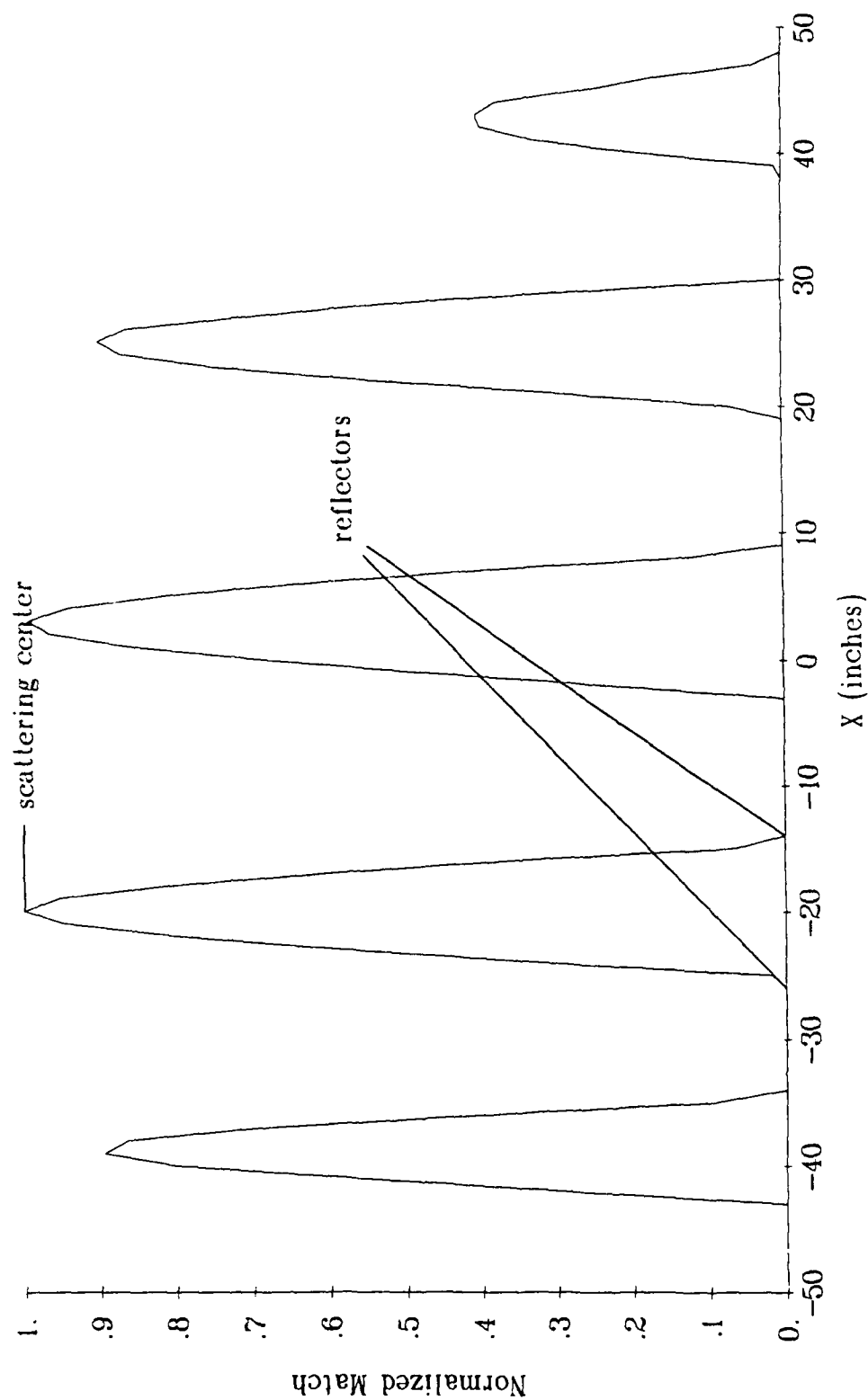


Figure 5.19. Swept-frequency reconstruction of 2 point reflectors at  $Z=100''$  using  $\Delta f=2.5$  kHz (27.5 and 30 kHz).

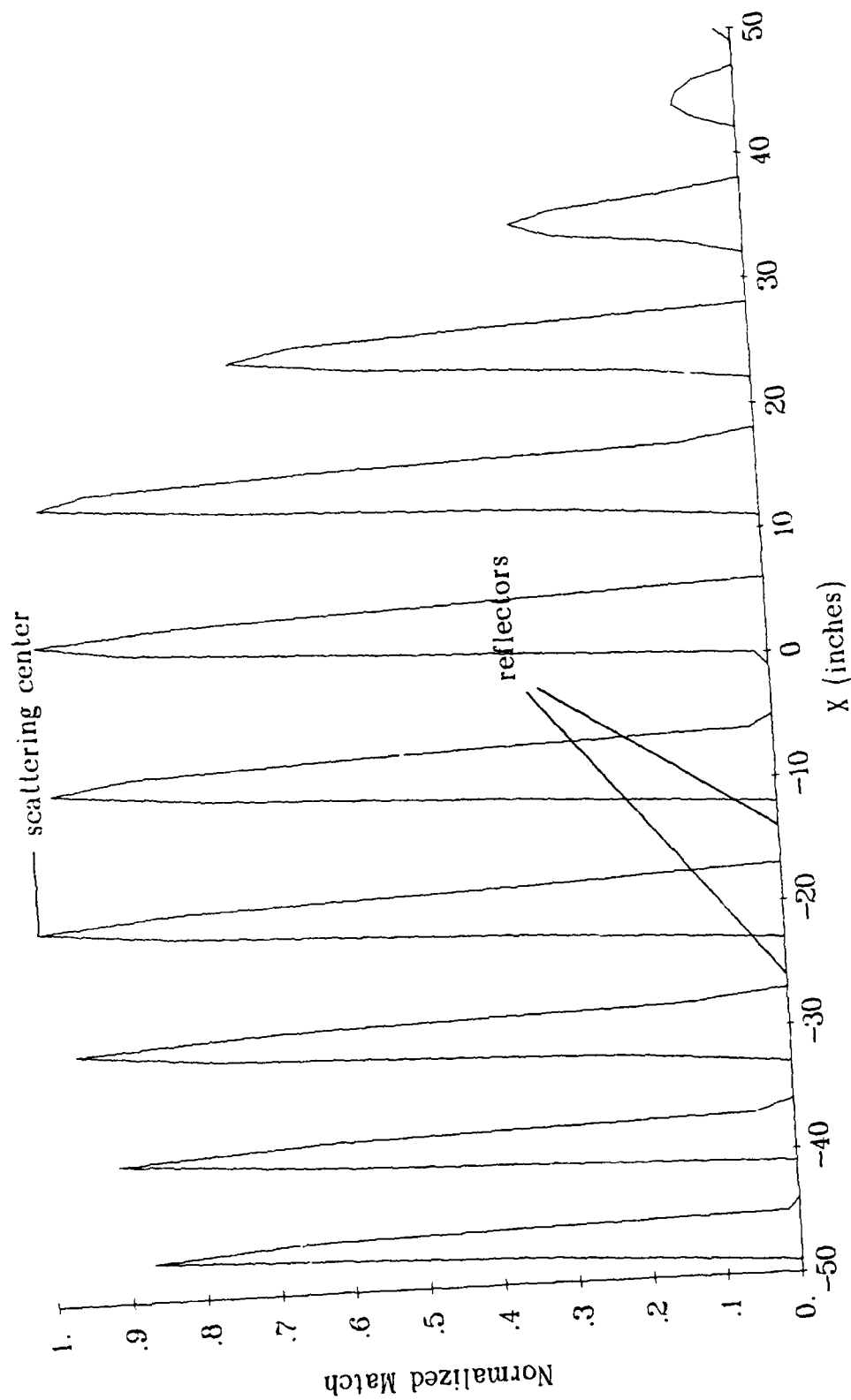


Figure 5.20. Swept-frequency reconstruction of 2 point reflectors at  $Z=100'$  using  $\Delta f=5$  kHz (25 and 30 kHz).

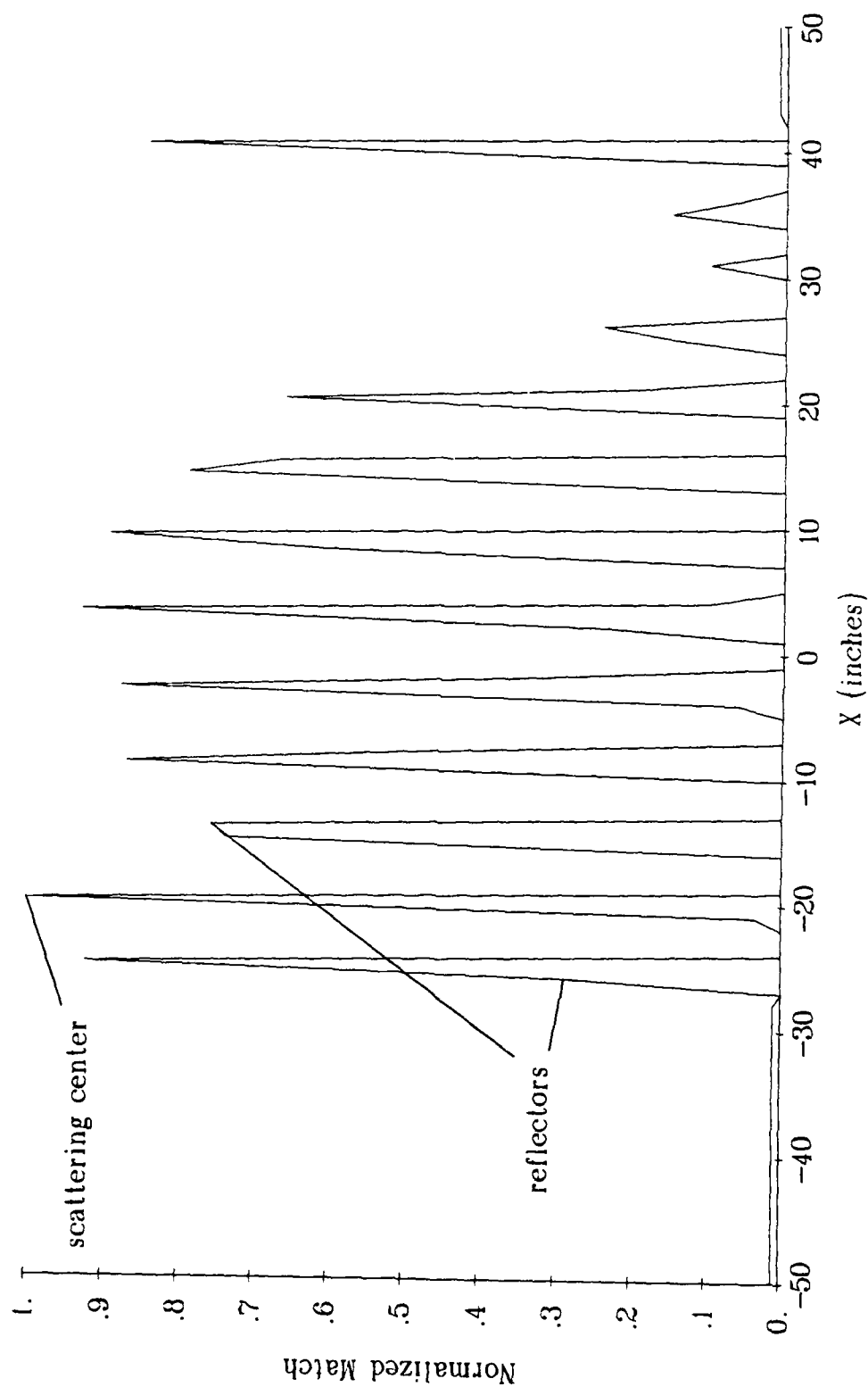


Figure 5.21. Swept-frequency reconstruction of 2 point reflectors at  $Z=100''$  using  $\Delta f=10$  kHz (20 and 30 kHz).

large with the lesser number of false peaks which occurs when  $\Delta f$  is small. One approach to this ideal would be to use a smaller  $\Delta f$ , but repeated. In Figure 5.22, 3 pairs of frequencies are used where  $\Delta f = 5$  kHz for each pair. The results are essentially the same as when a single pair of frequencies was used (Figure 5.20); thus, nothing has been gained.

One additional question which arose was whether the frequencies used could be lowered without sacrificing image resolution. The case shown in Figure 5.20 has been repeated for Figure 5.23, where  $\Delta f$  was kept at 5 kHz but the frequencies have been lowered from 25 kHz and 30 kHz to 10 kHz and 15 kHz. While the width of the peaks are essentially the same, the number of missed comparisons has grown considerably due to the fact that  $\Delta f$ , as a percentage of the frequencies, has increased.

The combinations of frequencies examined so far indicate that the false peaks can be reduced if a set of values for  $\Delta f$  are chosen where each is an irrational multiple of the others. One convenient method for the construction of such a set is to select frequencies with a logarithmic distribution, where each is compared to the highest. Such frequencies are given by

$$f_i = f_{min} + (f_{max} - f_{min}) \cdot \log_{10} \left( 1 + (i - 1) \frac{9}{N^F - 1} \right) \quad \text{for } i = 1, 2, \dots, N^F \quad (5.22)$$

where the minimum frequency  $f_{min}$ , maximum frequency  $f_{max}$ , and the number of frequencies  $N^F$  have been given. Such a set would then be used to make  $N^F - 1$  comparisons since we cannot compare  $f_{max}$  to itself.

A set of 20 frequencies, from 10 kHz to 30 kHz, was constructed and is



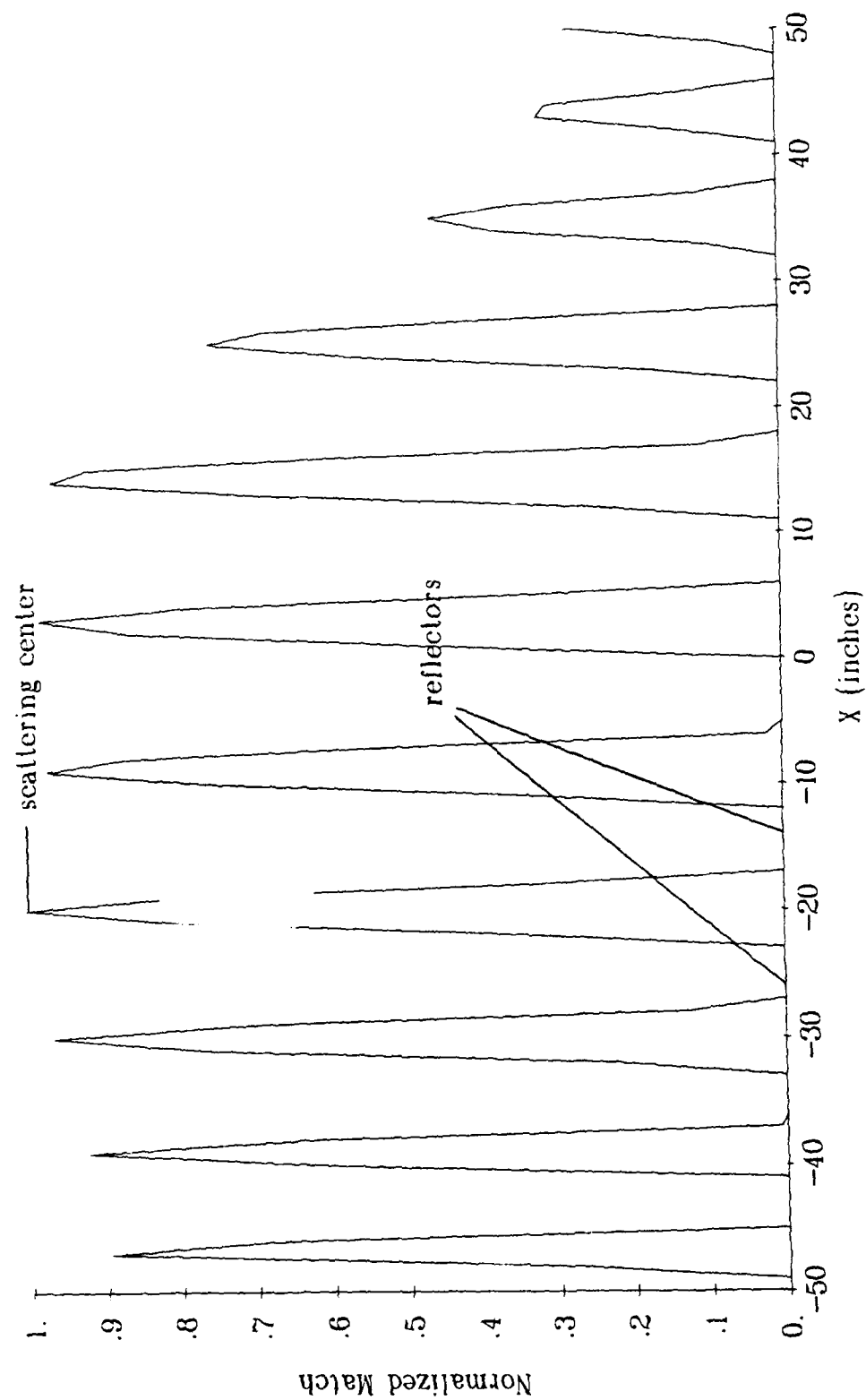


Figure 5.22. Swept-frequency reconstruction of 2 point reflectors at  $Z=100'$  using 3 pairs of frequencies having  $\Delta f=5$  kHz (15 and 20 kHz, 20 and 25 kHz, and 25 and 30 kHz).

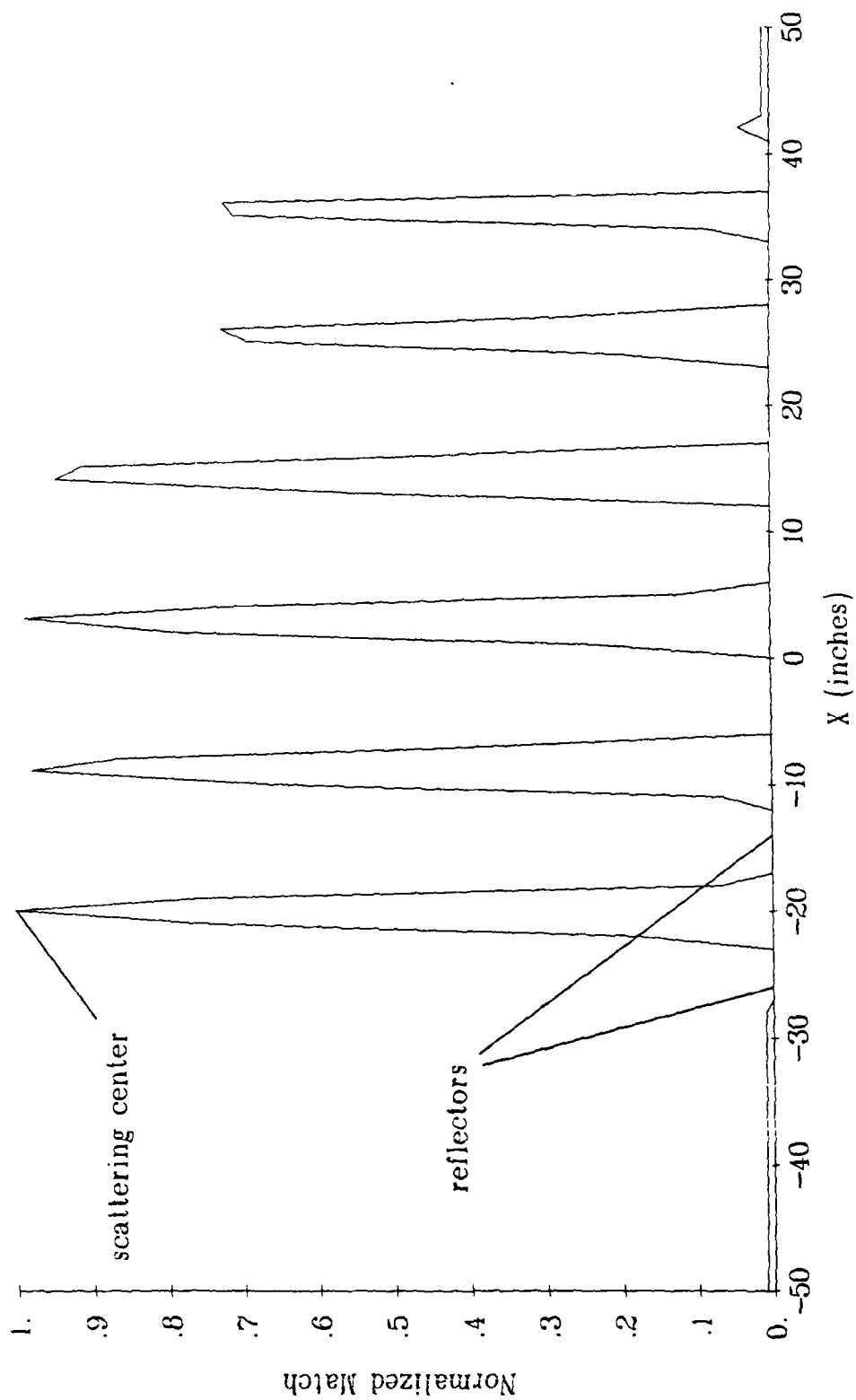


Figure 5.23. Swept-frequency reconstruction of 2 point reflectors at  $Z=100''$  using  $\Delta f=5$  kHz at relatively low frequencies (10 and 15 kHz).

shown in Table 5.4. A reconstruction using this set, shown in Figure 5.24, exhibits most of the characteristics we desire. Though the main peak is no longer as sharp as for the  $\Delta f = 10$  kHz case, the false peaks have been essentially eliminated. When the number of frequencies was increased or decreased, the results (not shown here) showed that the main peak was unchanged while the small false peaks decreased or increased, respectively, by a small amount. Therefore, all of the remaining swept-frequency simulations in this chapter use the set of frequencies shown in Table 5.4.

### 5.5 Locating Specular Scatterers

The ability of the swept-frequency method to locate specular scatterers has been explored through a series of simulations. In every case, a pair of point reflectors are used which are separated by 12" along a line parallel to the X-axis. Also, each simulation uses an array of 64 receivers separated by 0.5" which is centered on the X-axis, and the 20 frequencies listed in Table 5.4.

The following subsections examine the results when the scattering center (the point midway between the two point reflectors) is at different ranges; when it is at different lateral locations; when the scattering center and source have no offsets (i.e., they lie on the Z-axis); and when there are two sets of scatterers.

All contour plots will include lines at 10%, 20%, ..., 90% of the maximum, and will include a sketch of the receiver array (a line with a tic mark at each receiver) and source when possible. All hidden-surface plots will have data values below 0.005 (bad matches) erased, and values of 0.01 (missed comparisons) shown as plateaus.

Table 5.4. Logarithmic set of frequency comparisons.

Low Frequency (Hz)	High Frequency (Hz)	Difference (Hz)
10,000.00	30,000.00	20,000.00
13,368.09	30,000.00	16,631.91
15,788.96	30,000.00	14,211.04
17,680.08	30,000.00	12,319.92
19,232.18	30,000.00	10,767.82
20,548.53	30,000.00	9,451.47
21,691.39	30,000.00	8,308.61
22,701.21	30,000.00	7,298.79
23,605.76	30,000.00	6,394.24
24,424.93	30,000.00	5,575.07
25,173.46	30,000.00	4,826.54
25,862.57	30,000.00	4,137.43
26,501.00	30,000.00	3,499.00
27,095.71	30,000.00	2,904.29
27,652.29	30,000.00	2,347.71
28,175.34	30,000.00	1,824.66
28,688.68	30,000.00	1,311.32
29,135.50	30,000.00	864.50
29,578.50	30,000.00	421.50

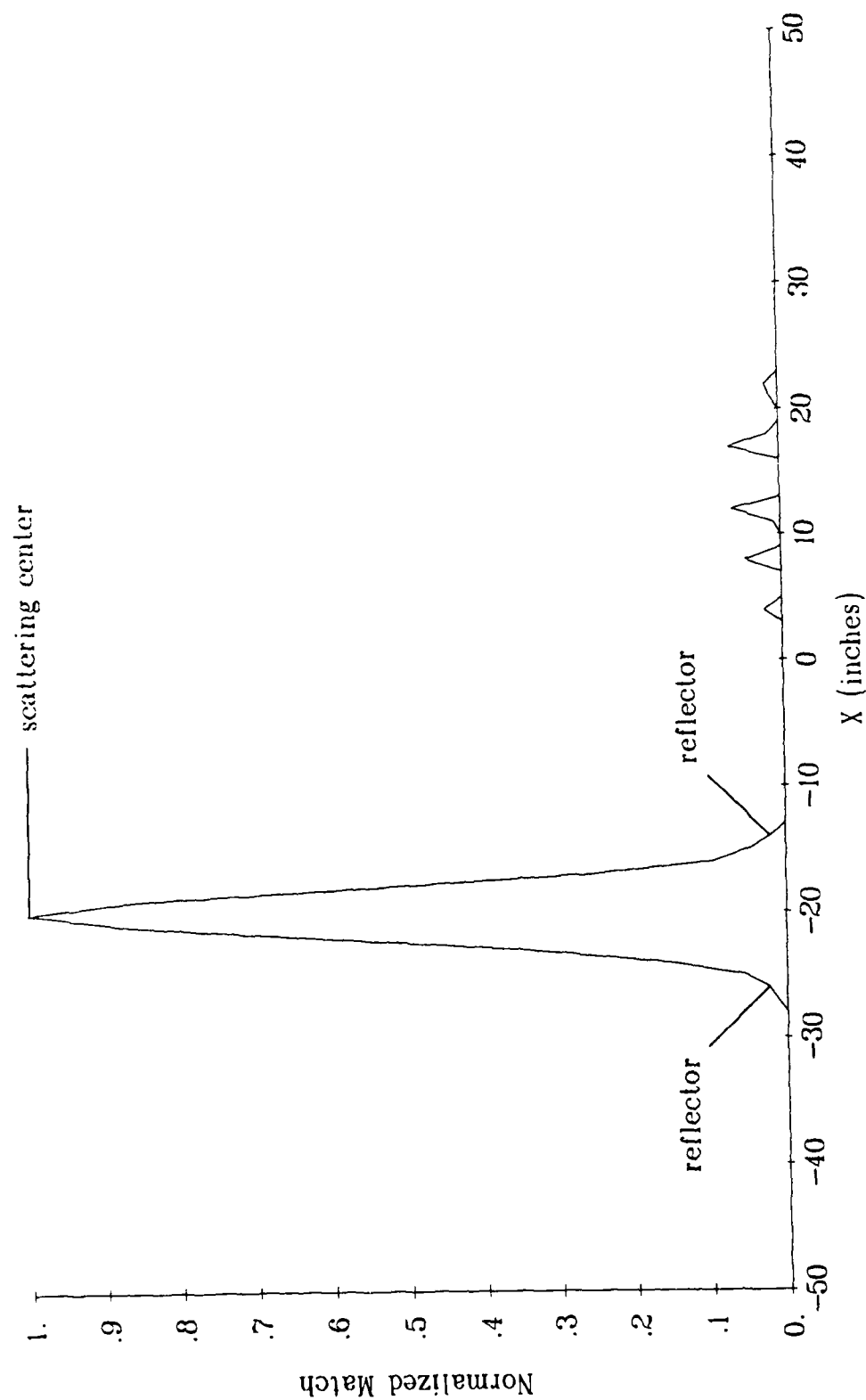


Figure 5.24. Swept-frequency reconstruction of 2 point reflectors at  $Z=100''$  using a logarithmic distribution of 20 frequencies (10 to 30 kHz) where the value of  $\Delta f$  is from 421.5 to 20,000 Hz.

### 5.5.1 Specular Results at Different Ranges

The simulations described in this section were selected to explore how the swept-frequency image of a pair of point reflectors varies with the range of the reflectors. In all of the simulations discussed in this section, the lateral location of the scattering center is  $X = -20''$ .

The reconstruction of a pair of reflectors whose scattering center is at  $(-20'', 25'')$  is shown in Figure 5.25. An expanded view of the results near the scattering center, shown in Figure 5.26, indicates that there is a small error in the location of the peak. Such an error might have been expected since, at such a small range, the farfield assumptions built into Eq. (5.18) would no longer be valid. Another view of this reconstruction, shown in Figure 5.27, exhibits the plateaus which were discussed earlier and which are areas of missed comparisons, i.e., where the frequency shift of the patterns from  $f(q)$  to  $\hat{f}(q)$  moved the patterns entirely off the end of the receiver array.

Figure 5.27 also shows several sharp spikes which will be called "sparse comparisons." Whereas a missed comparison occurs when the number of comparisons,  $N^C$ , has gone to zero, a sparse comparison occurs when  $N^C$  has gone to some small but non-zero value. Thus, even though the patterns may not line up at all, there are so few comparisons made that the amount of mismatch is very small, i.e., the amount of apparent match is very large. This phenomenon could be eliminated by treating cases where  $N^C$  is below some threshold as if they were cases of missed comparisons; however, this has not been done in the figures in this chapter so that the phenomenon can be observed.

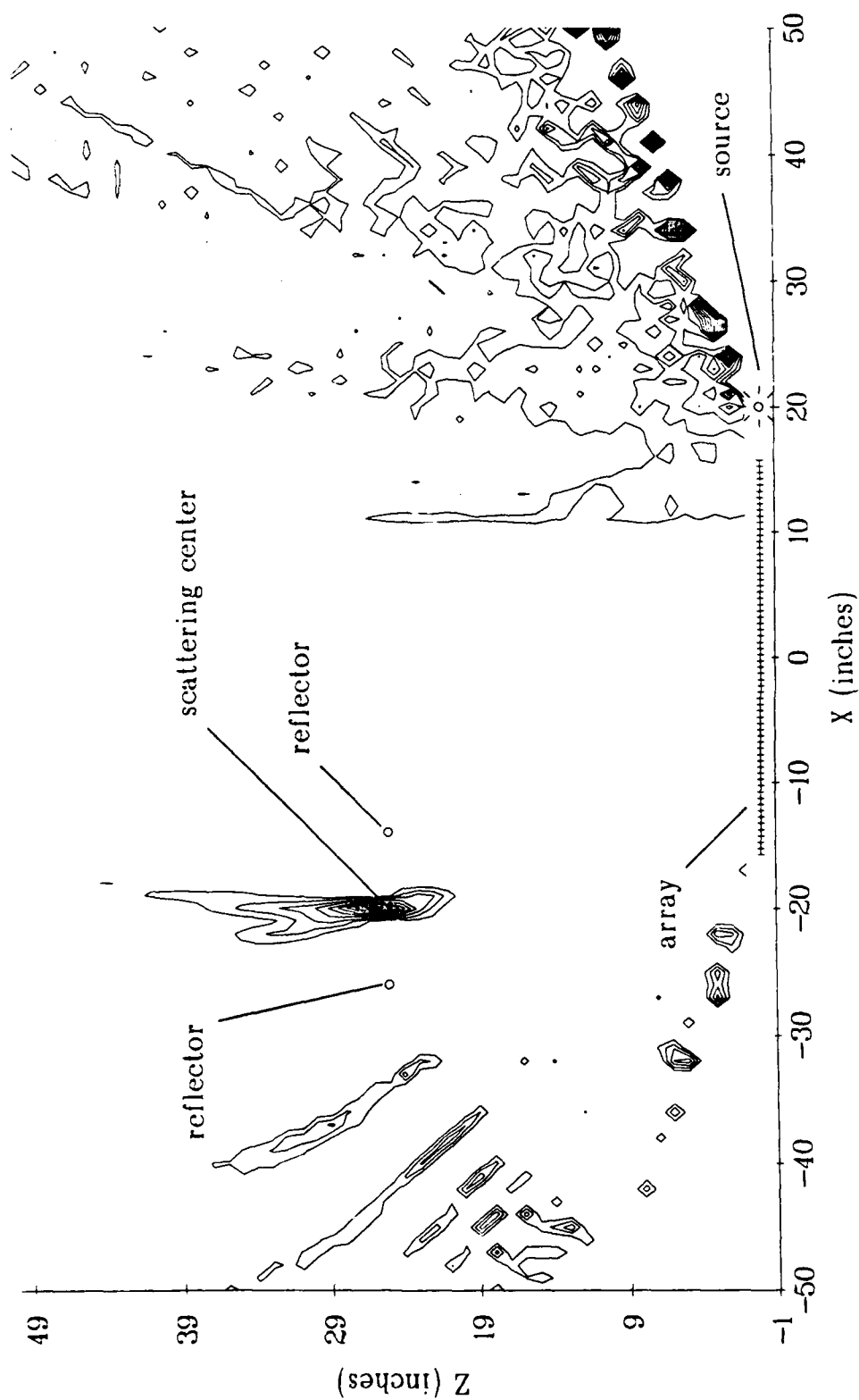


Figure 5.25. Swept-frequency reconstruction of 2 point reflectors centered at  $(-20'', 25'')$  with a source at  $(20'', 0)$ .

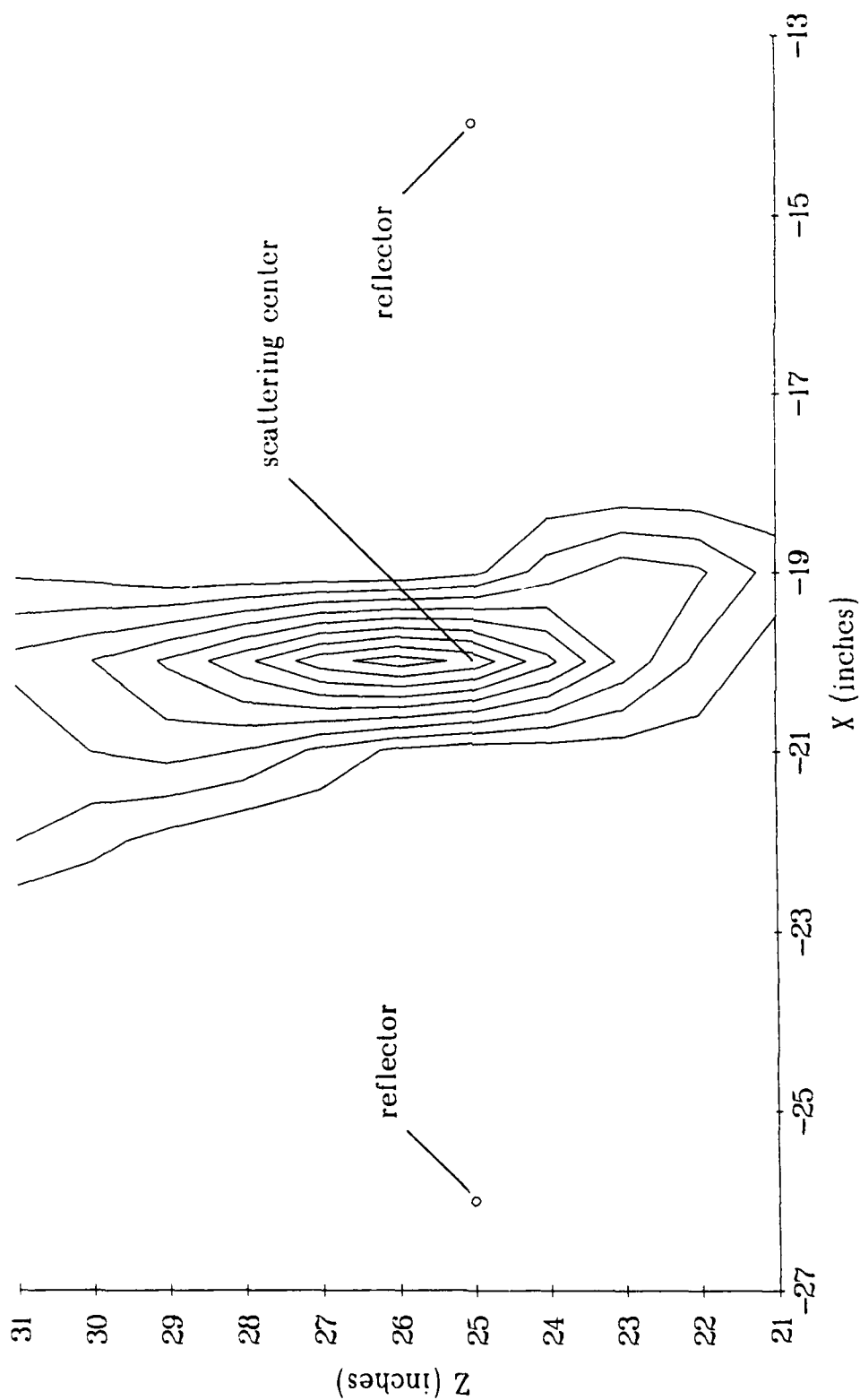


Figure 5.26. Swept-frequency reconstruction of 2 point reflectors centered at  $(-20'', 25'')$  with a source at  $(20'', 0)$ , showing a small amount of error in the location of the maximum.



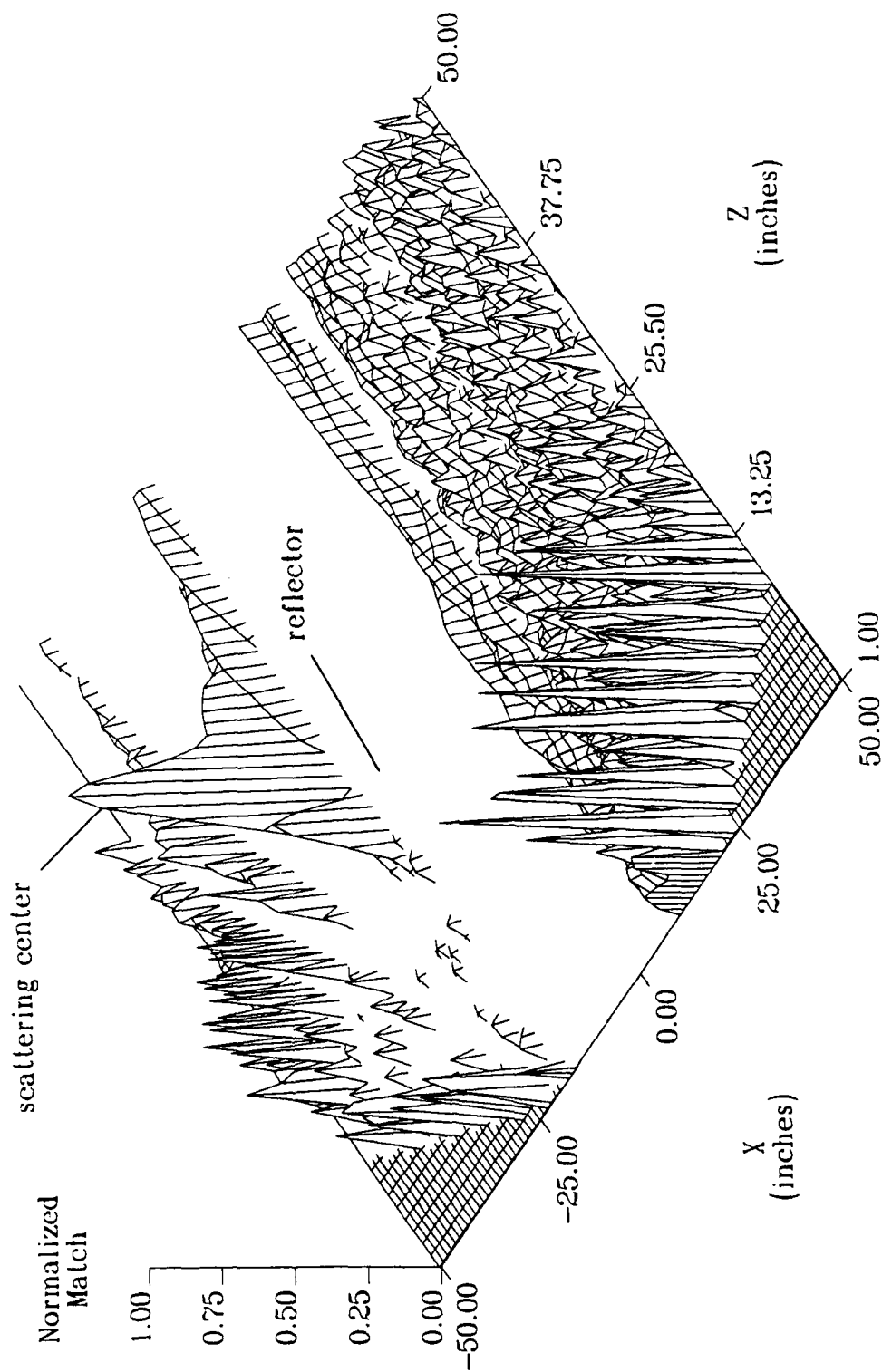


Figure 5.27. Swept-frequency reconstruction of 2 point reflectors centered at  $(-20'', 25'')$  with a source at  $(20'', 0)$ , showing sparse comparisons (spikes) and missed comparisons (plateaus).

In Figure 5.28, we have doubled the range so that the scattering center is now at  $(-20'', 50'')$ . While the error in the location of the peak has been reduced, the spread of the peak has increased — that is, the resolution has been decreased. This is even more apparent in Figure 5.29, where we also see that the range resolution has become much poorer.

When the range is again doubled to  $Z = 100''$ , the range resolution disappears. Figure 5.30 shows that the lateral resolution has also become poorer. However, if the lateral resolution were to remain the same as the range went to infinity (as might be suggested by Figure 5.30), we would have a remarkable imaging method. However, as is shown in Figure 5.31 for a range of  $Z = 400''$ , this is not the case — the lateral resolution also decreases with range, as for most other imaging methods. That is, while the lateral resolution remains the same as the range of the fictitious source increases, it gets poorer as the range of the true source increases.

### 5.5.2 Specular Results at Different Bearings

The simulations described in this section were selected to explore how the swept-frequency image of a pair of point reflectors varies with the lateral location of the reflectors. In all of the simulations discussed in this section, the range of the scattering center is  $Z = 50''$ .

We begin by reviewing Figures 5.28 and 5.29 from the previous section, where the lateral location of the scattering center was  $X = -20''$  and a certain amount of range resolution was exhibited. Next, we move the scattering center to  $X = 0$ . The results, shown in Figure 5.32, reveal that all range resolution has

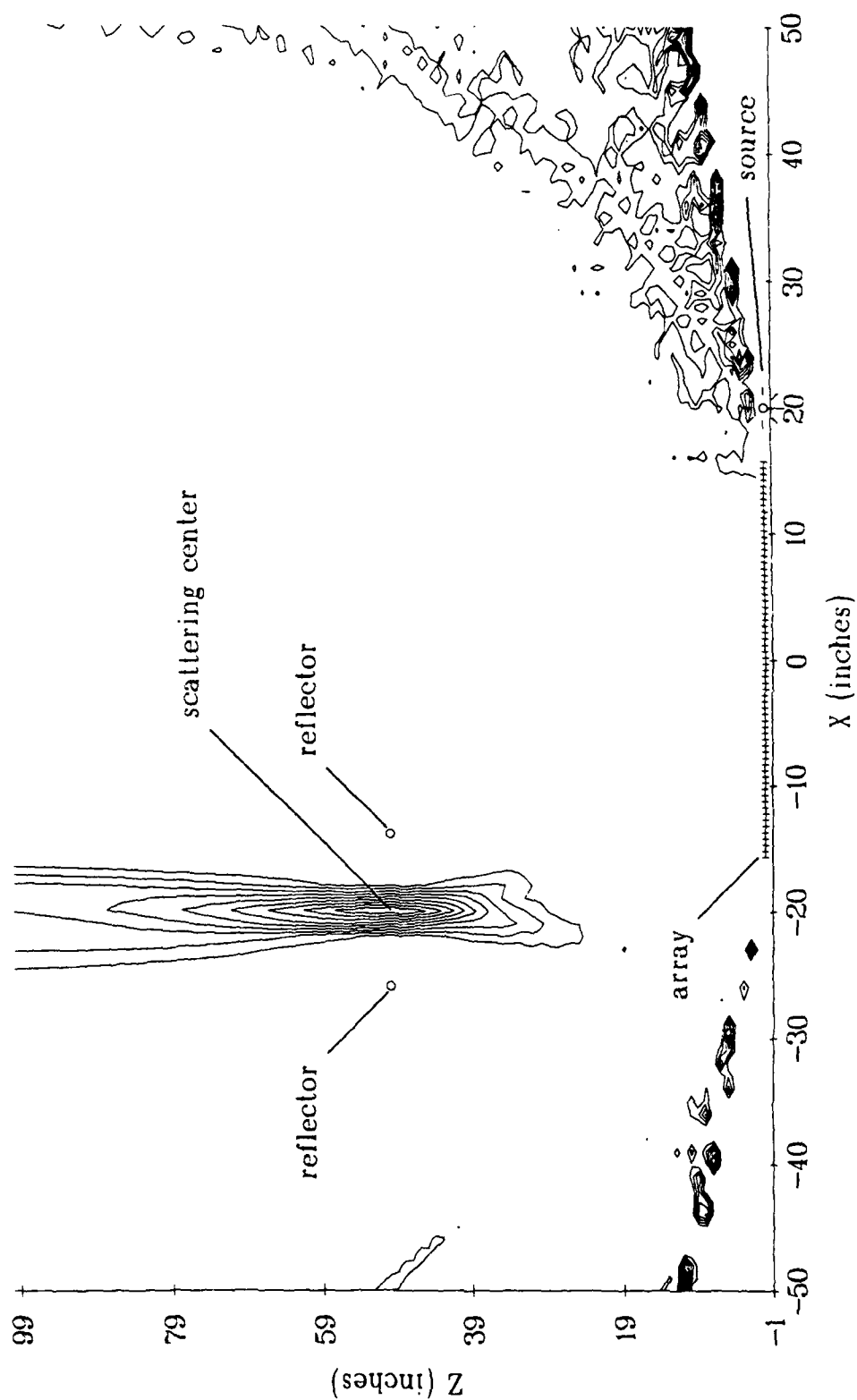


Figure 5.28. Swept-frequency reconstruction of 2 point reflectors centered at  $(-20'', 50'')$  with a source at  $(20'', 0)$ .

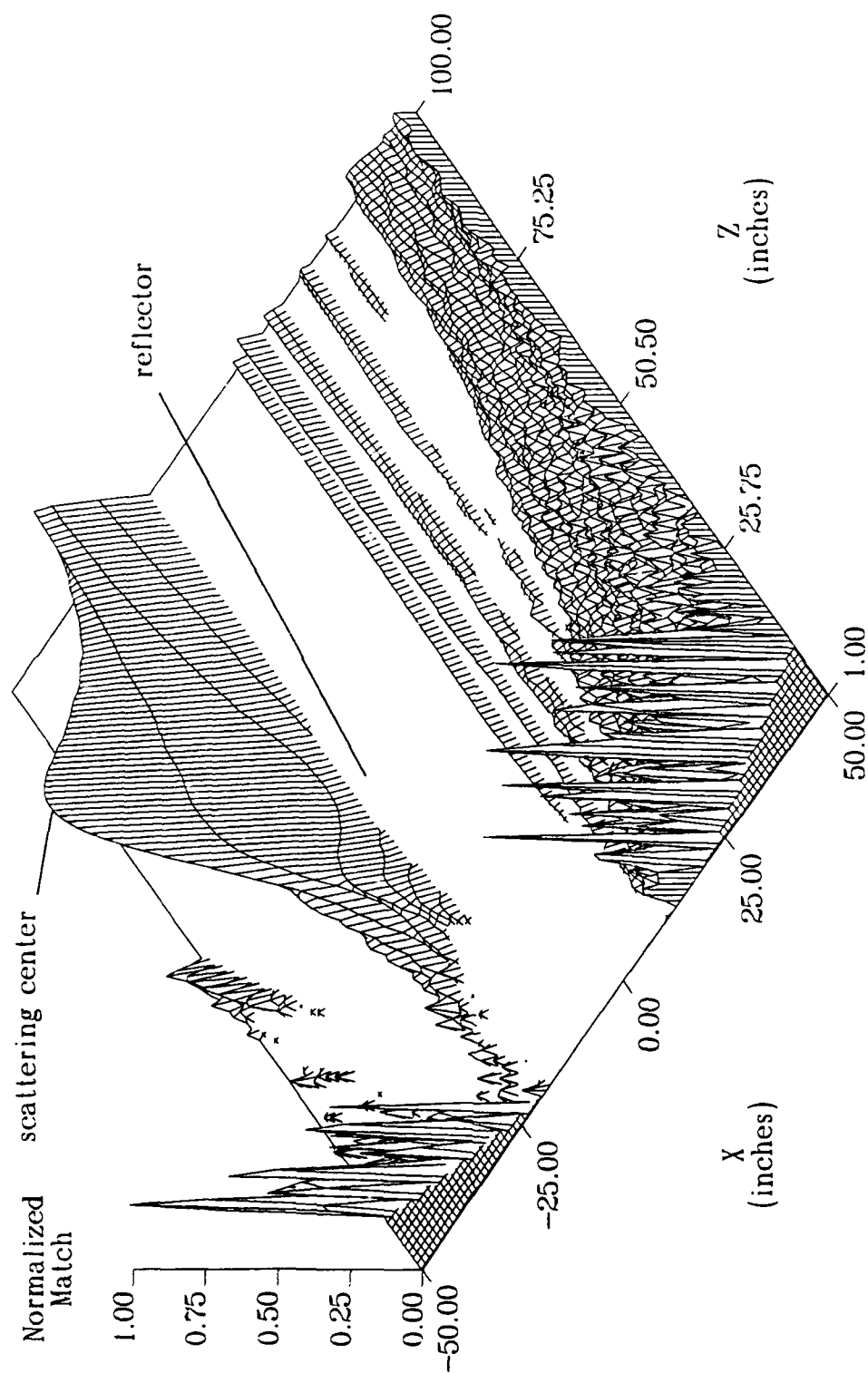


Figure 5.29. Swept-frequency reconstruction of 2 point reflectors centered at  $(-20'', 50'')$  with a source at  $(20'', 0)$ , showing sparse comparisons (spikes) and missed comparisons (plateaus).

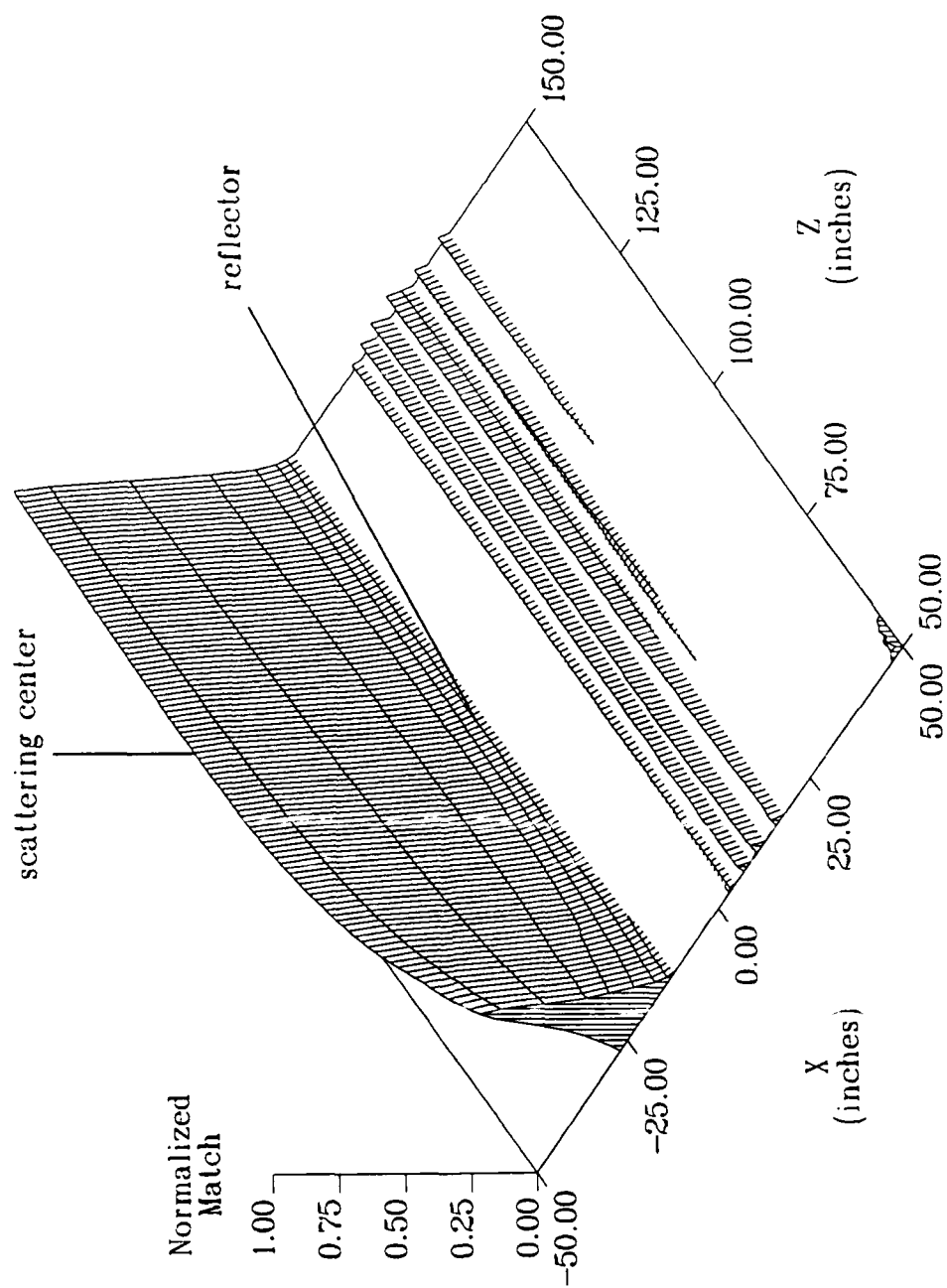


Figure 5.30. Swept-frequency reconstruction of 2 point reflectors centered at  $(-20'', 100'')$  with a source at  $(20'', 0)$ .

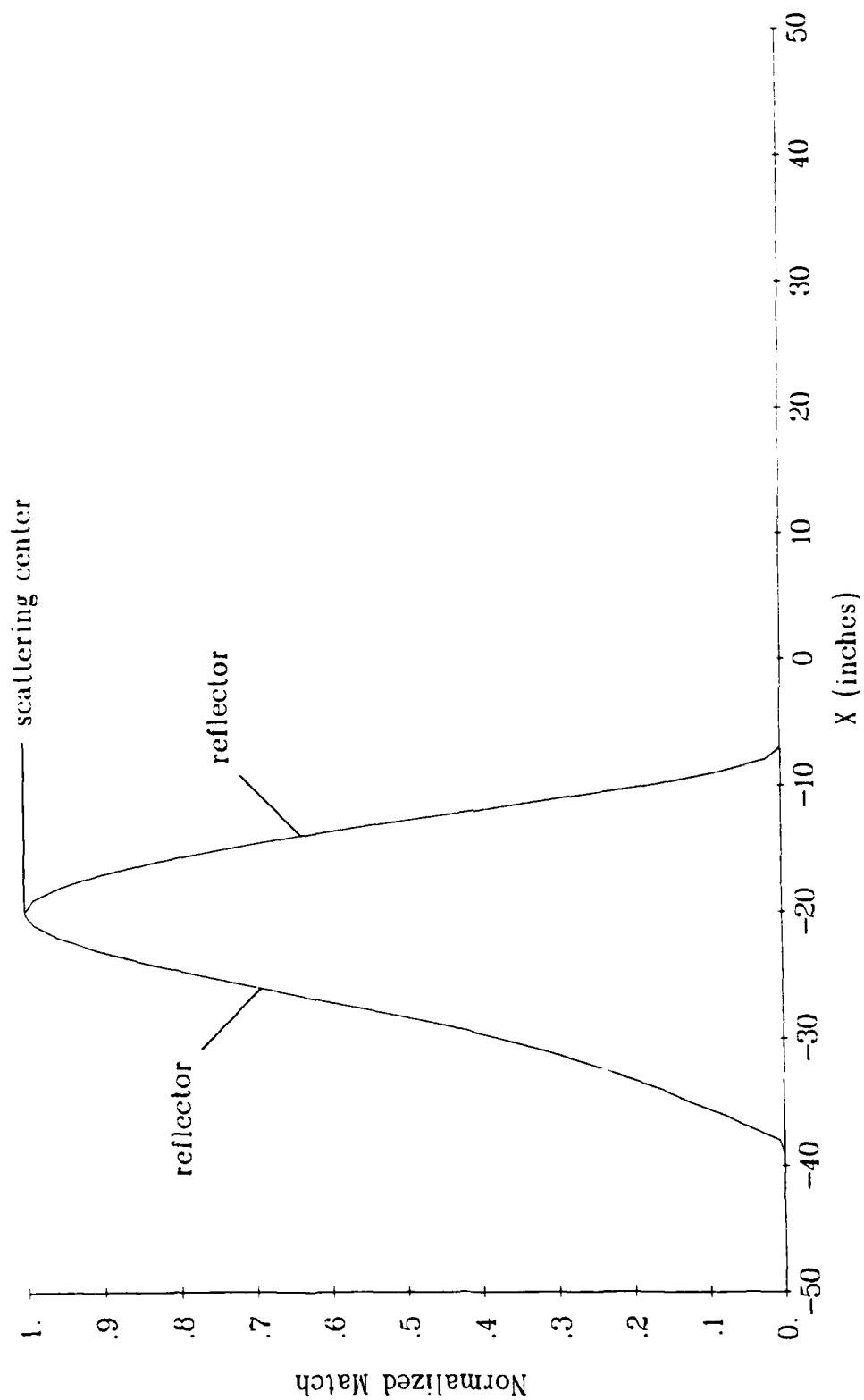


Figure 5.31. Swept-frequency reconstruction at  $Z=400''$  of 2 point reflectors centered at  $(-20'', 400'')$  with a source at  $(20'', 0)$ .

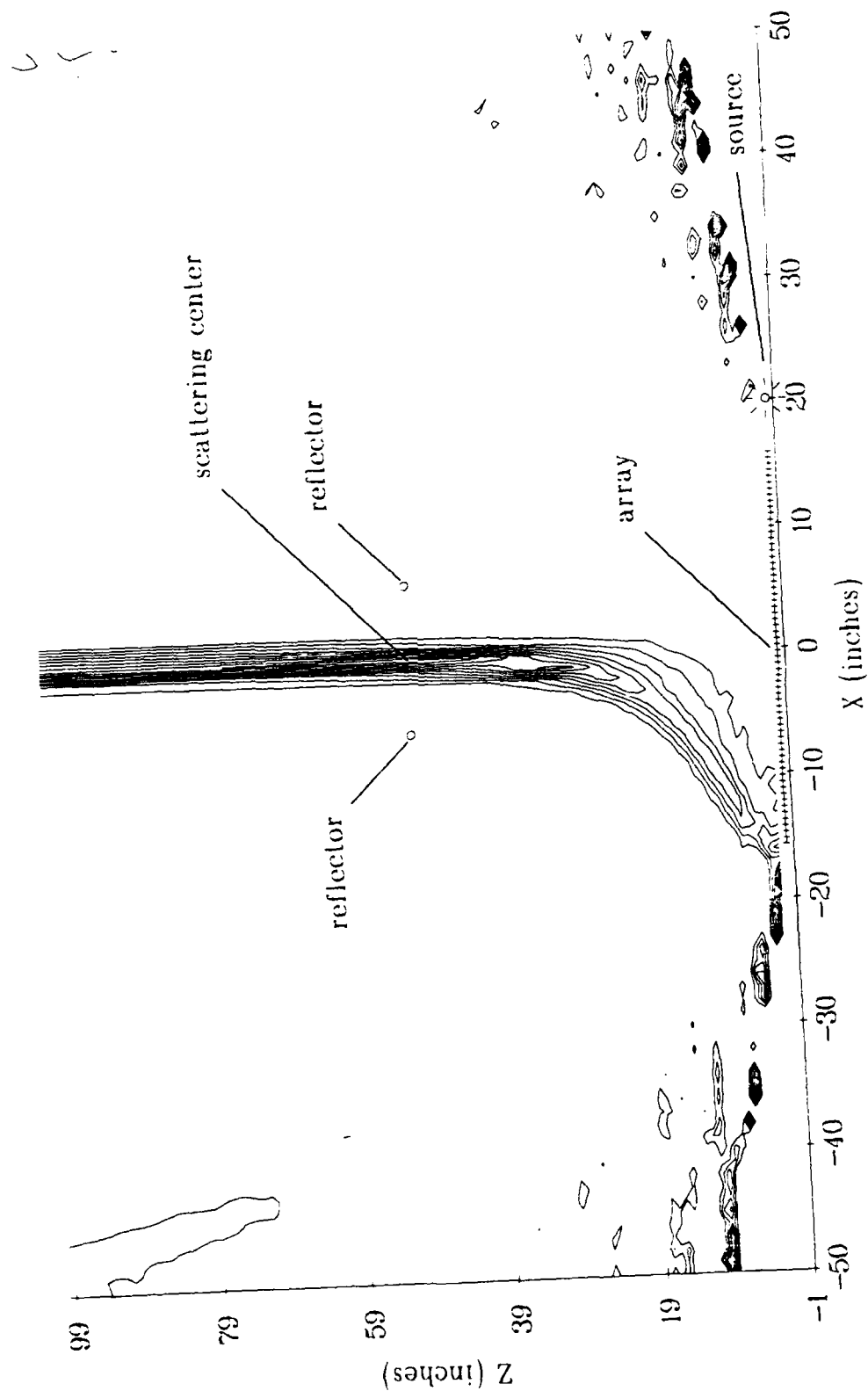


Figure 5.32. Swept-frequency reconstruction of 2 point reflectors centered at  $(0, 50'')$  with a source at  $(20'', 0)$ .

been lost, and that the region where a good match was found makes a strange curve where  $Z < 39''$ . Figure 5.33 shows that the missed and sparse comparisons are also still present, and that the match has a very minor maximum at the true scattering center.

When the scattering center is again moved laterally, to  $X = 20''$ , Figures 5.34 and 5.35 shown that the results are quite similar to the complementary case where the scattering center was at  $X = -20''$  (see Figures 5.28 and 5.29).

### 5.5.3 Specular Results with No Offsets

A single simulation is used in this section to examine how the the swept-frequency method reacts to the case where there are no offsets in the location of the source and scattering center — that is, they all lie on the normal to the receiving array. The results of this simulation, shown in Figures 5.36 and 5.37, indicate that the swept-frequency method has great difficulty in determining the range of the scattering center in this situation.

The result shown in Figures 5.36 and 5.37 might have been expected since the frequency-dependent shift of the patterns can be shown to be about the same, as the range of the fictitious source changes. What was not expected was the equally poor result, seen in the previous section in Figures 5.32 and 5.33, when the source was to the side, at  $Z = 20''$ .

### 5.5.4 Results Using Two Sets of Specular Scatterers

A single simulation is used in this section to examine how the swept-frequency method reacts to the case where there are two pairs of reflectors. The



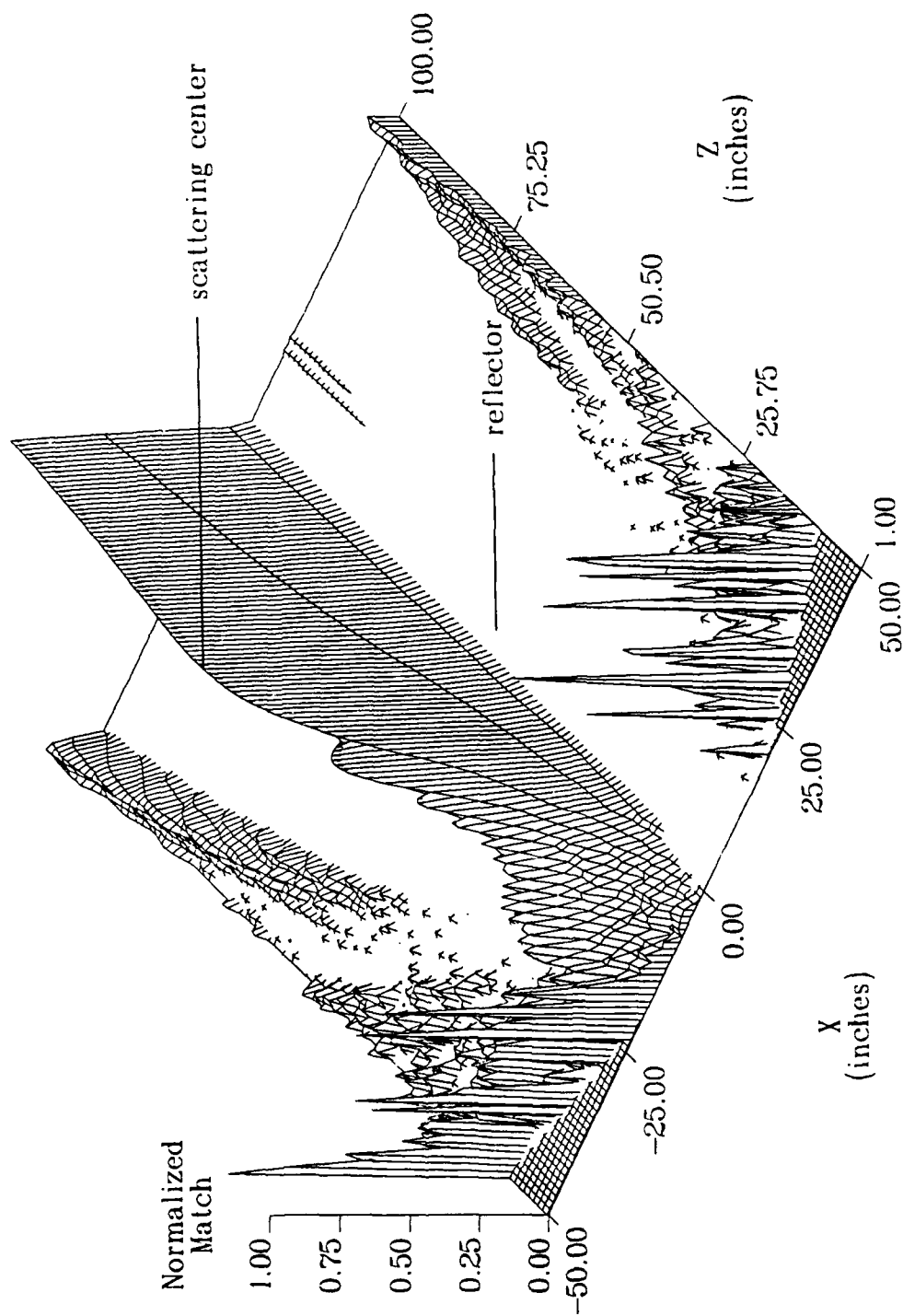


Figure 5.33. Swept-frequency reconstruction of 2 point reflectors centered at  $(0, 50')$  with a source at  $(20', 0)$ , showing sparse comparisons (spikes) and missed comparisons (plateaus).

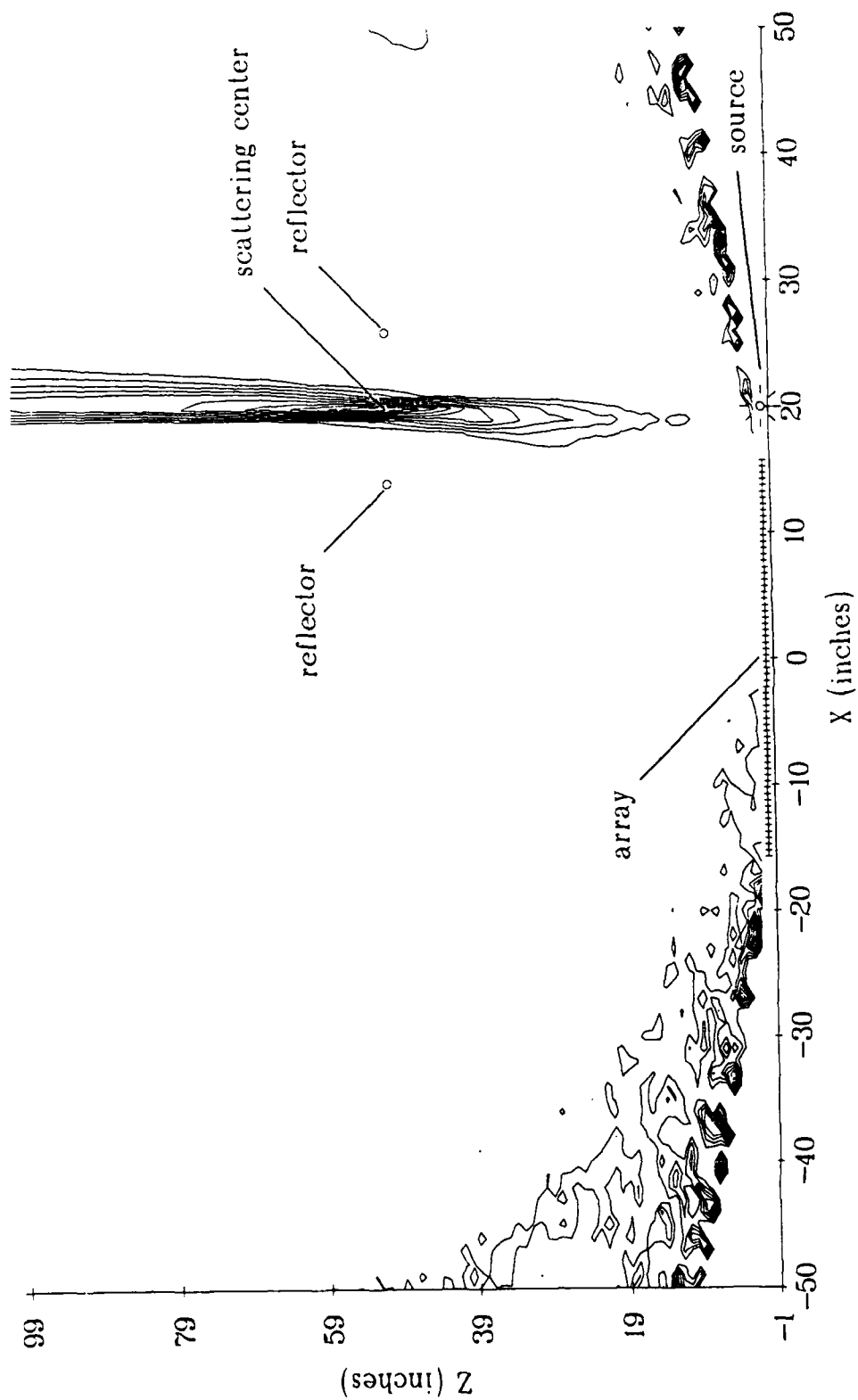


Figure 5.34. Swept-frequency reconstruction of 2 point reflectors centered at  $(20'', 50'')$  with a source at  $(20'', 0)$ .

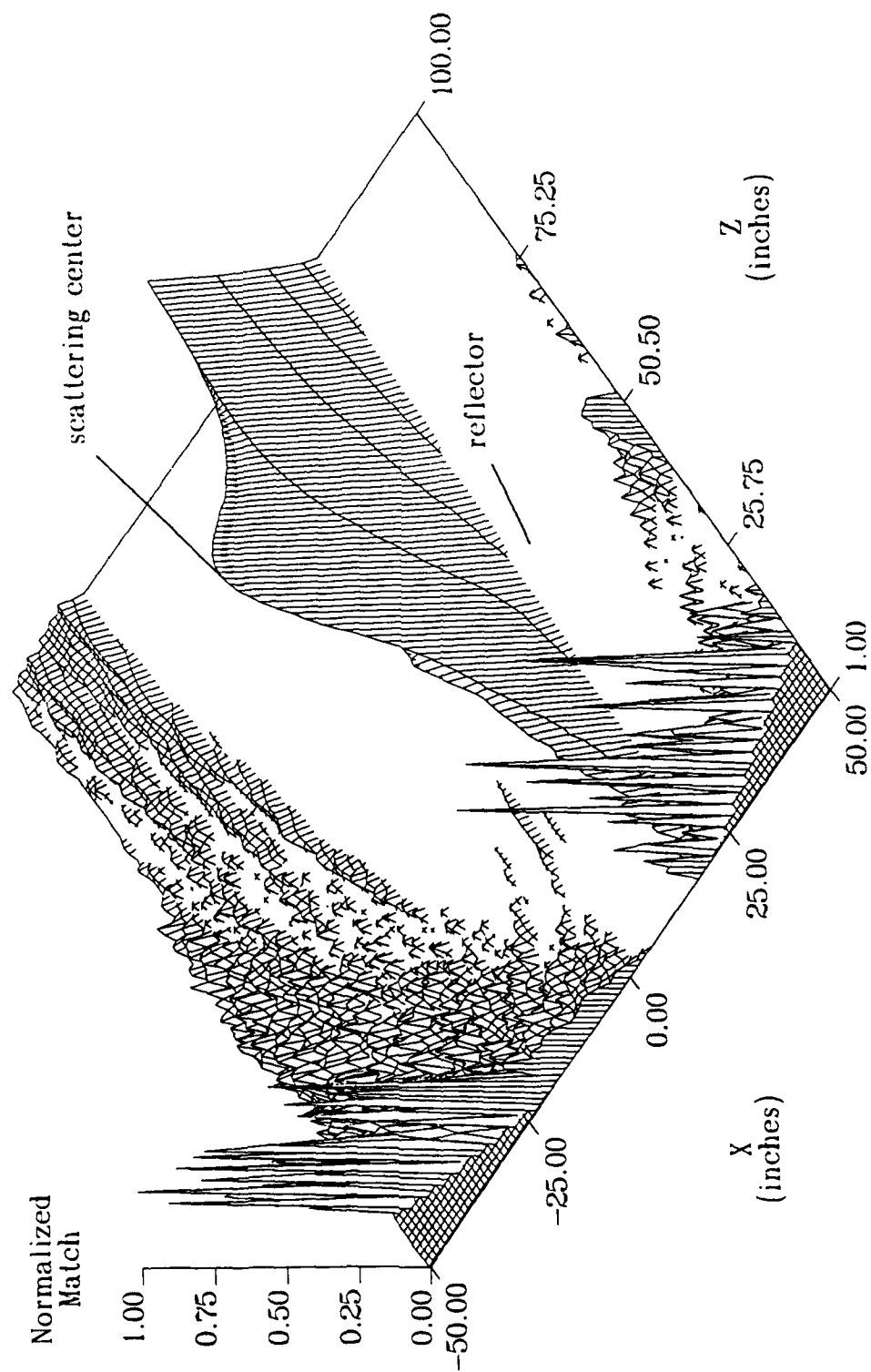


Figure 5.35. Swept-frequency reconstruction of 2 point reflectors centered at (20",50") with a source at (20",0), showing sparse comparisons (spikes) and missed comparisons (plateaus).

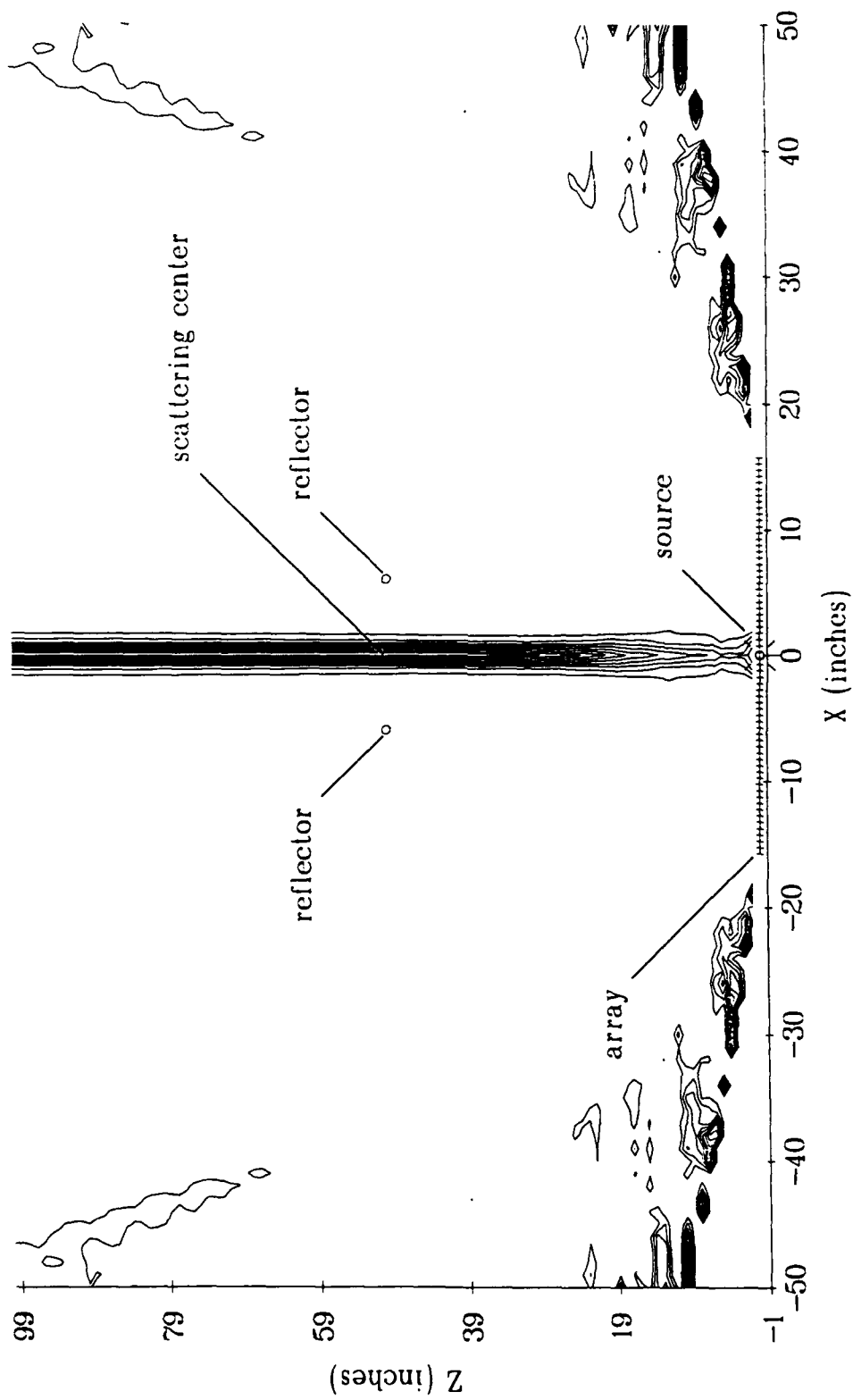


Figure 5.36. Swept-frequency reconstruction of 2 point reflectors centered at  $(0,50'')$  with a source at  $(0,0)$ .

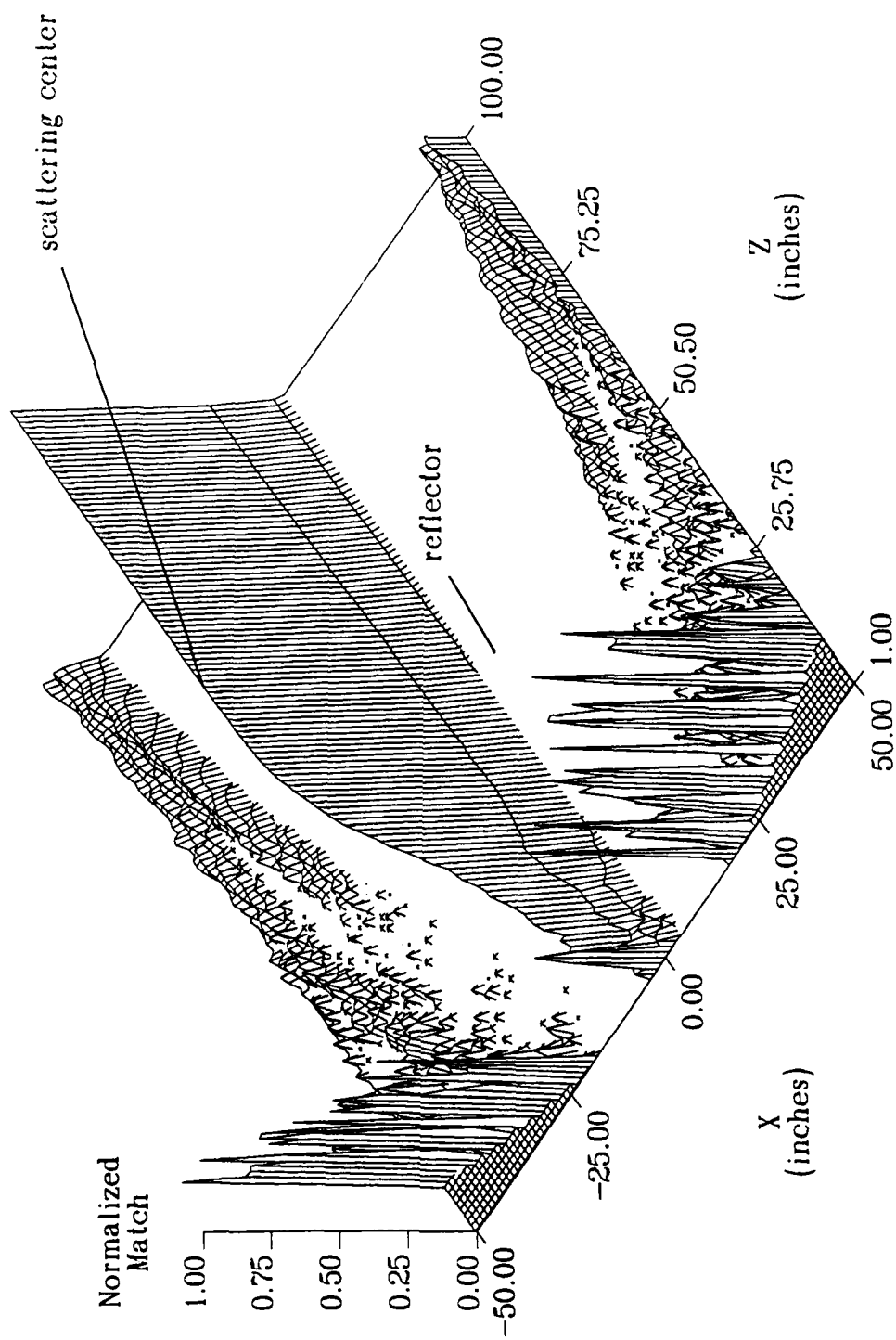


Figure 5.37. Swept-frequency reconstruction of 2 point reflectors centered at (0,50') with a source at (0,0), showing sparse comparisons (spikes) and missed comparisons (plateaus).

results shown in Figure 5.38 indicate where the reflectors have been located. In this figure, we have shown only that portion of the reconstructed field near the reflectors and have, in addition, renormalized the data to the maximum within this portion.

The entire reconstructed field is shown in Figure 5.39. Here, the size of the sparse-comparison spikes is so much greater than that of the peaks around the scattering centers that the latter have been made quite small by normalization.

A hidden-surface plot of that portion of the reconstructed field near the reflectors is shown in Figure 5.40, with the data again renormalized to the maximum within the portion shown. This figure indicates that the 4 reflectors have formed multiple scattering centers, among the various pairs of reflectors, with the peak near  $X = -10''$  perhaps representing the sum of 2 scattering centers where one is due to the inner pair of reflectors and one is due to the outer pair.

## 5.6 Locating Extended Scatterers

The simulations performed in Section 5.5 are now exactly repeated except that the two point reflectors are replaced with a plate reflector which is 12" wide and which is simulated using a summation of 200 terms. The logarithmic distribution of frequencies given in Table 5.4 is used in each case.

### 5.6.1 Plate Results at Different Ranges

The simulations described in this section were selected to explore how the swept-frequency image of a plate reflector varies with the range of the reflector. In all of the simulations discussed in this section, the lateral location of the center

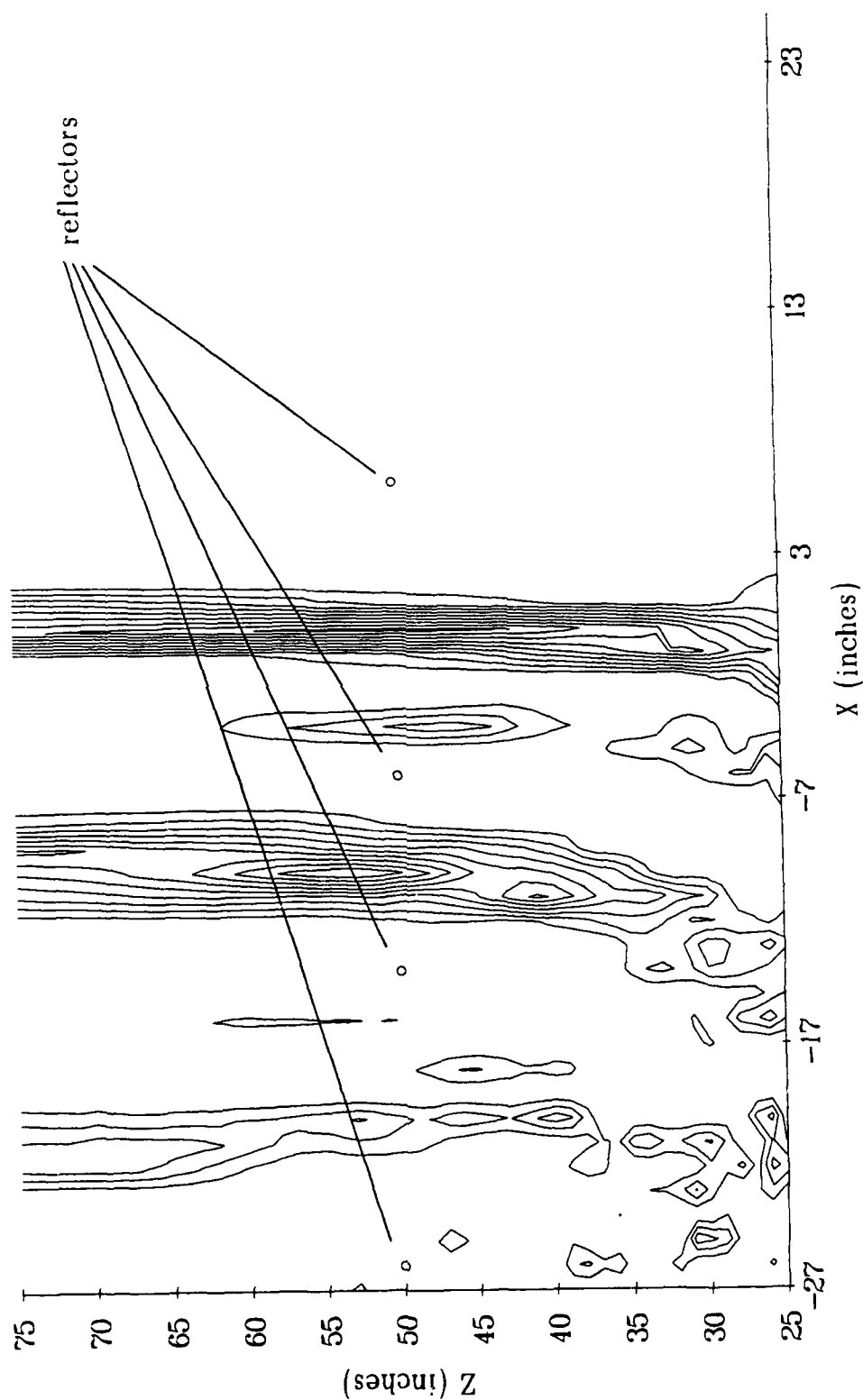


Figure 5.38. Swept-frequency reconstruction of 4 point reflectors at  $Z=50''$  and  $X=-26''$ ,  $X=-14''$ ,  $X=-6''$  and  $X=6''$  with a source at  $(20'', 0)$ .

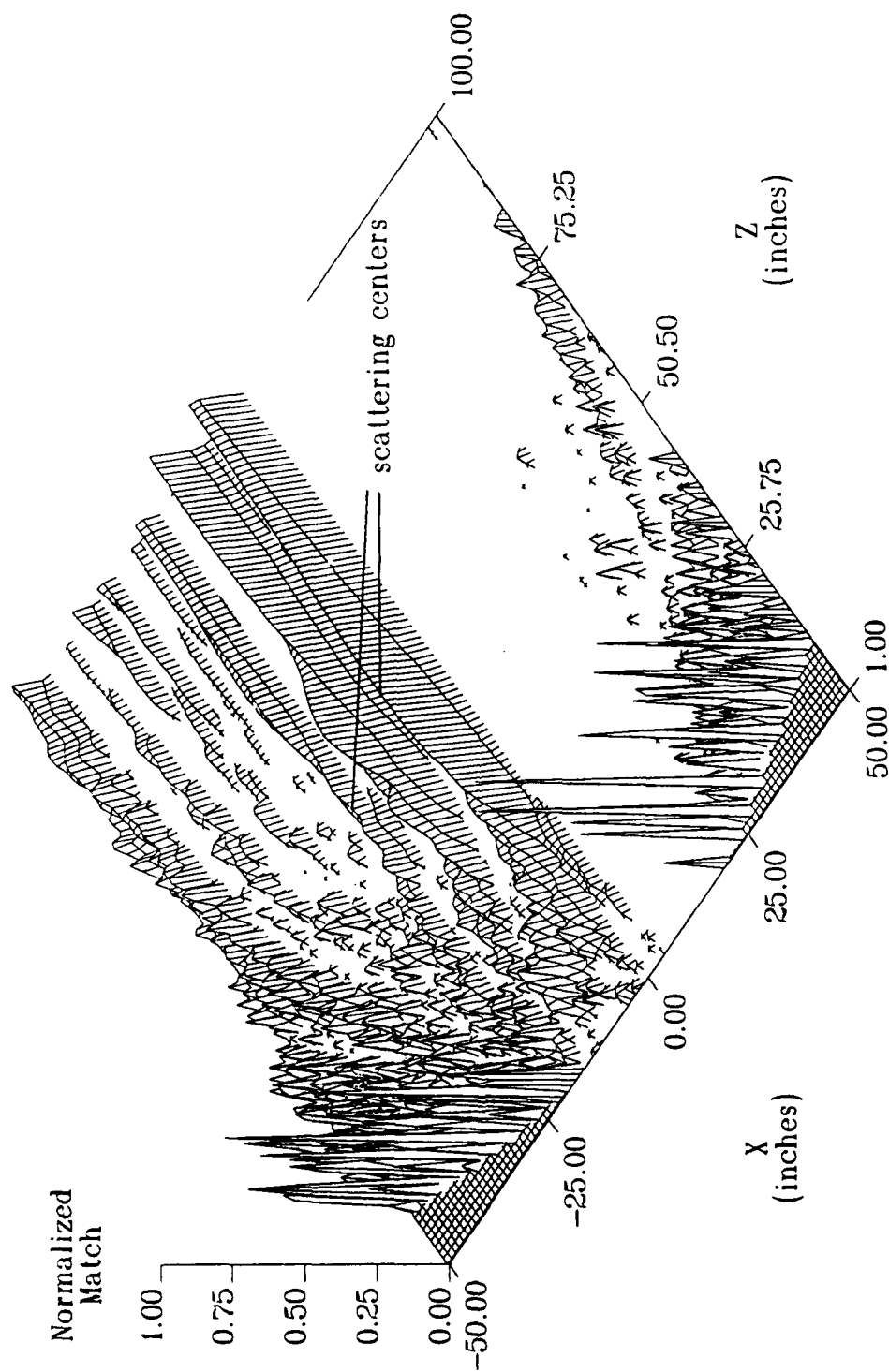


Figure 5.39. Swept-frequency reconstruction of 4 point reflectors at  $Z=50''$  and  $X=-26''$ ,  $X=-14''$ ,  $X=-6''$  and  $X=6''$  with a source at  $(20'', 0)$ ; also showing sparse and missed comparisons.



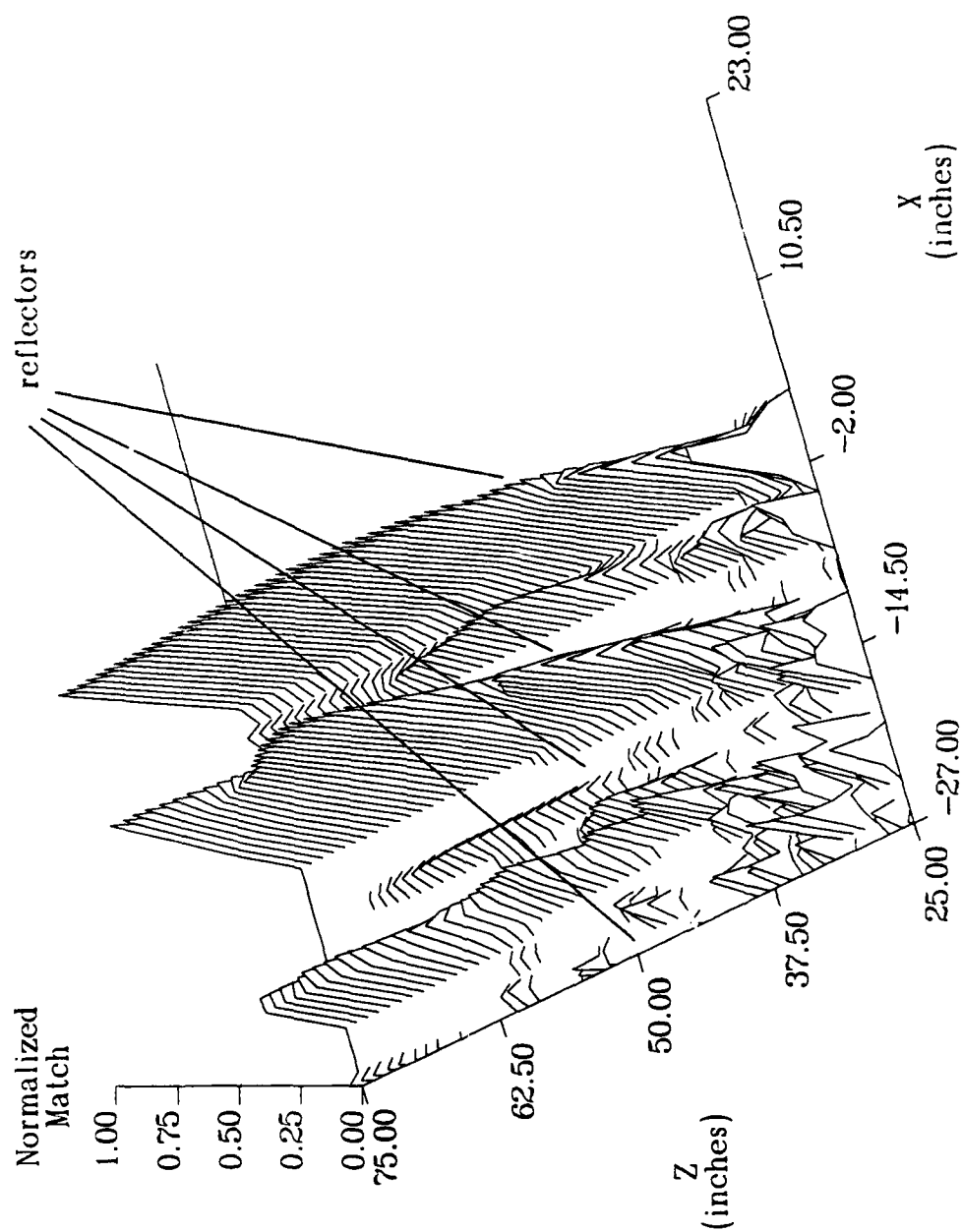


Figure 5.40. Swept-frequency reconstruction of 4 point reflectors at  $Z=50''$  and  $X=-26''$ ,  $X=-14''$ ,  $X=-6''$  and  $X=6''$  with a source at  $(20'', 0)$ . Match has been renormalized to maximum value in plot.

of the plate is  $X = -20''$ .

The reconstruction of a plate whose center is at  $(-20'', 25'')$  is shown in Figure 5.41 and exhibits the same small error in the location of the peak as was seen in the case of the point reflectors. It is interesting to also note that the range ambiguity extends along a line which is parallel to the Z-axis, rather than along a line running radially from the center of the receiver array. A hidden-surface plot of this same information, Figure 5.42, has a region showing a good match along the line at  $Z = 1''$ , between  $X = 0$  and  $X = 17''$ . It is not clear whether these are merely a large number of closely spaced sparse-comparison spikes or some other phenomenon. For example, it is shown in the next section that such regions can occur when the array is within the *actual* source's central lobe — an equivalent phenomenon may be occurring with the *fictitious* source in Figure 5.42.

In Figures 5.43 and 5.44, the range has been doubled to  $Z = 50''$ ; as expected, the range resolution has become poorer while the small error in the main peak has been eliminated. When the range is again doubled, to  $Z = 100''$ , all range resolution is lost as is seen in Figure 5.45.

### 5.6.2 Plate Results at Different Bearings

The simulations described in this section were selected to explore how the swept-frequency image of a plate varies with the lateral location of the plate. In all of the simulations discussed in this section, the range of the plate is  $Z = 50''$ .

We can consider the series discussed in this section as beginning with Figures 5.43 and 5.44, of the previous section, as they are for a plate centered at  $(-20'', 50'')$ . When the plate is then moved laterally, to  $X = 0$ , Figures 5.46 and

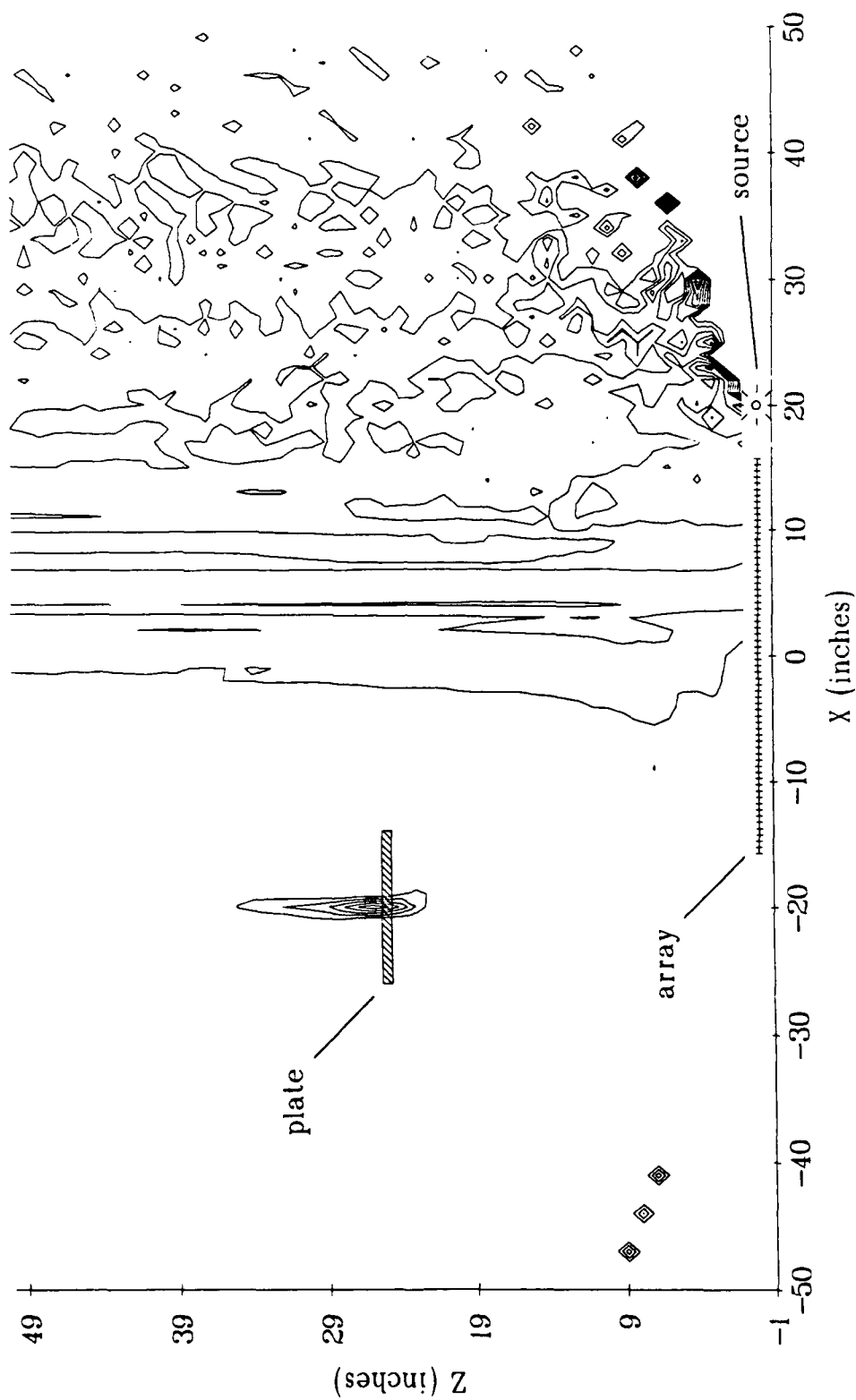


Figure 5.41. Swept-frequency reconstruction of a 12" plate centered at  $(-20'', 25'')$  with a source at  $(20'', 0)$ .

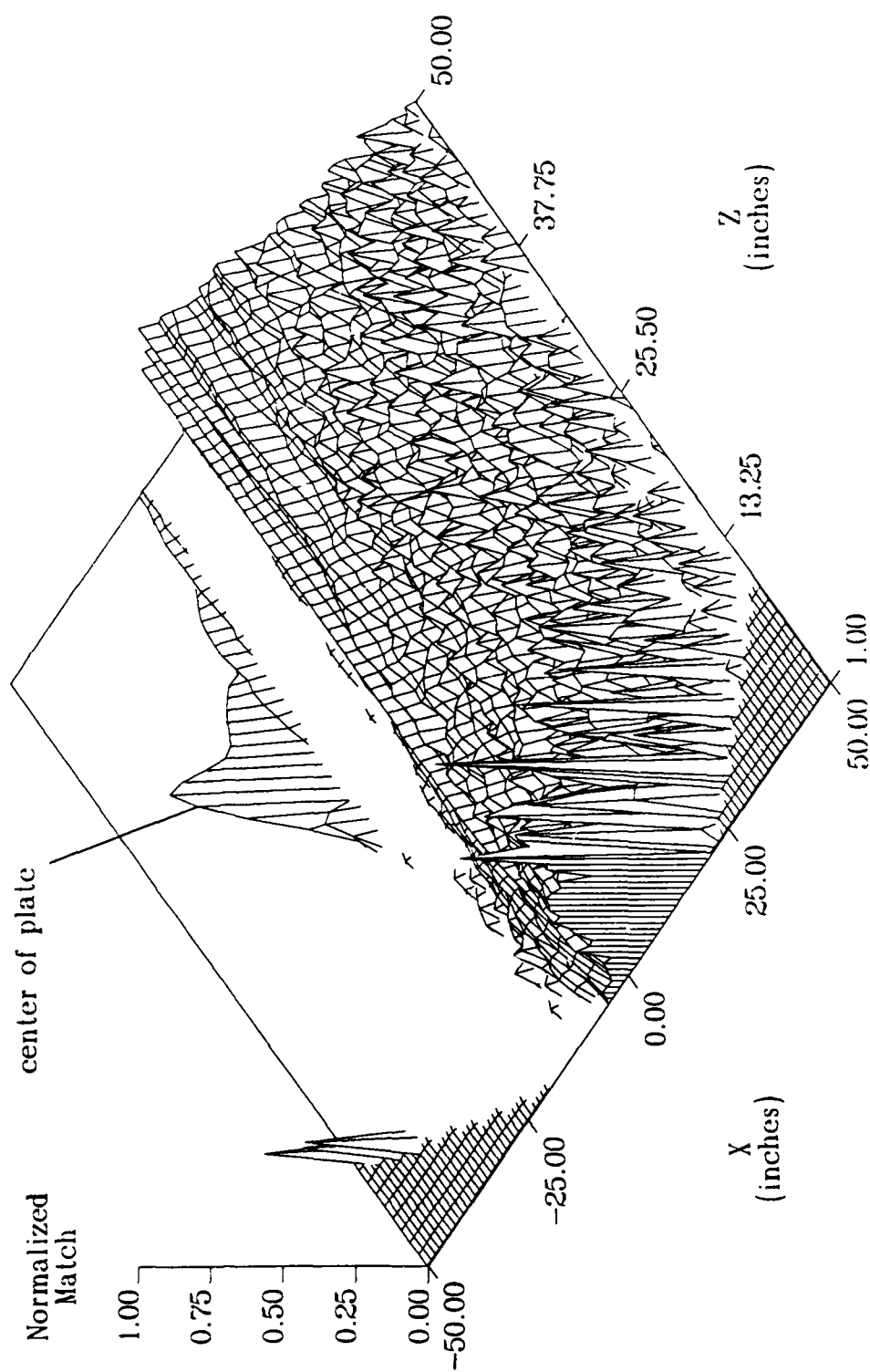


Figure 5.42. Swept-frequency reconstruction of a 12" plate centered at  $(-20'', 25'')$  with a source at  $(20'', 0)$ , showing sparse comparisons (spikes) and missed comparisons (plateaus).

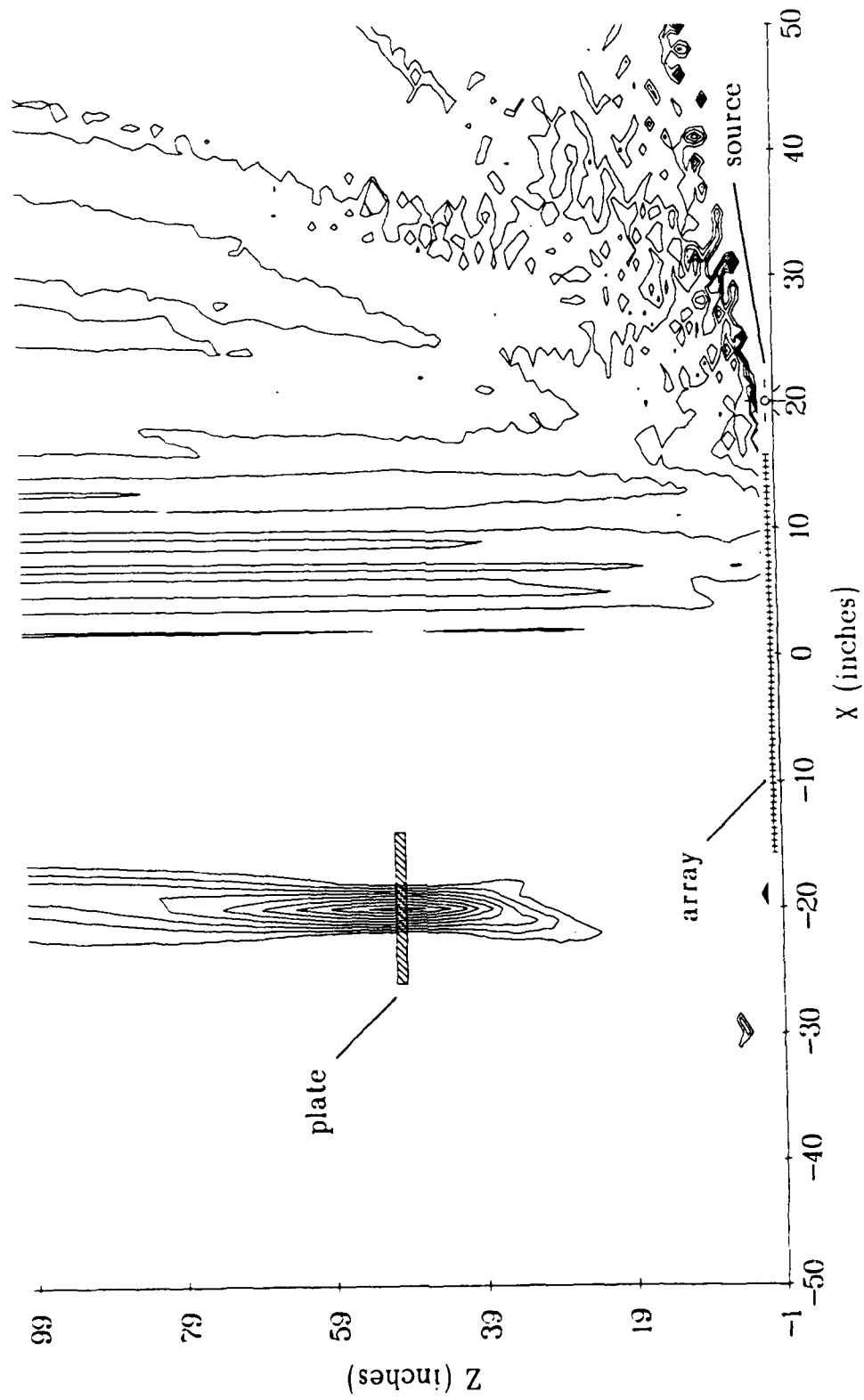


Figure 5.43. Swept-frequency reconstruction of a 12" plate centered at  $(-20'', 50'')$  with a source at  $(20'', 0)$ .

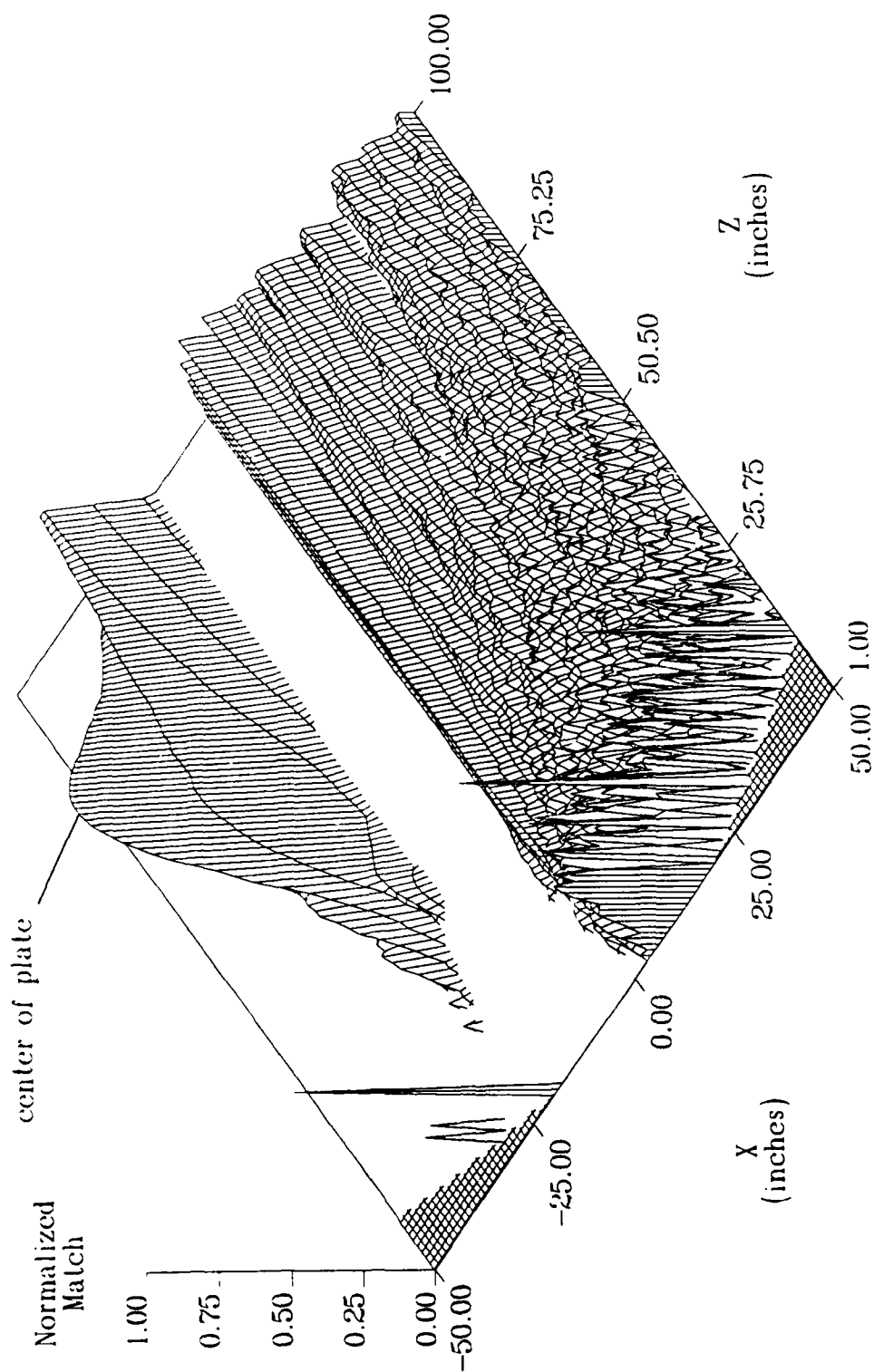


Figure 5.44. Swept-frequency reconstruction of a 12" plate centered at  $(-20'', 50'')$  with a source at  $(20'', 0)$ , showing sparse comparisons (spikes) and missed comparisons (plateaus).

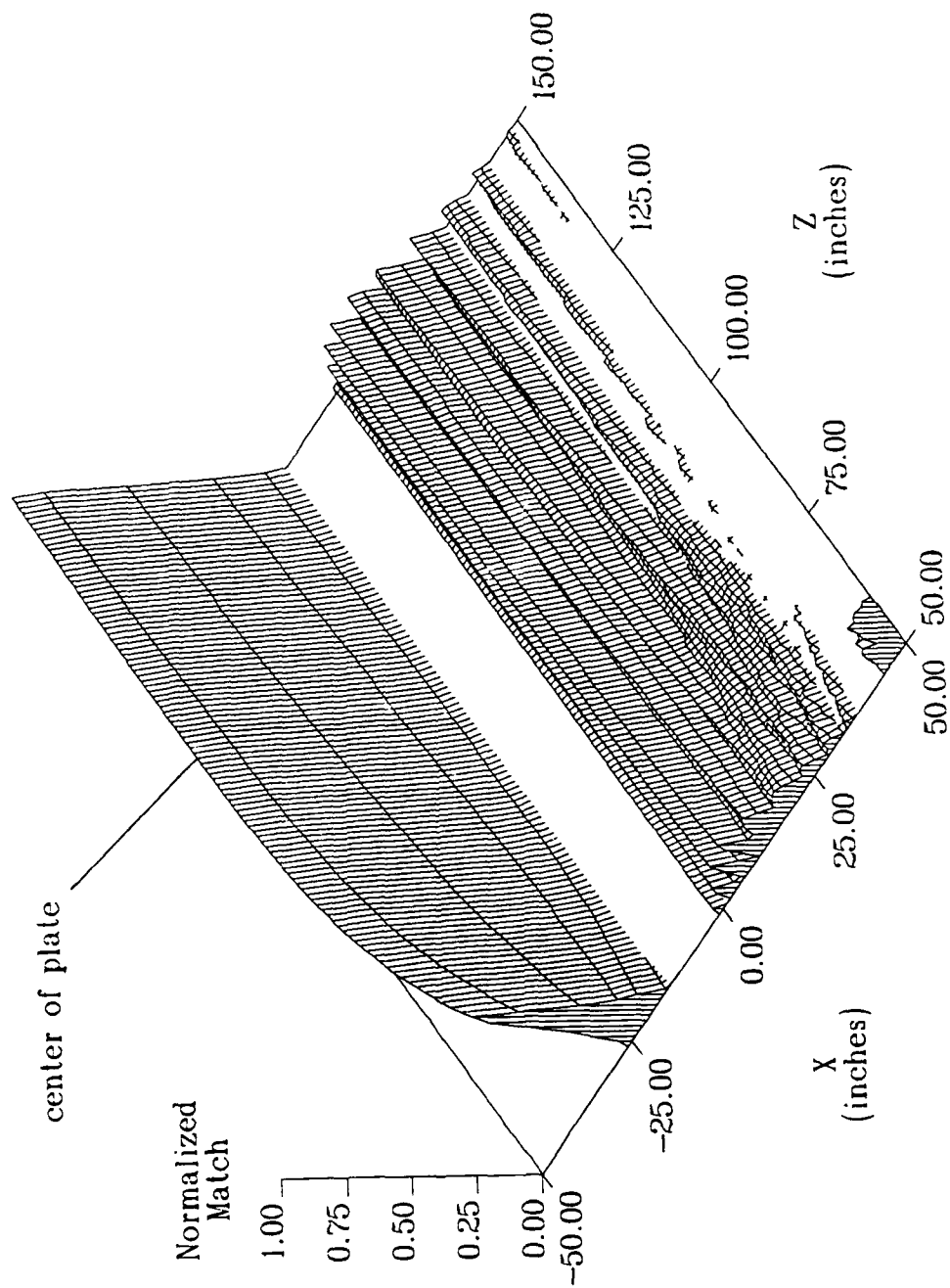


Figure 5.45. Swept-frequency reconstruction of a 12" plate centered at  $(-20', 100')$  with a source at  $(20', 0)$ .

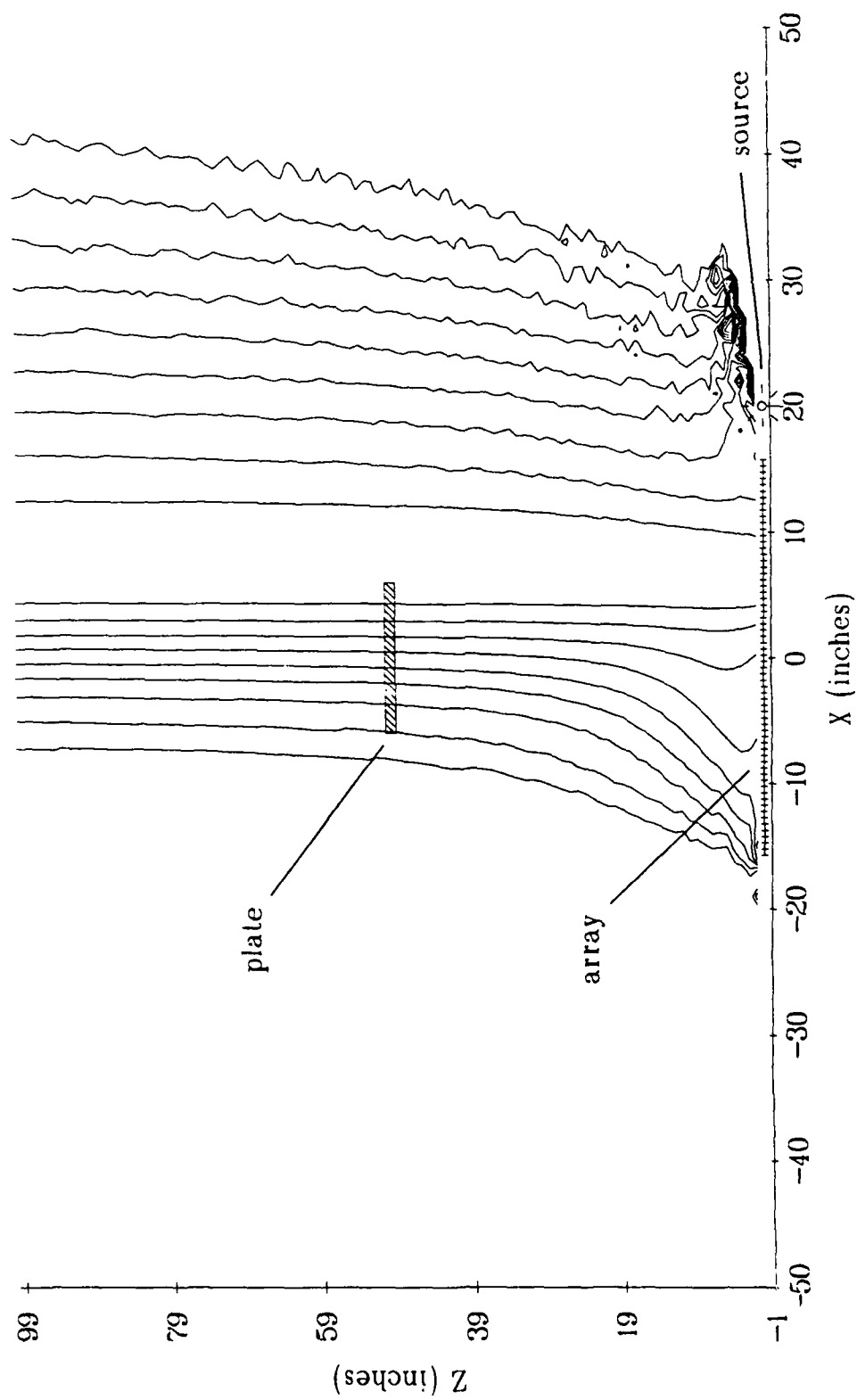


Figure 5.46. Swept-frequency reconstruction of a 12" plate centered at (0,50") with a source at (20",0).



5.47 show that in addition to a loss of all range resolution (as was experienced for the point reflectors), a major loss of lateral resolution is also experienced. When the center of the plate is moved still further to the right, to  $X = 20''$ , Figures 5.48 and 5.49 show that we do not see a recovery of range or lateral resolution as was seen for the point reflectors — the results continue to be extremely poor.

We can gain some insight as to the cause of these poor results for this last case, where the center of the plate was at  $(20'', 50'')$ , by examining the pattern recorded at the receiving array for two frequencies. These patterns, shown in Figure 5.50, reveal that we are receiving that portion of the plate's scattering pattern near the central lobe, where the amplitude varies rapidly. Therefore, when Eq. (5.18) is applied to shift the lower frequency to the higher frequency, a poor match results even when the fictitious scatterer is at the location of the true scatterer. The results when the center of the plate was further away from the source, as shown in Figures 5.43 and 5.44, were much better since we were then receiving that portion of the the plate's scattering pattern which was far away from the central lobe, where the amplitude was not changing as drastically.

### 5.6.3 Plate Results with No Offsets

As might have been expected after the previous section, when the plate and source are both on the Z-axis, as is shown in Figures 5.51 and 5.52, the image exhibits very poor resolution. In fact, Figure 5.52 indicates that the match for a fictitious scatterer at the location of the true scatterer is actually a bit worse (the trough) than for locations on either side.

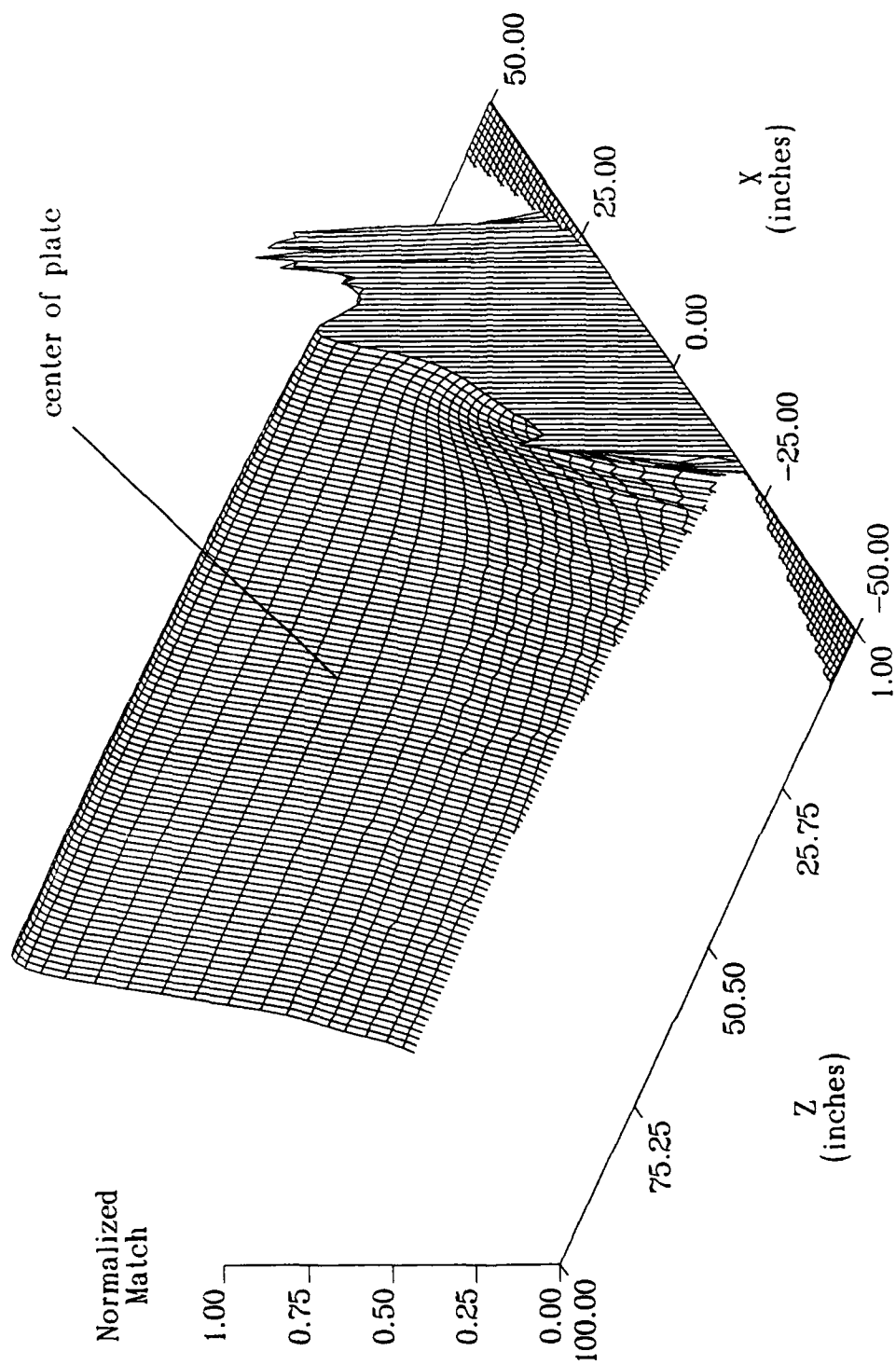


Figure 5.47. Swept-frequency reconstruction of a 12" plate centered at (0,50") with a source at (20",0), showing sparse comparisons (spikes) and missed comparisons (plateaus).

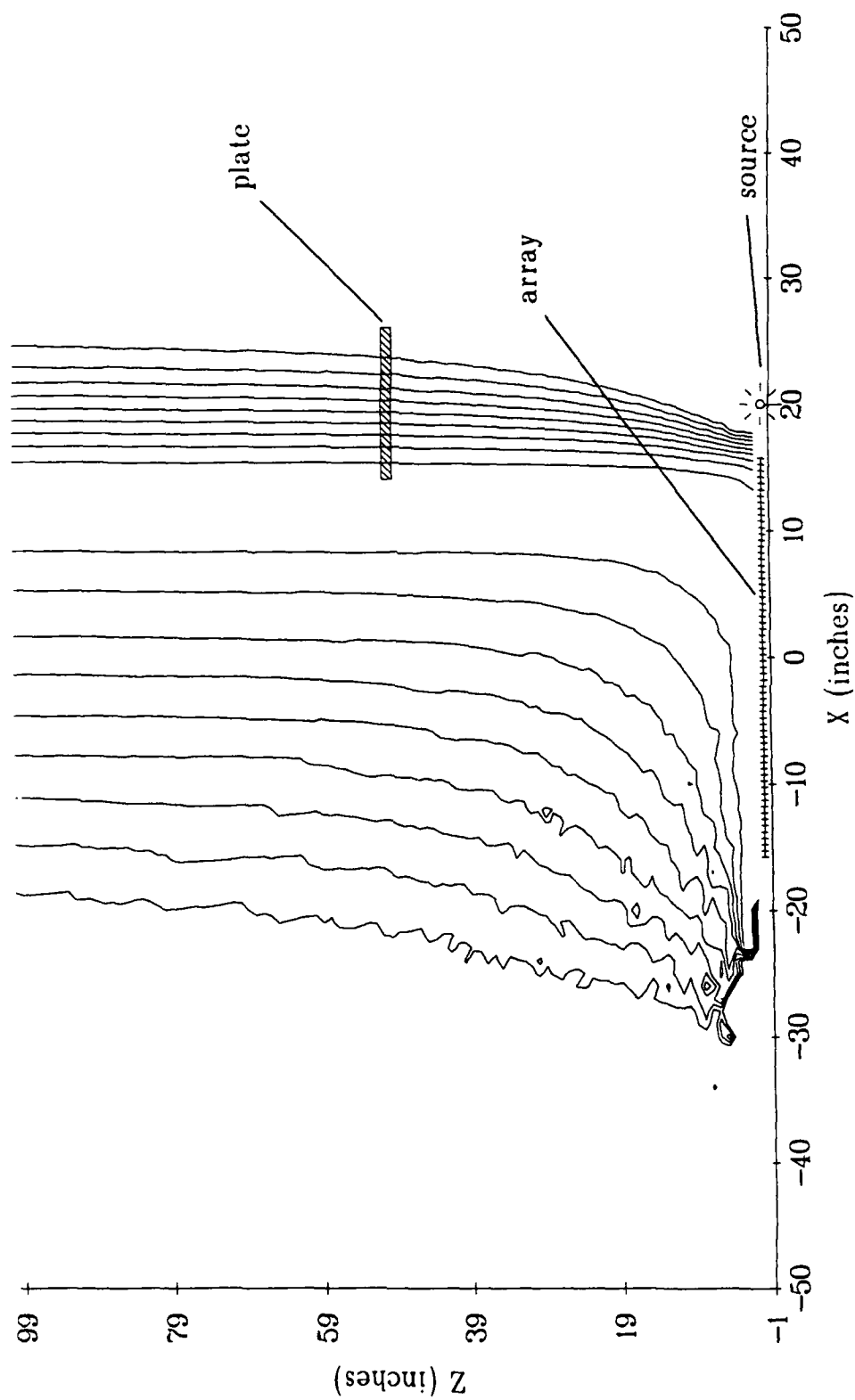


Figure 5.48. Swept-frequency reconstruction of a 12" plate centered at (20", 50") with a source at (20", 0).

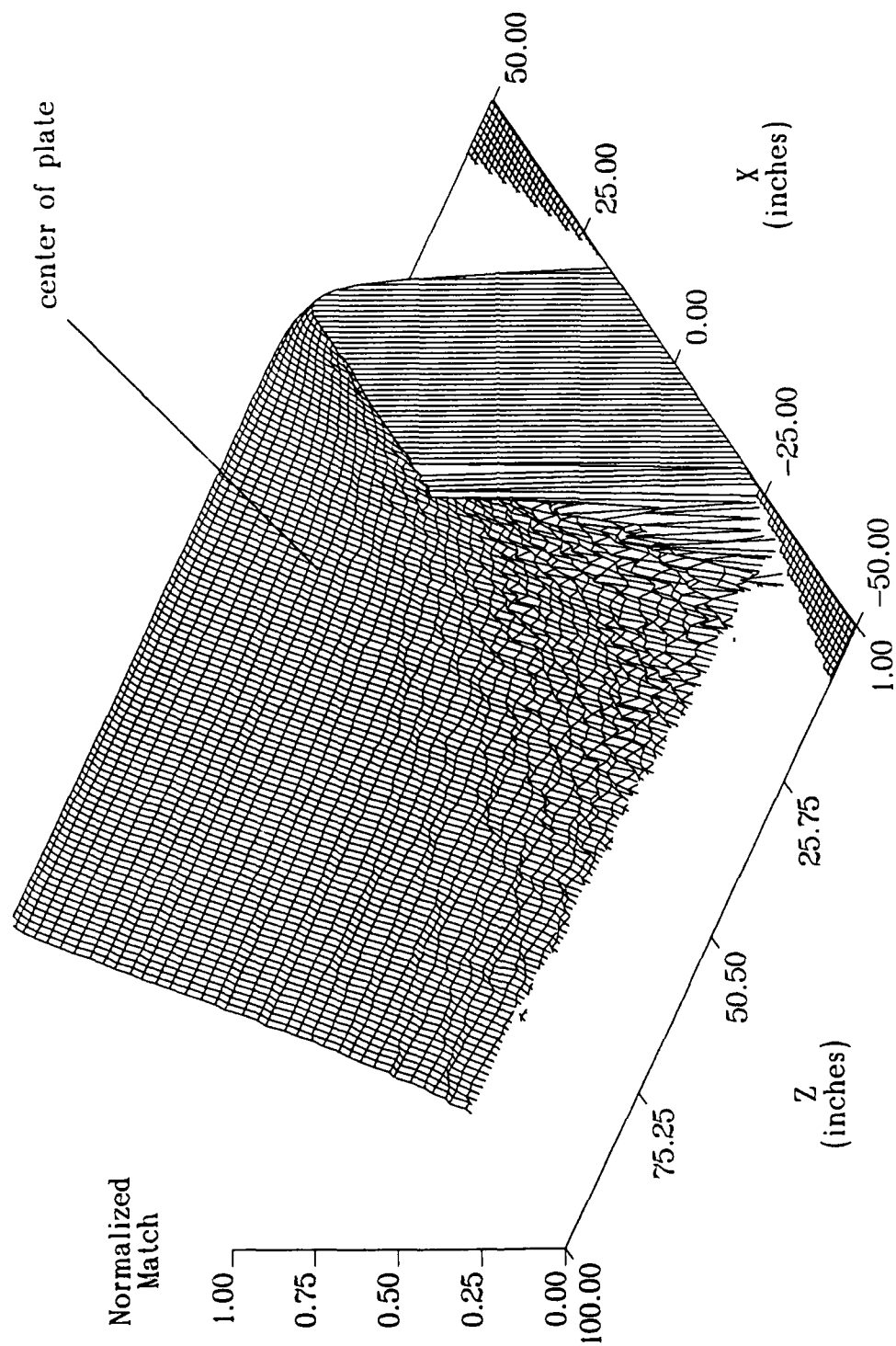


Figure 5.49. Swept-frequency reconstruction of a 12" plate centered at (20",50") with a source at (20",0), showing missed comparisons (plateaus).

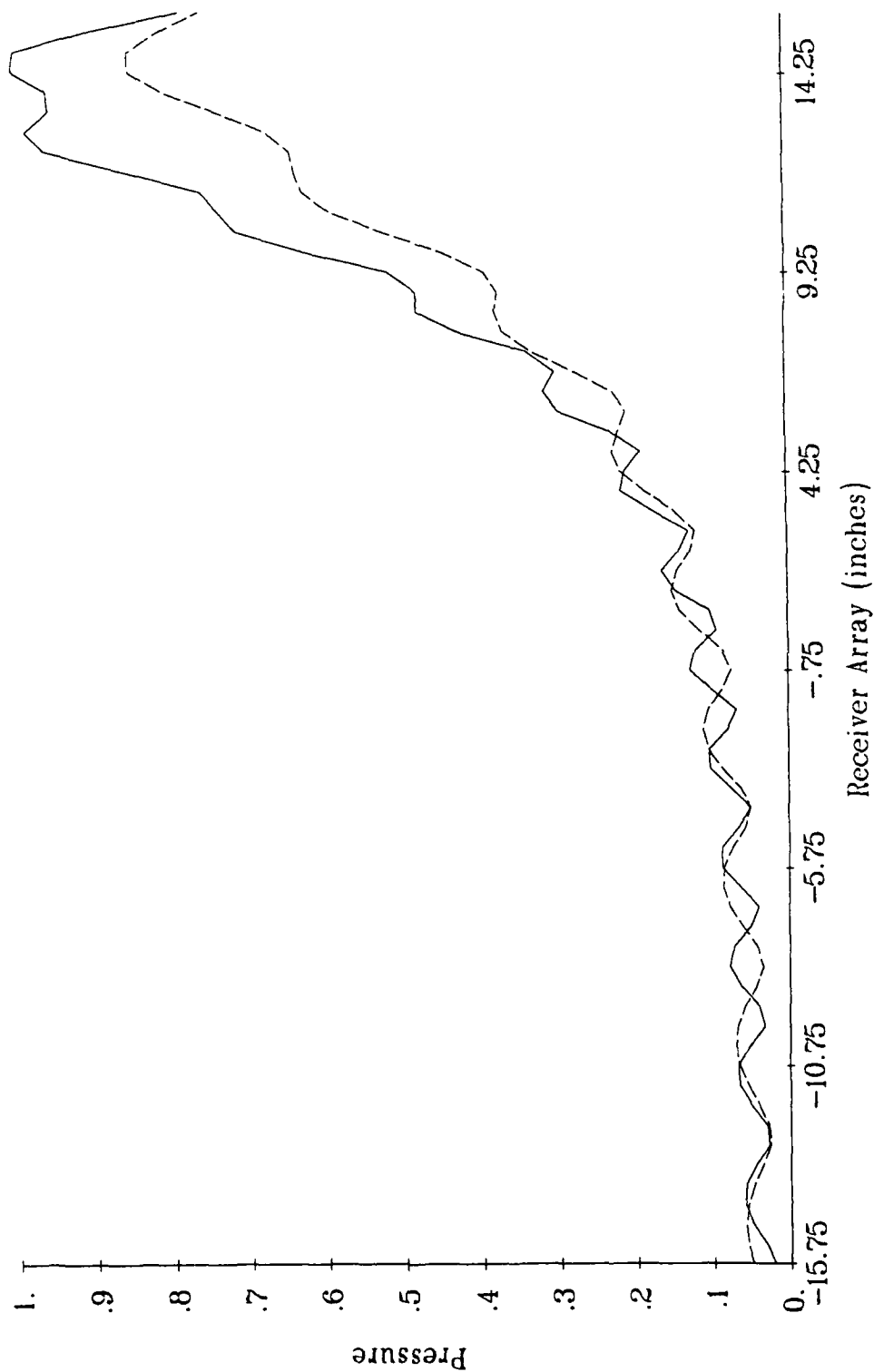


Figure 5.50. Patterns at an array on the X-axis (64 receivers) for 30 kHz (solid line) and 20 kHz (dashed line), due to a 12" plate centered at (20", 50") and a source at (20", 0).

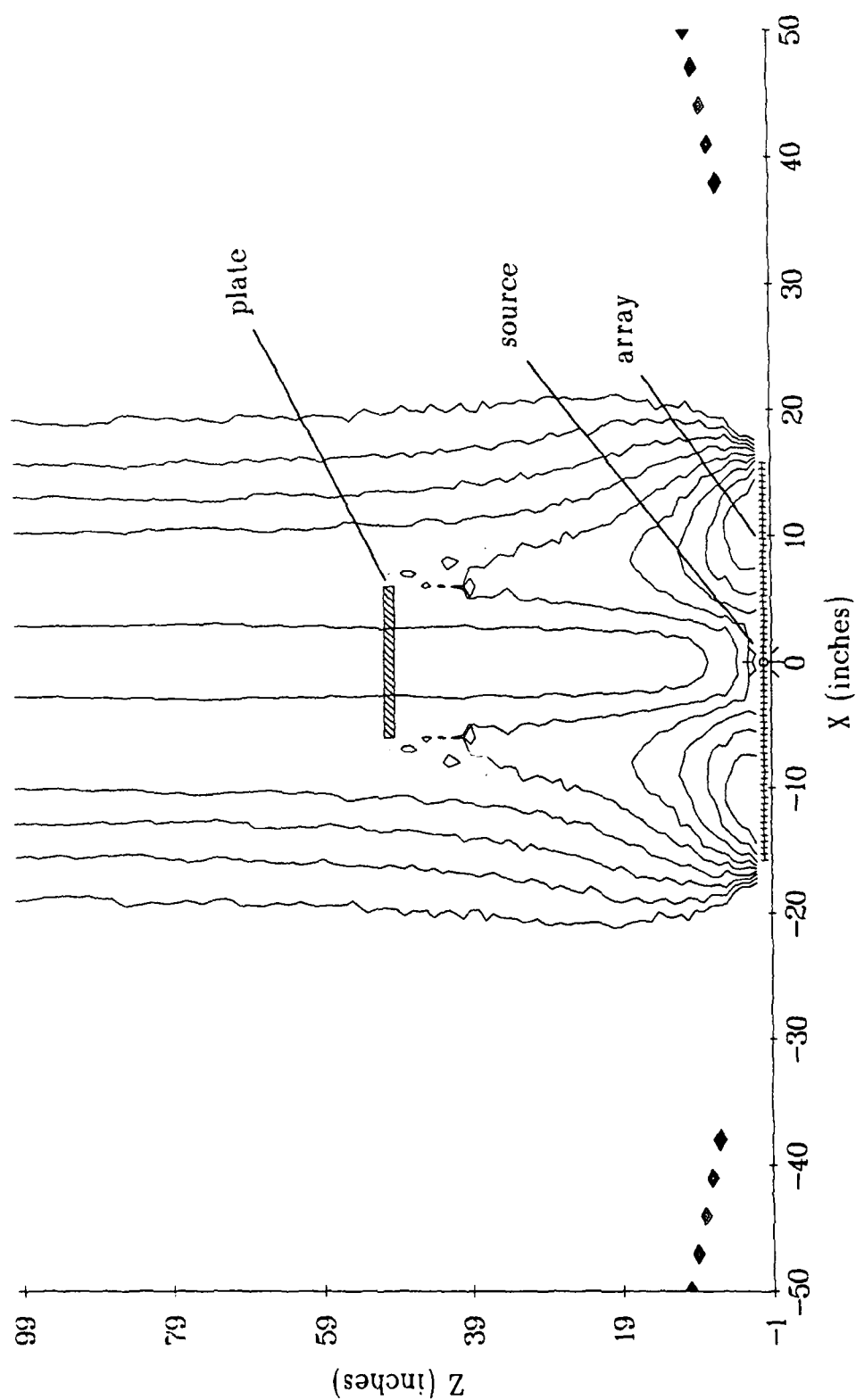


Figure 5.51. Swept-frequency reconstruction of a 12" plate centered at (0,50") with a source at (0,0).

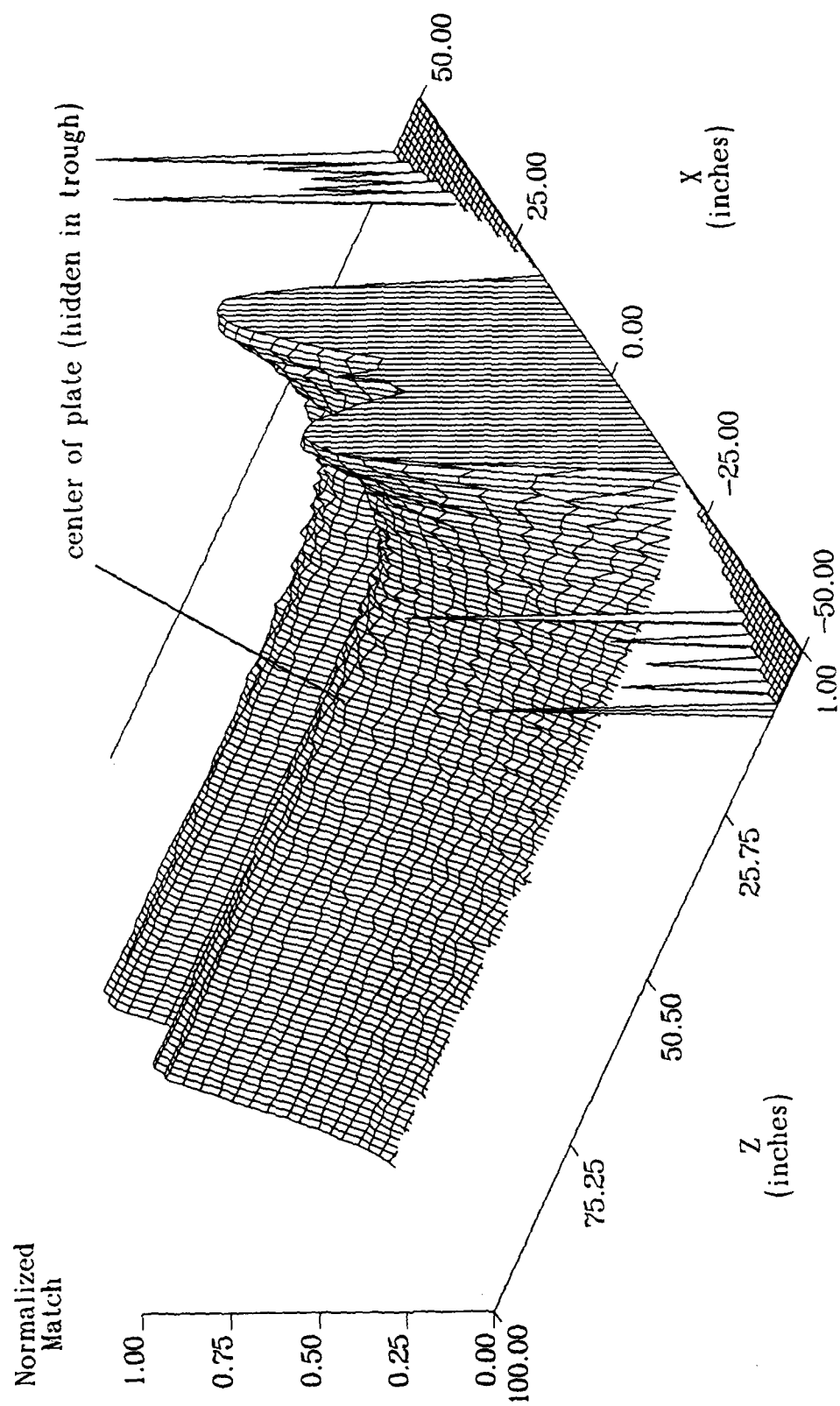


Figure 5.52. Swept-frequency reconstruction of a 12" plate centered at (0,0) with a source at (0,0), showing sparse comparisons (spikes) and missed comparisons (plateaus).

#### 5.6.4 Results Using Two Plate Scatterers

The results of a simulation with two 12" plates, centered at  $(-20", 50")$  and  $(0, 50")$ , are shown in Figures 5.53 and 5.54. While earlier simulations might have suggested that we would not be able to resolve the plate on the Z-axis, it is not clear why the offset plate cannot be located. It is possible that the off-axis contributions of the offset plate were essentially lost since they were so much lower than the central lobe of the on-axis plate.

#### 5.7 Comparison to Beam Forming

In addition to the simulations of the previous sections, the swept-frequency method can be evaluated by comparing it to the results obtained using a well-known method such as beamforming. The swept-frequency result for two point reflectors, 12" apart and centered at  $(-20", 1000")$ , is shown as the solid curve in Figure 5.55. The source is at  $(20", 0)$ . When the signals from the same two reflectors were analyzed by a beamformer, the curve in Figure 5.55 with the short dashes resulted. While this curve has a slightly sharper peak than the swept-frequency method, it is also in error by several inches.

Part of the reason for the error in the beamformer result is probably due to the fact that it assumes that it is receiving plane waves. The assumption would be slightly more valid if one, instead of two, reflectors were used. When this case was simulated, the curve in Figure 5.55 with the long dashes resulted, and exhibited a peak which was at the correct location and slightly sharper than the curve from the swept-frequency method. A swept-frequency curve using only one reflector, for comparison, would be useless because a single reflector exhibits



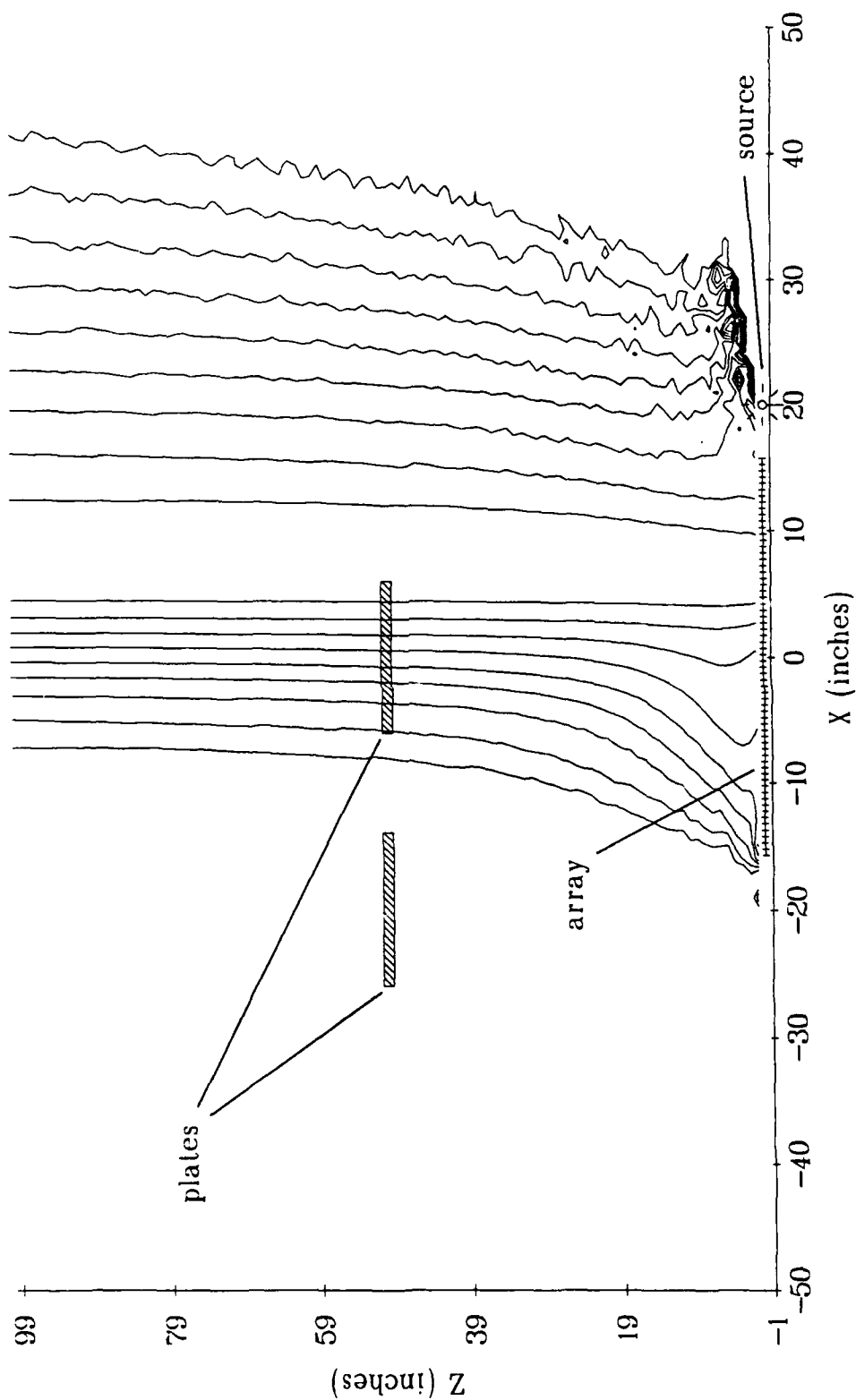


Figure 5.53. Swept-frequency reconstruction of two 12" plates centered at  $(-20'', 50'')$  and  $(0, 50'')$  with a source at  $(0, 0)$ .

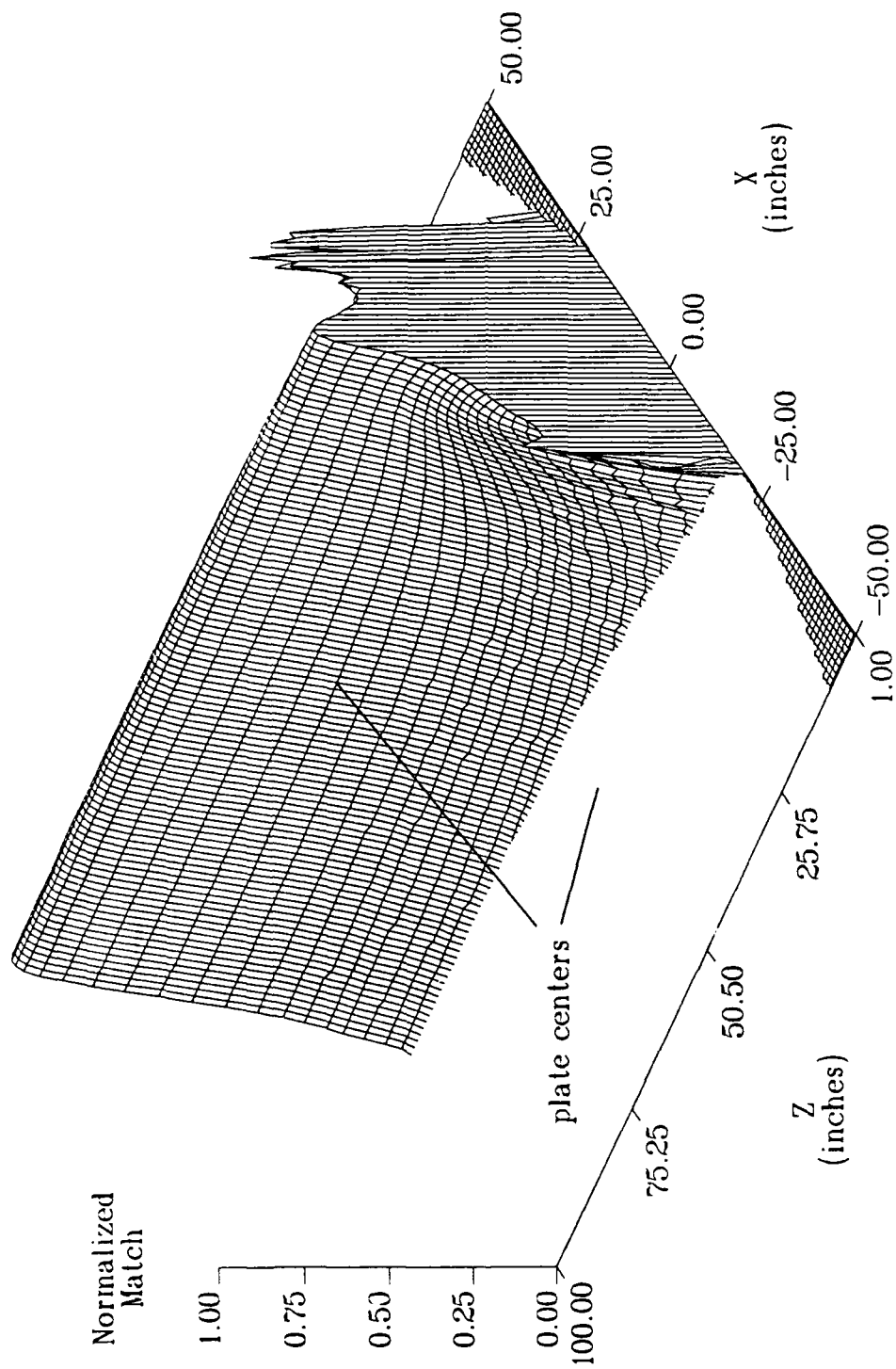


Figure 5.54. Swept-frequency reconstruction of two 12" plates centered at  $(-20'', 50'')$  and  $(0, 50'')$  with a source at  $(20'', 0)$ , showing missed comparisons (plateaus).

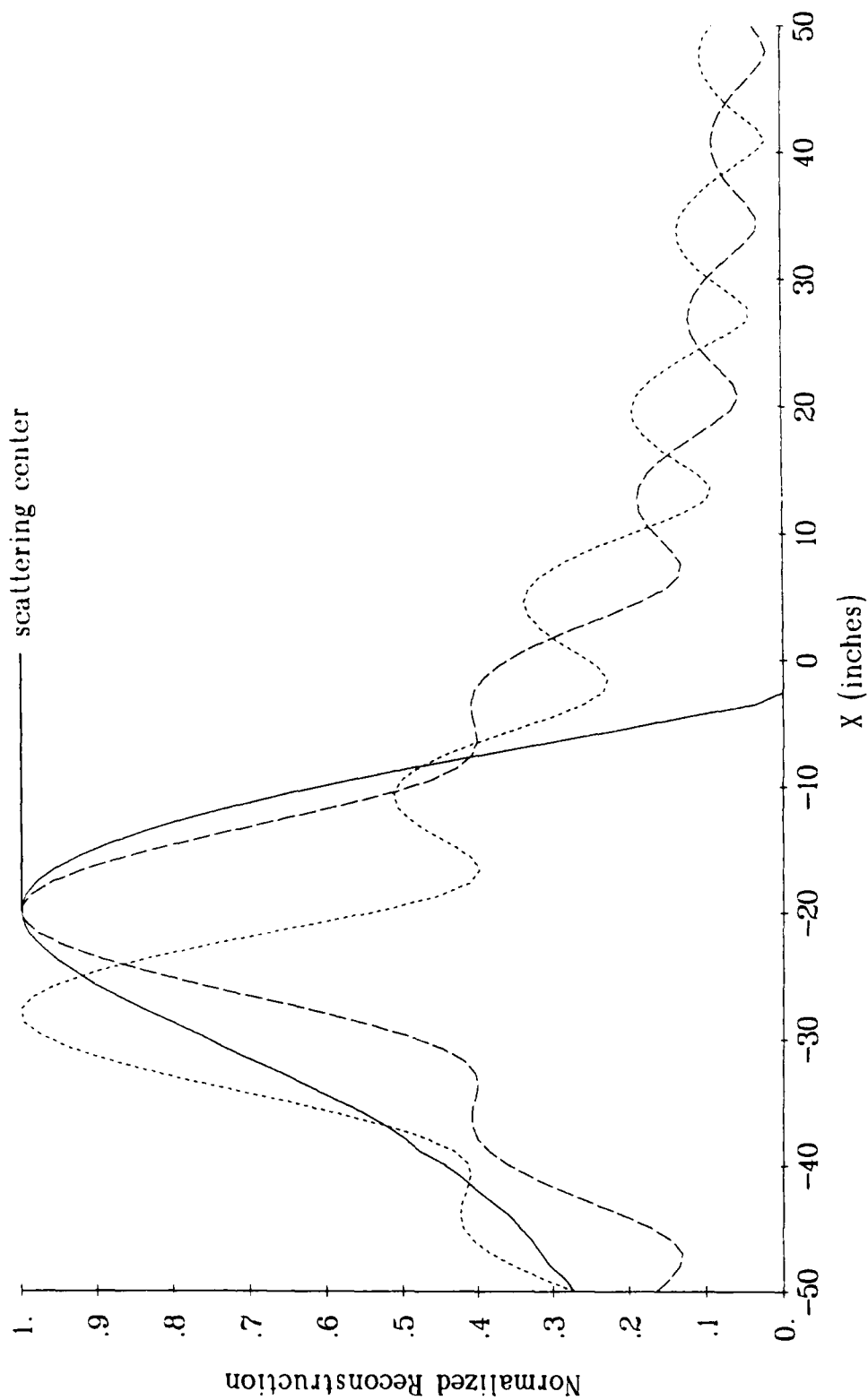


Figure 5.55. Reconstruction using swept-frequencies and 2 reflectors (solid line); beam forming and 1 reflector (long dashes); and beam forming and 2 reflectors (short dashes). All reflectors at  $Z=1000''$ .

no frequency dependence whatsoever.

The range of the reflectors used for the previous figure was made relatively large so as to approach the plane-wave requirement of the beamformer. When the range is reduced to 100", the results, shown in Figure 5.56, show that while the peak from the swept-frequency method has become much more precise, the beamformer results have become useless.

### 5.8 Results With Range Resolution

In most imaging systems which use multiple frequencies, the received signal is correlated with the transmitted one to determine the time-of-flight and therefore the range of the scatterer. Ermert and Karg<sup>28</sup> showed that the ambiguity function for differences in range  $\Delta z$  near a scatterer at range  $z$  was given by

$$\chi(\Delta z) = \left| \frac{\sin \left( \Delta k \cdot \Delta z \cdot \frac{z}{R} \right)}{\Delta k \cdot \Delta z \cdot \frac{z}{R}} \right| \quad (5.23)$$

where  $R$  is the distance between the center of the receiving array and the scatterer.

It would be interesting to roughly simulate how such a correlation could improve a swept-frequency image, using the same frequencies which are already being used in the frequency sweep. This can be done rather trivially by simply multiplying any of the normalized reconstructions shown previously in this chapter by the values provided by Eq. (5.23). In particular, the reconstruction shown in Figure 5.30 for a pair of reflectors centered at  $(-20", 100")$  would be a good candidate as it exhibits good lateral resolution but no range resolution.

Before proceeding, the definition of "bandwidth" needs to be addressed.

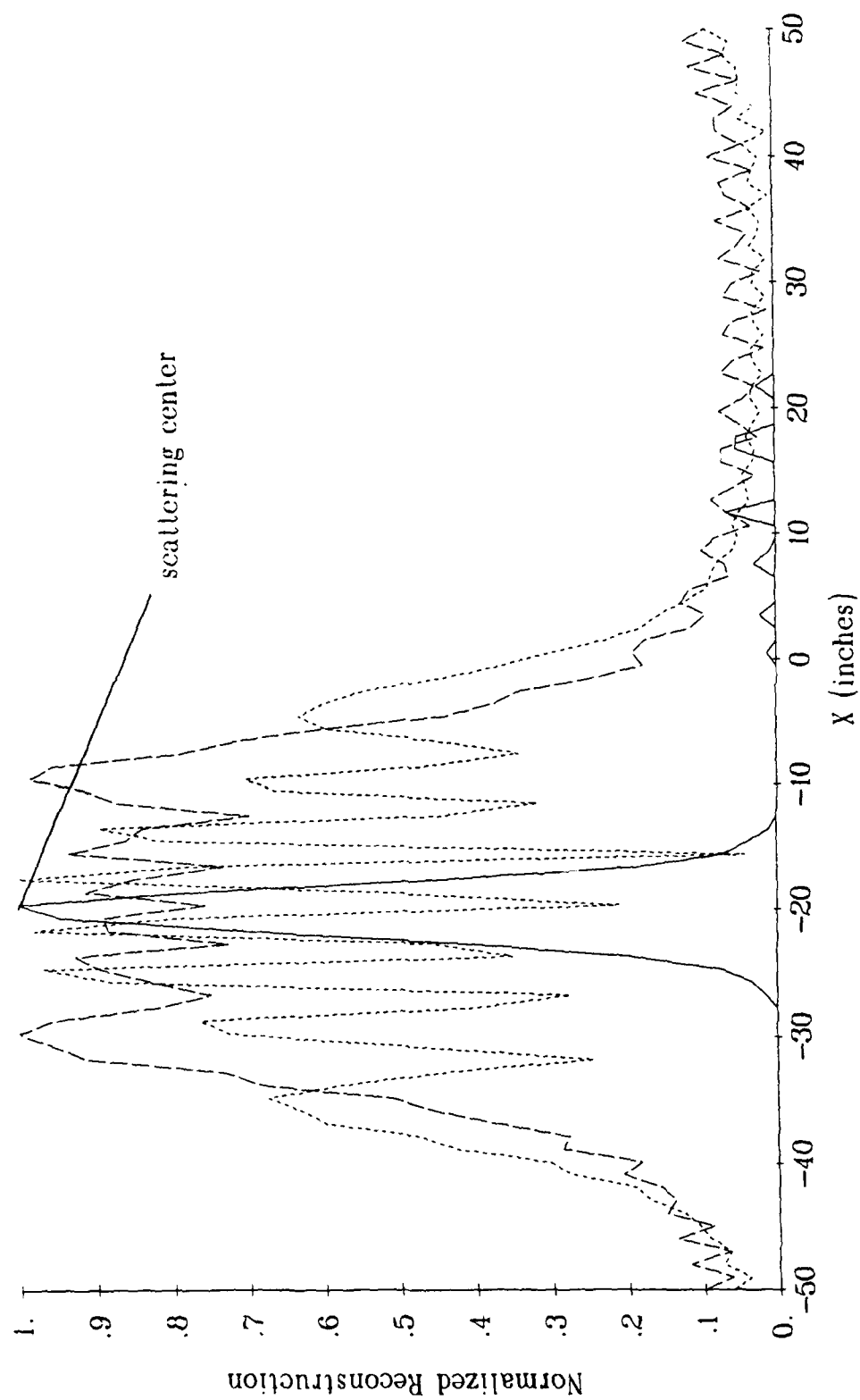


Figure 5.56. Reconstruction using swept-frequencies and 2 reflectors (solid line); beam forming and 1 reflector (long dashes); and beam forming and 2 reflectors (short dashes). All reflectors at  $Z=100''$ .

In Ermert and Karg, a continuous sweep of frequencies were used where the bandwidth  $\Delta f$  was defined as the difference between the maximum and minimum frequencies, with  $\Delta k = 2\pi \Delta f / c$ . However, in Figure 5.30, a continuous sweep is not used, and the difference between the frequencies being compared can vary from a low of 421.5 Hz to a high of 20,000 Hz. Therefore, each of these frequency differences were used for  $\Delta f$  and the results for the low and high differences shown in Figures 5.57 and 5.58, respectively.

### 5.9 Swept-Frequency Execution Times

Most of the swept-frequency processing in this chapter evaluated the reconstruction field at 101 points along the X-axis and at 100 points along the Z-axis, for a total of 10,100 points. In all cases, 20 frequencies and 19 frequency comparisons were used.

The MicroVAX II processor required about 11,200 seconds to evaluate these images when two point reflectors were used; and about 11,400 seconds when the plate reflector was used. It is not clear why the time to process the signals from the plate required slightly more time since the time to simulate the scattering is not included in the elapsed time.

These times indicate that it took approximately 1.109 or 1.129 seconds to reconstruct each field point when the point reflectors or plate reflector was used, respectively. These times are on the order of 3 times longer than that needed by the pattern-match or mismatch method to form an image point with a barrier present.

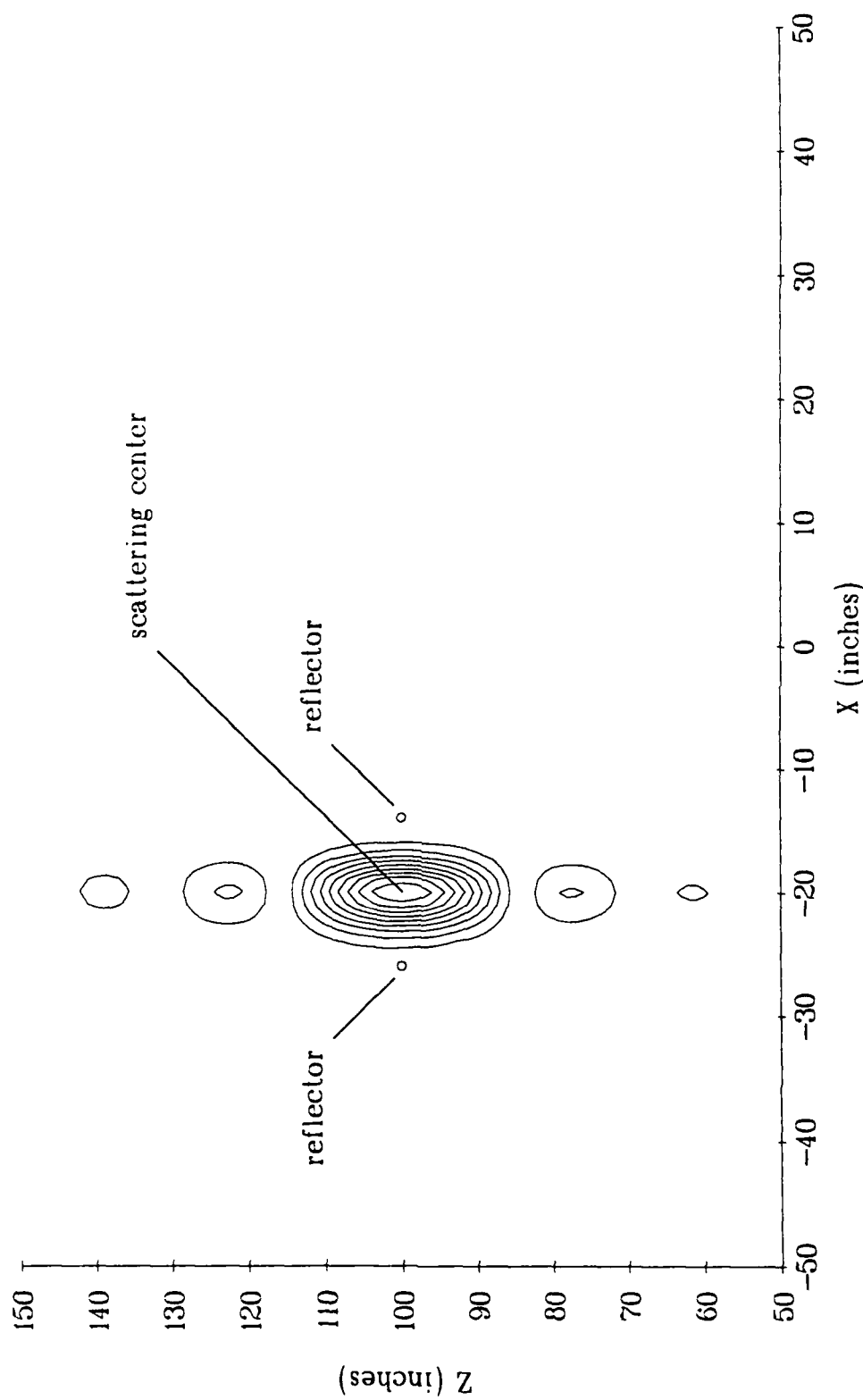


Figure 5.57. Swept-frequency reconstruction of 2 point reflectors centered at  $(-20', 100')$ , for a source at  $(20', 0)$ , with simulated range resolution for a bandwidth of 421.5 Hz.

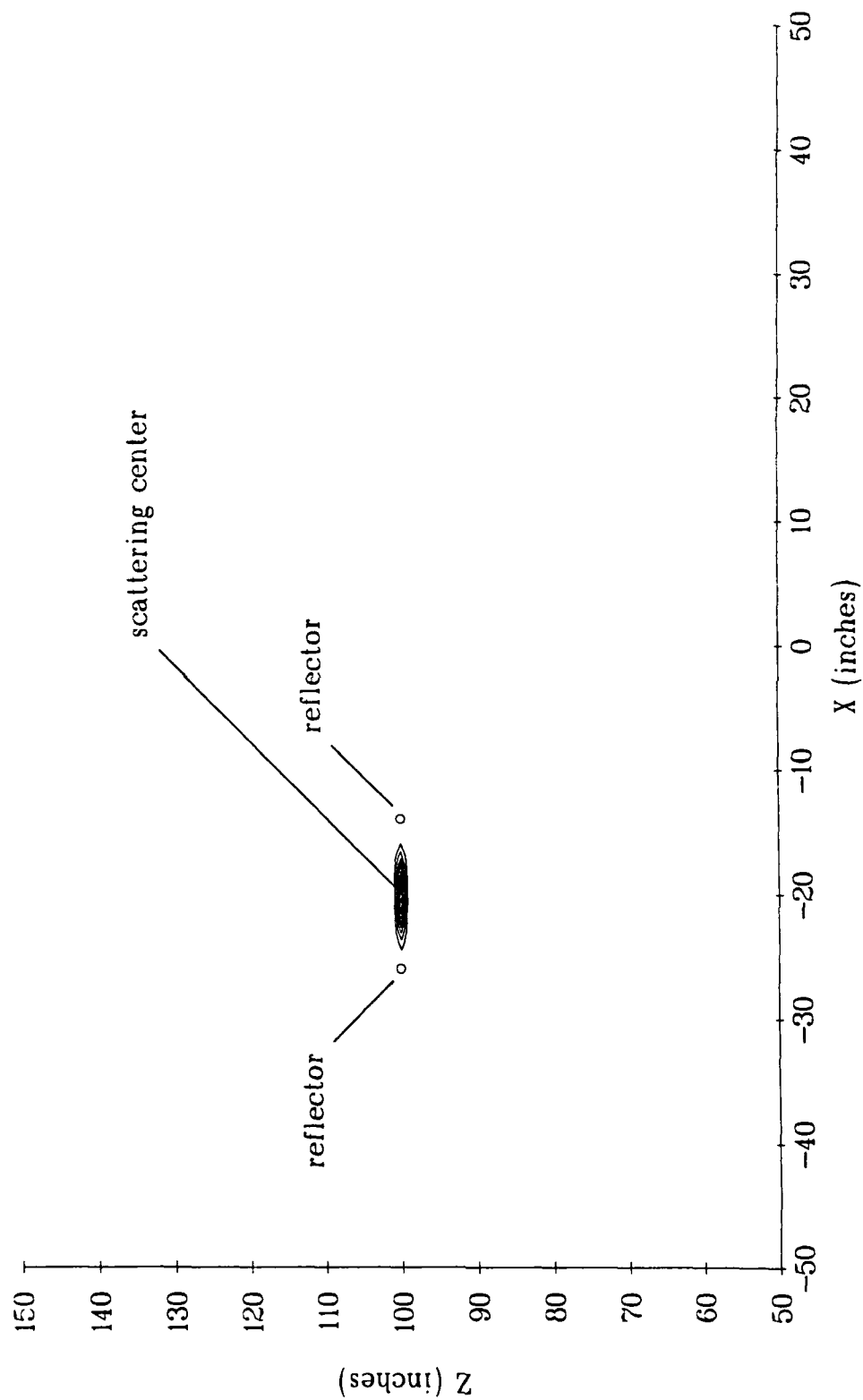


Figure 5.58. Swept-frequency reconstruction of 2 point reflectors centered at  $(-20'', 100'')$ , for a source at  $(20'', 0)$ , with simulated range resolution for a bandwidth of 20,000 Hz.



## Chapter 6

### Summary and Conclusions

A study of the major approaches to the generation of acoustical images has led to the development of several new methods, and some new observations concerning the localization of acoustic scatterers. The following sections will summarize these results and suggest further lines of investigation.

#### 6.1 Basic Issues

Three basic imaging methods have been studied: holography, beamforming, and receiver correlations. Of these, the holography method seems to have the greatest general usefulness since a beamformer will fail when the wavefronts are not planar and the correlation method will fail when there is more than one source or scatterer. Another, lesser known imaging method, built upon the concept of a fictitious scatterer, was investigated and shown to have several powerful capabilities and the ability to incorporate, as special cases, the three previously studied methods.

It was found that the proper distribution of receiver elements in sparse arrays can definitely improve the array's performance. However, there does not seem to be any further improvements to be had when the array is already fully populated, with receivers every half-wavelength.

A study of the use of complex signals to represent the information at the receivers revealed that significant range information is lost with such a representation, but could be recovered by recasting an imaging method to instead use the

time-of-flight.

## 6.2 High Resolution Methods

Two categories of high resolution array processing methods were examined: the autoregressive-moving average (ARMA) methods; and the minimum energy (ME) method and its variations including linear predictors (LP) and eigenvector analysis. While each holds some promise of enhancing the resolution, each also has some major obstacles which need to be investigated further before the method can be applied to the location of scatterers.

It does not seem possible to enhance either category of high resolution imaging to incorporate *a priori* information about the scatterers or their relative location. Nor does it seem possible to use the full time-history of the received signals so as to avoid the phase ambiguity described in Section 2.6. On the other hand, the two imaging methods investigated with simulations in this study (pattern-match and swept-frequency) could be modified to use such information. It would be interesting to investigate whether such a modification would yield a higher resolution than ARMA or ME methods.

### 6.2.1 ARMA Methods

The major question in applying this method is whether *any* extrapolation can predict a scattering function at angles beyond those subtended by the receiving array. While this is probably possible for simple scatterers, further work needs to be done to determine if robust extrapolation is possible for the general case. In the absence of prior knowledge about the scatterer, it seems that these methods should be used with great caution. A review of the literature suggests

that this sort of problem has not been considered since most workers have been seeking only the location of simple plane-wave sources.

In those cases where an ARMA spectral estimator can properly extrapolate data beyond the receiving array, the estimator would provide an enhanced resolution even in the absence of noise.

### 6.2.2 ME Methods

The major obstacle in applying minimum energy methods is their inability to work with any wavefront shape other than ones that are planar. Thus, while intuition would predict that an imaging method should yield better results as the object being imaged moved closer, these methods instead progress towards uselessness as the object moves closer. While both methods can be modified to accommodate any specific wavefront, no *adaptive* method is known for the determination of what this wavefront should be — it must be chosen by some other means. While this problem does not, technically speaking, rule out these methods, it means that they can be used only to locate scatterers which are in the farfield. No scatterer, no matter how simple its scattering function, can be handled if it is too close.

A great deal of progress has been made in accommodating coherent sources during the last few years and so this may no longer be an obstacle in applying the ME method to scatterers. The observation by Duckworth<sup>41</sup> that small, naturally occurring motions can provide the needed decorrelation is, on the one hand, a promising solution although it has yet to be established whether, on the other hand, such motion will smear the resulting image to the extent that the high

resolution method's enhancements are lost.

### 6.3 Pattern-Match and Mismatch Imaging

Two new imaging methods, called the pattern-match method and the mismatch method, were developed from the concept of a fictitious scatterer. The mismatch method is similar to the pattern-match method but uses a new approach to the comparison of two complex signals. The following sections review the work which has been done in this study, and then suggests several questions and variations which may make these new methods yet more useful.

#### 6.3.1 Review of the Simulations

It has been shown that, to the extent that the simulation of the diffraction phenomena is valid, the new methods are powerful tools for the analysis of pressure waves which have encountered a known disturbance. These methods can provide a superior reconstruction to the holography method in many cases when free-space conditions do not exist. The application to experimental data is limited only by the accuracy of the simulation, of the experimental diffraction or other propagation phenomena, which is used in the estimate of the signal from the fictitious source.

To test the new methods, a computer simulation of diffraction by a barrier was implemented. This simulation automatically analyzed the relative locations of the source, barrier, and receiver, and correctly determined in which of the 3 possible regions the receiver was located. Though developed for sources and receivers far from the barrier, the simulation was sufficiently accurate for the holography method to form the image of a reflection when the source was in

front of the barrier.

The simulations revealed that, when the acoustic source is partially hidden from the receiving array by a barrier, the pattern-match method reports that the source is at some location behind the barrier, without reporting an exact location; on the other hand, the holography method falsely reports that the source is at the edge of the barrier.

The mismatch method excludes more locations, from being possible source positions, than the pattern-match or holography methods. However, it is not clear that the resulting spike-like response would always be more desirable — without the pattern-match image as a guide, these spikes could be interpreted as additional sources.

It was shown that the new methods are not significantly affected by small errors in their knowledge of the environment, such as an error in the range of a barrier.

Although it is not clear whether the new methods can be considered to be linear processors, simulations using two sources indicate that they at least approximate the linear response of the holography method.

The new methods are generally slower than the holography method; however, it seems that this should not be considered to be an obstacle at this stage as ever-faster computer system may make this issue irrelevant.

### 6.3.2 Future Work: Composite Sources

In this study, only the pattern from a single fictitious source has been used in the search for the true source, even in cases when there was in fact two sources. However, when *a priori* information can establish the number of sources and their relative orientation, we could treat this *set* of sources as one composite fictitious source, and estimate the pattern which would have been received at the array due to each possible location of the composite fictitious source. This might be extremely effective when the object being sought can be characterized by a set of specular reflections whose relative separation and strength is known.

This same approach could be taken further to include the case of an extended source or scatterer. We would continue to need an algorithm which can estimate the pattern at the receiving array for each possible location of the extended fictitious object. This algorithm could either be purely theoretical, or could perform the appropriate interpolation upon a sufficiently extensive set of empirical measurements.

### 6.3.3 Future Work: Noise and Interference

Although this study has laid the groundwork for the use of the pattern-match and mismatch methods, actual applications, such as the guidance of a mobile robot, will doubtlessly encounter a variety of sources of noise and interference.

An investigation of these problems should begin by introducing isotropic noise into the simulations; if this reveals a problem, correlations between elements might be used in place of the simple phase calculations. In addition, directional

noise (representing, say, a fan in the robot's vicinity) should also be investigated.

Other environmental problems which might be considered could include additional barriers, errors in the knowledge of the receiver array elements, and the occurrence of motion during signal acquisition.

#### 6.3.4 Future Work: Mismatch Variations

There would seem to be an almost unlimited number of variations of the mismatch method.

In this study, the mismatch was equated to the "distance" between two complex numbers; this mismatch metric thus, more or less, gives the same weight to differences in phase as it does to differences in amplitude. These weights could, for example, be varied by calculating the phase and amplitude differences separately and then weighing them in some other manner. In some cases, it may be useful to allow the sign of the differences to have an effect.

In any of these variations, the resulting match could also be raised to some higher power, or inverted, so as to give a greater emphasis to the large mismatches.

In addition, any of these variations could be normalized to the amplitude of one of the complex numbers so that, for example, mismatches between small numbers are weighed more heavily than equal-sized mismatches between large numbers.

It would be quite useful to investigate how the mismatch method achieves its improvements, in those regions where it offers improvements over the pattern-

match method or holography, with the goal of extending its improvements to all cases. In particular, it may be that a diversity of frequencies could eliminate the false peaks, such as does a diversity of values for  $\Delta f$  in the swept-frequency method.

### 6.3.5 Future Work: Time-of-Flight

In this study, both match methods represent the time delay seen at each receiver as a complex number. As discussed in Section 2.6, when the transmitted signal is broadband, considerably more information is present than can be represented by a single complex number. In these cases, it is possible to adapt the pattern-match methods to retain and use the full time-of-flight (TOF) information content of the received signal.

To review, in the method used in Chapter 4, the complex signal from the single-frequency fictitious source was estimated at each receiver location. However, it would be just as easy to express this as a complex amplitude plus a TOF. The path length and hence the TOF is already present in the terms like  $\exp(jk \dots)$  in the expressions for  $p_d$ ,  $p_i$ , and  $p_r$ . This allows us to calculate the time-history to be expected at each receiver location from the fictitious source. A comparison of the actual signal's time-history with that of the fictitious source, summed across the receiver array, would then yield the match for that location of the fictitious source. An investigation of such an imaging method would also need to consider techniques for estimating the transmitter's waveform and time of transmission when those quantities are not known.



## 6.4 Swept-Frequency Imaging

A new imaging method which uses multiple frequencies was developed and tested using simulated reflections from point reflectors and a plate. The following sections review the new method, the results of the simulations, and a variety of developments which may make the new method yet more useful.

### 6.4.1 Review of Swept-Frequency Imaging

A new imaging technique has been developed which for the first time exploits the fact that an object's scattering pattern has a deterministic dependence upon the frequency of the acoustic wave which it is scattering. This development also borrowed the central concept of the mismatch method to form a metric which indicates whether a given scattering pattern exhibits the expected frequency dependence.

To test the new method, computer simulations of two categories of scatterers were implemented and tested: specular scatterers, represented by point reflectors; and extended scatterers, represented by a reflective plate. The latter, though implemented as a rather simple summation, proved to be highly accurate, yielding an unexpected but entirely appropriate representation of the scattering pattern at high frequencies and large plate dimensions.

The simulations reveal that the swept-frequency method can provide good range and lateral resolution in many circumstances, but can lose resolution when the scatterer is moved to the normal to the array of receivers, or to larger ranges. The reconstruction of a plate can also deteriorate when it is moved so that the array of receivers is within that portion of the plate's scattering pattern where

the amplitude varies rapidly.

When multiple scatterers were present, the simulations showed that the swept-frequency method can yield poor results. Multiple reflectors caused the image to have a peak at the scattering center formed by every possible pair of reflectors. Multiple plates yielded a rather useless image, though the results may have been partially due to the rapidly varying amplitude noted previously.

It was shown that a simple range calculation, as is often done with broadband pulses, could be combined with the swept-frequency method to provide an enhanced range resolution.

A comparison with a beamformer was performed which indicates that, while the beamformer may provide a higher resolution at very large ranges (so that it sees only plane waves), the swept-frequency method provided comparable or superior resolution at all ranges.

#### 6.4.2 Future Work: Amplitude Dependence

The poor results experienced when attempting to image the plate at certain locations was shown to be due to the plate's scattering pattern changing amplitude, as well as angle, as the frequency was varied. A similar problem could occur with other extended scatterers.

It may be possible to avoid this problem if we replaced the pattern across the array at each frequency with an artificial pattern designed so that its peaks and nulls are at the same location as the original. In other words, all patterns would be modified to be similar to those obtained from point reflectors. It may

even be possible to skip the actual generation of the artificial pattern and use only a table of peak and null locations since the interpolation, which must be done anyway, will be implicitly fitting such a pattern to its input table of values.

One of the challenges of such a development would be the creation of an algorithm which could find the desired locations in the scattering pattern of a plate near its central lobe — that is, the phenomena we are looking for are merely *local* peaks and nulls.

#### 6.4.3 Future Work: Phase Dependence

It is sometimes possible to treat the location of the scatterer as the source of a new spherical wave. Then, since we know the wavelength at each frequency, the location of the receivers, the location of the transmitter, and the location of the fictitious scatterer, it would be possible to determine the relative phase which we would expect to see at each receiver. A more sensitive measure of mismatch could thus be constructed by also comparing the expected and actual phases at each receiver and frequency. Such an algorithm would, in effect, be looking for spherical waves in the received information which correspond to the location of the fictitious scatterer.

An investigation into this enhancement would need, however, to first consider whether the phase of the scattered wavefront acts like that of a spherical wave centered at the scatterer — that is, does the scattering process result in a scattering *phase* pattern as well as a scattering *amplitude* pattern?

A yet more ambitious variation of this approach could also be investigated where the estimate of the phase was replaced with an estimate of the time-of-

flight. This would seem to also require that the simple comparison of phases be replaced with some manner of correlation.

#### **6.4.4 Future Work: Noise and Interference**

In Section 6.3.3, it was noted how various environmental events could cause a corruption of the pattern-match and mismatch methods. These same considerations apply to the swept-frequency method in some applications, such as for the guidance of a mobile robot.

#### **6.4.5 Future Work: Use of Frequencies**

There are several questions concerning the use of frequencies which might be investigated. It would be useful to determine an analytical or other approach to the selection of frequencies which yielded the maximum resolution while also eliminating false peaks. These goals may also be better met by weighing the results of the frequency comparisons unequally, instead of always weighing them equally as was done in this study.

In an experiment, considerable time can be saved by transmitting a broadband pulse instead of individual frequencies. It would thus be useful to investigate whether this would yield the same results as a stepped-frequency sweep for specular scattering. However, for extended scatterers, the interference between widely separated points on the scatterer may not occur at a given frequency (or, at least, may not occur in quite the same way) if the wave does not remain at that frequency for at least a certain length of time.

#### 6.4.6 Future Work: Scatterer Locations

In this study, we have sought only to find the scattering center rather than the location of the individual point reflectors or the boundaries of an extended scatterer. It would be useful to investigate how knowledge of the scattering center would be used in an actual application. For example, could a mobile robot avoid obstacles knowing only the location of their scattering center? If not, some algorithm could perhaps be developed which could estimate the boundaries of an extended object once its identity, scattering center, and orientation had been determined.



## References

- 1 C. W. Oseen, "Die einsteinsche, nadelstichstrahlung und die Maxwellschen gleichungen," *Annalen der Physik* **69**, pp.202-204 (1922).
- 2 E. K. Miller, "Comments on 'Resolution of coherent sources incident on a circular antenna array'," *Proceedings of the IEEE* **69** (1), p.122 (January 1981).
- 3 T. S. Graham, "A new method for studying acoustic radiation using long-wavelength acoustical holography," in *Acoustical Holography*, edited by A. F. Methereell and L. Larmore (Plenum Press, New York, 1970), Volume 2, pp.353-356.
- 4 E. E. Watson, "Detection of sound radiation from plates using long wavelength acoustical holography," Ph.D. dissertation, The Pennsylvania State University, State College, PA (1971).
- 5 E. E. Watson, "Detection of acoustic sources using long wavelength acoustical holography," *Journal of the Acoustical Society of America* **54**, pp.685-691 (1973).
- 6 D. L. VanRooy, "Digital reconstructions from ultrasonic systems", I.B.M. Scientific Center, Houston, Texas, Publication 320.2372 (August 1969).
- 7 D. L. VanRooy, "Digital ultrasonic wavefront reconstruction in the near field," I.B.M. Scientific Center, Houston, Texas, Publication 320.2402 (May 1971).
- 8 P. R. Stepanishen and K. C. Benjamin, "Forward and backward projection of acoustic fields using FFT methods," *Journal of the Acoustical Society of America* **71** (4), pp.803-812 (April 1982).
- 9 K. E. Eschenberg and S. I. Hayek, "Measurement of the nearfield intensity of vibrating ribbed plates by underwater nearfield imaging," *Journal of the Acoustical Society of America*, Supplement 1 **76**, p.S45 (Fall 1984).
- 10 K. E. Eschenberg and S. I. Hayek, "Measurement of submerged-plate intensity using nearfield acoustical holography," in *Inter-Noise 86*, edited by R. Lotz (Noise Control Foundation, Poughkeepsie, NY, 1986), pp.1229-1234.
- 11 K. E. Eschenberg and S. I. Hayek, "Imaging the nearfield of a submerged-plate using acoustical holography," in *Acoustical Imaging*, edited by H. W. Jones (Plenum Press, New York, 1987), Volume 15, pp.659-673.

- 12 E. G. Williams, H. D. Dardy, R. G. Fink, "Nearfield acoustical holography using an underwater automated scanner", *Journal of the Acoustical Society of America* **78** (2), pp.789-798 (August 1985).
- 13 R. L. Cohen, "Digital wavefront reconstruction for acoustical applications," PhD dissertation, The Pennsylvania State University, State College, PA (1979), p.203.
- 14 J. W. Goodman, *Introduction to Fourier Optics* (McGraw-Hill, San Francisco, CA, 1968), Chap.3, pp.48-54.
- 15 E. Skudrzyk, *The Foundations of Acoustics* (Springer-Verlag, Wien, 1971), p.285.
- 16 R. L. Cohen, "Digital wavefront reconstruction for acoustical applications," PhD dissertation, The Pennsylvania State University, State College, PA (1979), p.130.
- 17 M. S. Lang, "An experimental analysis of the basic phenomena involved in modern diffraction theories," PhD dissertation, The Pennsylvania State University, State College, PA (1980), p.367.
- 18 M. S. Narasimhan, M. Karthikeyan and S. Jegannathan, "Accurate determination of object-image distance for planar objects in acoustical imaging," *Journal of the Acoustical Society of America* **79** (2), pp.382-386 (February 1986).
- 19 J. P. Powers and D. E. Mueller, "A computerized acoustic imaging technique incorporating automatic object recognition," in *Acoustical Holography*, edited by P. S. Green (Plenum Press, New York, 1974), Volume 5, pp.527-539.
- 20 M. S. Lang, "An experimental analysis of the basic phenomena involved in modern diffraction theories," PhD dissertation, The Pennsylvania State University, State College, PA (1980), pp.379-383.
- 21 E. J. Pisa, S. Spinak and A. F. Metherell, "Color acoustical holography," in *Acoustical Holography*, edited by A. F. Metherell and L. Larmore (Plenum Press, New York, 1970), Volume 2, pp.295-304.
- 22 A. Korpel and R. L. Whitman, "Elimination of spurious detail in acoustic images," in *Acoustical Holography*, edited by P. S. Green (Plenum Press, New York, 1974), Volume 5, pp.373-390.



- 23 K. Sasaki, T. Sato and Y. Nakamura, "An effective utilization of spectral spread in holographic passive imaging systems," *IEEE Transactions on Sonics and Ultrasonics* **SU-25** (4), pp.177-184, July 1978.
- 24 F. P. Higgins, S. J. Norton and M. Linzer, "Optical interferometric visualization and computerized reconstruction of ultrasonic fields," *Journal of the Acoustical Society of America* **68** (4), pp.1169-1176 (October 1980).
- 25 D. H. Johnson, "The application of spectral estimation methods to bearing estimation problems," *Proceedings of the IEEE* **70** (9), pp.1018-1028 (September 1982).
- 26 G. Arfken, *Mathematical Methods for Physicists* (Academic Press, New York, 1971), 2nd printing, pp.662-666.
- 27 W. R. Hahn, "Optimum signal processing for passive sonar range and bearing estimation," *Journal of the Acoustical Society of America* **58** (1), pp.201-207 (July 1975).
- 28 H. Ermert and R. Karg, "Multifrequency acoustical holography," *IEEE Transactions on Sonics and Ultrasonics* **SU-26** (4), pp.279-286 (July 1979).
- 29 T. J. M. Jeurens, J. C. Somer, F. A. M. Smeets, A. P. G. Hoeks, "Two-dimensional Wiener inverse filtering in echographic imaging: possibilities and restrictions," in *Acoustical Imaging*, edited by A. J. Berkhout, J. Ridder, and L. F. van der Wal (Plenum Press, New York, 1985), Volume 14, pp.471-477.
- 30 J. H. Kim, B. S. Lee and S. P. Park, "Prior inverse filtering for high-resolution pulse-echo images," in *Acoustical Imaging*, edited by A. J. Berkhout, J. Ridder, and L. F. van der Wal (Plenum Press, New York, 1985), pp.447-458.
- 31 R. L. Cohen, "Digital wavefront reconstruction for acoustical applications," PhD dissertation, The Pennsylvania State University, State College, PA (1979), p.26.
- 32 E. Skudrzyk, *The Foundations of Acoustics* (Springer-Verlag, Wien, 1971), pp.498-499.

- 33 J. Ball, S. A. Johnson and F. Stenger, "Explicit inversion of the Helmholtz equation for ultra-sound insonification and spherical detection," in *Acoustical Imaging*, edited by K. Y. Wang (Plenum Press, New York, 1980), Volume 9, pp.451-461.
- 34 S. J. Norton and M. Linzer, "Ultrasonic reflectivity imaging in three dimensions: exact inverse scattering solutions for plane, cylindrical, and spherical apertures," *IEEE Transactions On Biomedical Engineering BME-28* (2), pp.202-220 (February 1981).
- 35 Y. Bresler and A. Macovski, "Three-dimensional reconstruction from projects with incomplete and noisy data by object estimation," *IEEE Transactions on Acoustics, Speech and Signal Processing ASSP-35* (8), pp.1139-1152 (August 1987).
- 36 R. F. Koppelman and P. N. Keating, "Three-dimensional acoustic imaging," in *Acoustical Imaging*, edited by A. F. Metherell (Plenum Press, New York, 1980), Volume 8, pp.267-279.
- 37 S. J. Norton and M. Linzer, "Backprojection reconstruction of random source distributions," *Journal of the Acoustical Society of America* **81** (4), pp.977-985 (April 1987).
- 38 A. K. Nigam, "Condenser-microphone arrays in acoustical holography - a review," *Journal of the Acoustical Society of America* **55** (5), pp.978-985 (May 1974).
- 39 G. C. Carter, "Variance bounds for passively locating an acoustic source with a symmetric line array," *Journal of the Acoustical Society of America* **62** (4), pp.922-926 (October 1977).
- 40 S. U. Pillai, Y. Bar-Ness and F. Haber, "A new approach to array geometry for improved spatial spectrum estimation," *Proceedings of the IEEE* **73** (10), pp.1522-1524 (October 1985).
- 41 G. L. Duckworth, "Adaptive array processing for acoustic imaging," in *Acoustical Imaging*, edited by K. Y. Wang (Plenum Press, New York, 1980), Volume 9, pp.177-204.
- 42 S. M. Kay and S. L. Marple, Jr., "Spectrum analysis — a modern perspective," *Proceedings of the IEEE* **69** (11), pp.1380-1419 (November 1981).

- 43 R. E. Abdel-Aal, C. J. Macleod and T. S. Durrani, "Expansion of acoustic hologram apertures using ARMA modelling techniques," in *Acoustical Imaging*, edited by E. A. Ash and C. R. Hill (Plenum Press, New York, 1982), Volume 12, pp.697-707.
- 44 P. R. Gutowski, E. A. Robinson and S. Treitel, "Spectral estimation: fact or fiction," IEEE Transactions On Geoscience Electronics **GE-16** (2), pp.80-84 (April 1978).
- 45 M. Wax, "Order selection for AR models by predictive least squares," IEEE Transactions on Acoustics, Speech and Signal Processing **ASSP-36** (4), pp.581-588 (April 1988).
- 46 S. Li and B. W. Dickinson, "Application of the lattice filter to robust estimates of AR and ARMA models," IEEE Transactions on Acoustics, Speech and Signal Processing **ASSP-36** (4), pp.502-512 (April 1988).
- 47 C. E. Shannon, "A mathematical theory of communication," The Bell System Technical Journal **27** (3), pp.379-423 (July 1948).
- 48 E. T. Jaynes, "Information theory and statistical mechanics," The Physical Review **106** (4), pp.620-630 (15 May 1957).
- 49 J. P. Burg, "Maximum entropy spectral analysis," Proceedings of the 37th Annual International Meeting of the Society of Explorational Geologist, Oklahoma City (1967), pp.85-86 .
- 50 R. N. McDonough, "Application of the maximum-likelihood method and the maximum-entropy method to array processing," in *Nonlinear Methods of Spectral Analysis*, edited by S. Haykin (Springer-Verlag, New York, 1979), Chapter 6, pp.181-244.
- 51 A. D. Pierce, *Acoustics: An Introduction to Its Physical Principles and Applications* (McGraw-Hill, New York, NY, 1981); p.431.
- 52 C. L. Byrne and R. M. Fitzgerald, "High-resolution beamforming with oversampled arrays," Journal of the Acoustical Society of America **74** (4), pp.1224-1227 (October 1983).
- 53 M. Kaveh and G. A. Lippert, "An optimum tapered Burg algorithm for linear prediction and spectral analysis," IEEE Transactions on Acoustics, Speech and Signal Processing **ASSP-31** (2), pp.438-444 (April 1983).
- 54 J. Capon, "High-resolution frequency-wavenumber spectrum analysis," Proceedings of the IEEE **57** (8), pp.1408-1418 (August 1969).

- 55 J. Capon, R. J. Greenfield and R. J. Kolker, "Multidimensional maximum-likelihood processing of a large aperture seismic array", *Proceedings of the IEEE* **55** (2), pp.192-211 (February 1967)
- 56 G. Bienvenu and L. Kopp, "Source power estimation method associated with high resolution bearing estimation," *Proceedings of the IEEE ICASSP*, pp.153-156 (1981).
- 57 R. O. Schmidt, "A signal subspace approach to multiple emitter location and spectral estimation," Ph.D. dissertation (Stanford University, Stanford, CA) (1981);
- 58 S. R. DeGraaf and D. H. Johnson, "Capability of array processing algorithms to estimate source bearings," *IEEE Transactions on Acoustics, Speech and Signal Processing ASSP-33* (6), pp.1368-1379 (December 1985).
- 59 C. D. Seligson, "Comments on 'High-resolution frequency-wavenumber spectrum analysis'," *Proceedings of the IEEE* **58** (6), pp.947-949 (June 1970).
- 60 R. N. McDonough, "Degraded performance of nonlinear array processors in the presence of data modeling errors," *Journal of the Acoustical Society of America* **51** (4), pp.1186-1193 (April 1972).
- 61 Y. Q. Yin and P. R. Krishnaiah, "On some nonparametric methods for detection of the number of signals," *IEEE Transactions on Acoustics, Speech and Signal Processing ASSP-35* (11), pp.1533-1538 (November 1987).
- 62 D. H. Johnson and S. R. DeGraaf, "Improving the resolution of bearing in passive sonar arrays by eigenvalue analysis," *IEEE Transactions on Acoustics, Speech and Signal Processing ASSP-30* (4), pp.638-647 (August 1982).
- 63 L. Zou and B. Liu, "One resolving two-dimensional sinusoids in white noise using different spectral estimates," *IEEE Transactions on Acoustics, Speech and Signal Processing ASSP-36* (8), pp.1338-1350 (August 1988).
- 64 Y. Bresler and A. Macovski, "On the number of signals resolvable by a uniform linear array," *IEEE Transactions on Acoustics, Speech and Signal Processing ASSP-34* (6), pp.1361-1375 (December 1986).

- 65 T. Shan and T. Kailath, "Adaptive beamforming for coherent signals and interference," *IEEE Transactions on Acoustics, Speech and Signal Processing* **ASSP-33** (3), pp.527-536 (June 1985).
- 66 J. E. Evans, J. R. Johnson and D. F. Sun, "Application of advanced signal processing techniques to angle of arrival estimates in ATC navigation and surveillance systems," M.I.T. Lincoln Laboratory, Lexington, MA, Technical Report 582 (June 1982).
- 67 R. T. Williams, S. Prasad, A. K. Mahalanabis and L. H. Sibul, "Localization of Coherent Sources Using A Modified Spatial Smoothing Technique," *Proceedings of the IEEE ICASSP*, pp.2352-2355 (1987).
- 68 H. Wang and M. Kaveh, "Coherent signal-subspace processing for the detection and estimation of angles of arrival of multiple wide-band sources," *IEEE Transactions on Acoustics, Speech and Signal Processing* **ASSP-33** (4), pp.823-831 (August 1985).
- 69 J. A. Cadzow, "A high resolution direction-of-arrival algorithm for narrow-band coherent and incoherent sources," *IEEE Transactions on Acoustics, Speech and Signal Processing* **ASSP-36** (7), pp.965-979 (July 1988).
- 70 Y. Bresler, V. U. Reddy and T. Kailath, "Optimum beamforming for coherent signal and interferences," *IEEE Transactions on Acoustics, Speech and Signal Processing* **ASSP-36** (6), pp.833-843 (June 1988).
- 71 A. D. Pierce, *Acoustics: An Introduction to Its Physical Principles and Applications* (McGraw-Hill, New York, 1981), p.427.
- 72 A. D. Pierce, *Acoustics: An Introduction to Its Physical Principles and Applications* (McGraw-Hill, New York, 1981), p.495.
- 73 M. Abramowitz and I. A. Stegun, *Handbook of Mathematical Functions* (Dover, New York, 1972), 9th printing, pp.321-322.
- 74 R. P. Kendig and S. I. Hayek, "Diffraction by a hard-soft barrier," *Journal of the Acoustical Society of America* **70** (4), pp.1156-1165 (October 1981).
- 75 D. C. Chan, N. H. Farhat, M. S. Chang and J. D. Blackwell, "New results in computer simulated frequency swept imaging," *Proceedings of the IEEE* **65** (8), pp.1214-1215 (August 1977).

- 76 N. H. Farhat, T. Dzekov and E. Ledet, "Computer simulation of frequency swept imaging," Proceedings of the IEEE **64** (9), pp.1453-1454, (September 1976).
- 77 N. H. Farhat, "High resolution longwave frequency swept holographic imaging," IEEE Ultrasonics Symposium Proceedings, pp.68-72 (1975).
- 78 N. H. Farhat, "A new imaging principle," Proceedings of the IEEE **64** (3), pp.379-380 (March 1976).
- 79 D. N. Swingler and C. S. Nilsen, "Comments on 'Computer simulation of frequency swept imaging'," Proceedings of the IEEE **65** (8), pp.1223-1224, (August 1977).
- 80 W. M. Waters, "Comments on 'A new imaging principle'," Proceedings of the IEEE **66** (5), pp.609-610 (May 1978).
- 81 E. J. Skudrzyk, S. I. Hayek and A. D. Stuart, "Acoustic Diffraction Part I: Plane Diffraction and Wedges," Applied Research Laboratory, The Pennsylvania State University, State College, PA, Technical Memorandum 73-109, p.62 (1973).
- 82 E. J. Skudrzyk, S. I. Hayek and A. D. Stuart, "Acoustic Diffraction Part I: Plane Diffraction and Wedges," Applied Research Laboratory, The Pennsylvania State University, State College, PA, Technical Memorandum 73-109, p.63-64 (1973).
- 83 E. Skudrzyk, *The Foundations of Acoustics* (Springer-Verlag, Wien, 1971), p.518.
- 84 E. Skudrzyk, *The Foundations of Acoustics* (Springer-Verlag, Wien, 1971), p.515.
- 85 S. D. Conte and C. de Boor, *Elementary Numerical Analysis: An Algorithmic Approach* (McGraw-Hill, New York, 1972), second edition, pp.234-235.

## Appendix

### Fourier Derivation of the Holography Equation

A method for the derivation of the holography reconstruction equation using a Fourier transform of the wave equation was suggested by Eschenberg and Hayek<sup>11</sup> and is shown in greater detail here. As in Chapter 2, the two-dimensional Helmholtz wave equation when the pressure has a harmonic time dependence is given by

$$\nabla^2 R(x, z) + k^2 R(x, z) = 0 \quad (\text{A.1})$$

with the Laplacian defined here as

$$\nabla^2 = \frac{\partial^2}{\partial x^2} + \frac{\partial^2}{\partial z^2}. \quad (\text{A.2})$$

After multiplying all terms by  $(1/\sqrt{2\pi}) \exp(-jk_x x)$  and then integrating over all values of  $x$  we have

$$\mathcal{F} \left( \frac{\partial^2 R(x, z)}{\partial x^2} \right) + \mathcal{F} \left( \frac{\partial^2 R(x, z)}{\partial z^2} \right) + \mathcal{F} (k^2 R(x, z)) = 0 \quad (\text{A.3})$$

where  $\mathcal{F}$  and  $\tilde{R}$  represent the forward Fourier transform. We wish to modify each term of Eq. (A.3) so that it is expressed only in terms of the Fourier transform of  $R$ . This is a trivial matter for the last term since  $k_x$  is independent of the variable of integration  $x$ . The order in which the integration and derivative are performed in the second term can also be interchanged in a trivial manner since the Fourier transform has no dependence on  $z$ . However, the first term of Eq. (A.3) is more complicated since the Fourier transform has a dependence on  $x$ .

A series of expansions can provide the needed substitution. We begin

by noting that the second derivative of the Fourier transform with respect to  $x$  equals zero because there is no dependence on  $x$  left after the Fourier transform (it has been replaced with a dependence on  $k_x$ ). This quantity can be expanded as

$$\begin{aligned}
 & \frac{\partial^2 \mathcal{F}(R(x, z))}{\partial x^2} \\
 &= \frac{1}{\sqrt{2\pi}} \int_{-\infty}^{\infty} \frac{\partial^2}{\partial x^2} [R(x, z) e^{-j k_x x}] dx \\
 &= \frac{1}{\sqrt{2\pi}} \int_{-\infty}^{\infty} \frac{\partial}{\partial x} \left[ \frac{\partial R(x, z)}{\partial x} e^{-j k_x x} - j k_x R(x, z) e^{-j k_x x} \right] dx \\
 &= \frac{1}{\sqrt{2\pi}} \int_{-\infty}^{\infty} \left[ \frac{\partial^2 R(x, z)}{\partial x^2} e^{-j k_x x} - j 2 k_x \frac{\partial R(x, z)}{\partial x} e^{-j k_x x} \right. \\
 &\quad \left. - k_x^2 R(x, z) e^{-j k_x x} \right] dx \\
 &= \mathcal{F} \left( \frac{\partial^2 R(x, z)}{\partial x^2} \right) - j 2 k_x \mathcal{F} \left( \frac{\partial R(x, z)}{\partial x} \right) - k_x^2 \tilde{R}(k_x, z) \\
 &= 0
 \end{aligned} \tag{A.4}$$

or

$$\mathcal{F} \left( \frac{\partial^2 R(x, z)}{\partial x^2} \right) = j 2 k_x \mathcal{F} \left( \frac{\partial R(x, z)}{\partial x} \right) + k_x^2 \tilde{R}(k_x, z). \tag{A.5}$$

A similar expansion of the first derivative of the Fourier transform yields

$$\frac{\partial \mathcal{F}(R(x, z))}{\partial x} = \mathcal{F} \left( \frac{\partial R(x, z)}{\partial x} \right) - j k_x \tilde{R}(k_x, z) = 0 \tag{A.6}$$

or

$$\mathcal{F} \left( \frac{\partial R(x, z)}{\partial x} \right) = j k_x \tilde{R}(k_x, z). \tag{A.7}$$



Substituting Eq. (A.7) into Eq. (A.5) we find

$$\mathcal{F} \left( \frac{\partial^2 R(x, z)}{\partial x^2} \right) = -k_x^2 \tilde{R}(k_x, z). \quad (\text{A.8})$$

Finally, we substitute this result into Eq. (A.3) and use  $k^2 = k_x^2 + k_z^2$  to arrive at

$$\frac{\partial^2 \tilde{R}(k_x, z)}{\partial z^2} + k_z^2 \tilde{R}(k_x, z) = 0 \quad (\text{A.9})$$

which is the same as Eq. (2.6).

---

The Pennsylvania State University  
Applied Research Laboratory  
P.O. Box 30  
State College, PA 16804